

# **A Multiwavelength Analysis of the Effect of Cluster Environments on Galaxy Evolution**

©2021

**Jennifer Rose Cooper**

B.A. Mathematical Geophysics, Cornell University, 2014

B.A. Archaeology, Cornell University 2014

M.S. Physics, California State University Los Angeles, 2017

Submitted to the graduate degree program in Department of Physics and Astronomy and the Graduate Faculty of the University of Kansas in partial fulfillment of the requirements for the degree of Doctor of Philosophy.

Committee members

---

Gregory Rudnick, Chairperson

---

Allison Kirkpatrick

---

Thomas Cravens

---

Christopher Rogan

---

Christophe Royon

---

David Mechem, External Reviewer

Date defended: May 7, 2021

The Dissertation Committee for Jennifer Rose Cooper certifies  
that this is the approved version of the following dissertation :

A Multiwavelength Analysis of the Effect of Cluster Environments on Galaxy Evolution

---

Gregory Rudnick, Chairperson

Date approved: June 10, 2021

# Abstract

In this work, we present analysis to constrain the role of local environment on galaxy evolution. The hot, dense galaxy cluster environment is utilized as a comparative laboratory to galaxies that reside in the less dense field where it is ‘alone’. Within clusters, the buildup of red, passive galaxies is observed to be in excess of the field, yet the mechanisms responsible for this graveyard of galaxies remain to be clearly identified. This indicates that external gas quenching in the cluster environment such as through ram-pressure stripping is potentially dominating over any internal processes that deplete the gas supply. Observations focusing on the cores of clusters reveal that galaxies are typically already quenched and in a passive state, indicating that the processes responsible occur while the galaxy is located in the outskirts. Therefore, expanding observations beyond the cores is crucial towards deriving a more representative sample across varying cosmic densities and is more likely to capture the site of galaxy transformation *in situ*. With current telescope capability ranging from spectroscopy to deep imaging, a thorough inspection of individual members of a galaxy cluster is feasible.

This study combines the power of ground-based wide-field imaging with space-based slitless spectroscopy to deliver a multifaceted look into galaxies in clusters as they were more than 5 billion years ago. This is accomplished in 2 distinct ways: 1) determination of the passive fraction through a binary classification in  $UVJ$  color-color space to determine whether a galaxy is star-forming or quiescent and 2) further refine these efforts with  $H\alpha$ -based star-formation rate observations from the *Hubble Space Telescope (HST)/WFC3*. The first portion of this thesis is devoted towards an aggregate view of the EDisCS clusters, where cluster membership is defined to at least the infall radius of each galaxy cluster. This data sample consists of 13 mid-mass clusters in the range  $0.4 < z < 0.8$ , with spectroscopic redshifts derived from the Low-Dispersion Prism on Magellan and photometric data collected with the Wide Field Imager on the 2.2m Max Planck

Gesellschaft/European Southern Observatory (MPG/ESO) telescope, the MOSAIC instrument on the Cerro Tololo Inter-American Observatory (CTIO) Blanco or the Mayall 4-meter telescope.

On a cluster-by-cluster basis, the passive fraction increases with a decrease in redshift, which is directly related to the buildup of passive galaxies over time. When compared to stellar mass, nearly all of the most massive cluster galaxies are passive across the redshift range, which is in agreement with the literature. As mid-mass clusters, EDisCS has a lower passive fraction than massive clusters such as Planck and GLASS, which may indicate that external quenching processes from the local environment are less dominant in EDisCS. Regardless of environment, the most massive galaxies are predominantly passive, while the cluster cores are mainly ( $> 90\%$ ) quiescent at all stellar masses and redshifts. Additionally, the passive fraction displays a radial dependence at higher  $z$  ( $0.6 < z < 0.8$ ) that is not apparent at lower redshifts and higher stellar masses. This suggests that the infall region is a site of galaxy transformation and a quenching event may be captured between our high and low redshift bins.

Next, we investigate select areas from the cores and infall regions of 4 EDisCS clusters at  $z \sim 0.5$  with *HST*/WFC3 G102 grism and F105W imaging, which provide  $H\alpha$ -based star-formation rates (SFRs) and undistorted images of the stellar and gas disks. The data reduction involves introducing a redshift prior from previous observations to the software to aid in the correct determination of the  $H\alpha$  line. The SFRs are calculated assuming a Chabrier IMF with corrections for post-AGB emission, dust extinction, and contribution from the [NII] doublet. The SFR vs. stellar mass relation does not show any difference between the cluster and field environments, which is in agreement with other main sequence studies at similar redshift ranges. However, there are a number of *UVJ* passive galaxies in this sample that display prominent  $H\alpha$  emission while appearing on the main sequence. This indicates that passive galaxies can still have active star-formation, despite appearing ‘red’. In conjunction with the results from the first part of this study on the passive fraction, photometrically ‘red’ galaxies can still be actively forming stars and this reinforces the importance of combined methods to investigate galaxy evolution.

The final portion of this study aims to reduce manual labor derived from astronomical obser-

vations. From the *HST* Cycle 20 data, there were 13,000+ grism extractions, with some having multiple emission line maps in addition to the stellar images. Sorting through each of the images is a tedious task and may be ignored in the case of large sky surveys. However, these images contain critical information and should be inspected for basic quality metrics at a minimum, particularly if poor modeling or an artifact presents as a plausible signal. With this in mind, a convolutional neural network is trained to distinguish between an image that has contamination, a detection, is noisy, or is on the edge of the chip. A set of more than 1,000 grism emission line maps are used to train a convolutional neural network on 2, 3, or 4 image classes. A top accuracy of 86% is achieved with the GLASS Cycle 21 data with 2 classes defining either contaminated or uncontaminated images. Accuracy decreases with an increase in the number of classes, which is likely due to low resolution extractions and unique emission maps. While accuracy rates  $>90\%$  are desirable, this neural network proves that grism data can be trained and automatically classified in less than half the time it would take a human to complete the same task.

In conclusion, we have demonstrated 2 powerful and complementary tools to investigate the role of environment galaxy evolution in clusters. The star-formation rate results revealing *UVJ*-quiescent core galaxies with significant  $H\alpha$  emission contributes an interesting point towards how much weight can be given to passive fraction results. With the latter, we are only able to determine rest-frame colors that generally correlate with star-formation. However, core galaxies, which have been the culprit of higher proportions of ‘dead’ galaxies in clusters, may actually have ongoing star-formation, which is evident in the lack of differences between environments on the main sequence diagram. The galaxy may appear redder for a variety of reasons including AGN, heated gas, or that they are in the process of quenching. Further observations of galaxies in various environments comparing rest-frame colors and star-formation rates for galaxies, along with high resolution spectra, will help refine this result.

# Contents

<b>1</b>	<b>Introduction</b>	<b>1</b>
1.1	Characterizing Galaxies in the Universe . . . . .	1
1.2	Star Formation in Galaxies . . . . .	2
1.3	The Role of Cosmic Environment on Galaxy Evolution . . . . .	4
1.3.1	Gas Depletion Mechanisms . . . . .	6
1.4	Quenching Timescales . . . . .	7
1.5	Methods for Observing Processes in Galaxies . . . . .	8
1.6	Protoclusters: A Search for the Beginning of Clusters . . . . .	11
1.7	Machine Learning Overview . . . . .	11
1.8	This Work . . . . .	13
1.9	Commonly Used Terminology . . . . .	15
<b>2</b>	<b>Characteristics of the Sample</b>	<b>17</b>
2.1	Introduction . . . . .	17
2.2	Photometric and Spectroscopic Observations of the Cluster Cores . . . . .	17
2.3	Wide Field Catalog of EDisCS Clusters . . . . .	19
2.3.1	Photometric Corrections . . . . .	22
2.4	Stellar Mass Derivation & Comparison . . . . .	23
2.5	Environmental Definitions . . . . .	24
2.5.1	Cluster Core . . . . .	26
2.5.2	Infall Region . . . . .	26
2.5.3	Field Sample . . . . .	27
2.6	Sample Overview . . . . .	29

<b>3</b>	<b>EDisCS Quiescent Fraction - Investigating the Evolutionary Transition</b>	<b>41</b>
3.1	EDisCS Passive Fraction . . . . .	41
3.1.1	Passive v. Star-forming Galaxies . . . . .	43
3.2	Results . . . . .	44
3.2.1	$f_{passive}$ vs. Redshift . . . . .	44
3.2.2	$f_{passive}$ vs. Stellar Mass . . . . .	45
3.2.3	$f_{passive}$ vs. Cluster-centric Radius . . . . .	49
3.3	Discussion . . . . .	53
3.4	Conclusions & Future Work . . . . .	57
<b>4</b>	<b>H<math>\alpha</math> Star-Formation Rate Relation</b>	<b>59</b>
4.1	<i>HST</i> /WFC3 observations . . . . .	59
4.1.1	Data Reduction . . . . .	63
4.1.2	H $\alpha$ Line Extraction & Redshift Prior . . . . .	63
4.1.3	Star-formation Rate Corrections . . . . .	66
4.2	Results . . . . .	68
4.2.1	Galaxy Sample Properties . . . . .	68
4.2.2	Stellar Mass - SFR Relations . . . . .	74
4.3	Visual Inspection of Galaxies with GRIZLI . . . . .	76
4.4	Main Sequence Comparisons . . . . .	76
4.5	Discussion . . . . .	81
4.5.1	<i>UVJ</i> -quiescent galaxies with H $\alpha$ emission . . . . .	83
4.6	Conclusions & Future Work . . . . .	85
<b>5</b>	<b>Machine Learning with <i>HST</i> grism data</b>	<b>87</b>
5.1	Applications of Machine Learning to <i>HST</i> Grism Extractions . . . . .	87
5.1.1	The Convolutional Neural Network . . . . .	88
5.1.1.1	Training . . . . .	89

5.2	System Specifics . . . . .	92
5.2.1	PyTorch: Python’s Machine Learning Toolkit . . . . .	92
5.2.2	Computer Hardware . . . . .	92
5.2.3	vgg16 Architecture . . . . .	93
5.3	Training Data & Class Definitions . . . . .	93
5.4	Results . . . . .	94
5.5	Discussion . . . . .	96
5.6	Conclusions & Future Work . . . . .	100
<b>6</b>	<b>Conclusions</b>	<b>102</b>
6.1	Future Work . . . . .	105
<b>A</b>	<b><i>HST</i> Catalogs &amp; Data Products</b>	<b>107</b>
<b>B</b>	<b>GRIZLI Prior Code</b>	<b>112</b>
<b>C</b>	<b>PyTorch CNN Code</b>	<b>115</b>

# List of Figures

1.1	This illustration shows the star formation rate vs. stellar mass relation, which is known as the main sequence. Galaxies located along the blue oval are star-forming, where more massive galaxies create stars at a fast rate. Galaxies with extremely high star formation rates can be starbursting, which is shown as purple stars above main sequence. Finally, as galaxies quench, their star formation decreases and they eventually fall off of the main sequence. . . . .	4
1.2	This illustration shows the rest-frame $UVJ$ diagram with the Williams et al. (2009) boundaries for either quiescent or star-forming as black lines. Galaxies will typically be located somewhere among the passive clump or the star-forming sequence. . . . .	9
2.1	This figure compares the two stellar mass derivations with $B - V$ and $U - V$ for the EDisCS core observations. Both the core and field galaxies align on a 1-to-1 line, indicating that the new $U - V$ are reliable. . . . .	24
2.2	This illustrates the environmental definitions within a galaxy cluster, where each red/blue star represents an individual galaxy. The orange circle is the virial radius and the region encompassed within this area is defined as the core. Outside of the virial radius is the infall region. . . . .	28
2.3	The distribution of cluster members as a function of $R_{200}$ . The full sample is shown as the grey dash while the mass-complete sample is in purple. The virial radius distance is demonstrated by the vertical dashed line. The LDP survey includes cluster membership to a max of $7R_{200}$ . . . . .	29

2.4 (Top Left) The distribution of mass-complete samples from the EDisCS core survey for the core (green dash) and field (purple) environments. The median values for each sample is demonstrated by the vertical line. The core sample is more deficient in massive galaxies when compared to the field sample. (Top Right) Rest-frame *UVJ* color-color diagram for the mass-complete sample with Williams et al. (2009) boundaries for quiescent (upper left) or star-forming galaxies. (Bottom Left) The distribution of mass-complete samples from the LDP survey for the core (green dash), infall (blue) and field (purple) environments. The median values for each sample is demonstrated by the vertical line. Similarly to the EDisCS core sample above, the core sample is more deficient in massive galaxies when compared to the infall and field samples. (Bottom Right) Rest-frame *UVJ* color-color diagram for the mass-complete sample with Williams et al. (2009) boundaries for quiescent (upper left) or star-forming galaxies. . . . . 31

2.5 (Left) The RA and Dec FOV for each cluster in the EDisCS core survey, where everything with a redshift is a grey dot. Cluster members are circles that are either red for *UVJ*-passive or blue for star-forming. Filled circles represent mass-complete cluster members. The orange oval represents  $R_{200}$  around the brightest cluster galaxy; some clusters do not show this due to the FOV being within  $R_{200}$ . A majority of these observations cover  $R_{200}$  within each cluster. (Center) *UVJ* color-color diagrams for the mass-complete cluster members at all radii (green circle) and field galaxies (purple stars) with the Williams et al. (2009) definitions for passive (upper left) and star-forming regions. (Right) The stellar mass distributions and median values for cluster (green) and field (purple) galaxies. . . . . 36

2.6 (Left) The RA and Dec FOV for each LDP cluster, where everything with an LDP redshift is a grey dot. Cluster members are circles that are either red for *UVJ*-passive or blue for star-forming. Filled circles represent mass-complete cluster members. The orange oval represents  $R_{200}$  around the brightest cluster galaxy. The blank areas without any dots represent a mask for bright stars where observations could not be completed. The combined LDP and WFI observations extend far beyond the core into the infall region in each cluster. (Center) *UVJ* color-color diagrams for the mass-complete cluster members at all radii (green circle) and field galaxies (purple stars) with the Williams et al. (2009) definitions for passive (upper left) and star-forming regions. (Right) The stellar mass distributions and median values for cluster (green) and field (purple) galaxies. . . . . 40

3.1 The interloper fraction,  $f_{int}$ , as a function of stellar mass. The spectroscopic sample has a shallower mass-completeness level ( $\text{Log}M_*/M_\odot > 10.4$ ) than the photometric sample, so the interloper fraction is extrapolated to cover those mass bins. Note that there were no identified interlopers in the  $\text{Log}M_*/M_\odot$  11.0 – 11.2 mass bin, however, an average of the  $f_{int}$  from  $\text{Log}M_*/M_\odot > 11.0$  is used. . . . . 42

3.2 The passive fraction vs. redshift for each of the LDP EDisCS clusters. Cluster members are shown as green circles and the field (outside  $\pm 0.02$  of  $z_{cluster}$ ) as a purple dashed line with the shaded region corresponding to a  $1\sigma$  binomial error. The buildup of passive galaxies is evident with the increased passive fraction at lower redshifts. The cluster members include all galaxies within the FOV for the cluster. . . . . 45

- 3.3 The passive fraction vs. redshift for each of the LDP EDisCS clusters, but separated by the internal cluster environment. Cluster core members are shown as green circles, cluster infall members as blue triangles, and the field (outside  $\pm 0.02$  of  $z_{cluster}$ ) as a purple dashed line with the shaded region corresponding to a  $1\sigma$  binomial error. Blue and green points are calculated within the same bin, but are staggered for ease of interpretation. The buildup of passive galaxies is still evident with the increased passive fraction at lower redshifts. There isn't a clear trend of passive galaxies with intracluster environment, however, for clusters at  $z < 0.6$ , all but two of the seven have infall regions entirely comprised of passive galaxies. . . . . 46
- 3.4 The passive fraction vs. stellar mass for all EDisCS clusters in the VLT sample, where the cluster  $f_{passive}$  are filled circles and those in the field are shown as open squares. Points encompass the same bin range but are staggered for ease of interpretation. These data only encompass the cluster cores from White et al. (2005). Galaxies are binned by stellar mass and redshift into a lower (Left;  $0.4 < z < 0.6$ , red) and higher (Right;  $0.6 < z < 0.8$ , yellow)  $z$  bin. A comparison to the  $0.5 < z < 1.0$  field  $f_{passive}$  from Muzzin et al. (2013) is shown in grey, the Planck clusters ( $0.5 < z < 0.7$  van der Burg et al. 2018) as brown circles, and comparison field as open brown squares, and GLASS clusters ( $0.3 < z < 0.5$  Morishita et al. 2017) as the purple circles. On the left pane, the black star is positioned as a  $f_{passive} = 1$ ; from Equation 3.1, it is possible to determine a  $f_{passive} > 1$  with the field correction. The  $f_{passive}$  dependency on redshift is apparent with the EDisCS clusters, with an approximate 20% increase in the  $f_{passive}$  from high to low- $z$ . In the low- $z$  bin, only the most massive galaxies have significantly differentiated  $f_{passive}$ , indicating that environmental quenching is not dominant here. Additionally, the core at all  $z$  has a lower  $f_{passive}$  than the massive Planck and GLASS clusters. . . . . 47

- 3.5 The passive fraction vs. stellar mass for all EDisCS clusters in the LDP sample, where cluster galaxies are circles and those in the field are shown as open squares. Galaxies are binned into four stellar masses and by redshift into a lower ( $0.4 < z < 0.6$ , red) and higher ( $0.6 < z < 0.8$ , yellow)  $z$  bin. A comparison to the field  $0.5 (< z < 1.0)$   $f_{passive}$  from Muzzin et al. (2013) is shown in grey, the Planck clusters van der Burg et al. (2018) as brown circles and comparison field as open brown squares, and GLASS clusters Morishita et al. (2017) as the purple circles. The  $f_{passive}$  environmental dependence is much more apparent here, where the low- $z$  bin has a clear and significant difference from the field. . . . . 48
- 3.6 The passive fraction vs. stellar mass separated by intracluster environment for mass-complete galaxies in the LDP cluster (circle) and field (open square) samples. The grey band represents the field sample from Muzzin et al. (2013) ( $0.5 < z < 1.0$ ) and comparison  $f_{passive}$  from cluster studies in Morishita et al. (2017) and van der Burg et al. (2018). (Left) The core sample  $f_{passive}$  vs.  $\text{Log}M_*/M_\odot$ . Nearly all of the galaxies within the virial radius in the low- $z$  sample (red) are quiescent, which is a contrast from the high- $z$  sample (orange) where the lowest mass galaxies are 40% star-forming. (Right) The infall LDP sample  $f_{passive}$  vs.  $\text{Log}M_*/M_\odot$ . The same relation as on the left, but for galaxies beyond the virial radius in the infall region. While the low- $z$  sample displays a similar trend to the lower mass core galaxies, the high- $z$  sample has a strong trend of quiescence with stellar mass. The most massive galaxies are passive in both the core and infall regions. . . . . 50

- 3.7 The passive fraction vs. stellar mass separated by both of the original EDisCS core (circles and dashed line; White et al. 2005) and LDP (triangles and solid line; Just et al. 2019) observations. Orange markers are for the high- $z$  sample while the red is the low- $z$ . The LDP observations are limited to the virial radius while the VLT sample covers the general central core area, but is approximately one magnitude deeper in photometric completeness. The low- $z$  clusters have similar  $f_{passive}$  at all masses, but the high- $z$  sample is less clear. . . . . 51
- 3.8 The passive fraction vs. cluster-centric distance for the EDisCS LDP sample across the mass-complete sample where low- $z$  is in red and high- $z$  in orange. Comparisons to GAMA clusters from Barsanti et al. (2018) at  $z \sim 0.2$  (green open squares), to the Planck Clusters (van der Burg et al., 2018) (brown circles) and from the ELIAS-N1/XMM-LSS fields (Pintos-Castro et al., 2019) as triangles split into high (yellow;  $0.5 < z < 0.7$ ) and low- $z$  bins (red;  $0.3 < z < 0.5$ ). This reveals the passive-dominated cores of clusters, followed by a decrease in the infall region in high- $z$  clusters. While there are a higher fraction of quiescent galaxies at lower redshifts, it is interesting that the outskirts of the clusters are predominantly passive as well. 52
- 3.9 The passive fraction vs. cluster-centric distance for the EDisCS LDP sample in two mass-complete bins. (Top) The lower bin of the mass-complete sample reveals that nearly all of the low- $z$  cluster sample is quiescent. However, this is in stark contrast to the high- $z$  sample, which shows a sharp downturn outside of the virial radius to a  $f_{passive}$  low of 30% from  $2.5 - 3.5R_{200}$ . A gradual increase to 60% is apparent at the outskirts of the cluster. (Bottom) The higher mass sample of the mass-complete galaxies displays a different trend with radial distance. In both redshift bins, 80% or more of the galaxies are passive, with the core entirely devoid of star-forming galaxies. . . . . 54

4.1	The RA and Dec spatial distribution of galaxies in each cluster. Grey dots represent all objects in the FOV that have an LDP redshift, red/blue points signify <i>UVJ</i> -identified quiescent/star-forming cluster member sources, and the virial radius is indicated by the orange circle. <i>HST</i> /WFC3 G102 observations are represented by the black squares, where the two unused infall pointings in Cl1059 are dashed. The distributed sampling among the core and infall region allows for a direct comparison of SFRs by environment. . . . .	62
4.2	(Top) <i>HST</i> WFC3 F105W ( $1.05\mu\text{m}$ infrared direct image of the CL1301-11.2 pointing. (Bottom) <i>HST</i> WFC3 G102 grism data, which provides a spatially resolved spectrum for every object in the FOV of the F105W image. The spectrum for each object is extracted within the grism wavelength range after a polynomial fit to the continuum is subtracted off. . . . .	64
4.3	This collection of data products represents a comparison between the same galaxy with a blind GRIZLI extraction (top row) and with an LDP prior (bottom row). Initially, GRIZLI identifies it as a 2.99 S/N in $\text{H}\alpha$ galaxy at $z = 0.685$ . With the prior, it is now a 3.99 S/N in $\text{H}\alpha$ $z = 0.434$ , resulting in a redshift difference of 0.25. The F105W direct image of the stellar content is on the far left, followed by the detected $\text{H}\alpha$ emission line map. In the third panel is the $p(z)$ from the redshift fitting algorithm (black line), with a blue line indicating the applied Gaussian redshift-prior in the bottom panel. The $p(z)$ after the prior is applied (black line - bottom row, middle panel) is much more constrained than the blind $p(z)$ . Note the redshift scale differences between the extractions. The rightmost panel shows the 1D spectra in green with a fit (red). The blind extraction for the $p(z)$ is very uncertain and could easily be a high or low- $z$ galaxy. The application of the prior dramatically alters the results of the redshift determination. The ability of the prior to be successfully applied to a low S/N $\text{H}\alpha$ galaxy is important towards creating a sample that is not biased towards strong $\text{H}\alpha$ line galaxies. . . . .	65

4.4 (Top) A  $UVJ$  diagram color-coded by  $A_V$  is shown for a subset of the ULTRAVISTA catalog that is similar in redshift and mass distribution to the  $HST$  sample in this study. (Middle) The median in 0.2 bins in  $U - V$  and  $V - J$  from the top plot is shown, which is used to match in color-color space to the  $HST$  sample. If a galaxy falls outside the distribution of ULTRAVISTA, it is matched to the nearest bin.  $UVJ$ -quiescent galaxies have low  $A_V$  as expected and redder star-forming galaxies have elevated values. (Bottom) The spread of each bin across the 75 – 25 percent quartile. The spread is noticeably small in the passive region. Black lines in all plots are the Williams et al. (2009) boundaries. . . . . 69

4.5 (2 left panels): RA and Dec postage stamps show the stellar continuum from the F105W  $1.05\mu\text{m}$  direct image and the  $H\alpha$  emission extraction at  $0.957\mu\text{m}$ . (2 right panels): The fitted redshift, shown as the black line, is fully consistent with the photometric redshift prior probability distribution in blue. The 1D spectrum data are shown in green, with a best fit template in red. Note the prominent  $H\alpha$  emission line at  $0.95\mu\text{m}$  with a S/N of 36.6. . . . . 70

4.6 The GRIZLI-extracted redshift (no prior) vs the GRIZLI-extracted redshift with an applied spectroscopic (top left) or photometric (bottom left) prior for cluster core (blue circle), infall (purple triangle), and field (green star) galaxies. A majority of objects fall along the 1-1 line in black, indicating that the GRIZLI extractions without a prior can be reliable. A pointing with a significantly higher background is apparent in the blind GRIZLI redshifts above the 1-to-1 line in the top and bottom left, which is mostly corrected with the LDP spectroscopic or photometric prior. Several low S/N H $\alpha$  galaxies are also corrected through the prior. The 68% confidence levels for the photometric redshifts are shown with error bars, while the error on the spectroscopic redshifts is insignificant on this scale. This photometric relation has noticeably more scatter around the 1-to-1 line, which is a reflection of the reduced accuracy of photo-z measurements. The GRIZLI-extracted redshifts with a spectroscopic (top right) or photometric (bottom right) prior are shown in comparison to their blind redshift. . . . . 71

4.7  $U - V$  vs.  $V - J$  rest-frame colors color-coded by H $\alpha$ -based SFR for the mass-complete sample of *HST*-observed galaxies. Galaxies with S/N < 3 in H $\alpha$  are grey open symbols, which are predominantly located in the quiescent clump. The SFR color-coded points are the final sample of 67 galaxies selected for S/N > 3 and emission line extraction quality. 51 of the 67 of the sources with F(H $\alpha$ ) S/N > 3 lie in the star-forming region, with 16 residing in the quiescent region. The stellar continuum and H $\alpha$  emission line maps for the 16 passively-classified galaxies are shown in Appendix 4.14. Black dashed lines follow the quiescent and star-forming definition of Williams et al. (2009). . . . . 72

- 4.8 (Left) The distribution of the stellar masses for each of the core, infall, and field mass-complete samples is shown in the blue, purple, and green-dashed histograms. The median value for each sample is the vertical line. (Right) The same three samples are shown with their distributions in redshift space, with the median shown again as the vertical lines. A more significant difference in  $z$  is apparent between the field and cluster samples and is corrected following the equation in § 4.1.3. The elevated median for the infall sample is due to the lack of two samples for Cl1059 at  $z = 0.4564$ , which is the lowest  $z$  cluster. Thus, the median  $z$  is offset to a higher value than the core which includes galaxies from this cluster. . . . . 73
- 4.9 The  $H\alpha$ -based  $SFR - M_*$  main sequence relation for 163  $S/N > 3$  and 82  $S/N < 3$  (down arrow) galaxies. (Left) The locations of these galaxies are distributed among the cluster core (blue circles), infall region (purple triangles), and field samples (green stars), where the mass-completeness line is denoted by the vertical black line and filled in symbols. The  $< 3$   $S/N$  galaxies are plotted at their  $3\sigma$  limit, which occupy the lower end of the SFRs on the main sequence here. These data are systematically above the main sequence relations defined by Whitaker et al. (2012) and Schreiber et al. (2015), which is shown in Figure 4.15. The scatter is larger than the literature, but is still expected due to varying star-formation histories and other disturbances throughout a galaxy lifetime. A comparison is shown to the EDisCS narrow band  $H\alpha$  SFRs in Finn et al. (2005) (orange squares) at  $z = 0.75$  and  $H\alpha$  SFRs Vulcani et al. (2016) from the GLASS clusters at  $0.4 < z < 0.7$  (grey dashed line +  $1\sigma$  scatter). (Right) This same sample is now color-coded by location in Figure 4.7, where blue circles are star-forming and salmon triangles are quiescent. The quiescent galaxies mostly occupy the lower portion of the main sequence, which also have suppressed SFRs. . . . . 75

4.10 Each panel shows the SFR vs. stellar mass as in the left panel of Figure 4.9, but separated by cluster. Each cluster reveals a similar distribution of galaxies above the Vulcani et al. (2016) mean distribution, as well as galaxies with lower SFRs. This indicates that no cluster is offset with respect to the others and influencing the combined relation. The highest- $z$  cluster in the bottom right, C11227, has noticeably fewer galaxies, which is also evident in Figure 4.1. . . . . 77

4.11 The difference in SFR for each of the three environments (blue=core, purple=infall, field=green) from the Vulcani et al. (2016) GLASS clusters  $H\alpha$  main sequence. The median values for each environment are signified by the corresponding vertical line, which are  $\sim 0.7$  dex below the GLASS relation. . . . . 78

4.12 The MIPS  $24\mu\text{m}$  SFRs derived from the EDisCS core pointings of this sample from Finn et al. (2010) compared to the  $H\alpha$  SFRs in this study. There are only matches between the core (blue circle) and field (green triangle) because these *Spitzer* pointings did not extend to the infall region. Left arrows are non-detections in  $24\mu\text{m}$  at the 80% completeness limit. The  $\sim 0.7$  dex offset from the  $24\mu$  SFRs is similar to the one seen with GLASS. . . . . 78

4.13 The distance from the center of the cluster (defined as the BCG in White et al. (2005) is computed for each core and infall galaxy and compared to the SFR. The mass-complete sample is shown as blue stars for cluster members and the average for the field is the dashed green line, where error bars on the median are the  $1\sigma$  confidence level from a bootstrap resampling. Galaxies with  $S/N$  in  $H\alpha < 3$  are the grey arrows and are not accounted for in the median values. All but three of these upper limits are for *UVJ* quiescent galaxies and so the apparent radial dependence in the fraction of galaxies with upper limits just reflects the well-known radial dependence in the quiescent fraction in clusters. For the robust  $H\alpha$  detections, no significant radial trend exists for the mass-complete sample. . . . . 79

4.14	The stellar continuum (left) and $H\alpha$ line emission map (right) for each UVJ quiescent galaxy shown as a pair of images. The direct F105W images for each galaxy show signatures of early-type galaxies with a lack of spiral arms or clumpy morphology. The $H\alpha$ emission maps are typically low intensity or diffuse distributions, which makes inferences about the gas morphology difficult. . . . .	80
4.15	The main sequence for the galaxies with $S/N > 3$ in the core (blue circle), infall (purple triangle) and field (green stars) regions, where UVJ quiescent galaxies are circled in red and galaxies with less than $S/N < 3$ are shown as the down arrows. Comparison lines to field main sequence derivations are shown in grey (Whitaker et al., 2012) and brown (Schreiber et al., 2015), which are at least 0.5 dex below the $H\alpha$ relations. . . . .	81
5.1	The tensor given to the CNN is a 4-D array, where the image height and width are six pixels and the number of channels is 3, one for each of red, green and blue (RGB). The pixel values of each channel are in a matrix of the image dimensions that will be used to create a filter. Each image has these properties and the total number of images analyzed by the CNN at a time is the batch size. . . . .	89
5.2	Two pairs of grism images show how a filter is created for a galaxy detection in $H\alpha$ (top) and artifact (bottom). Darker purple indicates a higher flux detection within a given emission line, while yellow is equivalent to no detection. The yellow pixels then are masked out in both images to leave the main feature with purple pixel values of the image that is common among the class. . . . .	90
5.3	The top left matrix, which is an $8 \times 8$ minimized representation of the artifact filter, can be pooled into a smaller $4 \times 4$ matrix by keeping the largest value within each set of four cells. The activation map on the bottom row retains the main feature of the artifact filter by reducing the clumps of standalone pixels derived from noise. . . . .	91

5.4	(Top) The input image that the CNN is being asked to classify. The computer has already been trained on four classes, which are listed in the bottom panel on the vertical axis. The assigned probability on a scale from zero to one is on the horizontal axis. The CNN determines that this image is more than >98% probable to be an artifact, with <1% for either a noisy or compact galaxy. . . . .	91
5.5	Each of the six GRIZLI image sequences shows the F105W stellar component on the left, followed by the H $\alpha$ and [SII] emission line maps within the same FOV for the same source. The defined class is based upon any of the emission maps produced by GRIZLI and is labeled in the upper right corner. These classes are not based solely on scientific classification, but with more emphasis on a visual interpretation to demonstrate the abilities of a CNN. Several classes are combined in the results as follows. The artifact and poor model classes are merged into a single class since the main feature is nearly identical between the two types. Additionally, diffuse and compact are merged as a detection class. The four main classes, starting from the top are detection, noisy, artifact/poor model, and edge of chip. . . . .	95
5.6	In this grism extraction, the H $\alpha$ disk in the 4th panel is linearly extended, which would easily fit the artifact/poor model filter. The resulting probabilities only result in ~60% chance that this is contaminated, with a 40% chance of usable data. . . .	98
5.7	In this grism extraction, the H $\alpha$ disk in the 4th panel is not apparent, but the artifact in the noise on the right hand side likely fits the contamination filter since it is a faint linear line. The resulting probabilities only result in ~50% chance that this is contaminated or not, indicating that the model did not have a good fit to this image.	98
5.8	In this grism extraction, the H $\alpha$ disk is resolved and clumpy. . . . .	99
5.9	In this grism extraction, the H $\alpha$ disk in the 4th panel is compact and ~ 20 pixels in area. However, there is also an artifact in the top left. . . . .	99

## List of Tables

2.1	From the original EDisCS (White et al., 2005) observations of 60,933 sources, a total of 21,006 photometric and 1,400 spectroscopic objects remain after the photometric quality cuts. All 1,372 sources with spectroscopic information have accompanying photometric observations. . . . .	19
2.2	From the original 385,000 source catalog, a total of 48,912 objects remain following both spectroscopic and photometric quality cuts. This table lists the numbers for sources with a photometric or spectroscopic redshift in either the cluster or field. Nearly all spectroscopic sources have photometric counterparts, where those without are likely too faint to be detected in the LDP survey. . . . .	21
2.3	Cluster information from Just et al. (2019): 1. Cluster name. 2. J2000 right ascension (hours). 3. J2000 Declination (deg). 4. Cluster redshift (Halliday et al., 2004; Milvang-Jensen et al., 2008)). 5. Cluster velocity dispersion in $\text{km s}^{-1}$ (Halliday et al., 2004; Milvang-Jensen et al., 2008). 6. Cluster virial radius in Mpc. 7. Cluster virial mass in units of $M_{\odot}$ with power of ten in parentheses (using Equation 10 of Finn et al. 2005). 8. Wide-field imaging bands observed in each field. Rows containing a * at the end of the Cluster ID only have EDisCS core data (White et al., 2005) and do not have observations from the LDP survey included in this study. This is due to unreliable photometry as discussed in Just et al. (2019). However, each cluster listed here has coverage within the cluster core from White et al. (2005). The † with C11202-1223 indicates that this cluster is included in the EDisCS core sample, but is not in the LDP survey due to time restrictions. $\sigma$ and $R_{200}$ information is from Vulcani et al. (2013). . . . .	25

- 4.1 Parameters for each of the clusters in this study from Just et al. (2019). 1. EDisCS Cluster ID 2. Right ascension in hours 3. Declination in degrees 4. Cluster redshift 5. Velocity dispersion. 6. Virial radius in Mpc 7. Infall radius in Mpc 8. Virial mass. The range in velocity dispersions between the clusters is small in order to reduce cluster to cluster variation. Each of the clusters has an infall radius between three – four Mpc from the BCG-defined center. The multiband wide-field observations in each cluster extend past the infall region for sufficient cluster coverage (Just et al., 2019). . . . . 60
- 4.2 Information for each of the 14 pointings observed with *HST*/WFC3. In column 1, the prefix of the Pointing ID relates to the Cluster ID from Table 4.1 column 1. Columns 2 and 3 contain the RA/Dec information. For the Location column, I and C refer to *infall* and *core*, respectively, where *infall* is outside of  $R_{200}$  as specified in Table 4.1 column 6. The number of sources extracted with GRIZLI in each pointing are listed in column 5. The number of galaxies with  $H\alpha$  S/N > 3 and without contamination in the cluster (6) and field (7) for each pointing, where  $H\alpha$  S/N < 3 are designated within parentheses. An x signifies that the pointing was not utilized. All of these sources have a wide-field catalog counterpart with rest-frame colors and stellar mass calculations. For C11059, the two pointings (12.2 & 12.3) in the core do not have well-calibrated photometric wide-field data and thus replacement observations and redshifts are utilized from previous VLT/FORS observations (White et al., 2005). The two infall pointings (C11059-12.0 & C11059-12.1) do not have substitute coverage and are not included in analysis. . . . 61

5.1	Results for the CNN on the EDisCS Cycle 20 and GLASS Cycle 21 observations.	
	1. Dataset used in the training, where EDisCS is data from any of the 14 pointings listed in Chapter 4. 2. Orbit depth of the observation. 3. Grism used, where G102 spans the wavelength range from $0.7 - 1.1\mu\text{m}$ . 4. Number of images used in the training set, where $\sim \frac{1}{10}$ of this number is available in the test and validation sets. 5. Accuracy on the test set. 6. Accuracy on the 374 $\text{H}\alpha$ extractions from Chapter 4. The accuracy increases with a reduction in classes, ultimately leaving the best classifier as the one distinguishing between contaminated and uncontaminated data. . . . .	97
A.1	Information for core galaxies. 1. Pointing ID - GRIZLI Object ID 2. Right Ascension 3. Declination 4. Redshift 5. Cluster-centric distance in Mpc. 6. Stellar Mass 7. $\text{H}\alpha$ flux in cgs units 8. Star-formation rate. 9. $U-V$ rest-frame color 10. $V-J$ rest-frame color 11. $UVJ$ classification based on Williams et al. (2009) where sf and q represent star-forming and quiescent, respectively. . . . .	108
A.2	Information for infall galaxies. 1. Pointing ID - GRIZLI Object ID 2. Right Ascension 3. Declination 4. Redshift 5. Cluster-centric distance in Mpc. 6. Stellar Mass 7. $\text{H}\alpha$ flux in cgs units 8. Star-formation rate. 9. $U-V$ rest-frame color 10. $V-J$ rest-frame color 11. $UVJ$ classification based on Williams et al. (2009) where sf and q represent star-forming and quiescent, respectively. . . . .	109
A.3	Information for field galaxies. 1. Pointing ID - GRIZLI Object ID 2. Right Ascension 3. Declination 4. Redshift 5. Stellar Mass 6. $\text{H}\alpha$ flux in cgs units 7. Star-formation rate. 8. $U-V$ rest-frame color 9. $V-J$ rest-frame color 10. $UVJ$ classification based on Williams et al. (2009) where sf and q represent star-forming and quiescent, respectively. . . . .	110
A.4	$S/N_{\text{H}\alpha} < 3$ Galaxies . . . . .	111

# Chapter 1

## Introduction

### 1.1 Characterizing Galaxies in the Universe

One of the key questions facing the astronomical sciences is how galaxies evolve over cosmic time and what factors are capable of influencing this process. Early on in the 20th century, nearby galaxies were classified by Edwin Hubble into two basic types of morphology: spiral and elliptical (Hubble, 1926). Despite the primitive nature of this cosmic assessment, this broad classification proves to be timeless and forms the foundations of many studies in the present day. Following a century's worth of advancements in technology capabilities and manpower dedicated to exploring the cosmos, a vast wealth of galaxies in all types of shapes, sizes, and colors have been discovered and provide an increasingly complicated window into the world of galaxy evolution.

The bimodal nature of galaxy morphology can still be seen through more recent large sky observations in surveys such as the Sloan Digital Sky Survey (SDSS; Tempel et al. 2011) and the 2dF Galaxy Redshift Survey (Madgwick, 2003), all of which have provided a more in depth look to the Universe and its components; Sandage (2005) provides a comprehensive overview of the historical evolution of these classifications over the past century that provides an ever-increasing picture of the nature of the Universe. However, there is more to the cosmic story of simply classifying galaxies. Spiral galaxies tend to be blue and star-forming, denoted as 'late-type' while elliptical, or 'early-type' present as red, with little to no star-formation and a featureless light distribution (Roberts, 1963; Roberts & Haynes, 1994). These two populations of galaxies correlate with other properties such as the ratio of the flux above and below the 4000 Å break ( $D_{n4000}$ ; Kauffmann et al. 2003), color (Baldry et al., 2004; Williams et al., 2009), and star-formation (Conselice, 2014).

## 1.2 Star Formation in Galaxies

Star formation is a cosmic process that governs the conversion of a galaxy's gas to stars and is characterized by the balance of cold gas accretion and feedback (Dutton et al., 2010; Bouché et al., 2010). While we can only capture an instantaneous image of this process at various stages, our foundational knowledge of atomic physics allows for convenient conversions from an emission line flux to a star-formation rate (SFR). Assumptions concerning quantities such as the light-to-mass ratio and star formation history of each galaxy are required in order to calculate the SFR. Since we are not able to directly observe individual stars in a large majority of extragalactic galaxies, we must utilize a tracer to determine how many there are and their respective ages. The Kennicutt-Schmidt Law defines the relation between the surface gas density and star-formation rate (Schmidt, 1959; Kennicutt, 1998), so we are able to derive SFRs from observations of gas. The Hydrogen-alpha ( $H\alpha$ ) emission line is a well-suited recombination tracer and the luminosity is directly proportional to the ionizing radiation.

Now that we have an observable emission line, how can this be related to star formation and its intricacies? HII regions contain hot, massive stars (classification O), which are short-lived and are capable of ionizing the surrounding gas into  $H\alpha$ . These stars are associated with areas that are forming stars (O'Dell 2001), and in conjunction with their lifetimes on the order of millions of years, have the ability to trace star formation on 20 million year timescales. The motivation to search for  $H\alpha$  across the Universe is driven by a prominent emission line that allows for detection to low levels of surface brightness and reduced susceptibility to dust extinction than other common SFR tracers such as [OII]. Previous  $H\alpha$  studies include the NEWH $\alpha$  survey (Lee et al., 2012), the H- $\alpha$  Galaxy Survey (James et al., 2004), and WISP, which surveys the Universe out to a redshift ( $z$ ) of 1.5 (Atek et al., 2010).

A recently defined relation between the SFR and stellar mass, known as the star-forming main sequence, is a tight correlation illustrating that more massive galaxies are forming stars at a quicker rate (Figure 1.1; Daddi et al. 2007; Noeske et al. 2007; Whitaker et al. 2012). The overall observed scatter in the main sequence is likely due to varying star formation histories of each galaxy (Hop-

kins et al., 2014; Domínguez Sánchez et al., 2014), where this scatter is consistent across stellar mass and redshift at  $\sim 0.3$  dex (Whitaker et al., 2012; Tacchella et al., 2016). The normalization of the star-forming main sequence evolves with time, where galaxies at  $z \sim 2$  and  $\sim 1$  have a main sequence that is 20x (Daddi et al., 2007) and 7x higher (Elbaz et al., 2007), respectively, than at  $z \sim 0$  (Brinchmann et al., 2004a). This decline in overall star formation to the present day poses many questions surrounding the nature and fate of the Universe.

While the main sequence is generally presented with a slope ranging from 0.2 – 1.2 (Speagle et al., 2014), there have been numerous studies that show that bulge-dominated massive galaxies contribute towards a flattening in the SFR at higher masses (Karim et al., 2011; Whitaker et al., 2012, 2014; Schreiber et al., 2015; Erfanianfar et al., 2016). This ‘internal’ quenching mechanism is directly related to the morphology and stellar mass of the galaxy and results in a less efficient conversion of gas to stars (Martig et al., 2009) due to disk stability and is referred to as mass quenching. There are other types of internal quenching processes that are derived from the galaxy itself and not interaction with another object or environment; these include an expulsion of the gas through AGN feedback (Fabian, 2012), supernovae explosions and stellar winds (Dekel & Silk, 1986), a cutoff in gas accretion (Larson et al., 1980), and starvation, which is the natural depletion of the gas supply. Processes that suppress star formation through an external event or environment include the removal of the gas via ram-pressure stripping (Gunn & Gott, 1972; Quilis et al., 2000), tidal interaction (Byrd & Valtonen, 1990), mergers, and harassment (Moore et al., 1999; Treu et al., 2003). Additionally, some ram-pressure stripping and merger events have been observed to first create enhanced SFR activity, followed by a suppression phase (Poggianti et al., 2016; Jaffé et al., 2016; Vulcani et al., 2018). These two types of quenching are not mutually exclusive and their respective effects across redshift, mass, and environment are still under investigation.

Galaxies with an elevated SFR  $\sim 2.5 \times$  those above the main sequence can potentially be in a ‘starbursting phase,’ which can be the result of mergers and interactions (Hopkins et al., 2006; Cox et al., 2008), disk instability (Kennicutt, 1998; Romeo & Fathi, 2016) or ram-pressure stripped tails (Poggianti et al., 2017). Starburst galaxies are representative of a short-lived phase rather than

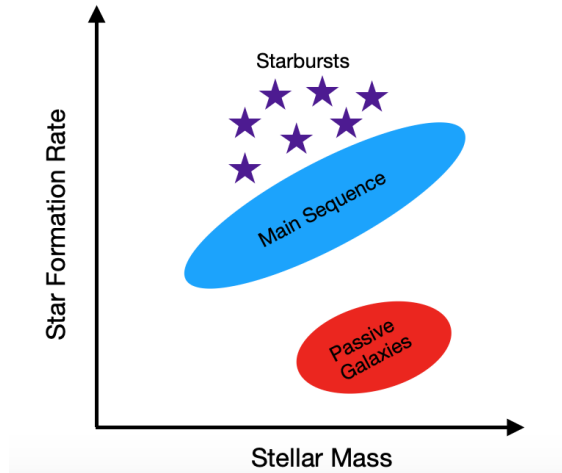


Figure 1.1: This illustration shows the star formation rate vs. stellar mass relation, which is known as the main sequence. Galaxies located along the blue oval are star-forming, where more massive galaxies create stars at a fast rate. Galaxies with extremely high star formation rates can be starbursting, which is shown as purple stars above main sequence. Finally, as galaxies quench, their star formation decreases and they eventually fall off of the main sequence.

a specific morphology (Karl et al., 2010), but are an important insight to the transition from star-forming to quiescent states. In contrast to these starbursters, there are galaxies that lie below the main sequence where their star formation is reduced. As galaxies begin to shut off star formation and fall off the main sequence, they enter the green valley (Baldry et al., 2004; Martin et al., 2007), which is hypothesized to be the transition between star forming and quiescent states. The term ‘green’ actually has nothing to do with observable color and is based off of banter about the Green Valley retirement community in Arizona. The green valley is therefore the place in which galaxies go to ‘retire’ on their way to becoming quiescent. When star formation is nearly or completely reduced, galaxies are classified as quiescent and are not on the main sequence. These galaxies tend to be the most massive red galaxies in the Universe and comprise the majority of the local stellar mass.

### 1.3 The Role of Cosmic Environment on Galaxy Evolution

Primordial density fluctuations in the early Universe expanded into the large-scale structure of galaxies in filaments, clusters, and groups that we see today (Peebles, 1982). The variation of

cosmic environments for individual galaxies can range from overdensities in cluster cores to unchaperoned in the field. With this in mind, the exploration of ‘nature vs. nurture’ scenario in galaxy evolution has come forward in an attempt to explain differences in observed galaxy populations (Dressler, 1980); however, this has been debated by the varying accretion times of massive elliptical and mixing of galaxy populations during halo assembly (De Lucia et al., 2012; Wetzel et al., 2013). Intrinsic mechanisms fall into the ‘nature’ category, while external interactions are the result of the local environment.

The most dense regions of the universe consist of galaxy clusters with thousands of members that are gravitationally bound and contain a hot intracluster medium (ICM). Many of the most massive galaxies reside in the cluster cores, with the brightest cluster galaxy (BCG) generally being at the minimum or center of the cluster potential well and elliptical in shape. There are an increased number of massive, passive galaxies in dense environments when compared to the field (Dressler, 1980; Postman et al., 2005; Baldry et al., 2004; Postman et al., 2005; Peng et al., 2010; Wetzel et al., 2012). Numerous studies on the central cores (area within  $\sim R_{200}$ ) of galaxy clusters have revealed that the star formation is suppressed (Balogh et al., 1997; Kauffmann et al., 2004; Postman et al., 2005; Pannella et al., 2009; Peng et al., 2010; Finn et al., 2010; Vulcani et al., 2010; Paccagnella et al., 2016; Old et al., 2019) when compared to the field, indicating that ‘external’ quenching mechanisms are dominating over internal processes. In Lewis et al. (2002); Gómez et al. (2003), this suppression of SFRs also occurred in the outskirts of galaxy clusters at low redshift ( $z < 0.1$ ), indicating that the dense cores are not solely responsible for environmentally-based galaxy quenching. However, several recent studies including Vulcani et al. (2016), Erfanianfar et al. (2016) and Tiley et al. (2020) have found that at redshifts between 0.5 and 1.0, there is little dependence on the SFR between the field and dense environments such as within groups and clusters. Studies with reduced cluster-to-cluster variation in parameters (e.g. mass and velocity dispersion) and increased sample sizes (Moran et al., 2007; Patel et al., 2011; Oemler et al., 2013) are needed to further quantify these star formation rates more in depth across various cosmic densities, halo masses and a range of SFRs.

Cluster membership extends far beyond the virial radius and encompasses the infall region where galaxies are accreted into the cluster environment. Several studies have also found that SFRs are decreased in the outskirts of clusters (Lewis et al., 2002; Gómez et al., 2003), reinforcing the hypothesis that regions of elevated density are behind environmentally-driven quenching and thus, reducing the SFR. Ram-pressure stripping events at cluster-centric radii  $>$  the virial radius support this extrinsic quenching process (Gullieuszik et al., 2017; Jaffé et al., 2018; Gavazzi et al., 2018). The infall region of galaxy clusters has the potential to host the sites of galaxy transformation and quenching processes *in situ* that may differ from those in the core. Just et al. (2019) found that 30 - 70% of the galaxies in local clusters were located in the infall region at  $z \sim 0.6$ , meaning that these galaxies may become the majority of cluster galaxies at  $z \sim 0$ . This finding reinforces the importance of the cluster infall region with respect to the environmentally-driven transformation of galaxies.

### 1.3.1 Gas Depletion Mechanisms

As galaxies form stars, the gas reservoir will be consumed unless it is replenished. Some processes deplete this gas more rapidly and result in a decline in star-formation. One process unique to the cluster environment is ram-pressure stripping (RPS), which is a result of the hot ICM interacting with an infalling galaxy; this is observed in the form of a disturbed gas disk, with a possible extension through tail, while the stellar disk remains intact (Gunn & Gott, 1972; Quilis et al., 2000; Bekki, 2009; Poggianti et al., 2016). RPS has been observed frequently in the nearby Coma and Virgo clusters (Vollmer et al., 2001; Boselli & Gavazzi, 2006; Smith et al., 2010; Boselli et al., 2016), in groups (Rasmussen et al., 2006, 2008; Hess & Wilcots, 2013), and as well as in simulations (Abadi et al., 1999; Quilis et al., 2000; Roediger & Brüggén, 2007; Vollmer, 2013). While this appears to be an efficient process in both neutral hydrogen (HI; Haynes et al. 1984; Cayatte et al. 1990; Kenney 2004; Jaffé et al. 2015 and ionized hydrogen ( $H\alpha$ ; Gavazzi et al. 2002; Yagi et al. 2010; Yoshida et al. 2012), molecular gas stripping is perhaps less efficient than its atomic counterparts (Kenney & Young, 1989; Boselli et al., 2014). A survey targeting ‘jellyfish’

galaxies (Fumagalli et al., 2014), or those with extended gas tails, known as GASP (GAs Stripping Phenomena in galaxies with MUSE) (Poggianti et al., 2017), found that a number of these RPS events have been observed to first create enhanced SFR activity, followed by a suppression phase (Poggianti et al., 2016; Jaffé et al., 2016; Vulcani et al., 2018). The timescale for this process ranges from 300 Myr - 3.2 Gyr, which is supported by both observations and simulations (Vollmer et al., 2004; Roediger & Hensler, 2005; Boselli & Gavazzi, 2006; Crowl & Kenney, 2008; Tonnesen, 2019).

Similar to RPS, strangulation or starvation results when the gas reservoir of a galaxy has been depleted or removed after falling into the ICM and leaves the stellar disk unchanged. As the supply of gas is diminished, the SFR decreases (Larson et al., 1980; Bekki et al., 2002; Boselli & Gavazzi, 2006), but on timescales ( $\sim 1$  Gyr) that are typically longer than RPS (Larson et al., 1980; Bekki et al., 2002). While less dramatic than a jellyfish-type display, starvation can result in passive disks (Bundy et al., 2010; Cantale et al., 2016a) or enlarged bulges (Kawata & Mulchaey, 2008).

Finally, a process that is not necessarily environment-dependent are mergers, where two galaxies interact with another in a variety of ways. In contrast to the previous two scenarios, mergers can result in an alteration of the stellar and gas disk. This can take the form of cannibalism, where smaller satellite galaxies are accreted into the halo of the larger galaxy or major-mergers, where the collision of similar-sized galaxies can produce results ranging from starburst activity (Rodighiero et al., 2011) to transformation into elliptical morphologies (Toomre & Toomre, 1972).

## 1.4 Quenching Timescales

Various theories regarding the quenching timescales have suggested a delayed-then-rapid quenching procedure as galaxies fall into a cluster environment, meaning that their SFRs are unaffected for the first two – four Gyr (Wetzel et al., 2013), followed by a rapid quenching period. This is driven by the lack of SFR suppression in galaxies on the main sequence that are located in dense environments. This supports a rapid timescale for quenching and transition from star forming to passive states since low SFR galaxies are typically below the main sequence. Foltz et al. (2018) collated a

significant number of studies (McGee et al., 2011; Wetzel et al., 2013; Muzzin et al., 2014; Taranu et al., 2014; Haines et al., 2015; Fossati et al., 2017) on quenching timescales and classified them by environment, revealing that quenching is occurring more rapidly with a decreased redshift and that groups and clusters quench faster than the molecular depletion timescale. This approximate quenching timescale is in agreement with models of star formation and environmental quenching in clusters that predict quenching will occur within three Gyr of infall (Taranu et al., 2014).

## 1.5 Methods for Observing Processes in Galaxies

In order to quantify the above processes relating to the gas and stellar content of galaxies, observations at a number of different wavelengths and methods are required. Photometric surveys provide measured fluxes in a given filter, which can then be converted to a magnitude; a commonly used system is the *Johnson UVB* (Johnson & Morgan, 1953) which is a set of wide-band filters in ultraviolet (U 364 nm), blue (B 442 nm) and visual (V 540 nm). This was later expanded to include redder filters in the Johnson-Cousins system for red (R 635 nm) and infrared (IR 880 nm) (Cousins, 1976). With the advancement of technology, numerous pass bands exist across the electromagnetic spectrum and when the fluxes are plotted against the observed wavelength for a given object, this constitutes a spectral energy distribution (SED). An SED is able to provide key features that can give information on the redshift, stellar mass, and age of the object (Couch et al., 1983).

The Butcher-Oemler Effect was derived from photometric observations, which found that there are a higher fraction of blue galaxies in distant cluster cores than in nearby ones (Butcher & Oemler, 1978). This sparked a number of other photometric follow-up studies on rich clusters and proved this effect to be widespread beyond  $z > 0.2$  (Rakos & Schombert, 1995; Margoniner et al., 2001; Urquhart et al., 2010). A more recent adaption of this binary classification is through the *UVJ* color-color scheme, where the rest-frame  $U - V$  and  $V - J$  colors with Williams et al. (2009) boundaries (listed below) allow for a clear identification of passive or star-forming galaxies.

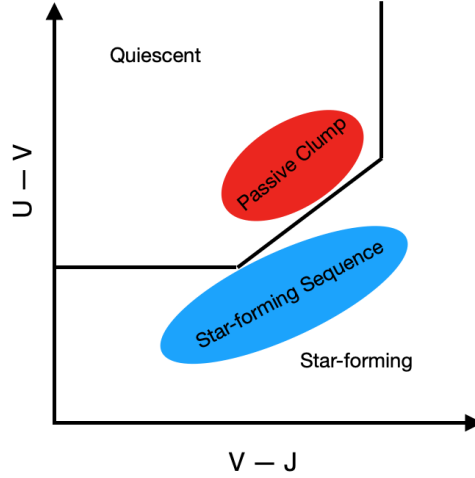


Figure 1.2: This illustration shows the rest-frame  $UVJ$  diagram with the Williams et al. (2009) boundaries for either quiescent or star-forming as black lines. Galaxies will typically be located somewhere among the passive clump or the star-forming sequence.

$$(U - V)_{rest} = 1.3$$

$$(V - J)_{rest} = 1.6$$

$$(U - V)_{rest} - 0.88(V - J)_{rest} = 0.54$$

Galaxies located within the upper left region are defined as the ‘passive clump’ and those outside of these boundaries are considered star-forming, as shown in Figure 1.2. This follows the notion that passive galaxies are redder, while star forming ones tend to be bluer. Photometric observations of galaxies with these rest-frame colors can be quickly classified as passive or star-forming. The passive fraction ( $f_{passive}$ ), or the proportion of galaxies that are passive from the entire population, can then be determined for a sample.

In contrast to photometric observations, spectroscopy involves the flux dispersion over a wavelength interval. This allows for features such as absorption and emission lines to be clearly identified, which photometric observations may miss. Spectroscopic observations of the galaxies from Butcher & Oemler (1978) revealed that the blue galaxies have emission lines from star-formation

(Dressler & Gunn, 1983; Couch & Sharples, 1987; Poggianti et al., 1999).

Several forms of spectroscopic arrangements include a long slit or slitless instrument depending on the goal of the study. With the former, the aperture is elongated and the captured light is refracted through a prism. Emission and absorption lines can be identified along with Doppler shift, but this is restricted to the observed area within the slit. This technique can be advantageous with observations near a luminous source because the observer can still achieve a high signal-to-noise ratio by blocking the bright source with the area outside of the slit. With slitless spectroscopy, there is no slit and all of the objects within the FOV of the detector are dispersed through a prism or grism (prism with a grating).

The *Hubble Space Telescope*/Wide Field Camera 3 is well-equipped to observe extragalactic emission lines with slitless spectroscopy, and more specifically, the  $H\alpha$  line which is an aforementioned tracer of star formation. In conjunction with the near-IR spectroscopic grism, an undistorted 2D image of the observed galaxy in both the stellar continuum and detected emission line are resulting products available for analysis. 3DHST (Momcheva et al., 2016) observed more than 100,000 galaxies in the CANDELS fields with WFC3 to produce robust redshifts and emission line identifications. This showcased the power of the grism and led to numerous publications regarding star formation rates (Nelson et al., 2012, 2013; Wuyts et al., 2013; Dickey et al., 2016; Nelson et al., 2016; Whitaker et al., 2017) and a solidification of the main sequence in the field over 10 billion years of cosmic time (Whitaker et al., 2012, 2014). The success of this study led to other surveys utilizing the same combination of instruments such as the Grism Lens-Amplified Survey from Space (GLASS) (Treu et al., 2015), which was able to target  $H\alpha$  emission line galaxies in varying cosmic environments to unveil differences in SFRs (Vulcani et al., 2015, 2016; Abramson et al., 2018) and reinforce the abilities of the *HST* grism even in crowded cosmic regions. Additionally, the WFC3 is capable of a dual observation mode, which utilizes grism spectroscopy and direct imaging at the same time. This is advantageous for reducing the amount of required observing time and obtaining multiple science products for the same objects.

## 1.6 Protoclusters: A Search for the Beginning of Clusters

Recent technology advancements have allowed observations of protoclusters at high redshift, which gives insight on how these structures formed and evolve into the clusters that we see today. The early universe originally had a high abundance of star-forming galaxies as these low-mass structures were initially formed (Kauffmann et al., 2004; Peng et al., 2010). At  $z > 2$ , protoclusters are typically dominated by massive, star-forming galaxies (Overzier et al., 2008; Galametz et al., 2010; Hatch et al., 2011; Shimakawa et al., 2014) and it is suggested that these evolve into the passively-dominated clusters at  $z < 1$  (Muzzin et al., 2012; Foltz et al., 2015; Balogh et al., 2016). The several billion years between stages reveals a myriad of results, with significant quenching already in place in a set of protoclusters at  $2 < z < 3$  (Kodama et al., 2007) and in a  $z \sim 1.6$  cluster (Bauer et al., 2011; Quadri et al., 2012; Lee-Brown et al., 2017), while some at  $1 < z < 1.8$  still have massive star-forming galaxies (Brodwin et al., 2013; Bayliss et al., 2014; Webb et al., 2015a,b).

However, we have to ponder what mechanisms are responsible for quenching. Interestingly, Muldrew et al. (2015) predicts that halo collapse could be a rapid process at  $z \sim 1.5$ , which would then produce conditions capable of stripping galactic gas. Thus, it is safe to say that a singular property such as galaxy mass or redshift is not responsible for the shut-off in star-formation, but may be embedded in more complex traits such as the halo mass and age. Understanding the physical mechanisms that deplete a gas supply are crucial towards bridging the gap of the cluster transition from star-forming to passive galaxy prevalence.

## 1.7 Machine Learning Overview

While our technology advancements have allowed for the automatic observation, processing, and storage of millions of astronomical objects consisting of petabytes or more of data, there are simply not enough hours from each astronomer to sort through this data in a timely manner. For example, the first iteration of Galaxy Zoo was estimated to consume a minimum of 27,000 hours for a trained

graduate student (Pinkowski, 2010), which is far more than the expected time commitment for even a doctoral degree. Thus, the resources and time of hundreds of thousands of volunteers were solicited to make this feat possible. The first edition of Galaxy Zoo was completed in just 6 months, proving to be a large success. However, the glaringly obvious conundrum here is the amount of human hours required to complete this task. While impressive, there has to be a less labor-intensive approach to solve this problem, and as new telescopes are constructed, more and more data will be accumulated. For example, from the *HST* Cycle 20 program observations discussed earlier in this thesis, the total grism object extractions totaled more than 13,000 objects! Even though the final number of galaxies was reduced to  $\sim 1\%$  of these observations, other programs and all-sky surveys can quickly amass hundreds of thousands of objects, and we are once again faced with the unfeasible task of sifting through these data.

Thus, this introduces the need for automated classification that removes the thousands of hours required for a human to click through images and determine various properties. Initially started in the mid 1990s, the computational resources available at the time limited classification schemes to small datasets and lower data quality. Nevertheless, successful algorithms classifying galaxies based on parameters such as morphology and color (Abraham et al., 1994; Naim et al., 1995; Conselice, 2003; Pović et al., 2009; Dieleman et al., 2015; Diaz et al., 2019) have become more popular over time with the advent of computationally-powerful laptops and local cluster resources. Similar to the citizen science initiatives, automated classification has also been tested on larger surveys such as COSMOS (Cassata et al., 2007) and GAMA (Alpaslan et al., 2015). These first steps to automated classification can be improved through the use of machine learning and supervised learning methods, which actually trains the computer to search for trends and correlations among datasets and images.

Machine learning, which is a subset of the larger field of artificial intelligence, employs computers to not only learn, but improve algorithms through experience. They build a mathematical model that will make decisions after being trained on a presorted dataset and can then apply the accumulated knowledge on a new dataset. Three different types of machine learning methodologies

exist: 1) supervised, which is designated with inputs and outputs to teach the computer, 2) unsupervised, where the decision model is decided by the computer and optimized to find potentially hidden patterns, and 3) reinforcement learning, which interacts with the environment to continuously adapt and improve. Here, only the first method of supervised learning is utilized, which is explained in further detail in the following sections.

Supervised learning includes a number of various approaches that have been applied for astronomical purposes such as neural networks (Ball et al., 2004; Dieleman et al., 2015; Diaz et al., 2019; de Diego, José A. et al., 2020), Bayesian classifiers (Quireza et al., 2007; Henrion et al., 2011; Ferreira et al., 2020), linear discriminant analysis (Ferrari et al., 2015; Abolfathi et al., 2018; de Diego, José A. et al., 2020) random forests (Richards et al., 2011; Biswas et al., 2013; Clarke et al., 2020) and decision trees (Jarrett et al., 2000; Suchkov et al., 2005; Barchi et al., 2020). This field is rapidly accelerating as researchers discover the high versatility and efficiency of such algorithms and papers in the realm of machine learning in astronomy are now submitted numerous times per week on the arXiv to solve research questions such as gravitational wave detection (George & Huerta, 2018a), exoplanet detection (Shallue & Vanderburg, 2018), lens fitting and identification (Voigt & Bridle, 2010; Lanusse et al., 2018) and signal analysis (Hoyle, 2016; George & Huerta, 2018b) across a variety of instruments and wavelengths.

## **1.8 This Work**

In this thesis, we inspect the role of local environments on galaxy evolution using the aforementioned observation methods. This study combines the power of ground-based wide-field imaging with space-based slitless spectroscopy to examine galaxies in the field and within clusters as they were more than 5 billion years ago. This is accomplished in two specific ways: 1) assess the photometric observations with the *UVJ*-defined passive fraction across the EDisCS clusters as a function of cluster radius, stellar mass, and redshift and 2) further analyze the spectroscopically observed star-formation rates of galaxies residing in clusters in three distinct environments (cluster core, infall region, and field) with *HST*. The first portion of this thesis is devoted towards a

photometric view of the EDisCS clusters by determining the passive fraction in relation to stellar mass, redshift, and cluster-centric distance. This data sample consists of two sets of observations of mid-mass clusters in the range  $0.4 < z < 0.8$ . The original observations of EDisCS focused on the central core regions and obtained both photometric and spectroscopic information with the Very Large Telescope (VLT) and New Technology Telescope (NTT). Follow-up wide-field observations include spectroscopic redshifts derived from the Low-Dispersion Prism on Magellan and photometric data collected with the Wide Field Imager on the 2.2m Max Planck Gesellschaft/European Southern Observatory (MPG/ESO) telescope, the MOSAIC instrument on the Cerro Tololo Inter-American Observatory (CTIO) Blanco or the Mayall 4-meter telescope.

Next, we investigate select areas from the cores and infall regions of four EDisCS clusters at  $z \sim 0.5$  with *HST*/WFC3 G102 grism and F105W imaging, which provide  $H\alpha$ -based star-formation rates (SFRs). The data reduction involves introducing a redshift prior from previous EDisCS observations to the software to aid in the correct determination of the  $H\alpha$  line. The SFRs are calculated assuming a Chabrier IMF with corrections for post-AGB emission, dust extinction, and contribution from the [NII] doublet. We attempt to determine the effect of local environment on SFR-stellar mass relation by separating galaxies into three distinct local environments (cluster core, infall region, and field).

The final portion of this study aims to reduce manual labor derived from astronomical observations. WFC3 G102 observations easily produce thousands of extractions, where some objects have multiple emission line maps. Previously, grism extractions have been inspected by eye for morphological classification, artifact contamination, and poor modeling, which can be a cumbersome task for even small observation programs. However, these images contain critical information and should be inspected for basic quality metrics at a minimum, particularly if poor modeling or an artifact presents as a plausible signal. With this in mind, a convolutional neural network (CNN) is trained to distinguish between an image that is unusable, diffuse, compact, or noisy. This CNN is trained on *HST* grism observations with either 2 or 10-orbit depth to determine if automatic classification is possible with grism data.

This work is divided as follows. The datasets used in the study are described in detail in Chapter 2, including stellar mass calculations, photometry corrections, and quality cuts. In Chapter 3, we present the passive fraction analysis as a function of redshift, stellar mass, and cluster-centric distance for EDisCS clusters. A comparative field sample is derived from galaxies residing outside the cluster redshift range ( $\pm 0.02$ ) within the FOV. This is followed by an excerpt from Cooper et al. (2021, *submitted*) in Chapter 4 where we present  $H\alpha$ -based SFRs for select galaxies in the EDisCS sample. Observations are collected across a range of cluster-centric distances to directly compare local environment with  $H\alpha$  emission. In Chapter 5, we present the image classification neural network study on grism extractions. Finally, in Chapter 6, we present a summary and set of conclusions derived from the preceding chapters. In Appendix A, the code used to create the neural network is provided. All magnitudes are given in the AB system and we assume a Chabrier IMF (Chabrier, 2003). We adopt a  $\Lambda$ CDM cosmology with  $\Omega_m = 0.307$ ,  $\Omega_\Lambda = 0.693$ , and  $H_0 = 67.7 \text{ km s}^{-1} \text{ Mpc}^{-1}$  (Planck Collaboration et al., 2016).

## 1.9 Commonly Used Terminology

The following terminology and acronyms are frequently used in the subsequent chapters and are defined for clarity here.

- **CNN:** Abbreviation for Convolutional Neural Network. More discussion on this topic is in Chapter 5.
- **$H\alpha$ :** Abbreviation for the hydrogen-alpha Balmer series emission line. This can be utilized as a star-formation rate tracer.
- **Local Environment:** This refers to the immediate environment of a galaxy, namely the density.
- **Quenching:** The process in which a gas reservoir is depleted from a galaxy. This can be either intrinsic, which is dependent upon individual galaxy characteristics, or extrinsic, which

is dependent upon external factors and interactions such as with the local environment.

- **SFR**: Abbreviation for star-formation rate.
- $f_{passive}$ : Abbreviation for passive fraction, which is the number of *UVJ*-passive galaxies divided by the total number of galaxies. This is discussed in more detail in Chapter 3.
- $R_{200}$ : Term for the radius of the cluster within which the density is  $200\times$  the critical density of the Universe. Also referred to as the virial radius.

## Chapter 2

### Characteristics of the Sample

#### Abstract

In this chapter, the EDisCS photometric and spectroscopic datasets that established this cluster sample are briefly discussed in Section 2.2. The subsequent wide field survey that defined cluster membership out to multiple virial radii is presented in Section 2.3. The methodology for stellar mass calculations are detailed in Section 2.4, along with photometric corrections. The environmental definitions of core, infall and field are detailed in Section 2.5.

#### 2.1 Introduction

The ESO Distant Cluster Survey (EDisCS; White et al. 2005) is an ESO Large Program derived from the optically brightest objects of the Las Campanas Distant Cluster Survey (Gonzalez et al., 2001) and comprises 20 clusters within  $0.4 < z < 0.8$ . The velocity dispersion ( $\sigma_v$ ) of these clusters ranges from  $200 - 1200 \text{ km s}^{-1}$  (Halliday et al., 2004; Milvang-Jensen et al., 2008) and is characteristic of local cluster progenitors due to mid-mass halo sizes (Milvang-Jensen et al., 2008). The main goal of EDisCS is to examine the evolution of cluster populations over a large span of cosmic time and compare results with respect to halo mass and local cluster populations.

#### 2.2 Photometric and Spectroscopic Observations of the Cluster Cores

The EDisCS Collaboration utilized various ground-based telescopes to clearly identify membership and determine individual galaxy properties in each of the 20 clusters. The core regions, which

are typically on the order of 0.5 – 2 Mpc across, are defined as the area within the virial radius and typically include the BCG. For EDisCS, the cores have been extensively studied with deep optical imaging and spectroscopy on VLT (White et al., 2005; Halliday et al., 2004; Milvang-Jensen et al., 2008; Vulcani et al., 2012) and near-IR observations on the New Technology Telescope (White et al., 2005; Rudnick et al., 2009) which has allowed further EDisCS studies such as brightest cluster galaxy identification (White et al., 2005; Whiley et al., 2008), morphologies (Desai et al., 2007; Simard et al., 2009; Vulcani et al., 2011b,a), fundamental-plane parameters (Saglia et al., 2010), red-sequence identification (De Lucia et al., 2004), weak lensing (Clowe et al., 2006),  $24\mu\text{m}$  MIPS SFRs (Finn et al., 2010) and [OII] SFRs (Poggianti et al., 2006, 2009; Vulcani et al., 2010). Cluster cores are dense regions that are attractive for studying cluster properties and are well-suited for observations due to high contrast with the background and density of objects within a given FOV. However, physical processes affecting the evolution of a galaxy appear to occur as these sources enter a cluster environment and thus the cores likely only provide information on their fate. This is reinforced through observations that the cores typically include a higher fraction of massive red disk or quiescent galaxies (Dressler, 1980; Bell et al., 2004; Kauffmann et al., 2004; Erfanianfar et al., 2016). A spatially-expanded view of clusters is required to gather information on environmentally-driven quenching mechanisms across a representative sample of galaxies within a cluster.

Imaging of the cores was completed in  $6.5' \times 6.5'$  fields of view to sufficiently cover numerous galaxies within the virial radius with either the VLT or NTT. Low redshift ( $< 0.5$ ) EDisCS clusters have photometry in the *BVIK* bands, while the high redshift clusters ( $> 0.5$ ) are imaged in *VRIJK*. Spectroscopic observations were completed with the 600RI+19 grism, which has a wavelength coverage from  $0.53 - 0.9 \mu\text{m}$  (Halliday et al., 2004; Milvang-Jensen et al., 2008).

The following series of photometric quality cuts are applied to catalog to remove stellar artifacts and constrain for the limiting magnitude in the I-band. The magnitude limit differs by 0.5 depending on the observation bands for each cluster.

Local Environment	$N_{sources}$ with Photometric Redshift	$N_{sources}$ with Spectroscopic Redshift
<i>Cluster Member</i>	4,031	603
<i>Field</i>	16,975	769
<i>Total</i>	21,006	1,372

Table 2.1: From the original EDisCS (White et al., 2005) observations of 60,933 sources, a total of 21,006 photometric and 1,400 spectroscopic objects remain after the photometric quality cuts. All 1,372 sources with spectroscopic information have accompanying photometric observations.

$$wmin > 0.3$$

$$Starflag < 1$$

$$I_{totBVIK} < 24.0$$

$$I_{totVRIJK} < 24.5$$

After these cuts are applied to the catalog,  $\sim 21,000$  photometric observations remain, with  $\sim 25\%$  identified as cluster members. Details are listed in Table 2.1. Details for each of the 16 clusters in the EDisCS core sample including the virial mass, infall radius, velocity dispersion and imaging are listed in Table 2.3 (Just et al., 2019). This dataset is referred to as the EDisCS VLT core sample.

### 2.3 Wide Field Catalog of EDisCS Clusters

Galaxy clusters extend far beyond their cores and virial radii, and in order to achieve a more informed understanding of the role of environment on galaxy evolution, it is important to extend analyses to projected radii greater than  $R_{200}$ . This is a challenging task, as the reduced density of the cluster density profile results in a decreased contrast with the foreground and background

(Newman et al., 2013). Large and wide-field spectroscopic studies are required to conclusively establish membership in these regions, and since such programs are challenging, there are few studies of cluster outskirts beyond the local universe (Geach et al., 2006; Patel et al., 2009b; Dressler et al., 2013; Spérone-Longin et al., 2020). After thoroughly characterizing the cores of EDisCS clusters, a ground-based spectroscopic survey using the LDP aimed to extend observations beyond the central cluster core regions. The spectroscopic observations were completed with the Low-Dispersion Prism (LDP) on the Inamori-Magellan Areal Camera and Spectrograph (IMACS; (Bigelow et al., 1998; Dressler et al., 2006) on the 6.5m Magellan Baade telescope. These observations produced a deep catalog of 25,000 redshifts with an accuracy of  $\sigma = 0.007$  and a high spectroscopic completeness up to  $R_{AUTO} < 23.3$  (Just et al., 2019). A set of observed  $BVRIZK_s$  measured colors and magnitudes are available from photometric observations, where  $VRI$  were observed with the Wide Field Imager (WFI) on the 2.2m Max Planck Gesellschaft/European Southern Observatory (MPG/ESO) telescope (Baade et al., 1999), while  $Bz$  were completed on the MOSAIC instrument on the Cerro Tololo Inter-American Observatory (CTIO) Blanco or Mayall 4-meter telescope. Image reduction techniques and determination of cluster properties such as the infall radius and velocity dispersion are described in more detail in Just et al. (2019). This survey forms the basis of the studies in this thesis and hereafter, is referred to as the ‘LDP survey’. The following paragraphs describe the quality metrics applied to the full catalog to determine a suitable sample for the studies described in Chapters 3 and 4.

In the combined spectroscopic and photometric catalog produced from the LDP survey, there are more than 385,000 objects.  $\sim 40,000$  have a spectroscopic ‘LDP’ redshift and 287,000 have a photometric value derived from EAZY (Brammer et al., 2008). Photometric catalogs are derived from SourceExtractor (Bertin & Arnouts, 1996), with the R-band image serving as the detection map. The following photometric quality metrics are applied to the catalog, where  $wK$  is the normalized weight in the  $K_s$ -band image,  $sexflagR$  is the SourceExtractor photometry flag in the R-band image,  $classStarR$  is the SourceExtractor star classification in the R-band image and  $fB1$  is the flux  $\mu Jy$  in the B-band from a 1" aperture. The latter cut ensures that the source is detected

Local Environment	$N_{sources}$ with Photometric Redshift	$N_{sources}$ with Spectroscopic Redshift
<i>Cluster Member</i>	3,069	1,153
<i>Field</i>	45,431	17,140
<i>Total</i>	48,500	18,293

Table 2.2: From the original 385,000 source catalog, a total of 48,912 objects remain following both spectroscopic and photometric quality cuts. This table lists the numbers for sources with a photometric or spectroscopic redshift in either the cluster or field. Nearly all spectroscopic sources have photometric counterparts, where those without are likely too faint to be detected in the LDP survey.

and is not a partial or missing observation due to the image edge.

$$wK > 0.3$$

$$sexflagR = 0$$

$$classStarR < 0.97$$

$$fB1 > -5$$

$$fB1_{error} > 0$$

This results in a subsample of  $\sim 122,000$  objects with an available photometric or spectroscopic redshift. The magnitude-limited completeness is up to  $m_R < 23.3$ , which leaves a sample of 48,912 objects. This limit is determined through the differential number of sources detected in R-band per magnitude bin and is described in more detail in Just et al. (2019). Table 2.2 describes the number of sources per redshift type and dependent upon local environment, where a cluster member has a  $z$  within 0.02 of  $z_{cluster}$ . Each of the clusters from the catalog are listed in Table 2.3 with their respective redshift, velocity dispersion, virial radius, enclosed virial mass, and the available imaging.

### 2.3.1 Photometric Corrections

As described in Just et al. (2019), there were multiple calibration challenges with the wide-field photometry that we use in this work, especially with the WFI photometry, which was not taken under photometric conditions. The WFI photometry in Just et al. (2019) was calibrated to the EDisCS core photometry and a subsequent calibration step was applied to minimize the residuals of photometric vs. spectroscopic redshifts. Despite this, the calibration has produced reasonably good photometric redshifts and it later became apparent that the rest-frame  $UVJ$  colors had additional calibration issues, likely resulting from a non-trivial by-product of the multiple zeropoint calibration steps that we undertook in Just et al. (2019). While the  $UVJ$  colors for each cluster had a clear quiescent clump and SF sequence, they were each systematically shifted with respect to each other, and to the quiescent clump as defined from the well-calibrated EDisCS photometry on the cluster cores.

We therefore undertook an additional calibration step in which we used the median colors of quiescent galaxies in the wide-field sample and shifted the  $U - V$  and  $V - J$  colors such that this clump matched the median  $UVJ$  colors of the spectroscopically confirmed galaxies from EDisCS that had no emission lines in their spectra. Although calculated for just the quiescent galaxies, these shifts were applied to all galaxies on a cluster-by-cluster basis. These shifts were  $< 0.2$  in color but resulted in all of our fields having well matched  $UVJ$  sequences. This gives us the ability to robustly separate galaxies in different regions of  $UVJ$  space. The adjustment to the colors was also important for our use of the  $U - V$  color to compute stellar mass to light ratios and stellar masses. In practice, the correction was mostly applied to the rest-frame  $V$ -band magnitude. The rest-frame  $U$ -band magnitude was derived from well-calibrated  $B$ -band observations and the  $J$ -band magnitude was calibrated well to the 2MASS photometry. The  $V$  magnitude was more tied to the problematic WFI photometry due to it being taken in unphotometric conditions and large effective seeing.

## 2.4 Stellar Mass Derivation & Comparison

The stellar masses for the LDP sample were originally calculated from  $B$ -band mass-to-light ratios in Just et al. (2019). However, we have since determined that the rest-frame colors required an adjustment and thus, also affected the observed  $V$ -band flux. Stellar masses are then recalculated using Equation 2.1 relating the rest-frame  $U - V$  color and the mass-to-light ratio in  $V$ -band, which is based on Taylor et al. (2011). The mass-completeness limit is derived from a subset of the highest redshift galaxies in clusters ( $\sim 0.7 - 0.8$ ) and at one magnitude brighter than the limit of  $r = 23.3$ . These galaxies are then 'faded' to the magnitude limit and the stellar masses are reduced by the same factor, which results in a mass-complete value. This value is  $> 10^{10.6} M_*/M_\odot$ , which assumes that the mass-to-light ratio of the brightest galaxies is the same as those near the R-band magnitude limit. SED-fitting for our data is not utilized here due to unreliable photometry on the observed flux values that requires numerous corrections, so stellar masses cannot be determined with this method. However, we are able to correct the colors (e.g.  $U - V$ ) as we have previously calculated these in the EDisCS cores. Therefore, stellar masses derived from  $U - V$  are comparable to the EDisCS core stellar masses.

$$\text{Log}_{10}M_* = 0.998 \times (U - V) - 1.272 + \text{Log}_{10}L_V \quad (2.1)$$

Here,  $\text{Log}_{10}L_V = \text{Log}_{10}(4\pi f_V D_L^2 / L_{\odot V}(1 + z))$  and  $f_V$  is the flux in  $V$ -band,  $D_L$  is the distance luminosity, and  $L_{\odot V}$  is the luminosity of the sun in  $V$ -band. While the  $U - V$  colors derived from EAZY do not give errors on the individual magnitudes, we can assume there are systematic errors from the photometric shifts as well as variations from dust extinction and star formation histories that could result in a scatter of 0.3 dex. For example, a 0.1 shift in  $U - V$  changes the stellar mass by 0.1 since this equation is a linear relation.

Similarly for the EDisCS core sample, stellar masses were initially derived assuming a Kroupa IMF (Kroupa, 2001) using a  $B - V$  mass-to-light ratio (Bell et al., 2003). Although these stellar

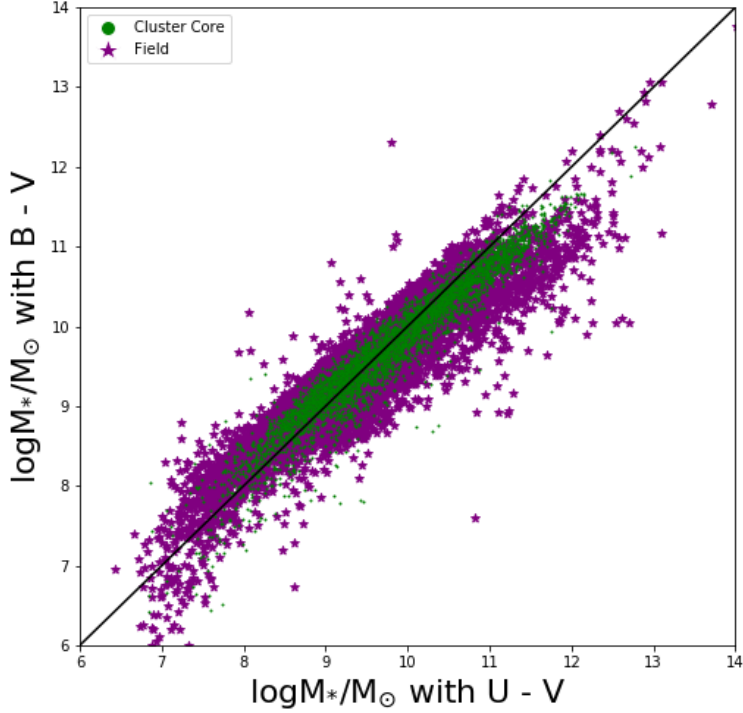


Figure 2.1: This figure compares the two stellar mass derivations with  $B - V$  and  $U - V$  for the EDisCS core observations. Both the core and field galaxies align on a 1-to-1 line, indicating that the new  $U - V$  are reliable.

masses are considered robust, we recalculate them using Equation 2.1 for continuity. A comparison of the two mass calculations is shown in Figure 2.1. Both the core and field galaxies align well when comparing methods and result in  $\pm 0.6$  dex scatter. This reinforces the usage of the  $U - V$ -derived stellar masses in both samples. The turnoff at the high mass end in  $U - V$  is likely due to dustier and subsequently redder galaxies, while the low mass end with elevated  $B - V$  could be due to starburst events. The mass-completeness limit for the EDisCS core sample is  $> 10^{9.8} M_*/M_\odot$ .

## 2.5 Environmental Definitions

Within this thesis, environmental definitions are the crux of analysis and conclusions with which comparisons of local density can be made. The following sections describe the cluster core, infall

Cluster ID (1)	R.A. (2)	Dec. (3)	z (4)	$\sigma$ (5)	$R_{200}$ (6)	$M_{200}$ (7)	Imaging (8)
Cl1018.8-1211	10:18:47	-12:11:53	0.4734	$486^{+59}_{-63}$	$0.93^{+0.11}_{-0.12}$	$1.53^{+0.63}_{-0.52}$ (14)	VRIK
Cl1037.9-1243	10:37:51	-12:43:27	0.5783	$319^{+53}_{-52}$	$0.58^{+0.10}_{-0.09}$	$4.06^{+2.38}_{-1.68}$ (13)	BVRIZK
Cl1040.7-1155	10:40:40	-11:56:04	0.7043	$418^{+55}_{-46}$	$0.70^{+0.09}_{-0.08}$	$8.47^{+3.80}_{-2.50}$ (13)	BVRIZK
Cl1054.4-1146	10:54:25	-11:46:20	0.6972	$589^{+78}_{-70}$	$0.99^{+0.13}_{-0.12}$	$2.38^{+1.08}_{-0.75}$ (14)	BVRIZK
Cl1054.7-1245	10:54:44	-12:45:52	0.7498	$504^{+113}_{-65}$	$0.82^{+0.18}_{-0.11}$	$1.44^{+1.21}_{-0.49}$ (14)	BVRIZK
Cl1059.2-1253*	10:59:07	-12:53:15	0.4564	$510^{+52}_{-56}$	$0.99^{+0.10}_{-0.11}$	$1.78^{+0.60}_{-0.53}$ (14)	VRIK
Cl1103.7-1245a*	11:03:35	-12:46:46	0.6261	$336^{+36}_{-40}$	$0.59^{+0.06}_{-0.07}$	$4.61^{+1.65}_{-1.46}$ (13)	BVRI
Cl1138.2-1133	11:38:10	-11:33:38	0.4796	$732^{+72}_{-76}$	$1.40^{+0.14}_{-0.15}$	$5.20^{+1.69}_{-1.46}$ (14)	BVRIK
Cl1202.7-1224*†	12:02:43	-12:24:30	0.424	$518^{+92}_{-104}$	1.07		BVIK
Cl1216.8-1201	12:16:45	-12:01:18	0.7943	$1018^{+73}_{-77}$	$1.61^{+0.12}_{-0.12}$	$1.16^{+0.27}_{-0.24}$ (15)	BVRIK
Cl1227.9-1138	12:27:59	-11:35:13	0.6357	$574^{+72}_{-75}$	$1.00^{+0.13}_{-0.13}$	$2.29^{+0.97}_{-0.78}$ (14)	BVRIK
Cl1232.5-1250	12:32:31	-12:50:36	0.5414	$1080^{+119}_{-89}$	$1.99^{+0.22}_{-0.16}$	$1.61^{+0.59}_{-0.37}$ (15)	VRIzK
Cl1301.7-1139	13:01:40	-11:39:23	0.4828	$687^{+82}_{-86}$	$1.31^{+0.16}_{-0.16}$	$4.29^{+1.73}_{-1.42}$ (14)	VRIK
Cl1353.0-1137	13:53:02	-11:37:28	0.5882	$666^{+136}_{-139}$	$1.19^{+0.24}_{-0.25}$	$3.67^{+2.74}_{-1.85}$ (14)	VRIK
Cl1354.2-1230	13:54:10	-12:31:01	0.762	$648^{+105}_{-110}$	$1.05^{+0.17}_{-0.18}$	$3.05^{+1.74}_{-1.30}$ (14)	BVRIZK
Cl1411.1-1148	14:11:05	-11:48:29	0.5195	$710^{+125}_{-133}$	$1.33^{+0.23}_{-0.25}$	$4.63^{+2.90}_{-2.15}$ (14)	VRIK
Cl1420.3-1236*	14:20:20	-12:36:30	0.4962	$218^{+43}_{-50}$	$0.41^{+0.08}_{-0.09}$	$1.36^{+0.97}_{-0.74}$ (13)	VRIK

Table 2.3: Cluster information from Just et al. (2019): 1. Cluster name. 2. J2000 right ascension (hours). 3. J2000 Declination (deg). 4. Cluster redshift (Halliday et al., 2004; Milvang-Jensen et al., 2008)). 5. Cluster velocity dispersion in  $\text{km s}^{-1}$  (Halliday et al., 2004; Milvang-Jensen et al., 2008). 6. Cluster virial radius in Mpc. 7. Cluster virial mass in units of  $M_{\odot}$  with power of ten in parentheses (using Equation 10 of Finn et al. 2005). 8. Wide-field imaging bands observed in each field. Rows containing a \* at the end of the Cluster ID only have EDisCS core data (White et al., 2005) and do not have observations from the LDP survey included in this study. This is due to unreliable photometry as discussed in Just et al. (2019). However, each cluster listed here has coverage within the cluster core from White et al. (2005). The † with Cl1202-1223 indicates that this cluster is included in the EDisCS core sample, but is not in the LDP survey due to time restrictions.  $\sigma$  and  $R_{200}$  information is from Vulcani et al. (2013).

region and field as defined in EDisCS and the LDP survey.

### 2.5.1 Cluster Core

The core regions, which are typically on the order of 0.5 – 2 Mpc across, are defined as the area within the virial radius and can include the BCG. For EDisCS, the cores have been extensively studied with deep optical imaging and spectroscopy on VLT (White et al., 2005; Halliday et al., 2004; Milvang-Jensen et al., 2008; Vulcani et al., 2012) and near-IR observations on the New Technology Telescope (White et al., 2005; Rudnick et al., 2009) which has allowed further EDisCS studies such as brightest cluster galaxy identification (White et al., 2005; Whiley et al., 2008), morphologies (Desai et al., 2007; Simard et al., 2009; Vulcani et al., 2011b,a), fundamental-plane parameters (Saglia et al., 2010), red-sequence identification (De Lucia et al., 2004), weak lensing (Clowe et al., 2006),  $24\mu\text{m}$  MIPS SFRs (Finn et al., 2010) and [OII] SFRs (Poggianti et al., 2006, 2009; Vulcani et al., 2010). Cluster cores are dense regions that are attractive for studying cluster properties and are well-suited for observations due to high contrast with the background and density of objects within a given FOV. However, physical processes affecting the evolution of a galaxy appear to occur as these sources enter a cluster environment and thus the cores likely only provide information on their fate. This is reinforced through observations that the cores typically include a higher fraction of massive red disk or quiescent galaxies (Dressler, 1980; Bell et al., 2004; Kauffmann et al., 2004; Erfanianfar et al., 2016). A spatially-expanded view of clusters is required to gather information on environmentally-driven quenching mechanisms across a representative sample of galaxies within a cluster.

### 2.5.2 Infall Region

Galaxy clusters extend far beyond their cores and virial radii, and in order to achieve a more informed understanding of the role of environment on galaxy evolution, it is important to extend analyses to projected radii greater than  $R_{200}$ . This is a challenging task, as the reduced density of the cluster density profile results in a decreased contrast with the foreground and background

(Newman et al., 2013). Large and wide-field spectroscopic studies are required to conclusively establish membership in these regions, and since such programs are challenging, there are few studies of cluster outskirts beyond the local universe (Geach et al., 2006; Patel et al., 2009b; Dressler et al., 2013; Spérone-Longin et al., 2020). EDisCS observations beyond the central cluster core region include wide-field imaging with MIPS ( $\sim 50' \times 20'$  FOV; *Mann et al. in prep*), CO observations with ALMA (SEEDisCS), (Spérone-Longin et al., 2020) and the Low-Dispersion Prism (LDP;  $30' \times 30'$  FOV) on IMACS/Magellan (Just et al., 2019). This information is crucial towards establishing cluster membership beyond the central core as in previous EDisCS studies and allows for targeted follow-up observations of groups or infalling populations.

Just et al. (2019) utilized the theory of secondary infall to identify the infall region of the galaxy clusters with the equations given in White & Zaritsky (1992). This theory describes how shells of mass evolve with redshift when centered on a cosmic perturbation; shells that are contained within a critical mass will eventually follow a gravitational collapse and become bound. The outermost boundary of the mass shell that experiences collapse at the cluster redshift is defined as the infall radius.

An illustration of the intracluster environmental definitions is shown in Figure 2.2. A distribution of the LDP cluster member sample as a function of radius is shown in Figure 2.3. There are a significant number of galaxies with cluster-centric distances  $> \sim R_{200}$ , which extends beyond the virial radius. This reinforces the importance of expanding observations beyond the core region to produce a more representative sample of the cluster environment. The power of the LDP survey is shown through cluster membership identification out to  $7R_{200}$  in some clusters (Just et al., 2019).

### 2.5.3 Field Sample

A field sample, which is assumed to occupy a less dense and interactive region of the universe, is established in order to form a comparison set of galaxies in an effort to constrain environmental effects from the cosmic web. Nearly  $\frac{3}{4}$  of all galaxies in the universe reside in the field and have been the subject of many surveys such as 3DHST (Momcheva et al., 2016) and CANDELS (Grogin

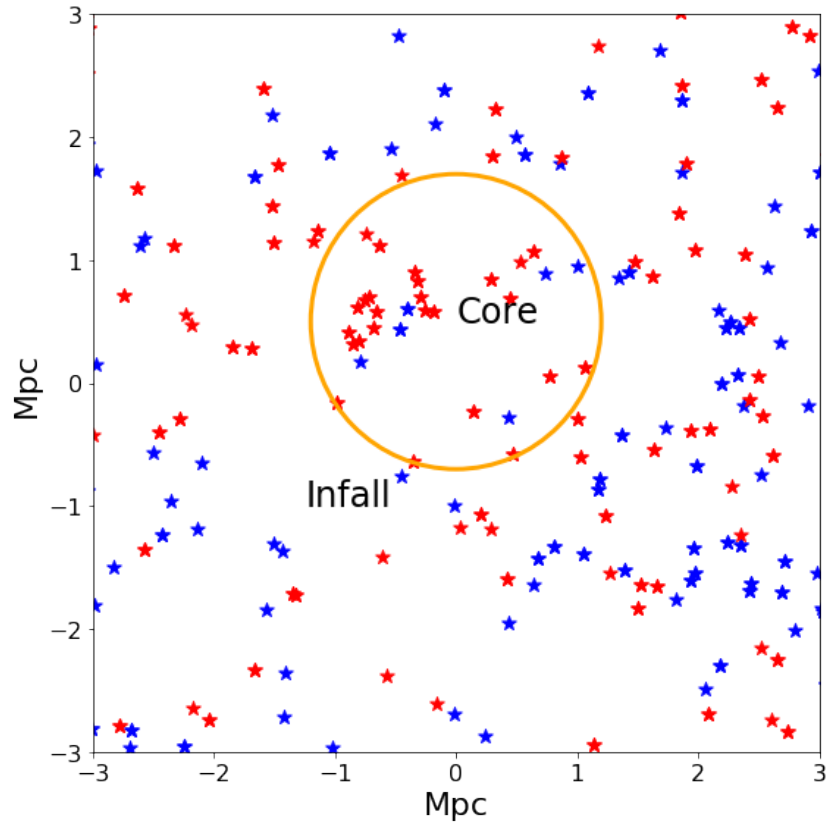


Figure 2.2: This illustrates the environmental definitions within a galaxy cluster, where each red/blue star represents an individual galaxy. The orange circle is the virial radius and the region encompassed within this area is defined as the core. Outside of the virial radius is the infall region.

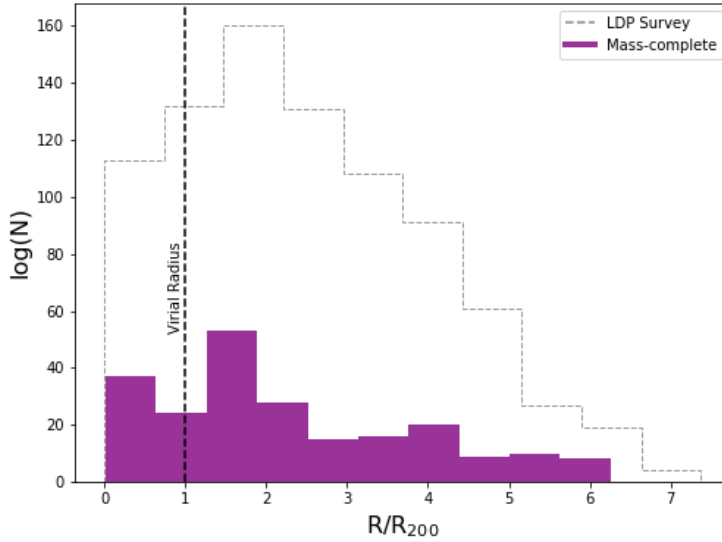


Figure 2.3: The distribution of cluster members as a function of  $R_{200}$ . The full sample is shown as the grey dash while the mass-complete sample is in purple. The virial radius distance is demonstrated by the vertical dashed line. The LDP survey includes cluster membership to a max of  $7R_{200}$ .

et al., 2011). In this study, *HST*-observed galaxies within each pointing FOV in the range of  $0.4 < z < 0.9$  that lie outside  $\pm 0.02$  of each cluster redshift are considered to be in the field.

## 2.6 Sample Overview

This thesis makes use of two separate surveys covering the EDisCS clusters. In total, 13 clusters have wide field observations (LDP), while 16 only cover the core region (EDisCS Core). Between the 2 surveys, there is an overlap of 805 galaxies. Obtained fluxes in the photometric portion of each survey can be converted into rest-frame  $U - V$  and  $V - J$  colors with EAZY (Brammer et al., 2008)<sup>1</sup>. This is completed through a convolution of the best-fit EAZY spectral templates with Johnson  $U$ ,  $V$  and 2MASS  $J$ -band filters. This allows for a color-color selection technique with the Williams et al. (2009) lines described in Section 1.5 to determine if a galaxy is quiescent or star-forming. The entire mass-complete sample mass distribution with median values for each

<sup>1</sup><https://github.com/gbrammer/eazy-photoz>

environment shown as vertical lines and a  $UVJ$  diagram are shown in Figure 2.4 for both the EDisCS Core and LDP surveys. The  $UVJ$  diagram on the right has the Williams et al. (2009) cuts as listed in Section 1.5. Additionally, our sample does not have many dusty galaxies, which explains the vertical signature in  $V - J$ . This trend is also observed in the ULTRAVISTA datasets (Muzzin et al., 2013). Notably, many of the LDP cluster core and infall galaxies are located in the passive region of the  $UVJ$  diagram. K-S 2-sample tests for the LDP survey between the core-infall, core-field and infall-field have statistics of 0.17, 0.08, 0.14 and p-values of 0.16, 0.85, and 0.003. While the core-infall and core-field samples are likely from the same distribution, the very low p-value from the infall-field indicates these samples are statistically different.

Figures 2.5 and 2.6 show a 3-panel overview of each cluster for the EDisCS core and LDP observations, respectively. The left panel is a spatial RA/Dec view of the cluster, where filled colored dots represent a cluster member galaxy with stellar mass  $> 10^{9.8}M_{\odot}$  for the EDisCS core or  $10^{10.6}M_{\odot}$  for the LDP survey that is quiescent (red) or star-forming (purple) as determined from the  $UVJ$  diagram in the middle panel. Open colored dots represent cluster members below the mass completeness limit. Grey dots are sources that have a spectroscopic redshift in the field and the orange circle is the virial radius. In the  $UVJ$  diagram, mass-complete galaxies in the field are purple stars and cluster members are green circles. The black lines designate the boundaries between quiescent and star-forming, as described in Section 1.5 from Williams et al. (2009). Distributions of the masses by environment are shown in the left column. The mass-complete samples in each cluster are predominantly in the passive clump, which will be discussed more in depth in Chapter 3.

c

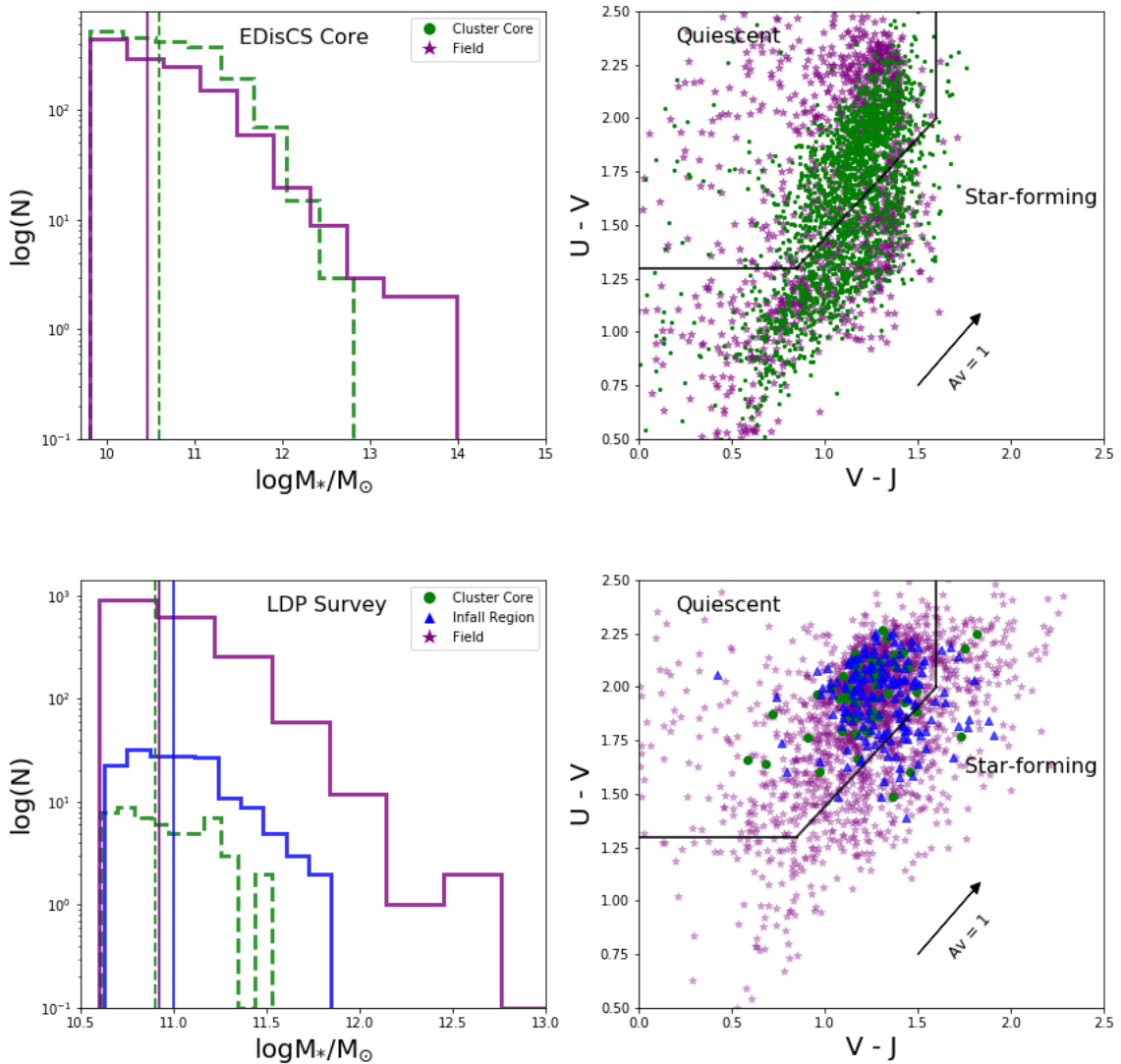
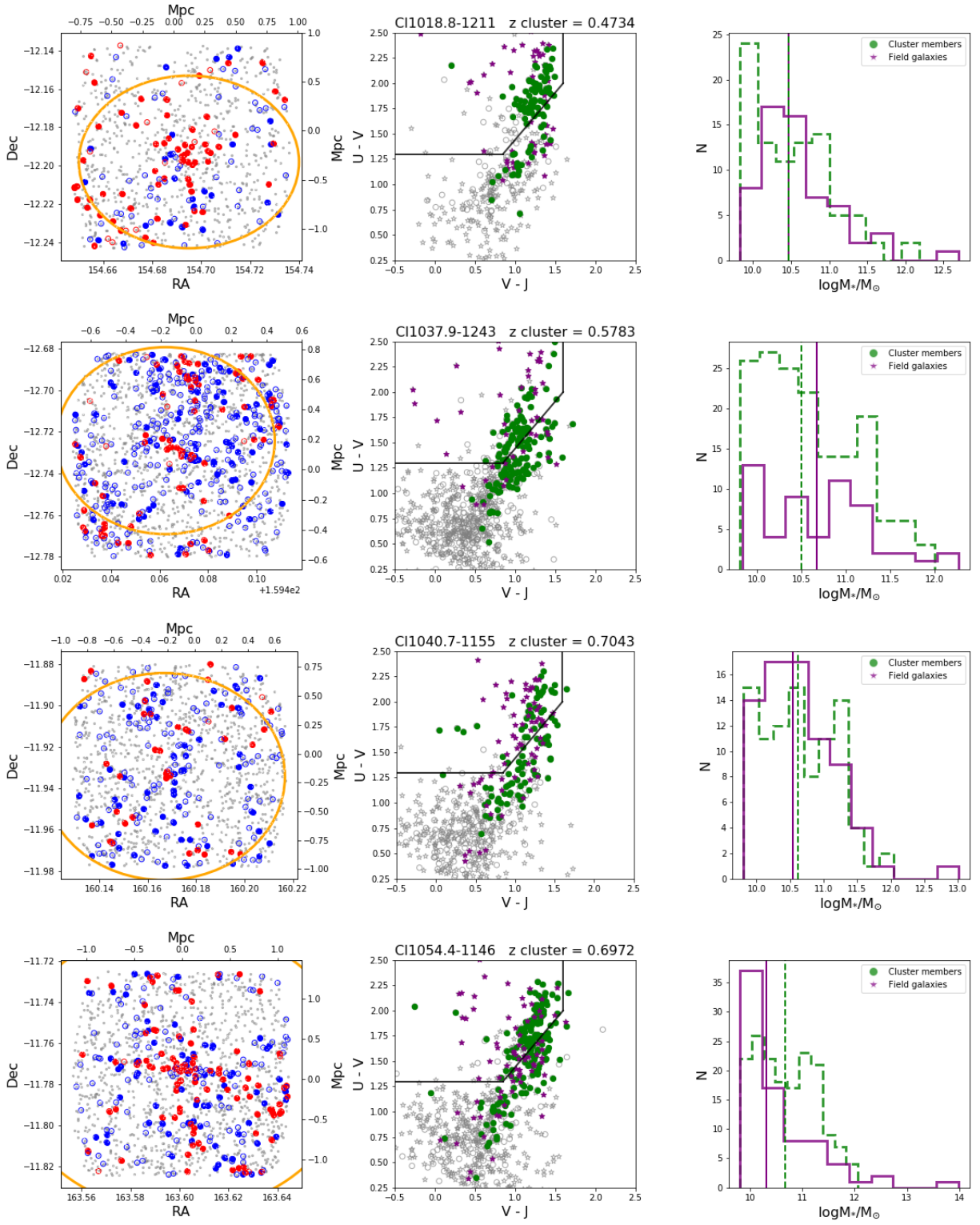
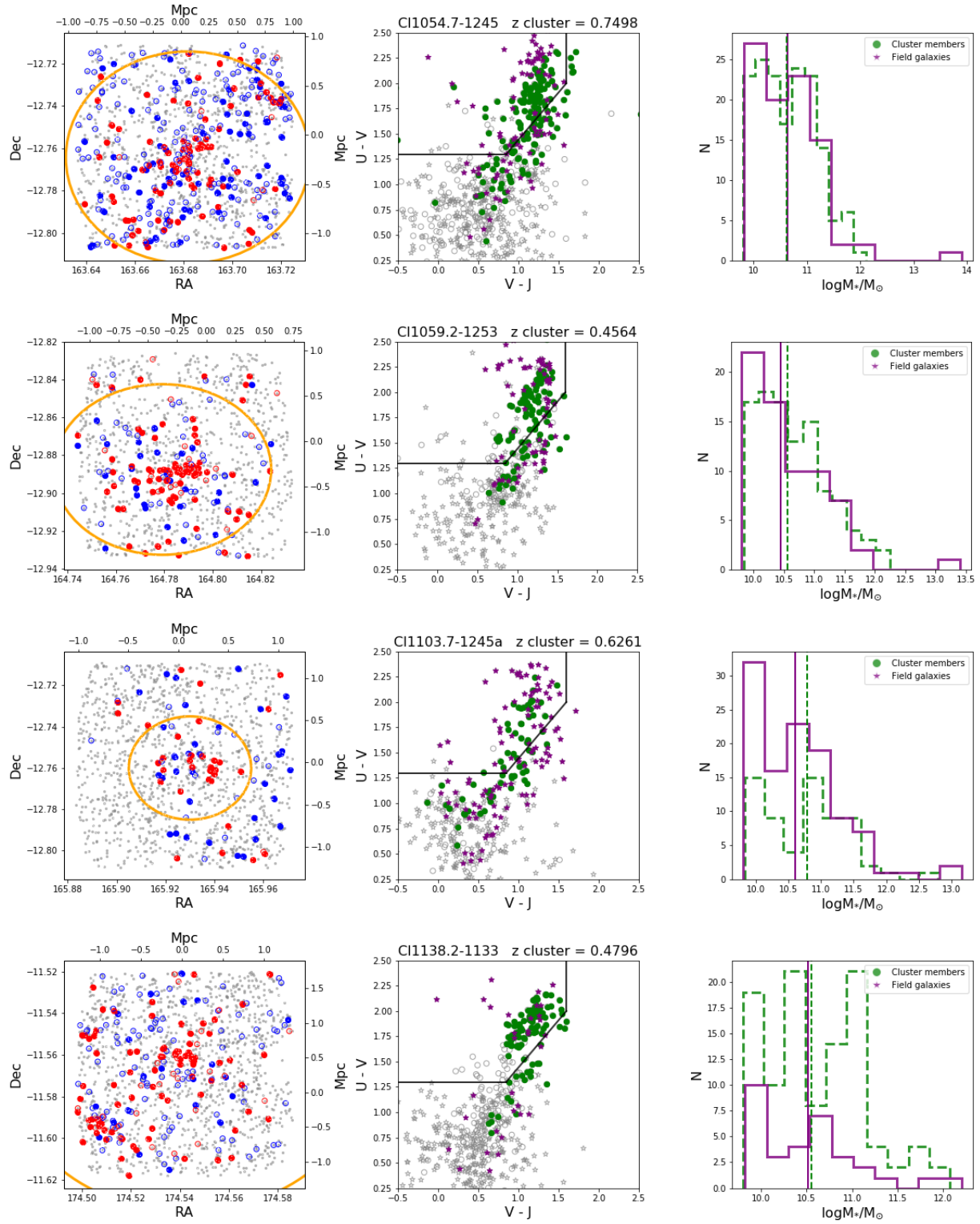
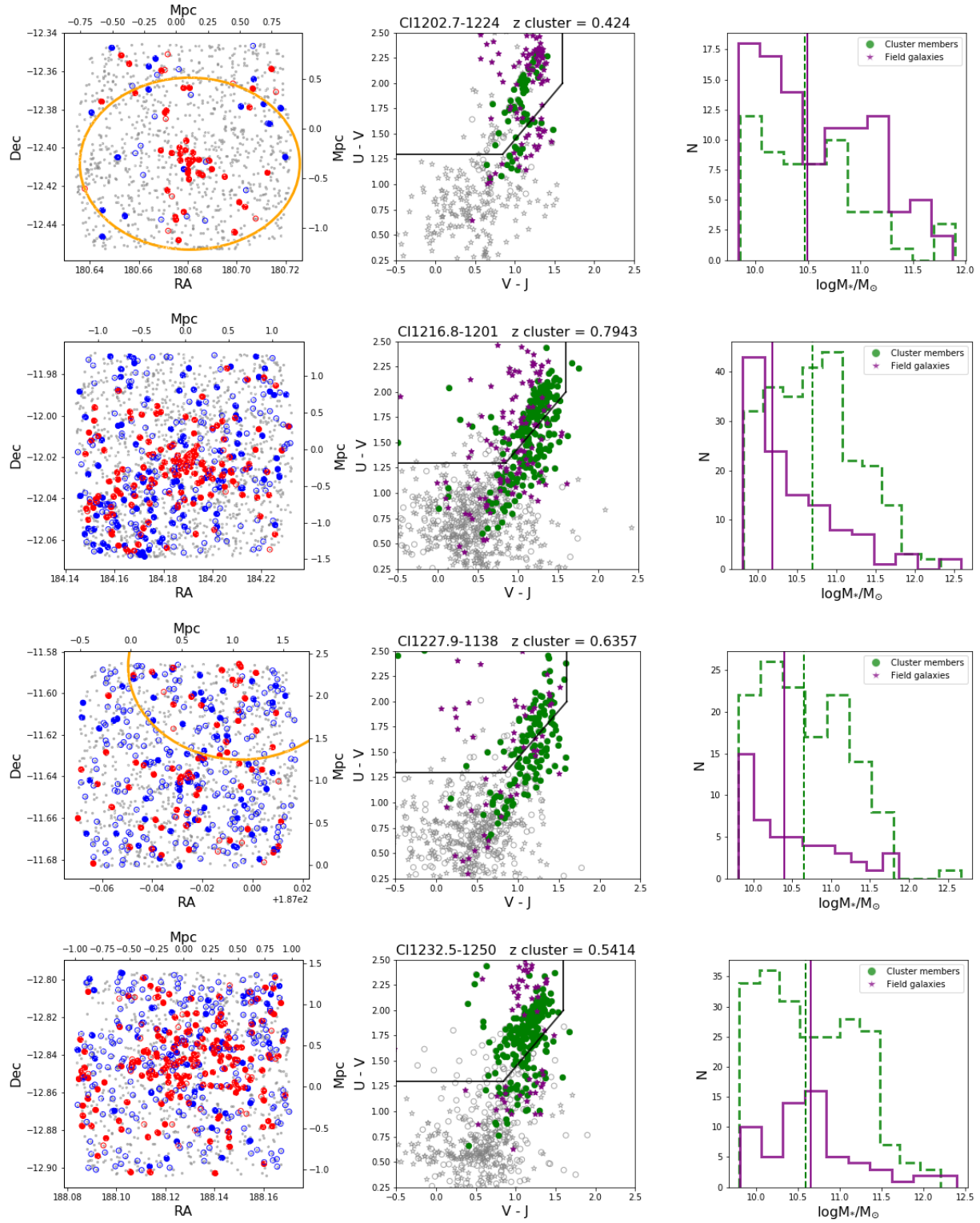
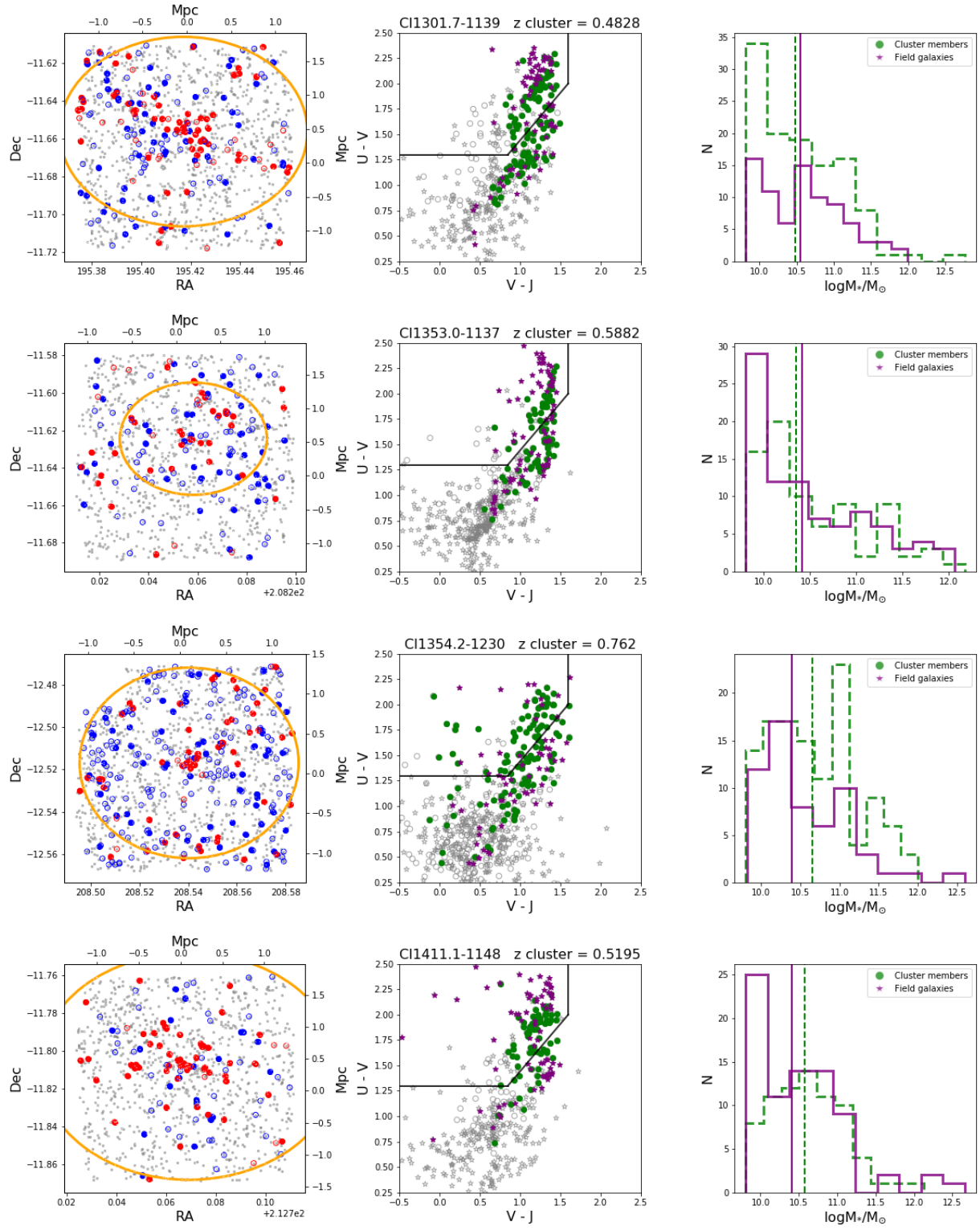


Figure 2.4: (Top Left) The distribution of mass-complete samples from the EDisCS core survey for the core (green dash) and field (purple) environments. The median values for each sample is demonstrated by the vertical line. The core sample is more deficient in massive galaxies when compared to the field sample. (Top Right) Rest-frame  $UVJ$  color-color diagram for the mass-complete sample with Williams et al. (2009) boundaries for quiescent (upper left) or star-forming galaxies. (Bottom Left) The distribution of mass-complete samples from the LDP survey for the core (green dash), infall (blue) and field (purple) environments. The median values for each sample is demonstrated by the vertical line. Similarly to the EDisCS core sample above, the core sample is more deficient in massive galaxies when compared to the infall and field samples. (Bottom Right) Rest-frame  $UVJ$  color-color diagram for the mass-complete sample with Williams et al. (2009) boundaries for quiescent (upper left) or star-forming galaxies.









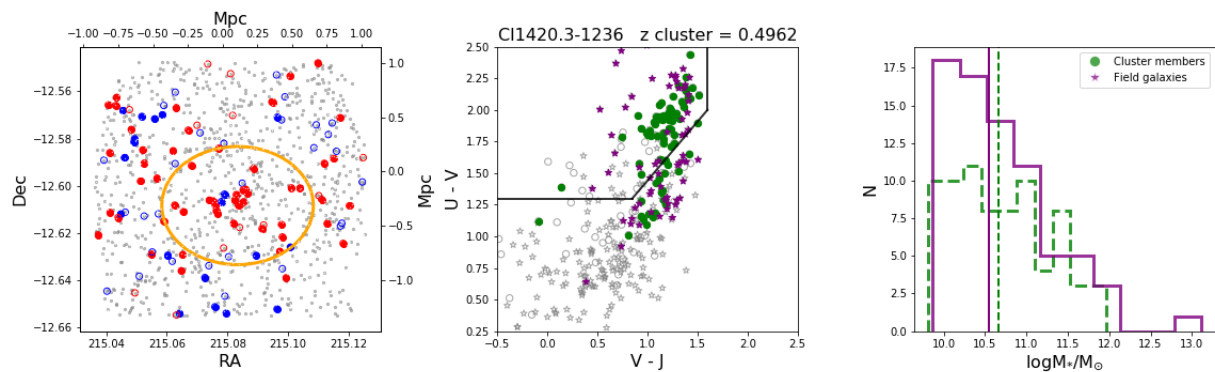
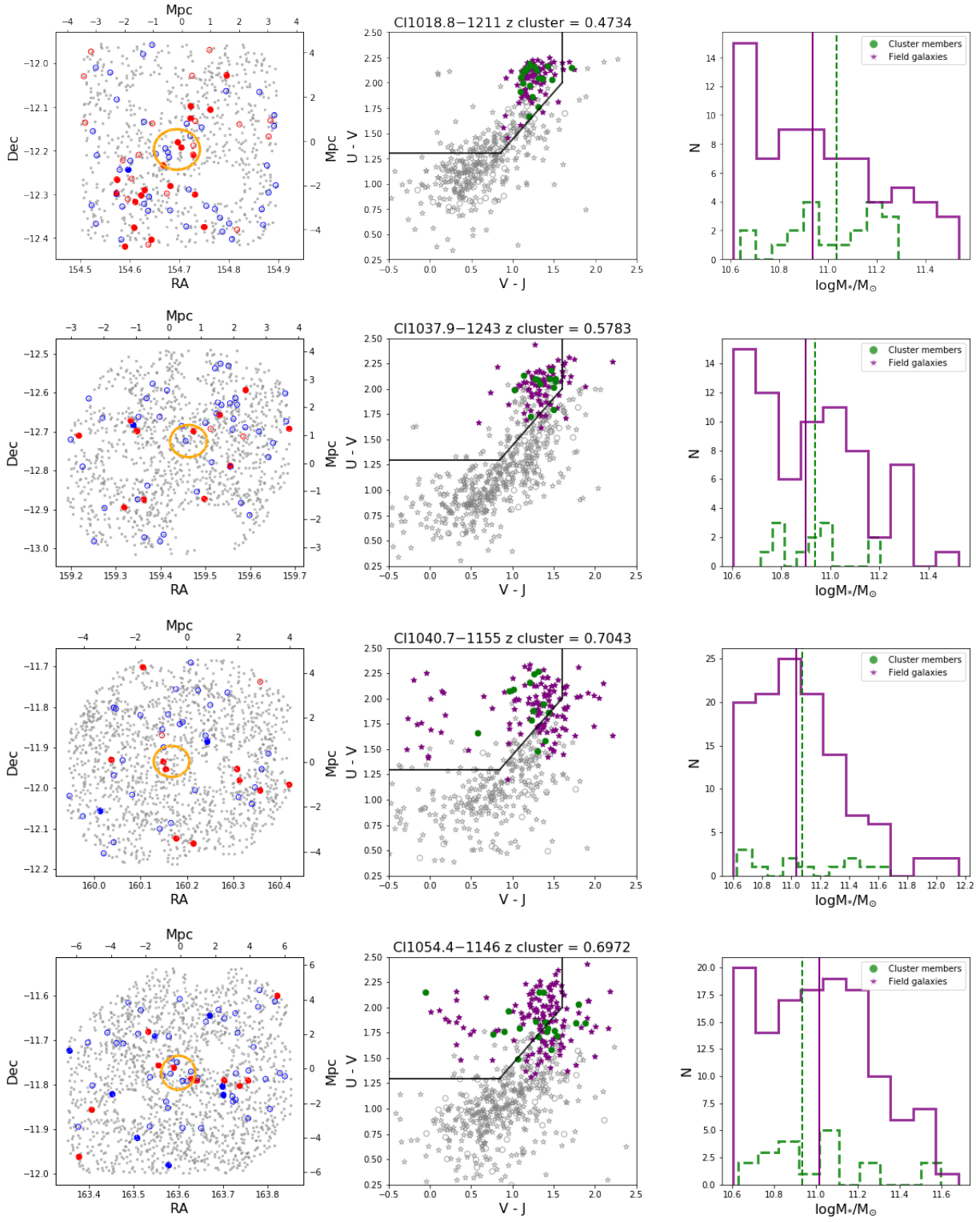
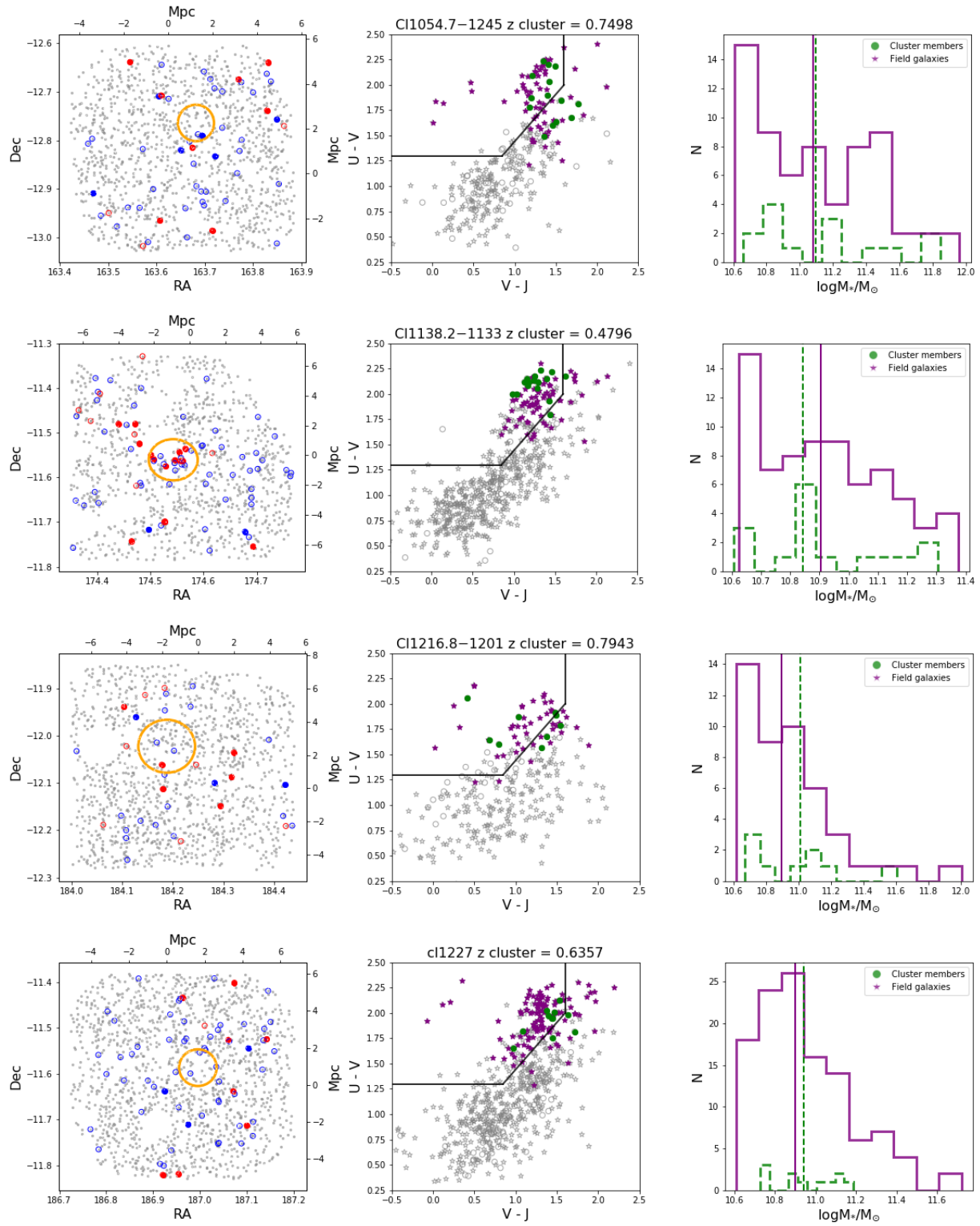
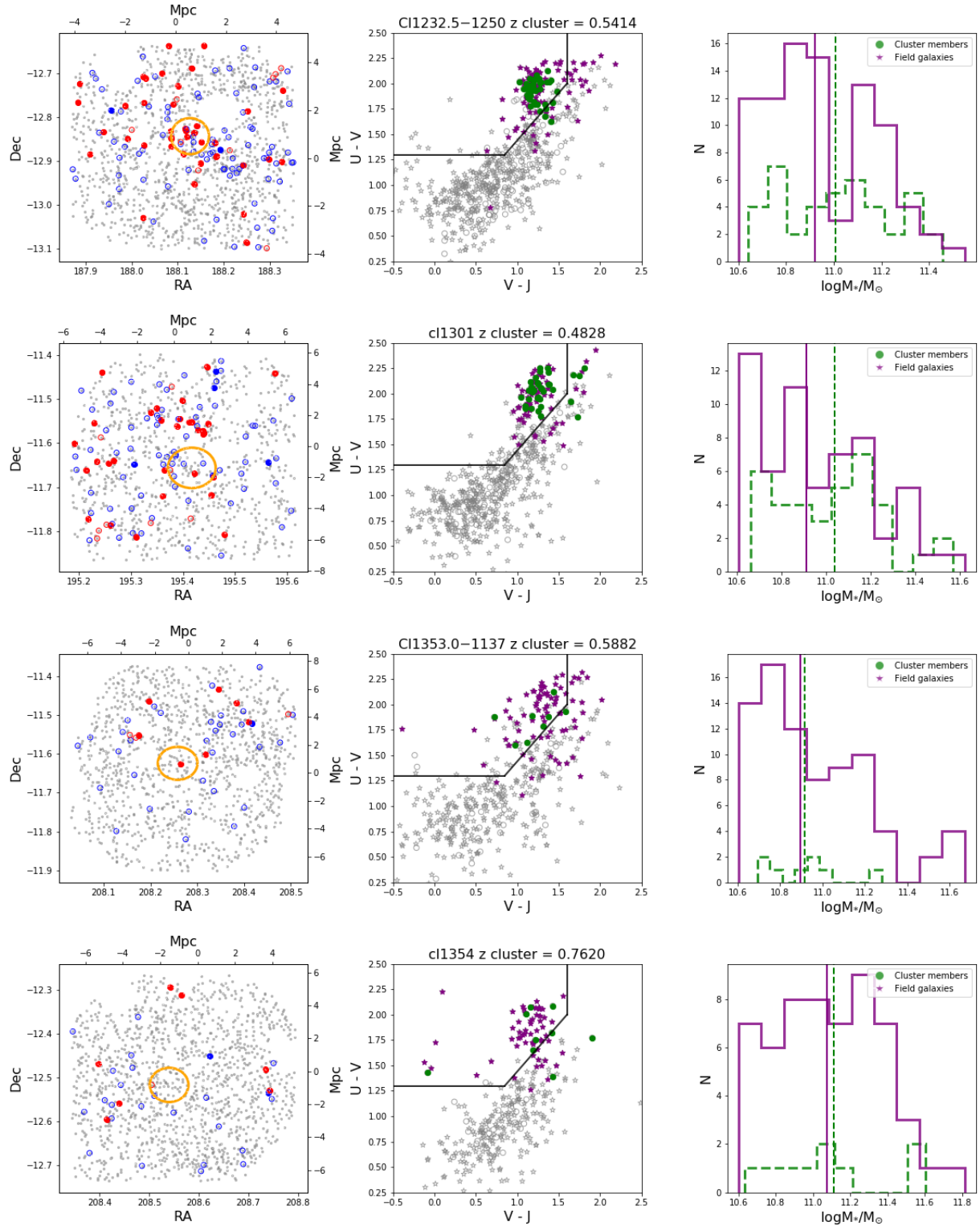


Figure 2.5: (Left) The RA and Dec FOV for each cluster in the EDisCS core survey, where everything with a redshift is a grey dot. Cluster members are circles that are either red for  $UVJ$ -passive or blue for star-forming. Filled circles represent mass-complete cluster members. The orange oval represents  $R_{200}$  around the brightest cluster galaxy; some clusters do not show this due to the FOV being within  $R_{200}$ . A majority of these observations cover  $R_{200}$  within each cluster. (Center)  $UVJ$  color-color diagrams for the mass-complete cluster members at all radii (green circle) and field galaxies (purple stars) with the Williams et al. (2009) definitions for passive (upper left) and star-forming regions. (Right) The stellar mass distributions and median values for cluster (green) and field (purple) galaxies.







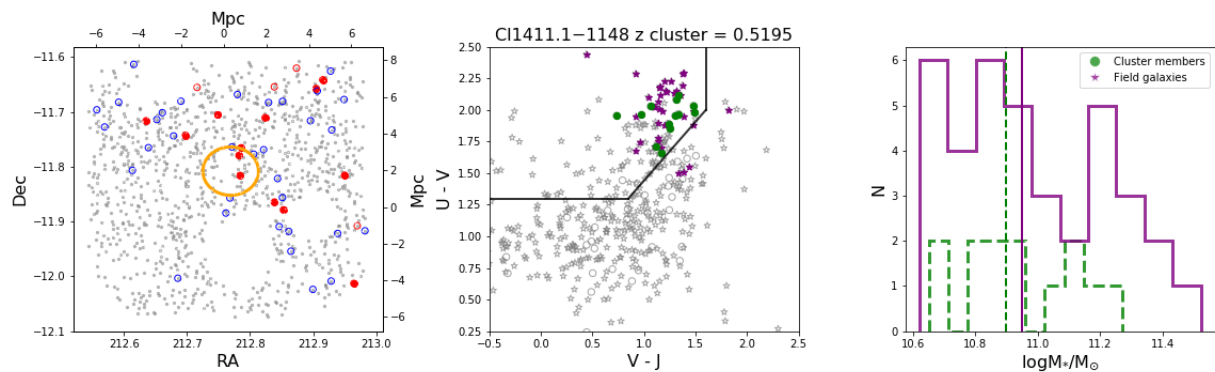


Figure 2.6: (Left) The RA and Dec FOV for each LDP cluster, where everything with an LDP redshift is a grey dot. Cluster members are circles that are either red for  $UVJ$ -passive or blue for star-forming. Filled circles represent mass-complete cluster members. The orange oval represents  $R_{200}$  around the brightest cluster galaxy. The blank areas without any dots represent a mask for bright stars where observations could not be completed. The combined LDP and WFI observations extend far beyond the core into the infall region in each cluster. (Center)  $UVJ$  color-color diagrams for the mass-complete cluster members at all radii (green circle) and field galaxies (purple stars) with the Williams et al. (2009) definitions for passive (upper left) and star-forming regions. (Right) The stellar mass distributions and median values for cluster (green) and field (purple) galaxies.

## Chapter 3

# EDisCS Quiescent Fraction - Investigating the Evolutionary Transition

### Abstract

This chapter presents an overview of the passive galaxy population of the EDisCS clusters. First, in Section 3.1, we introduce the passive fraction and correction for interlopers. In Section 3.2, we present the results for the passive fraction in the core, infall region, and field environments in relation to redshift, stellar mass and cluster-centric distance. In Section 3.3, we discuss the results, implications for the role of environment on galaxy evolution, and future work.

### 3.1 EDisCS Passive Fraction

The datasets described in Chapter 2 represent the basis of this work, which will combine results from both the original EDisCS (White et al., 2005) and more recent wide field observations in Just et al. (2019). In both surveys a distance of  $R/R_{200} < 1$  is defined as the cluster core and beyond this is considered the infall region. The role of environment on the passive fraction is investigated on an intracluster scale for a range of available comparisons to the field. Additionally, only galaxies above the respective mass-complete value are considered. From the EDisCS core survey, there are 2,505 cluster members with  $\text{Log}M_* > 9.8$ . After applying the quality and magnitude-limit cuts, there are 2,090 galaxies in the LDP survey with  $\text{Log}M_* > 10.6$ , of which 220 are cluster members. Field samples accompany each dataset that are limited to  $\pm 0.2$  from the cluster redshift.

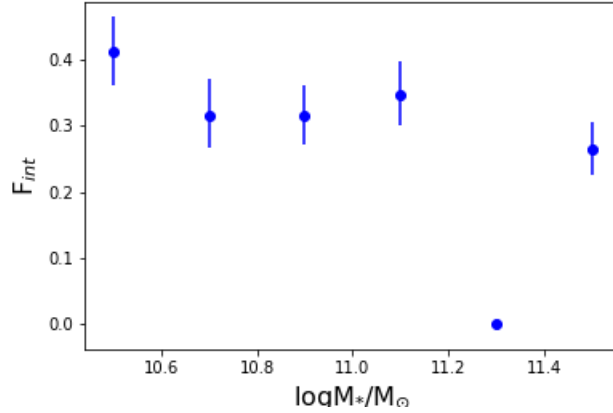


Figure 3.1: The interloper fraction,  $f_{int}$ , as a function of stellar mass. The spectroscopic sample has a shallower mass-completeness level ( $\text{Log}M_*/M_\odot > 10.4$ ) than the photometric sample, so the interloper fraction is extrapolated to cover those mass bins. Note that there were no identified interlopers in the  $\text{Log}M_*/M_\odot$  11.0 – 11.2 mass bin, however, an average of the  $f_{int}$  from  $\text{Log}M_*/M_\odot > 11.0$  is used.

This analysis divides results into two redshift bins: a low ( $0.4 < z < 0.6$ ) and high ( $0.6 < z < 0.8$ ) sample to search for temporal evolution of the passive fraction. All shown error bars are a  $1\sigma$  Wilson binomial confidence interval.

The passive fraction,  $f_{passive}$ , is simply derived as the number of passive galaxies divided by the total number of galaxies. However, with the photometric core sample in White et al. (2005), there is a significant amount of interlopers potentially masquerading as cluster core members that must be accounted for, as discussed in Pelló et al. (2009). A spectroscopically observed field galaxy that is classified as a cluster member in the photometric sample is defined as an interloper because a spectroscopic redshift supersedes a photometric one; the relative proportion of galaxies falling into this category, called the interloper fraction  $f_{int}$ , are examined as a function of stellar mass in Figure 3.1. While spectroscopic coverage is  $\sim 1\%$  of the total photometric sample,  $f_{int}$  can be extrapolated out to the entire photometric catalog. The mass-completeness limit for the spectroscopic sample is  $\text{Log}M_*/M_\odot > 10.4$ , so the  $f_{int}$  is approximated to the lower photometric mass-completeness limit of  $\text{Log}M_*/M_\odot > 9.8$  by averaging all points of  $f_{int}$  at stellar masses  $\text{Log}M_*/M_\odot < 11.0$ .

Seeing as the field typically has a lower  $f_{passive}$ , this indicates that star-forming galaxies could

be contaminating the core  $f_{passive}$ . In order to approximate the true  $f_{passive}$  of the cluster core, the fraction of interlopers  $\times$  the photometric field passive fraction are removed from the passive fraction of the spectroscopic and photometric-only core members (Equation 3.1). The numerator terms are restricted to passive galaxies while the denominator includes all galaxies, regardless of  $UVJ$  classification. This equation is calculated in stellar mass bins of 0.4 dex due to the dependence of  $f_{passive}$  on mass.

$$f_{passive,core} = \frac{N_{passive,spectroscopic,core} + N_{passive,photometric,core} - f_{int} \times N_{passive,photometric,field}}{N_{spectroscopic,core} + N_{photometric,core} - f_{int} \times N_{photometric,core}} \quad (3.1)$$

The first terms in the numerator and denominator are cluster member observations with spectroscopic redshifts. The 2nd terms following this are cluster member photometric observations that do not have a spectroscopic counterpart. Finally, the 3rd terms are field photometric observations that do not have a spectroscopic counterpart. The field  $f_{passive}$  in Equation 3.2 is only the first two terms of the equation for the core above in 3.1 because we assume the fraction of cluster members in the field is  $\ll$  than  $f_{int}$ .

$$f_{passive,field} = \frac{N_{passive,spectroscopic,field} + N_{passive,photometric,field}}{N_{spectroscopic,field} + N_{photometric,field}} \quad (3.2)$$

### 3.1.1 Passive v. Star-forming Galaxies

The bimodal population distribution of galaxies identified as either blue star-forming or quiescent red galaxies is well-established in the literature (Blanton et al., 2003; Kauffmann et al., 2003; Baldry et al., 2004; Brinchmann et al., 2004b; Davies et al., 2019). The straightforward binary classification scheme in Williams et al. (2009) utilizing rest-frame  $U - V$  and  $V - J$  colors has become a widely utilized metric to separate two distinct galaxy populations in the Universe as

either the passive clump or red sequence and the blue star-forming track. These definitions are presented in Section 1.4, where the upper left-hand portion of the diagram contains the quiescent population and those galaxies residing outside of these boundaries are star-forming. Rest-frame  $UVJ$  colors are available for each of the EDisCS clusters out to several virial radii (Just et al., 2019). Rest-frame  $V$ -band (551 nm) photometry is derived from observations on the Wide Field Imager, but the rest-frame  $U$ -band (365 nm) required extrapolation from  $B$ -band (Just et al. 2019) for low- $z$  clusters, while the  $J$ -band (1220 nm) photometry is derived from an interpolation of the  $K$ -band (2190 nm). The rest-frame  $UVJ$  colors calculated from Just et al. (2019) require a shift for the passive sequence to align with passive clump identified in the deep EDisCS core data. This is done on a cluster-by-cluster basis, which results in different shifts for each cluster. While the shifts are minor ( $<0.2$  in color), this is necessary to correctly compute stellar masses (Section 2.4) and identify quiescent or star-forming members. Additionally, the offset in  $U - V$  is applied to the rest-frame  $V$  flux because the  $U$ -band is assumed to be without error, which directly affects the stellar masses (see Section 2.3.1 for a discussion on photometry issues and calibration).

## 3.2 Results

### 3.2.1 $f_{passive}$ vs. Redshift

We present the results for the LDP EDisCS passive fraction in two intracluster environments as a function of stellar mass and cluster-centric distance. In Figure 3.2, the  $f_{passive}$  for each cluster in the LDP survey is compared to the field galaxies in a low and high- $z$  bin. A gradual trend from high to low- $z$  towards a  $f_{passive} \sim 1$  demonstrates the buildup of passive galaxies within the Universe over a several billion year timescale. At low- $z$ , a majority of the clusters have elevated  $f_{passive}$  when compared to the field, but this trend is less apparent at high- $z$ . A Spearman Rank coefficient and p-value for the clusters (-0.75, 0.03) confirm this inverse relationship, while the field (-0.48, 0.09) is less correlated. In this comparison, it is evident that the clusters are evolving more rapidly than the field.

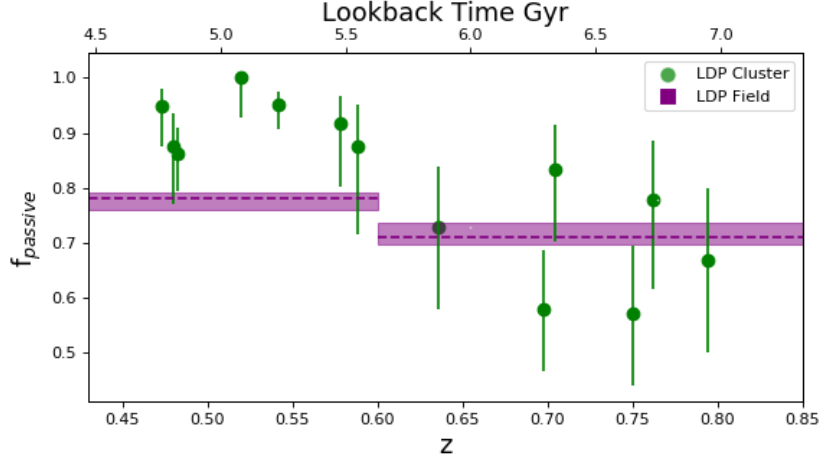


Figure 3.2: The passive fraction vs. redshift for each of the LDP EDisCS clusters. Cluster members are shown as green circles and the field (outside  $\pm 0.02$  of  $z_{cluster}$ ) as a purple dashed line with the shaded region corresponding to a  $1\sigma$  binomial error. The buildup of passive galaxies is evident with the increased passive fraction at lower redshifts. The cluster members include all galaxies within the FOV for the cluster.

Figure 3.3 is the same comparison as above, but divides the cluster into separate environments dependent upon intracluster radius into core and infall region for the LDP sample. Here, several low- $z$  clusters have core and infall regions solely composed of mass-complete quiescent members, which is also evident in the RA/Dec spatial plot in Figure 2.6. These same clusters also have systematically higher infall  $f_{passive}$  values than in the field, which may indicate the presence of various quenching processes between environments. The following sections will explore the  $f_{passive}$  in relation to stellar mass and intracluster redshift in order to constrain which quenching processes could be contributing to these results.

### 3.2.2 $f_{passive}$ vs. Stellar Mass

Here, we present the relation for  $f_{passive}$  vs. stellar mass for both the EDisCS VLT core and the LDP survey. First, the  $f_{passive}$  for the EDisCS core is shown in Figure 3.4, with a comparison to the Planck ( $0.5 < z < 0.7$ ; van der Burg et al. 2018) and GLASS ( $0.3 < z < 0.6$ ; Morishita et al. 2017) clusters. A field comparison is presented from EDisCS, Planck (van der Burg et al., 2018) ( $0.5 < z < 0.7$ ) and ULTRAVISTA (Muzzin et al., 2013) ( $0.5 < z < 1.0$ ). The redshift range for

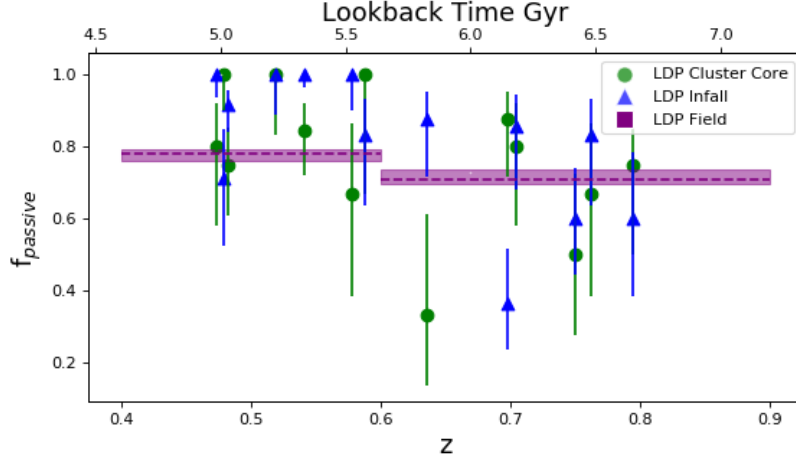


Figure 3.3: The passive fraction vs. redshift for each of the LDP EDisCS clusters, but separated by the internal cluster environment. Cluster core members are shown as green circles, cluster infall members as blue triangles, and the field (outside  $\pm 0.02$  of  $z_{cluster}$ ) as a purple dashed line with the shaded region corresponding to a  $1\sigma$  binomial error. Blue and green points are calculated within the same bin, but are staggered for ease of interpretation. The buildup of passive galaxies is still evident with the increased passive fraction at lower redshifts. There isn't a clear trend of passive galaxies with intracluster environment, however, for clusters at  $z < 0.6$ , all but two of the seven have infall regions entirely comprised of passive galaxies.

the ULTRAVISTA field is larger than our EDisCS sample and the Planck sample straddles both  $z$  bins. Including galaxies from an earlier epoch in ULTRAVISTA has the potential to lower the  $f_{passive}$  in this comparison set.

Mass quenching in both the field and core is evident with the positive relation between stellar mass and  $f_{passive}$ . This spatially-constrained core sample is elevated in respect to both the EDisCS and ULTRAVISTA field at low- $z$  and at stellar masses  $\text{Log}M_*/M_\odot < 11.4$ , which suggests environmental quenching. However, a  $f_{passive}$  difference of  $\sim 20\%$  exists at the highest stellar mass; this indicates that all of the most massive cluster galaxies are already quenched, which is likely due to intrinsic mass quenching. At high- $z$ , the separation of  $f_{passive}$  between core and field galaxies initiates at  $\sim \text{Log}M_*/M_\odot > 10.0$ , but disappears at masses greater than  $\text{Log}M_*/M_\odot > 11.0$ . Similarly to the low- $z$  clusters, nearly all of the most massive cluster galaxies are quenched. Additionally, there is moderate redshift dependence within the cluster sample with a shift of approximately 20% in the  $f_{passive}$  from high to low- $z$ , which supports the Butcher-Oemler effect (Butcher & Oemler, 1978) and subsequent findings (Balogh et al., 1999; Poggianti et al., 2006; Wagner et al., 2017;

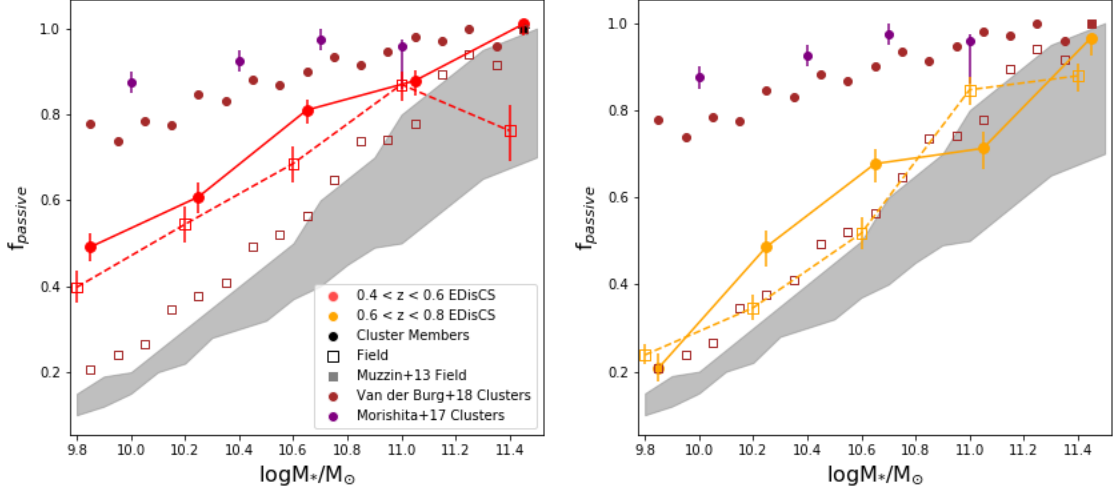


Figure 3.4: The passive fraction vs. stellar mass for all EDisCS clusters in the VLT sample, where the cluster  $f_{passive}$  are filled circles and those in the field are shown as open squares. Points encompass the same bin range but are staggered for ease of interpretation. These data only encompass the cluster cores from White et al. (2005). Galaxies are binned by stellar mass and redshift into a lower (Left;  $0.4 < z < 0.6$ , red) and higher (Right;  $0.6 < z < 0.8$ , yellow)  $z$  bin. A comparison to the  $0.5 < z < 1.0$  field  $f_{passive}$  from Muzzin et al. (2013) is shown in grey, the Planck clusters ( $0.5 < z < 0.7$  van der Burg et al. 2018) as brown circles, and comparison field as open brown squares, and GLASS clusters ( $0.3 < z < 0.5$  Morishita et al. 2017) as the purple circles. On the left pane, the black star is positioned as a  $f_{passive} = 1$ ; from Equation 3.1, it is possible to determine a  $f_{passive} > 1$  with the field correction. The  $f_{passive}$  dependency on redshift is apparent with the EDisCS clusters, with an approximate 20% increase in the  $f_{passive}$  from high to low- $z$ . In the low- $z$  bin, only the most massive galaxies have significantly differentiated  $f_{passive}$ , indicating that environmental quenching is not dominant here. Additionally, the core at all  $z$  has a lower  $f_{passive}$  than the massive Planck and GLASS clusters.

Jian et al., 2018; Pintos-Castro et al., 2019). The EDisCS points are below the two cluster studies for Planck and GLASS at all redshifts, which are both samples of massive clusters and may pre-process galaxies more than smaller clusters (De Lucia et al., 2012). However, the EDisCS high- $z$  field is in good agreement with the Planck field.

The relation for the LDP survey clusters and field is shown in Figure 3.5, with an additional field sample from ULTRAVISTA ( $0.5 < z < 1.0$ ; Muzzin et al. 2013). The low- $z$  sample is in moderate agreement with the Planck and GLASS clusters and is higher than both the LDP and ULTRAVISTA field samples. The LDP cluster and field  $f_{passive}$  at low- $z$  are more separated than

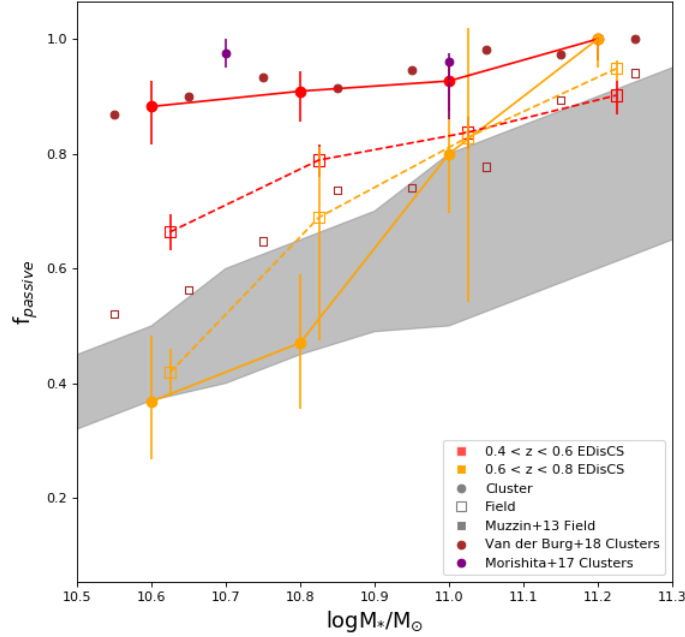


Figure 3.5: The passive fraction vs. stellar mass for all EDisCS clusters in the LDP sample, where cluster galaxies are circles and those in the field are shown as open squares. Galaxies are binned into four stellar masses and by redshift into a lower ( $0.4 < z < 0.6$ , red) and higher ( $0.6 < z < 0.8$ , yellow)  $z$  bin. A comparison to the field  $0.5 (< z < 1.0)$   $f_{passive}$  from Muzzin et al. (2013) is shown in grey, the Planck clusters van der Burg et al. (2018) as brown circles and comparison field as open brown squares, and GLASS clusters Morishita et al. (2017) as the purple circles. The  $f_{passive}$  environmental dependence is much more apparent here, where the low- $z$  bin has a clear and significant difference from the field.

in the VLT relation, which can indicate the presence of environmental quenching. However, the high- $z$  bin for the core does not show significant difference from the LDP and ULTRAVISTA field. However, the LDP cluster and field  $f_{passive}$  at low- $z$  are more separated than in the VLT relation; the 2-sample t-test statistic and p-value for cluster and field at low- $z$  are  $[-0.86, 0.41]$  for the VLT sample and  $[-2.34, 0.06]$  for the LDP sample, which demonstrates the larger differences in means (0.86 vs. 2.34). Mass quenching is potentially more evident in the high redshift epoch, as evident by the steep relation in high- $z$  bin and flat relation in low- $z$ . While the least massive galaxies at high- $z$  have yet to be quenched, this could be evidence of the Butcher-Oemler effect.

This relation for the LDP survey is then split by intracluster environment into the core and

infall samples in Figure 3.6, which is made possible by the wide-field survey of EDisCS (Just et al., 2019). For the core, both redshift regimes are mostly quiescent galaxies and are in good agreement with the Planck and GLASS cluster sample comparisons. However, the large error bars on the high- $z$  core make this statistically insignificant for the infall region as the uncertainty reaches into the shaded field area and overlaps with the LDP field. These large error bars are due to the low number of mass-complete galaxies at high- $z$  in the core. Both the low and high- $z$  core relations are only distinguishable from the field at the lowest masses.

For the infall region, the low- $z$  sample is very similar to the core with potential displays of environmental quenching. A 2-sample t-test between the infall and field at low  $[-2.22, 0.06]$  and high- $z$   $[0.52, 0.62]$  demonstrate the differences at these two epochs. While the low- $z$  LDP infall region is higher than the LDP field relation, the high- $z$  relations between the infall and field are indistinguishable, indicating a lack of environmental quenching at this epoch. However, a moderate Butcher-Oemler effect in the infall region is potentially present.

The EDisCS VLT and LDP core samples are compared in Figure 3.7. The low- $z$  core samples are in good agreement, while the high- $z$  regime is less clear due to the large error bars from the LDP sample.

### 3.2.3 $f_{passive}$ vs. Cluster-centric Radius

Finally, we present the  $f_{passive}$  as a function of cluster radius from the LDP survey, where the highest bin at  $4.5R_{200}$  encompasses all galaxies beyond this limit.  $R_{200} < 1$  is defined as the cluster core and beyond this distance is the infall region, where the cluster center is dictated as the BCG coordinates in White et al. (2005). Inspection beyond the cluster core is crucial towards capturing galaxies as they enter the cluster environment and the robust LDP observations sample out to multiple virial radii. This allows us to establish the  $f_{passive}$  at multiple points extending radially out from the cluster center.

In Figure 3.8, we present the  $f_{passive}$  out to  $5R_{200}$  for the mass-complete sample in both the high and low redshift bins. A comparison to Barsanti et al. (2018) local clusters, van der Burg

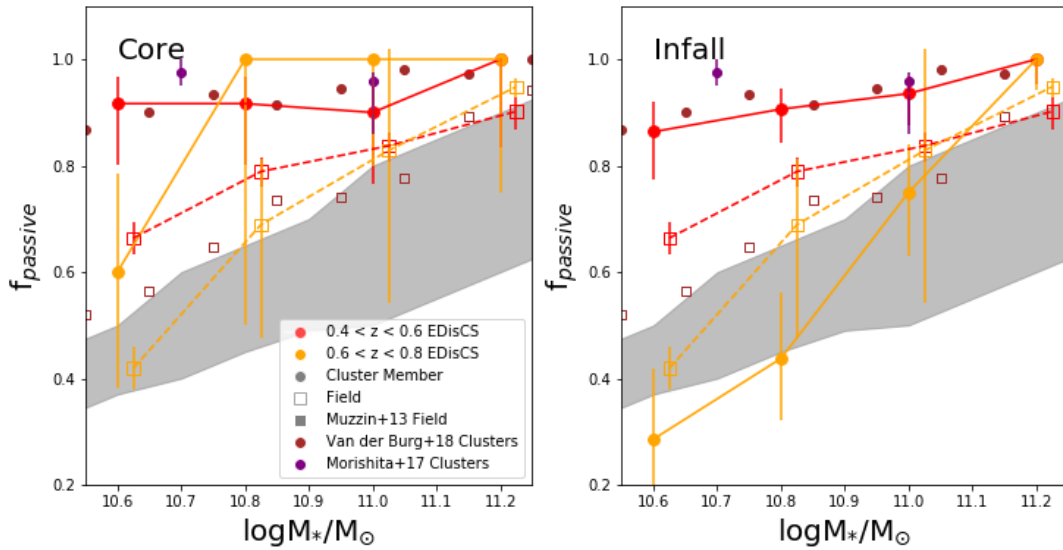


Figure 3.6: The passive fraction vs. stellar mass separated by intracluster environment for mass-complete galaxies in the LDP cluster (circle) and field (open square) samples. The grey band represents the field sample from Muzzin et al. (2013) ( $0.5 < z < 1.0$ ) and comparison  $f_{passive}$  from cluster studies in Morishita et al. (2017) and van der Burg et al. (2018). (Left) The core sample  $f_{passive}$  vs.  $\text{Log}M_*/M_\odot$ . Nearly all of the galaxies within the virial radius in the low- $z$  sample (red) are quiescent, which is a contrast from the high- $z$  sample (orange) where the lowest mass galaxies are 40% star-forming. (Right) The infall LDP sample  $f_{passive}$  vs.  $\text{Log}M_*/M_\odot$ . The same relation as on the left, but for galaxies beyond the virial radius in the infall region. While the low- $z$  sample displays a similar trend to the lower mass core galaxies, the high- $z$  sample has a strong trend of quiescence with stellar mass. The most massive galaxies are passive in both the core and infall regions.

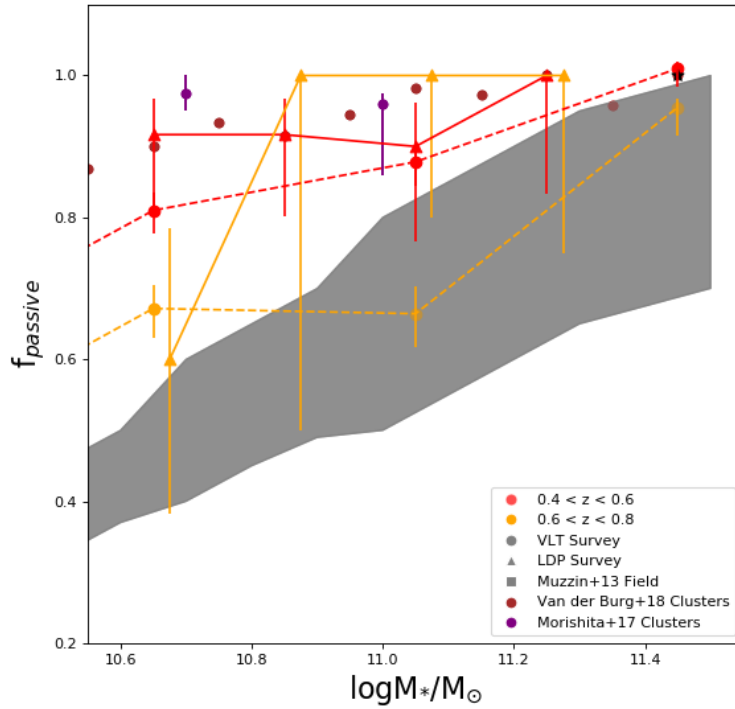


Figure 3.7: The passive fraction vs. stellar mass separated by both of the original EDisCS core (circles and dashed line; White et al. 2005) and LDP (triangles and solid line; Just et al. 2019) observations. Orange markers are for the high- $z$  sample while the red is the low- $z$ . The LDP observations are limited to the virial radius while the VLT sample covers the general central core area, but is approximately one magnitude deeper in photometric completeness. The low- $z$  clusters have similar  $f_{\text{passive}}$  at all masses, but the high- $z$  sample is less clear.

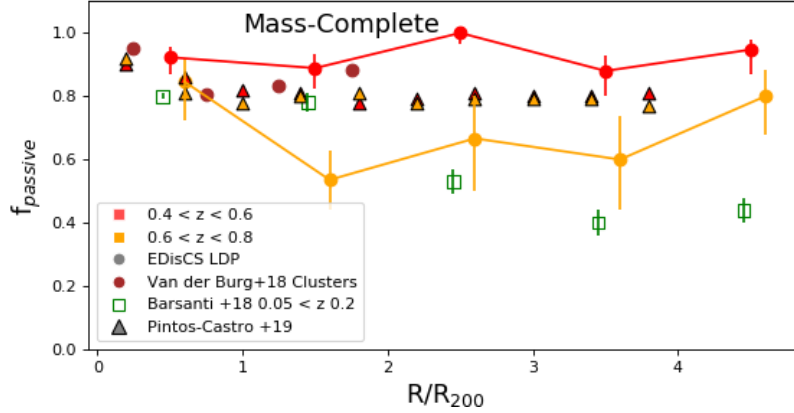


Figure 3.8: The passive fraction vs. cluster-centric distance for the EDisCS LDP sample across the mass-complete sample where low- $z$  is in red and high- $z$  in orange. Comparisons to GAMA clusters from Barsanti et al. (2018) at  $z \sim 0.2$  (green open squares), to the Planck Clusters (van der Burg et al., 2018) (brown circles) and from the ELIAS-N1/XMM-LSS fields (Pintos-Castro et al., 2019) as triangles split into high (yellow;  $0.5 < z < 0.7$ ) and low- $z$  bins (red;  $0.3 < z < 0.5$ ). This reveals the passive-dominated cores of clusters, followed by a decrease in the infall region in high- $z$  clusters. While there are a higher fraction of quiescent galaxies at lower redshifts, it is interesting that the outskirts of the clusters are predominantly passive as well.

et al. (2018) Planck clusters and Pintos-Castro et al. (2019) SpARCS clusters at similar redshifts to EDisCS are shown. Local cluster comparisons have the potential to show how the cluster environment will evolve with time. Within the cluster core, a large majority of galaxies are quiescent at all redshifts. For the low- $z$  sample, there is little to no radial dependence with  $f_{passive}$ , which is also seen in Figure 3.6, Pintos-Castro et al. (2019) and van der Burg et al. (2018). However, the high- $z$  sample displays a moderate valley-shaped trend (Spearman coefficient and p-value [-0.26, 0.62]), where the  $f_{passive}$  decreases to a low of  $\sim 50\%$  from the center to  $2R_{200}$  in the infall region, but elevates to  $>80\%$  at the cluster outskirts. In comparison to a lower redshift sample at 0.05 - 0.2 (Barsanti et al., 2018), there is moderate agreement at distances up to  $1.5R_{200}$  for the low- $z$  sample, which is similar to results in (Haines et al., 2015). At distances beyond this, the passive fraction is much less than is observed in EDisCS. It is important to note that in Barsanti et al. (2018) and Haines et al. (2015), the stellar mass limits are nearly 1.6 dex and 0.6 dex lower than in the LDP survey. The inclusion of lower mass galaxies would likely influence in the  $f_{passive}$  negatively as these galaxies are not as likely to be quenched than more massive ones.

In order to further quantify the  $f_{passive}$  dependence on radial distance and stellar mass, the mass-complete sample is then divided into lower ( $10.6 < \text{Log}M_*/M_\odot < 11.0$ ) and higher ( $\text{Log}M_*/M_\odot > 11.0$ ) bins. The results are shown in Figure 3.9, with each plot also separated by low and high- $z$  bins. The lower stellar mass bin reveals a very similar distribution to that of Figure 3.8, but with a much more reduced  $f_{passive}$  of  $\sim 30\%$  in the infall region. The low and high- $z$  bins are statistically different, which may indicate that these galaxies are beginning to experience quenching processes in the infall region during  $0.6 < z < 0.8$ . At the lower  $z$  epoch,  $>80\%$  of the galaxies in the infall region are photometrically quiescent, which suggests that time in the cluster environment results in a reddening of the individual galaxies. In the bottom panel for the galaxies with the highest stellar masses, the two redshift regimes are indistinguishable. This is likely due to the fact that the most massive galaxies are quiescent through mass quenching. The flattening of the radial dependence on stellar mass is also observed in Wetzel et al. (2013).

### 3.3 Discussion

In this study, we have calculated the  $f_{passive}$  as a function of redshift, stellar mass, and radial distance from the cluster center for the LDP EDisCS wide-field survey. There is a moderate environmental dependence of the  $f_{passive}$  between LDP cluster and field at low ( $0.4 - 0.6$ ) redshifts, but this is not apparent at higher  $z$ . When the LDP cluster environment is split into the core and infall region, the high- $z$  core region has a systematically higher  $f_{passive}$  than the infall and field, which may be due to small sample sizes and shallow observations that are only capturing the most massive (and therefore quiescent) galaxies.

There is a slight dependence on stellar mass for both the LDP and EDisCS core samples which is in agreement with the literature to support mass quenching (Peng et al., 2010; Muzzin et al., 2013; Pintos-Castro et al., 2019). This is reinforced through the finding that nearly all of the most massive galaxies are passive, regardless of environment, which is due to mass quenching of more massive galaxies at earlier epochs. Additionally, both sets of EDisCS cluster and field samples have an increase in the  $f_{passive}$  over time, which is supported through the buildup of passive galaxies

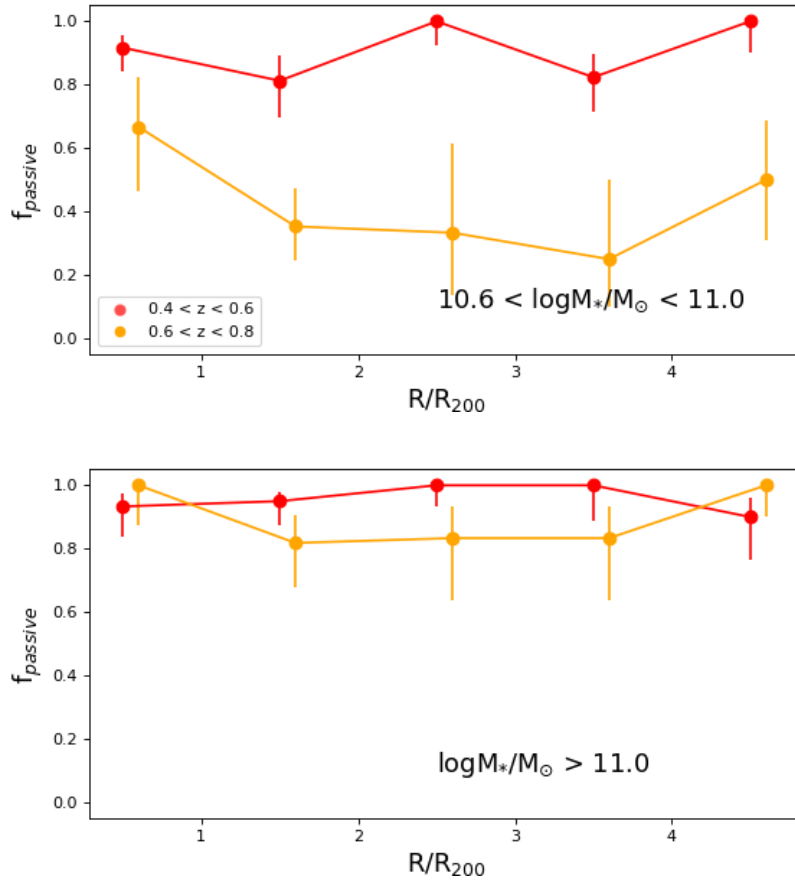


Figure 3.9: The passive fraction vs. cluster-centric distance for the EDisCS LDP sample in two mass-complete bins. (Top) The lower bin of the mass-complete sample reveals that nearly all of the low- $z$  cluster sample is quiescent. However, this is in stark contrast to the high- $z$  sample, which shows a sharp downturn outside of the virial radius to a  $f_{\text{passive}}$  low of 30% from  $2.5 - 3.5R_{200}$ . A gradual increase to 60% is apparent at the outskirts of the cluster. (Bottom) The higher mass sample of the mass-complete galaxies displays a different trend with radial distance. In both redshift bins, 80% or more of the galaxies are passive, with the core entirely devoid of star-forming galaxies.

in the Universe, where more passive galaxies accumulate with time (Fang et al., 2018). In the low- $z$  LDP sample, there is a clear distinction between the cluster and field  $f_{passive}$  to support environmental quenching. A majority of galaxies at this epoch in the cluster environment are photometrically passive.

However, this difference disappears at high- $z$  with both the LDP and ULTRAVISTA field comparisons. As clusters accrete galaxies from the field, there will be an influx of proportionally higher star-formers, which will lower the  $f_{passive}$  for the cluster. The delayed-then-rapid scenario envisions that there is a several Gyr delay period once the galaxy enters a cluster followed by a quick quenching event. It is possible that these redshift bins encompass the quenching event that result in a  $f_{passive}$  shift from 40 to 90% at  $\text{Log}M_*/M_\odot = 10.6$ . For example, ram-pressure stripping can happen on the order of a few 100 Myr (Kapferer et al., 2009), which is less than the time spanned by these redshift bins. Ram-pressure has been observed in nearby clusters (Poggianti et al., 2016; Vulcani et al., 2018), but observing limitations make this difficult to confirm at higher redshifts. Additionally, ram-pressure stripping that is strong enough to remove a majority of the star-forming gas from a galaxy requires specific conditions such as infalling into a rich cluster core at 1000  $\text{kms}^{-1}$ , which is likely not present in these EDisCS clusters. Therefore, we must also consider our small sample sizes both in terms of the number of clusters and galaxies with spectra, as well as the fact that a coordinated quenching on this scale is unlikely. It is entirely possible that the high- $z$  sample recently accreted star-forming galaxies or that the low- $z$  sample had an influx of passive galaxies.

This quenching event can be further constrained by separating out the  $f_{passive}$  vs. stellar mass relation by intracluster environment. The LDP survey has wide field coverage out to multiple virial radii that fully encompasses the core and infall regions. Within the core, nearly all galaxies are quiescent at both redshift bins, which is in agreement with Pintos-Castro et al. (2019). However, this is not the case in the infall region. A strong dependence on stellar mass at high- $z$  in the infall region is in contrast to a predominantly passive sample at low- $z$  (Figure 3.6). With this stark difference between the core and infall regions, it becomes apparent that the site of galaxy

transformation is beyond the virial radius in the infall region. It is possible that newly accreted galaxies from the field that reside in the infall region have yet to be quenched.

Now that the site of the quenching event has been refined the infall region, it can be further investigated on a radial basis. There is little to no  $f_{passive}$  dependence on radial distance at low- $z$  as most galaxies are already passive, which is in agreement with (Pintos-Castro et al., 2019). However, at the range of  $1.5 - 3.5R_{200}$  in the high- $z$  bin, a decrease in  $f_{passive}$  indicates that about half of the galaxies are still photometrically star-forming, but the quenching event does occur since galaxies at these distances are then passive at a later epoch. This holds true for stellar masses in the range  $10.6 < \text{Log}M_*/M_\odot < 11.0$ , but not at masses beyond 11.0. This suggests mass quenching is dominating at the massive end at all redshifts, but environmental quenching may be present at  $\text{Log}M_*/M_\odot < 11.0$ .

Finally, comparing the  $f_{passive}$  results from the EDisCS core and LDP observations shows agreement with one another, but larger sample sizes in the LDP survey would better constrain the binomial errors. It is important to note that the original EDisCS observations are solely classified as the core when in reality, it is a  $6.5' \times 6.5'$  FOV around the BCG, which is assumed to be the center of the cluster. Future work could include the constraint to galaxies within a given radial distance of the BCG for improved comparisons. Although many of the EDisCS clusters have a BCG that is located at the approximate physical center of the cluster (White et al., 2005), they were typically chosen by the brightest isopleth, so radial comparisons can be difficult to robustly define. However, Pintos-Castro et al. (2019) did not find a significant difference in results when using the BCG vs. the center of the overdensity.

Uncertainty with photometric redshifts is also discussed as the interloper contamination, which is corrected for in Equation 3.1. However, this is an estimation extrapolated from the comparison to the spectroscopic redshifts ( $\sim 1.5\%$  of the photometric sample) and does not reflect a galaxy-by-galaxy correction. As discussed in Section 2.3.1, the LDP photometric observations also have their own irregularities and are corrected to the EDisCS core passive clump for each cluster. It is also possible that our mass limit is too high and therefore minimizes effects by environment.

### 3.4 Conclusions & Future Work

In this chapter, we define the  $f_{passive}$  in three environments (core, infall, and field) at two redshift bins (low:  $0.4 < z < 0.6$  and high:  $0.6 < z < 0.8$ ) to quantify the role of environment on galaxy evolution.

The main findings are as follows:

1. Across all environments, the  $f_{passive}$  converges to one at the highest stellar masses. This supports mass quenching and that the most massive galaxies are passive.

2. The  $f_{passive}$  dependence on redshift is visible in both the EDisCS VLT core and the LDP sample. When separated by intracluster environment, this difference is only observed in the infall region and not in the cluster core.

3. Across all stellar masses at low- $z$ , EDisCS clusters have a higher  $f_{passive}$  than in the field. This is not apparent at high- $z$ . This could possibly be an environmental quenching event that happens at some point in the cluster environment, which is supported by the timescale for ram pressure stripping. However, we must also consider that our high- $z$  sample could have recently accreted a sample of star-forming galaxies, or that the low- $z$  sample accreted a subset of passive galaxies. Either of these events would influence the  $f_{passive}$  to produce the observed result and we cannot disentangle this possibility from a rapid quenching event.

4. At low- $z$ , the core and infall region galaxies are predominantly passive at all stellar masses, indicating that a quenching event has occurred at all locations in the cluster environment. However, the high- $z$  core is primarily composed of quiescent galaxies, while the high- $z$  infall region displays a positive correlation with stellar mass to support mass quenching. This suggests that as star-forming field galaxies are accreted into the cluster, the quenching event takes place in the infall region at some point between the high and low- $z$  epochs.

5. The Planck and GLASS clusters have  $f_{passive}$  values comparable to those in the LDP core and infall at low- $z$ , but are higher than the original EDisCS VLT core observations.

6. A radial dependence on  $f_{passive}$  is only observed in high- $z$  clusters at  $\text{Log}M_*/M_\odot$  between 10.6 and 11.0. It is possible that galaxies in the infall region are ram pressure stripped between

high and low  $z$ . The most massive galaxies in our study, which are greater than  $\text{Log}M_*/M_\odot = 11.0$ , are already passive due to mass quenching.

Now that we have concluded that an important site of galaxy transformation occurs in the infall region, the next to step is to investigate what exactly is causing galaxies to shift from star-forming to quiescent sources. Despite providing robust spectroscopic redshifts, the LDP data does not provide an introspective view of each galaxy. Thus, high resolution imaging of galaxies in the infall and core regions can give details on the gas dynamics and any potential quenching activities that have or are occurring.

## Chapter 4

### $H\alpha$ Star-Formation Rate Relation

#### Abstract

This chapter is an excerpt from Cooper et al. on the *HST*  $H\alpha$  observations of four EDisCS clusters. In Section 4.1, we introduce the *HST* observations, data reduction process, and star formation rate calculations. Results including the main sequence relation and star formation rate comparisons are presented in Section 4.2. Finally, in Section 4.5, we discuss a variety of scenarios to support the findings in the prior section.

#### 4.1 *HST*/WFC3 observations

We obtained *HST*/Wide Field Camera 3 F105W imaging and G102 grism spectroscopy in a Cycle 20 program (GO-12945: PI Rudnick) for four EDisCS clusters at  $z \sim 0.5$  to target star-forming  $H\alpha$  emitters. Details for each cluster in this study are listed in Table 4.1.

There are 14 pointings consisting of two orbits each (2800 seconds) that are distributed over the four clusters, where  $\sim 15\%$  of the time is devoted to F105W (rest-frame R-band) direct imaging and the remaining 85% used for G102 grism spectroscopy. This is a similar split between modes as in 3DHST (Nelson et al., 2012; Momcheva et al., 2016). The distribution of the pointings aims to equally cover the cluster core and infalling region in each cluster in order to sample a range of environments, as shown in Figure 4.1. Of the 14 pointings, only 12 are utilized due to unreliable photometry in C11059; this results in the loss of two infall pointings, which are designated as dashes in Figure 4.1. There are a total of 581 galaxies in these 12 pointings. This study divides

Cluster ID	R.A. (hours)	Dec. (degrees)	$z$	$\sigma$ (km s <sup>-1</sup> )	$R_{200}$ (Mpc)	$R_{infall}$ (Mpc)	$M_{200}$ (10 <sup>14</sup> M <sub>⊙</sub> )
(1)	(2)	(3)	(4)	(5)	(6)	(7)	(8)
Cl1059.2-1253	10:59:07	-12:53:15	0.4564	510 <sup>+52</sup> <sub>-56</sub>	0.99 <sup>+0.10</sup> <sub>-0.11</sub>	3.19	1.78 <sup>+0.60</sup> <sub>-0.53</sub> (14)
Cl1138.2-1133	11:38:10	-11:33:38	0.4796	732 <sup>+72</sup> <sub>-76</sub>	1.40 <sup>+0.14</sup> <sub>-0.15</sub>	4.62	5.20 <sup>+1.69</sup> <sub>-1.46</sub> (14)
Cl1227.9-1138	12:27:59	-11:35:13	0.6357	574 <sup>+72</sup> <sub>-75</sub>	1.00 <sup>+0.13</sup> <sub>-0.13</sub>	2.29	2.29 <sup>+0.97</sup> <sub>-0.78</sub> (14)
Cl1301.7-1139	13:01:40	-11:39:23	0.4828	687 <sup>+82</sup> <sub>-86</sub>	1.31 <sup>+0.16</sup> <sub>-0.16</sub>	4.34	4.29 <sup>+1.73</sup> <sub>-1.42</sub> (14)

Table 4.1: Parameters for each of the clusters in this study from Just et al. (2019). 1. EDisCS Cluster ID 2. Right ascension in hours 3. Declination in degrees 4. Cluster redshift 5. Velocity dispersion. 6. Virial radius in Mpc 7. Infall radius in Mpc 8. Virial mass. The range in velocity dispersions between the clusters is small in order to reduce cluster to cluster variation. Each of the clusters has an infall radius between three – four Mpc from the BCG-defined center. The multiband wide-field observations in each cluster extend past the infall region for sufficient cluster coverage (Just et al., 2019).

the local galaxy location into three distinct environments: cluster core, infall region, and the field. Details for each pointing including cluster membership and location are listed in Table 4.2.

The G102 grism spans a wavelength range of 0.7 – 1.1  $\mu\text{m}$ , which contains the  $\text{H}\alpha$  emission for  $0.4 < z < 0.7$ . As the brightest Balmer series emission line, the  $\text{H}\alpha$  flux can straightforwardly be transformed into a SFR (see § 4.1.2 for a further explanation) and is an excellent tracer of nearly instantaneous star-formation on  $\sim 10$  million year timescales. The ability to detect  $\text{H}\alpha$  to low surface brightness levels coupled with less dust extinction vulnerability than other tracers (e.g. [OII]) makes  $\text{H}\alpha$  well-suited for a comprehensive environmental-dependent study on gas transformative and quenching processes across a range of SFRs and cosmic densities.

The G102 grism resolution of 700 km s<sup>-1</sup> is much higher than the typical internal galaxy velocity dispersion, which results in a resolved  $\text{H}\alpha$  map of the galaxy. The emission line map is produced by subtracting a polynomial fit to the background from the 2D spectrum, where the emission line is initially masked. The residual provides an image of the galaxy at a given wavelength within the grism range for the masked emission line. An example of  $z \sim 1$   $\text{H}\alpha$  emission line maps are available from 3DHST observations in Nelson et al. (2012). Additionally, as a robust optical

Pointing ID	RA (hours)	Dec (degrees)	Location (cluster/infall)	$N_{galaxies}$	$N_{cluster}$ (H $\alpha$ )	$N_{field}$ (H $\alpha$ )
(1)	(2)	(3)	(4)	(5)	(6)	(7)
CI1059-12.0	10:59:08.16	-12:45:05.04	I	161	x	x
CI1059-12.1	10:59:03.36	-12:51:59.04	I	152	x	x
CI1059-12.2	10:59:14.16	-12:53:11.04	C	152	8(4)	15
CI1059-12.3	10:59:32.16	-12:54:12.64	C	179	17(2)	12
CI1138-11.0	11:38:16.56	-11:33:23.04	C	80	15(6)	13(24)
CI1138-11.1	11:38:51.60	-11:33:30.24	I	108	4	5(4)
CI1138-11.2	11:37:54.48	-11:30:23.04	I	179	3(1)	7
CI1227-11.0	12:28:02.40	-11:35:11.04	C	117	3(4)	3(2)
CI1227-11.1	12:28:08.16	-11:31:02.64	I	167	3	5(3)
CI1227-11.2	12:28:20.64	-11:30:59.04	I	129	3	9(3)
CI1301-11.0	13:01:35.76	-11:36:59.04	C	167	4(3)	3(6)
CI1301-11.1	13:01:25.44	-11:31:42.24	I	143	6(3)	6(1)
CI1301-11.2	13:01:33.36	-11:40:27.84	C	184	5(7)	1(5)
CI1301-11.3	13:01:02.88	-11:30:15.84	I	145	4	7(5)

Table 4.2: Information for each of the 14 pointings observed with *HST*/WFC3. In column 1, the prefix of the Pointing ID relates to the Cluster ID from Table 4.1 column 1. Columns 2 and 3 contain the RA/Dec information. For the Location column, I and C refer to *infall* and *core*, respectively, where *infall* is outside of  $R_{200}$  as specified in Table 4.1 column 6. The number of sources extracted with GRIZLI in each pointing are listed in column 5. The number of galaxies with H $\alpha$  S/N > 3 and without contamination in the cluster (6) and field (7) for each pointing, where H $\alpha$  S/N < 3 are designated within parentheses. An x signifies that the pointing was not utilized. All of these sources have a wide-field catalog counterpart with rest-frame colors and stellar mass calculations. For CI1059, the two pointings (12.2 & 12.3) in the core do not have well-calibrated photometric wide-field data and thus replacement observations and redshifts are utilized from previous VLT/FORS observations (White et al., 2005). The two infall pointings (CI1059-12.0 & CI1059-12.1) do not have substitute coverage and are not included in analysis.

tracer, H $\alpha$  can detect SFR to low surface brightness levels, which is crucial for creating a sample that encompasses galaxies as they are shutting off star formation. The SFR detection limit is variable depending on the extent and morphology of the galaxy, which makes defining a detection limit nontrivial. The lowest SFRs derived in this study are  $\sim 1 M_{\odot} \text{ yr}^{-1}$ , which is considered a typical value for a regular star forming galaxy such as the Milky Way.

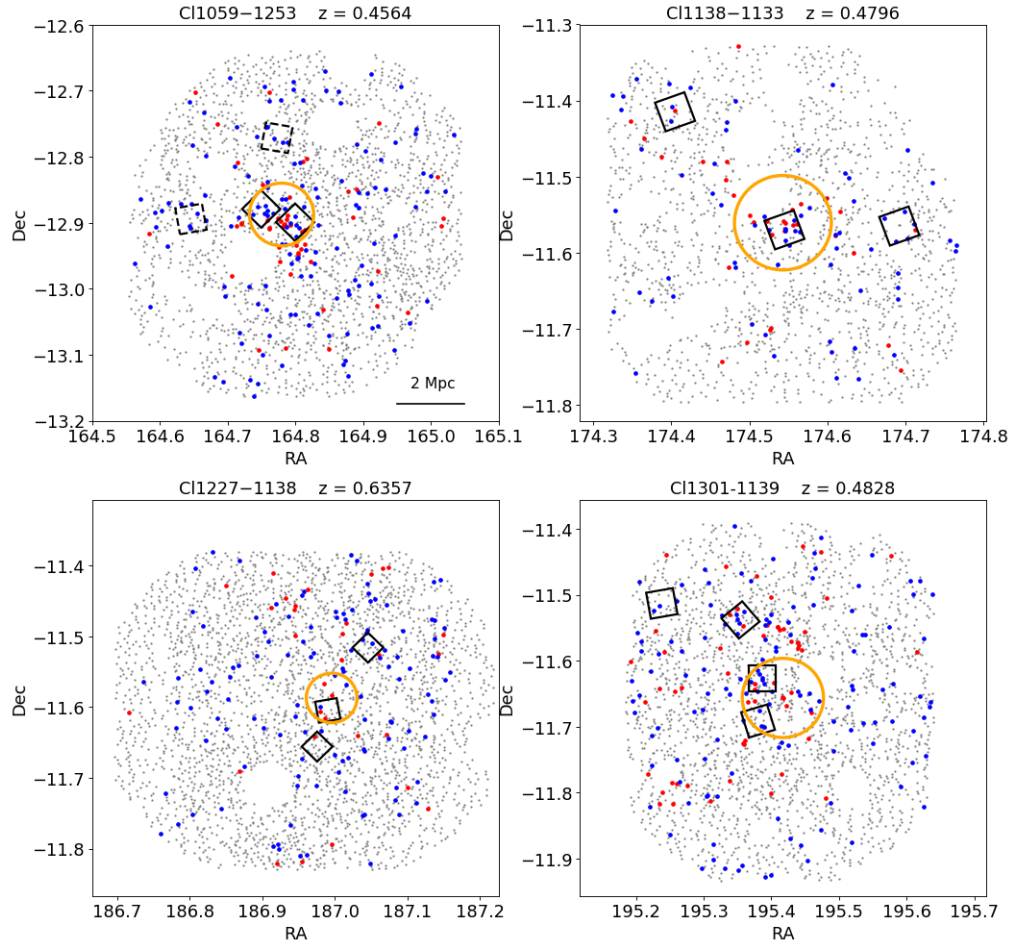


Figure 4.1: The RA and Dec spatial distribution of galaxies in each cluster. Grey dots represent all objects in the FOV that have an LDP redshift, red/blue points signify  $UVJ$ -identified quiescent/star-forming cluster member sources, and the virial radius is indicated by the orange circle.  $HST/WFC3$  G102 observations are represented by the black squares, where the two unused infall pointings in Cl1059 are dashed. The distributed sampling among the core and infall region allows for a direct comparison of SFRs by environment.

### 4.1.1 Data Reduction

GRIZLI (grism redshift & line analysis software for space-based slitless spectroscopy)<sup>1</sup> is a reduction and extraction pipeline in Python that allows for end-to-end processing of WFC3 data, starting from a query of the ESA Hubble Science archive to download all of the data associated with an observation ID. It then performs a routine calibration of the data, including image background sky subtraction, alignment and flat-fielding, resulting in the two drizzled mosaic data products shown in Figure 4.2. The WFC3 camera captures both an infrared  $1.05\mu\text{m}$  direct image (F105W) and the spectrum as a dispersed image for each object in the FOV (G102 grism). The 2D spectra are the streaks, which represent the flux of each object as it is spread out over the range ( $0.7 - 1.1\mu\text{m}$ ) of the grism. Several conditions may make a grism spectrum unusable, including contamination from a bright source, low signal-to-noise, or FOV restrictions. All sources included in our analysis are visually inspected for artifacts or poor modeling. While the analysis focuses on galaxies with  $S/N_{\text{H}\alpha} > 3$ , those with  $< 3$  are presented as down arrows in several figures.

### 4.1.2 $\text{H}\alpha$ Line Extraction & Redshift Prior

The redshifts in GRIZLI are fit using a coarse grid (resolution  $\sim 0.005$ ) with three line complex templates composed of 1) [OII]+[NeIII], 2) [OIII]+ $\text{H}\beta$ , and 3)  $\text{H}\alpha$ + [SII] + weaker red lines. Each of the line complexes has fixed line ratios in order to reduce line misidentification and break redshift degeneracies. A minima in the  $\chi$ -squared fit on the redshift grid allows for the best fit determination of the redshift.

To reduce the misidentification of other emission lines as  $\text{H}\alpha$ , a redshift prior is utilized during extraction within GRIZLI. Priors are derived from the LDP spectroscopic or the wide-field photometric redshift surveys discussed in § 2.3. To determine the probability distribution ( $P(z)$ ) in Equation 4.1,

---

<sup>1</sup>GRIZLI is written and developed by Gabriel Brammer and is publicly available as open-source software (Brammer et al., 2016). [github.com/gbrammer/grizli](https://github.com/gbrammer/grizli)

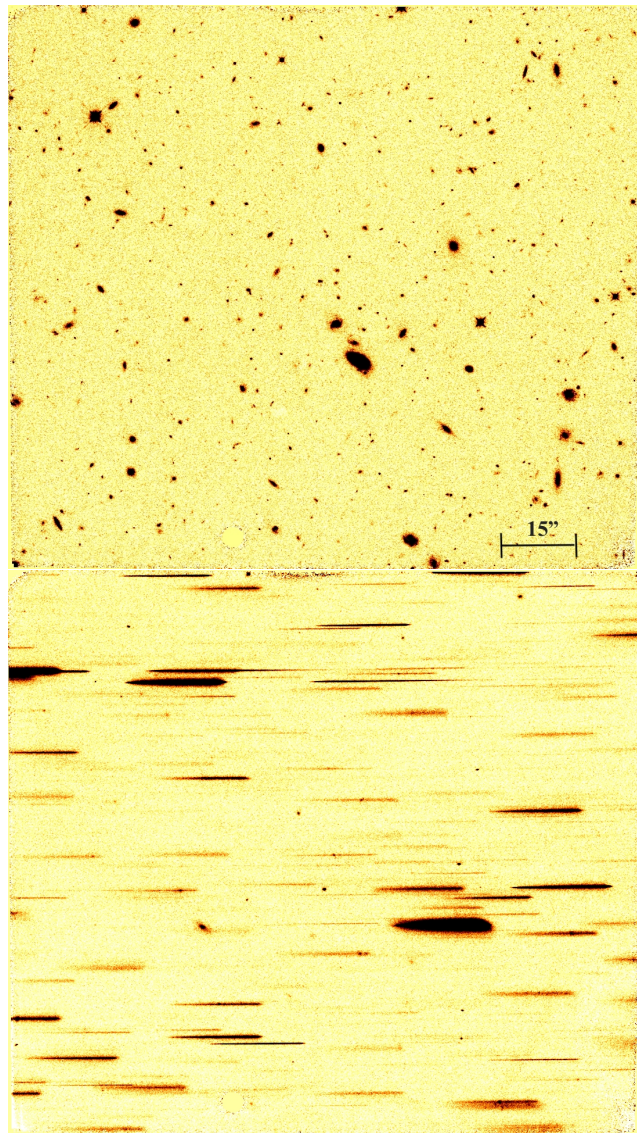


Figure 4.2: (Top) *HST* WFC3 F105W ( $1.05\mu\text{m}$  infrared direct image of the CL1301-11.2 pointing. (Bottom) *HST* WFC3 G102 grism data, which provides a spatially resolved spectrum for every object in the FOV of the F105W image. The spectrum for each object is extracted within the grism wavelength range after a polynomial fit to the continuum is subtracted off.

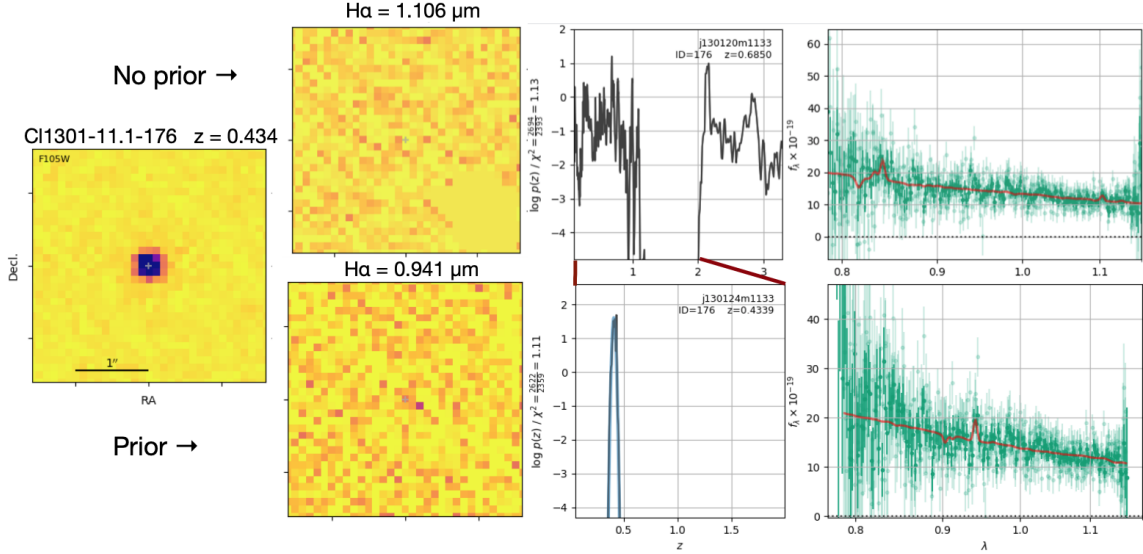


Figure 4.3: This collection of data products represents a comparison between the same galaxy with a blind GRIZLI extraction (top row) and with an LDP prior (bottom row). Initially, GRIZLI identifies it as a 2.99 S/N in H $\alpha$  galaxy at  $z = 0.685$ . With the prior, it is now a 3.99 S/N in H $\alpha$   $z = 0.434$ , resulting in a redshift difference of 0.25. The F105W direct image of the stellar content is on the far left, followed by the detected H $\alpha$  emission line map. In the third panel is the  $p(z)$  from the redshift fitting algorithm (black line), with a blue line indicating the applied Gaussian redshift-prior in the bottom panel. The  $p(z)$  after the prior is applied (black line - bottom row, middle panel) is much more constrained than the blind  $p(z)$ . Note the redshift scale differences between the extractions. The rightmost panel shows the 1D spectra in green with a fit (red). The blind extraction for the  $p(z)$  is very uncertain and could easily be a high or low- $z$  galaxy. The application of the prior dramatically alters the results of the redshift determination. The ability of the prior to be successfully applied to a low S/N H $\alpha$  galaxy is important towards creating a sample that is not biased towards strong H $\alpha$  line galaxies.

$$P(z) = (\sigma\sqrt{2\pi})^{-1} e^{-\frac{(z-\tau_{\text{prior}})^2}{2\sigma_z^2}} \quad (4.1)$$

the prior is multiplied by the GRILZI redshift fit, using either a Gaussian probability (Just et al., 2019) with a  $\sigma = 0.007$  or the average of the 68% photometric redshift confidence levels, respectively. Figure 4.3 is a demonstration of applying the prior to a low S/N H $\alpha$  galaxy that changes the determined redshift by  $>0.2$ , which is significant when cluster membership is determined within a 0.02 range in  $z$ . Example code for integrating the prior is detailed in Appendix C.

A full set of data products for a strong H $\alpha$  emission line C11059 cluster member is shown

in Figure 4.5. This galaxy has a spectroscopic prior applied, but it also had a well-determined redshift based solely on the blind GRIZLI extraction. A comparison between the available redshifts for each galaxy in this sample with and without priors is shown in Figure 4.6. The general agreement of GRIZLI  $z$  extractions without a prior to the wide-field catalog of spectroscopic and photometric redshifts supports the usage of this software in  $H\alpha$  line identification without previous information, but it is most important for low S/N emission lines or quiescent galaxies where a prominent emission line may not exist. These lower S/N sources are critical for encompassing a range of SFRs in a main sequence analysis and exclusion of these galaxies would introduce a bias towards strong emission line galaxies.

This dataset has three types of redshifts available: GRIZLI, GRIZLI + Gaussian prior from a spectroscopic LDP, and GRIZLI + Gaussian prior from a photometric wide-field, where the prior is described in Equation 4.1. GRIZLI is first run without any priors, and is then rerun to include a prior with either a spectroscopic LDP or photometric wide-field redshift for each galaxy. When compared for sources with  $H\alpha$  S/N  $> 3$ , the blind GRIZLI redshifts do remarkably well, with  $\sim 85\%$  matching the extracted redshift with an LDP prior and  $\sim 62\%$  for the photometric prior as shown in Figure 4.6.

### 4.1.3 Star-formation Rate Corrections

GRIZLI outputs a line flux, but there are several intrinsic properties that need to be accounted for while calculating a SFR. Following the prescription in Carleton et al. (2020), a series of corrections are applied to achieve a correct  $H\alpha$ -based SFR. The resolution of the grism is not fine enough to distinguish between the  $H\alpha$  and [NII] line doublet emission, indicating that measured line fluxes include the contribution of [NII] and therefore need to be reduced to account for the additional flux. Strom et al. (2017) find that the [NII] contribution is uniform across SFR per given stellar mass, so Carleton et al. (2020) calculates this reduction through a mass-dependent metallicity relation. The mass-metallicity relation is derived from Zahid et al. (2014), which is then transformed into an  $H\alpha$ /[NII] ratio (Kewley & Ellison, 2008), resulting in a flux reduction of  $\sim 33\%$  for our sample.

Carleton et al. (2020) required a  $\sim 25\%$  correction for  $z \sim 1$  galaxies, while 3D-HST (Wuyts et al., 2011) found  $\sim 20\%$ .

The  $H\alpha$  line is also contaminated with emission from post-AGB stars and this is remedied by subtracting  $f_{AGB} = 2 \times 1.37 \times 10^{29} \text{ erg s}^{-1} M_{\odot}^{-1}$  from the line luminosity (Carleton et al., 2020), where the factor of two comes from the 1:1 ratio of [NII]/ $H\alpha$  lines (Belfiore et al., 2016) and the  $1.37 \times 10^{29}$  factor comes from the expected contribution of ionization by the post-AGB stars. When compared to the  $H\alpha$  line luminosity ( $\sim 10^{40} - 10^{42}$ ), the post-AGB emission is negligible. This correction is equivalent to a reduction in the specific SFR of  $1.2 \times 10^{-12} \text{ yr}^{-1}$ .

Dust within each galaxy is responsible for the scattering of internal galactic light and thus, contributes towards suppressed  $H\alpha$  emission lines and SFRs. This is remedied by the use of the Calzetti et al. (2000) extinction law and the Wuyts et al. (2011) nebular emission,  $A_{H\alpha}$ , relation to the continuum emission,  $A_{cont}$ , at  $H\alpha$ . The relation is as follows:  $A_{H\alpha} = 1.9A_{cont} - 0.15A_{cont}^2$  (Carleton et al., 2020), where  $A_v$  is approximated through the use of the ULTRAVISTA catalog (Muzzin et al., 2013). The *HST* G102 grism does not allow for sufficient observations of the continuum, meaning that extinction at  $H\alpha$  is not calculated from these observations. MAGPHYS (da Cunha et al., 2008) is run on the ULTRAVISTA catalog (Muzzin et al., 2013) with the available photometry barring the exclusion of the ultraviolet and narrow band filters. The generated values for  $\tau$  in MAGPHYS represent the optical depth of the dust seen by young stars in their birth clouds or for the diffuse component for all stars outside the birth cloud, neither of which are appropriate for  $\tau$  of the entire galaxy. We then develop our own estimation of  $\tau$  to represent the optical depth across the galaxy with the following. Best-fit SEDs are available for attenuated and unattenuated models, which are the curves representing the light from all stars with birth cloud and diffuse dust and the light from all stars without dust included. The ratio of the energy at  $5500\text{\AA}$  from both models is then used to estimate  $\tau = -1 \times 10^{\text{attenuated}/10^{\text{unattenuated}}}$  and  $A_v = 1.086 \times \tau$ .

EDisCS galaxies in this study are then matched to ULTRAVISTA sources in *UVJ* color-space in bins of 0.2 as shown in Figure 4.4 in order to predict the extinction as accurately as possible. This final correction for  $A_{H\alpha}$  is applied to the Kennicutt & Evans (2012)  $H\alpha$  SFR, which is calculated

as

$$\text{Log}_{10}(SFR_{H\alpha}/M_{\odot}\text{yr}^{-1}) = \text{Log}_{10}(L_{H\alpha}/L_{\odot}) - 41.27 + 0.4A_{H\alpha} \quad (4.2)$$

where

$$L_{H\alpha}(L_{\odot}) = 4\pi f_{H\alpha} D_L^2 - 2 \times 1.37 \times 10^{29} \text{erg s}^{-1} \times \text{Log}_{10}(M_*/M_{\odot}) \quad (4.3)$$

as detailed in Equation 4.2.

## 4.2 Results

### 4.2.1 Galaxy Sample Properties

From the Just et al. (2019) catalog, there are 581 EDisCS galaxies in the 12 *HST* pointings FOV. This is further reduced to 326 after limiting the redshift range to  $0.4 < z < 0.7$ . Adopting a S/N in H $\alpha$  cut  $> 3$  results in 190 sources in the sample. Finally, removing extractions that are unsatisfactory due to poor contamination modeling, artifacts, or being on the edge of the chip result in a sample of 163 galaxies, of which 67 (30 core, 13 infall, 24 field) are above the mass-complete limit of  $\log_{10}(M_*/M_{\odot}) = 9.75$ . This mass-complete sample of H $\alpha$ -emitter galaxies is dominated by blue, star-forming objects as shown in the *UVJ* diagram in Figure 4.7. We discuss corrections to the wide-field photometry in more detail in Section 2.3.1.

In Figure 4.8, we present the distributions of the stellar masses and redshift for each environment in the mass-complete sample. While the core and infall have similar median values for  $M_*$  (K-S statistic of 0.12), the field masses average slightly higher, but follow a similar distribution with a 2-sample K-S statistic of 0.32 and 0.29 with the core and infall regions, respectively.

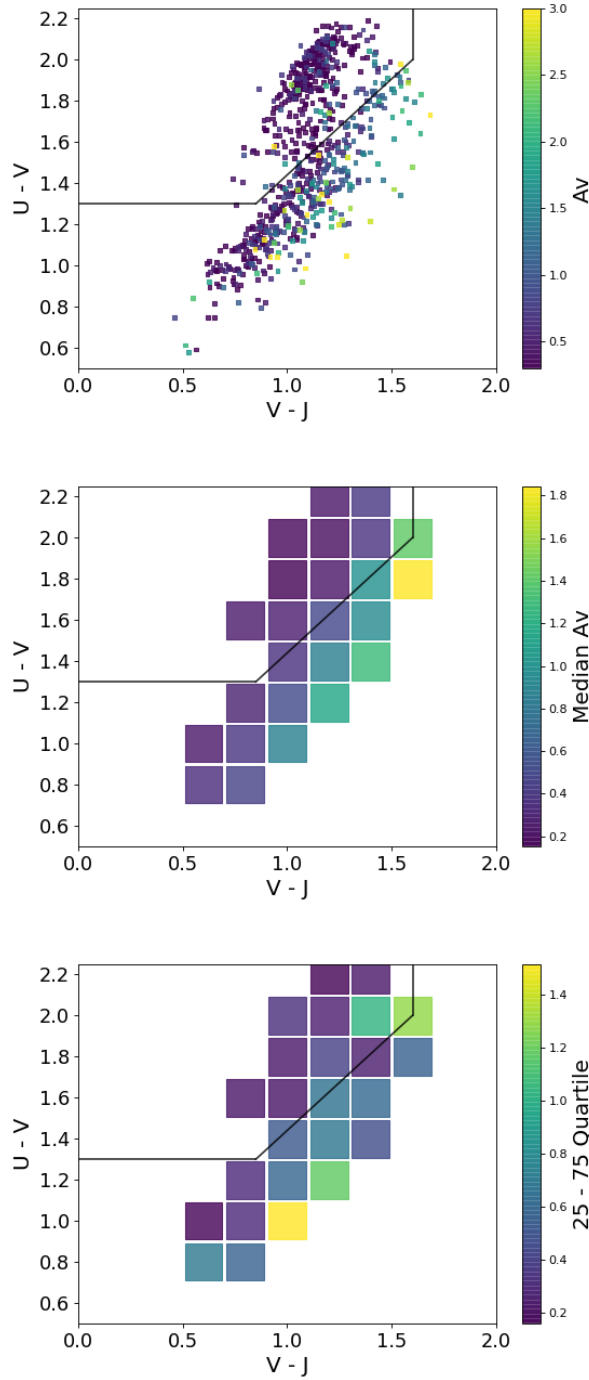


Figure 4.4: (Top) A  $UVJ$  diagram color-coded by  $A_V$  is shown for a subset of the ULTRAVISTA catalog that is similar in redshift and mass distribution to the  $HST$  sample in this study. (Middle) The median in 0.2 bins in  $U - V$  and  $V - J$  from the top plot is shown, which is used to match in color-color space to the  $HST$  sample. If a galaxy falls outside the distribution of ULTRAVISTA, it is matched to the nearest bin.  $UVJ$ -quiescent galaxies have low  $A_V$  as expected and redder star-forming galaxies have elevated values. (Bottom) The spread of each bin across the 75 – 25 percent quartile. The spread is noticeably small in the passive region. Black lines in all plots are the Williams et al. (2009) boundaries.

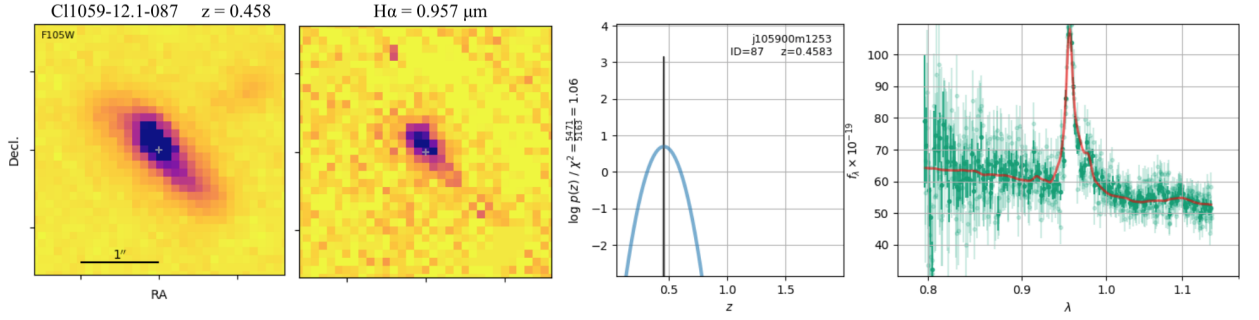


Figure 4.5: (2 left panels): RA and Dec postage stamps show the stellar continuum from the F105W  $1.05\mu\text{m}$  direct image and the  $\text{H}\alpha$  emission extraction at  $0.957\mu\text{m}$ . (2 right panels): The fitted redshift, shown as the black line, is fully consistent with the photometric redshift prior probability distribution in blue. The 1D spectrum data are shown in green, with a best fit template in red. Note the prominent  $\text{H}\alpha$  emission line at  $0.95\mu\text{m}$  with a S/N of 36.6.

In contrast, the redshift distributions have significant differences (K-S statistics: core-infall (0.60), core-field (0.65), infall-field (0.46)). We therefore correct the redshifts of field galaxies to the median of the cluster sample (0.48) following Schreiber et al. (2015) in Equation 4.4. Here,  $r = \text{Log}_{10}(1 + z)$ ,  $m_0 = 0.5$ ,  $a_0 = 0.15$ ,  $a_1 = 0.3$ ,  $m_1 = 0.6$ ,  $a_2 = 2.5$  and  $m = \text{Log}_{10}(M_*/10^9 M_\odot)$ . This allows us to correct for any variation in the SFR that comes from redshift evolution. The lack of an infall sample in C11059 at  $z = 0.4564$  is likely driving the variation in the median  $z$ 's between the core and infall distributions.

$$\text{Log}_{10}(\text{SFR}_{\text{MS}}[M_\odot/\text{yr}]) = m - m_0 + a_0 r - a_1 [\max(0, m - m_1 - a_2 r)]^2 \quad (4.4)$$

There are 16 galaxies identified as quiescent based upon the Just et al. (2019)  $UVJ$  rest-frame colors, with five of them being in the core, two in the infall, and nine in the field. These are identified as red triangles in the right panel of Figure 4.9. As seen in Figure 4.7, there are galaxies that are quiescent based on their  $UVJ$  colors, but which have significant  $\text{H}\alpha$  emission. We will discuss these galaxies in §4.5. GRIZLI produces a stellar continuum and emission line map for each observed galaxy, which is shown in Figure 4.14 for select galaxies.

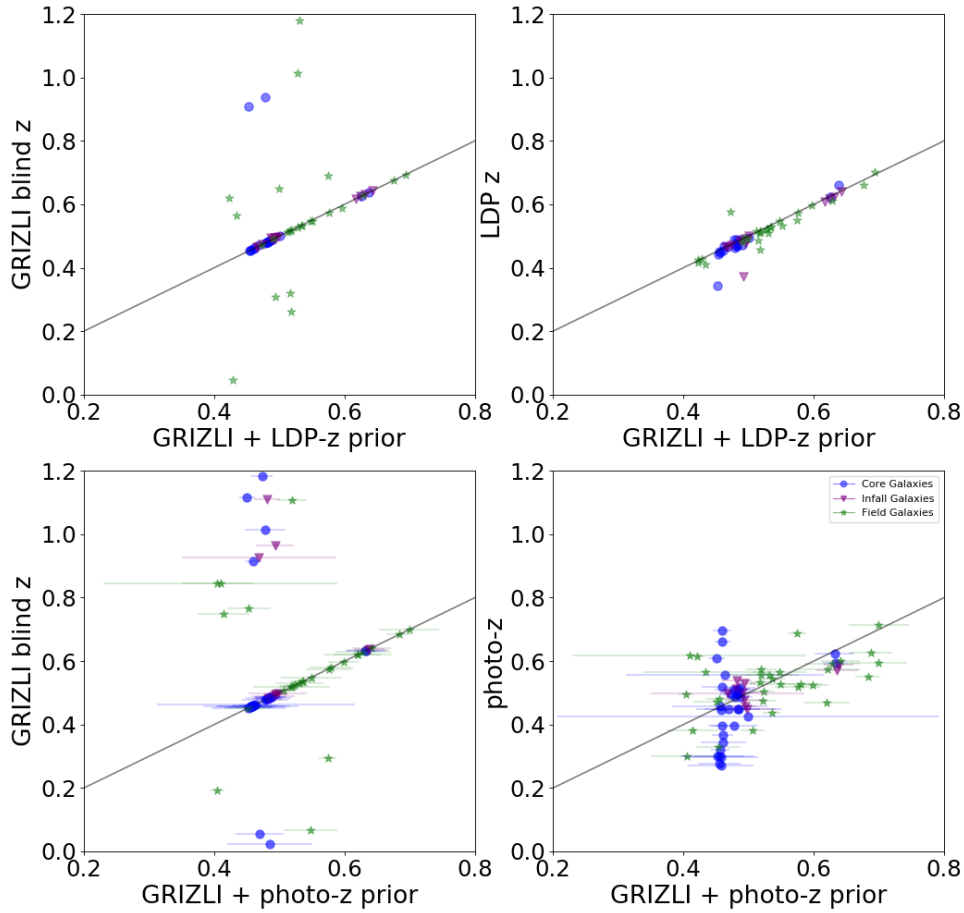


Figure 4.6: The GRIZLI-extracted redshift (no prior) vs the GRIZLI-extracted redshift with an applied spectroscopic (top left) or photometric (bottom left) prior for cluster core (blue circle), infall (purple triangle), and field (green star) galaxies. A majority of objects fall along the 1-1 line in black, indicating that the GRIZLI extractions without a prior can be reliable. A pointing with a significantly higher background is apparent in the blind GRIZLI redshifts above the 1-to-1 line in the top and bottom left, which is mostly corrected with the LDP spectroscopic or photometric prior. Several low S/N  $H\alpha$  galaxies are also corrected through the prior. The 68% confidence levels for the photometric redshifts are shown with error bars, while the error on the spectroscopic redshifts is insignificant on this scale. This photometric relation has noticeably more scatter around the 1-to-1 line, which is a reflection of the reduced accuracy of photo-z measurements. The GRIZLI-extracted redshifts with a spectroscopic (top right) or photometric (bottom right) prior are shown in comparison to their blind redshift.

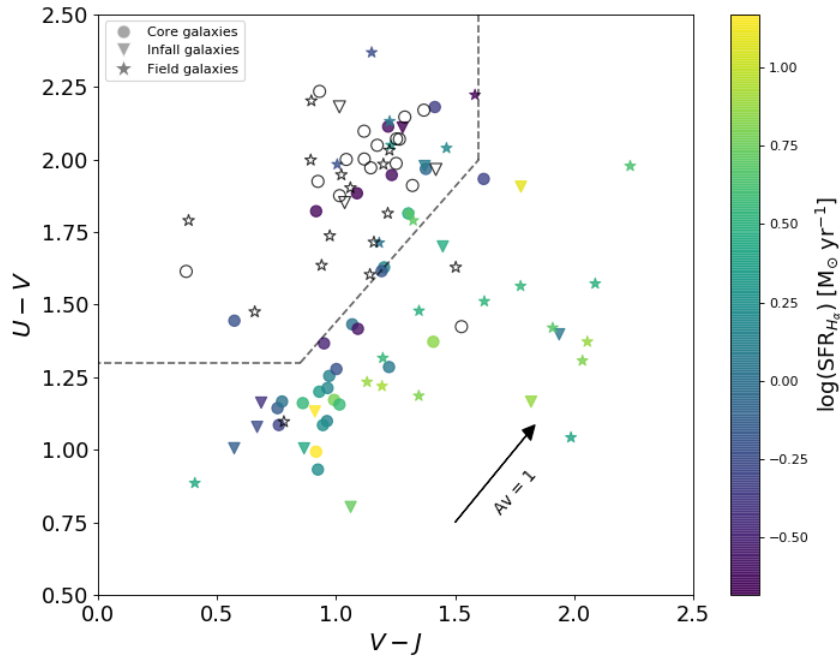


Figure 4.7:  $U - V$  vs.  $V - J$  rest-frame colors color-coded by  $H\alpha$ -based SFR for the mass-complete sample of *HST*-observed galaxies. Galaxies with  $S/N < 3$  in  $H\alpha$  are grey open symbols, which are predominantly located in the quiescent clump. The SFR color-coded points are the final sample of 67 galaxies selected for  $S/N > 3$  and emission line extraction quality. 51 of the 67 of the sources with  $F(H\alpha)$   $S/N > 3$  lie in the star-forming region, with 16 residing in the quiescent region. The stellar continuum and  $H\alpha$  emission line maps for the 16 passively-classified galaxies are shown in Appendix 4.14. Black dashed lines follow the quiescent and star-forming definition of Williams et al. (2009).

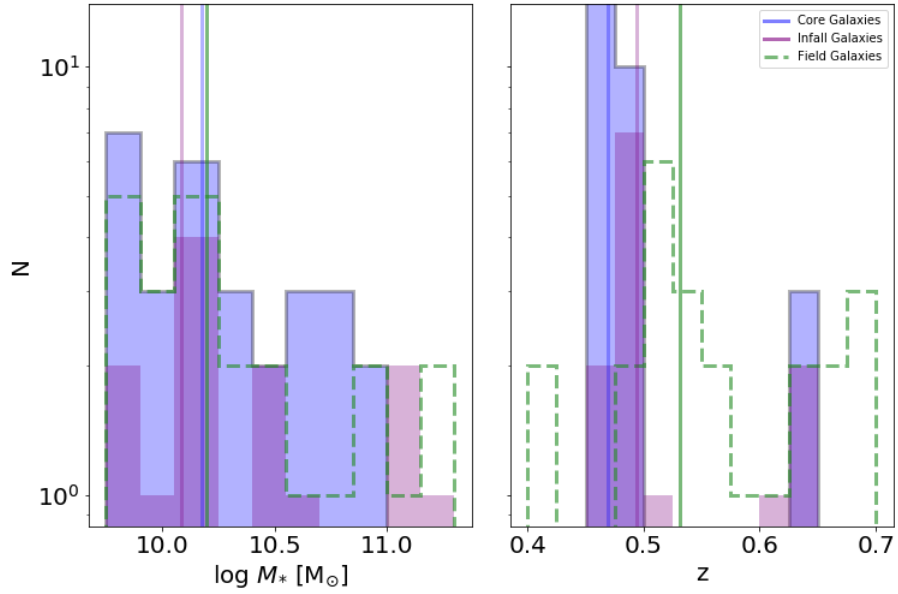


Figure 4.8: (Left) The distribution of the stellar masses for each of the core, infall, and field mass-complete samples is shown in the blue, purple, and green-dashed histograms. The median value for each sample is the vertical line. (Right) The same three samples are shown with their distributions in redshift space, with the median shown again as the vertical lines. A more significant difference in  $z$  is apparent between the field and cluster samples and is corrected following the equation in § 4.1.3. The elevated median for the infall sample is due to the lack of two samples for C11059 at  $z = 0.4564$ , which is the lowest  $z$  cluster. Thus, the median  $z$  is offset to a higher value than the core which includes galaxies from this cluster.

### 4.2.2 Stellar Mass - SFR Relations

In Figure 4.9, we present the  $H\alpha$ -derived SFR –  $M_*$  main sequence relation for four EDisCS clusters separated into three environments: core (blue circles), infall (purple triangles) and field (green stars) for 163 galaxies in the left panel. In the right panel, galaxies are divided by their classification from Figure 4.7, where red triangles are defined as *UVJ*-quiescent. Both panels include galaxies with S/N in  $H\alpha < 3$  as down arrows at their  $3\sigma$  upper limit SFR. A scatter of  $\sim 1$  dex is observed across all masses with a lack of flattening of the SFR relation for more massive galaxies in the cluster core as shown with Schreiber et al. (2015). The average SFR for the mass-complete sample with S/N  $> 3$  in  $H\alpha$  is 0.46 with a standard deviation of 0.48. The infall times of galaxies into the cluster environment can vary and contribute towards this large scatter, which is double the  $1\sigma$  value of 0.25 dex in GLASS clusters from Vulcani et al. (2016). The mean SFRs for the three EDisCS clusters in Finn et al. (2005) at  $z = 0.75$  are shown as orange squares. 2D image cutouts of the stellar and  $H\alpha$  maps for the *UVJ* quiescent are available in Figure 4.14. We also show the SFR –  $M_*$  distribution on a cluster-by-cluster basis in Figure 4.10. The apparent distribution of galaxies seen in Figure 4.9 is not dominated by any individual cluster, but rather contains small contributions from each cluster. The distribution of SFRs appears to be similar between the clusters.

As an alternative way of comparing the SFRs across environment, in Figure 4.11 we show the distribution of the SFR with respect to the cluster-based main sequence from Vulcani et al. (2016) for each of the three environments in the mass-complete sample. The median SFR for each environment is  $\sim 0.7$  dex below the relation, which may be due to the correction procedure. In a 2-sample K-S test for the mass-complete sample, the core and infall SFRs compared to the field have p-values of 0.50 and 0.348 and a statistic of 0.22 and 0.27. Therefore, we cannot rule out the null hypothesis that the core, infall, and field galaxies are drawn from the same SFR distribution.

In Figure 4.12, we compare our  $H\alpha$  SFRs to those derived from *Spitzer* MIPS  $24\mu\text{m}$  emission (Finn et al., 2010). This comparison is only for the core galaxies, as those were the only ones with MIPS coverage from Finn et al. (2010). Many of the galaxies from our study are non-detections in

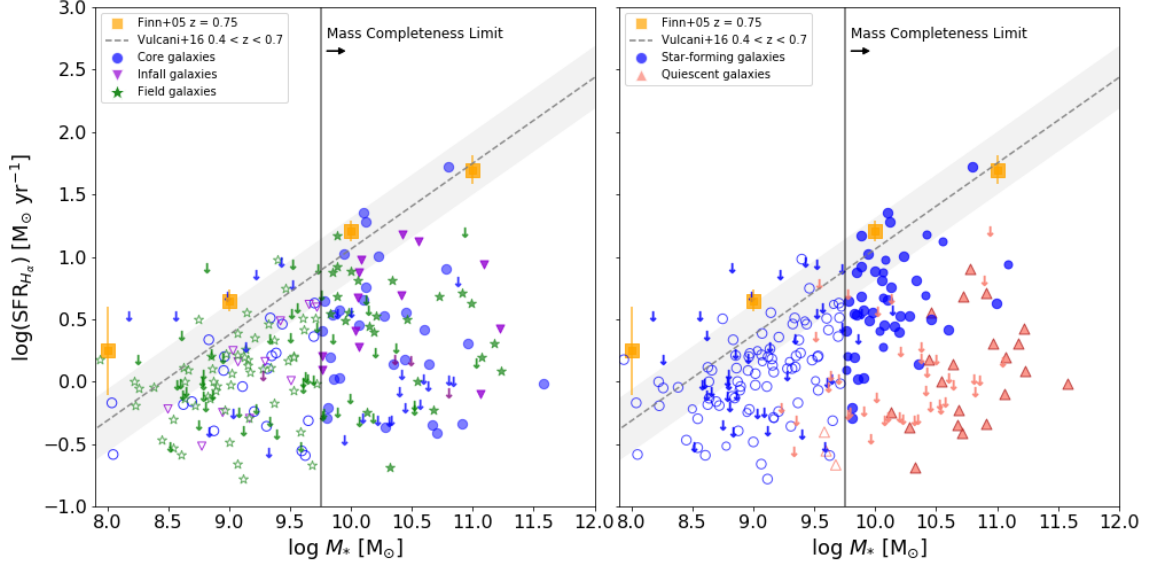


Figure 4.9: The  $H\alpha$ -based SFR –  $M_*$  main sequence relation for 163  $S/N > 3$  and 82  $S/N < 3$  (down arrow) galaxies. (Left) The locations of these galaxies are distributed among the cluster core (blue circles), infall region (purple triangles), and field samples (green stars), where the mass-completeness line is denoted by the vertical black line and filled in symbols. The  $< 3$   $S/N$  galaxies are plotted at their  $3\sigma$  limit, which occupy the lower end of the SFRs on the main sequence here. These data are systematically above the main sequence relations defined by Whitaker et al. (2012) and Schreiber et al. (2015), which is shown in Figure 4.15. The scatter is larger than the literature, but is still expected due to varying star-formation histories and other disturbances throughout a galaxy lifetime. A comparison is shown to the EDisCS narrow band  $H\alpha$  SFRs in Finn et al. (2005) (orange squares) at  $z = 0.75$  and  $H\alpha$  SFRs Vulcani et al. (2016) from the GLASS clusters at  $0.4 < z < 0.7$  (grey dashed line +  $1\sigma$  scatter). (Right) This same sample is now color-coded by location in Figure 4.7, where blue circles are star-forming and salmon triangles are quiescent. The quiescent galaxies mostly occupy the lower portion of the main sequence, which also have suppressed SFRs.

Finn et al. (2010), with an overall trend that  $H\alpha$  sources underestimate the SFRs when compared to  $24\mu\text{m}$  data. A mean offset of  $\sim 0.77$  dex between the  $24\mu\text{m}$  and  $H\alpha$  SFRs indicate that we might be slightly underestimating our extinction values, which is in agreement with the  $\sim 0.7$  dex offset in SFRs from Vulcani et al. (2016). The consistent offset suggests that we are recovering a majority of the obscured SF with our set of corrections.

In Figure 4.13, we plot the SFR result as a function of distance from the cluster center in relation to  $R_{200}$ , where the mass-complete cluster sample ( $> 10^{9.75}M_{\odot}$ ) is represented as the blue stars and the field galaxies are shown in green as a median SFR. Cluster galaxies below the mass-complete limit are plotted as grey down arrows at the  $3\sigma$  limit. The median for the mass complete cluster member sample in the core and infall region is shown as a purple triangle with  $1\sigma$  bootstrap re-sampling error bars. There is no observable difference in the SFRs between the three environments as in Figures 4.9.

### 4.3 Visual Inspection of Galaxies with GRIZLI

In Figure 4.7, 16 galaxies are identified as quiescent based upon the Just et al. (2019)  $UVJ$  rest-frame colors, with five of them being in the core, two in the infall, and nine in the field. These are identified on the right hand side of Figure 4.9 as salmon triangles. GRIZLI produces a stellar continuum and emission line map for each observed galaxy, which is shown in Figure 4.14. Many of the galaxies appear to have diffuse  $H\alpha$  with little-to-no stellar structure, indicating that these may be early-type galaxies.

### 4.4 Main Sequence Comparisons

The same main sequence from Figure 4.9 is shown below as Figure 4.15 with comparison to Whitaker et al. (2012) and Schreiber et al. (2015) at the median redshift of 0.487 for the sample. The comparison SFR derivations utilize a UV+IR flux, which are noticeably below the  $H\alpha$  data in this study and Vulcani et al. (2016). While both of these comparisons are derived from field

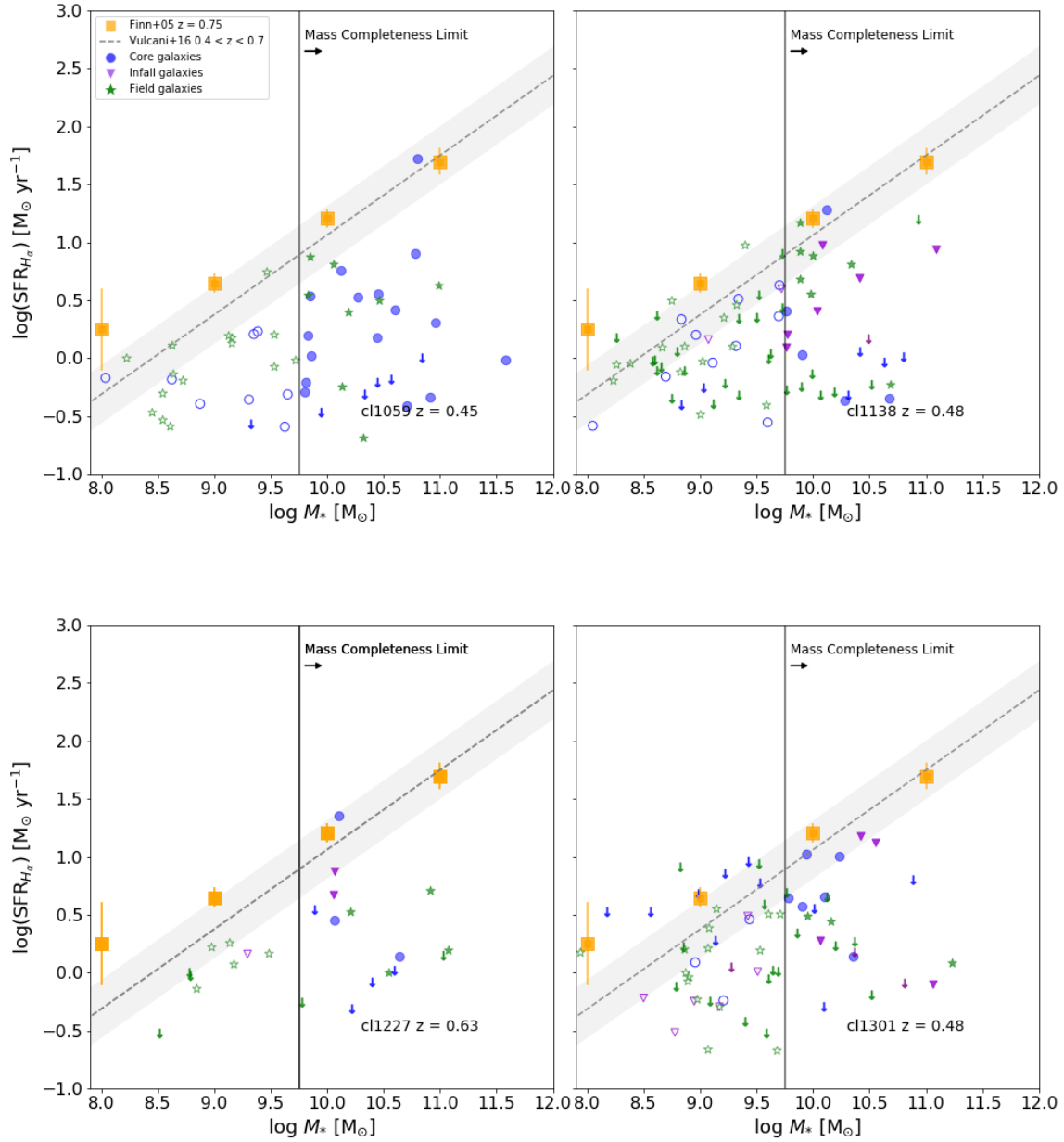


Figure 4.10: Each panel shows the SFR vs. stellar mass as in the left panel of Figure 4.9, but separated by cluster. Each cluster reveals a similar distribution of galaxies above the Vulcani et al. (2016) mean distribution, as well as galaxies with lower SFRs. This indicates that no cluster is offset with respect to the others and influencing the combined relation. The highest- $z$  cluster in the bottom right, Cl1227, has noticeably fewer galaxies, which is also evident in Figure 4.1.

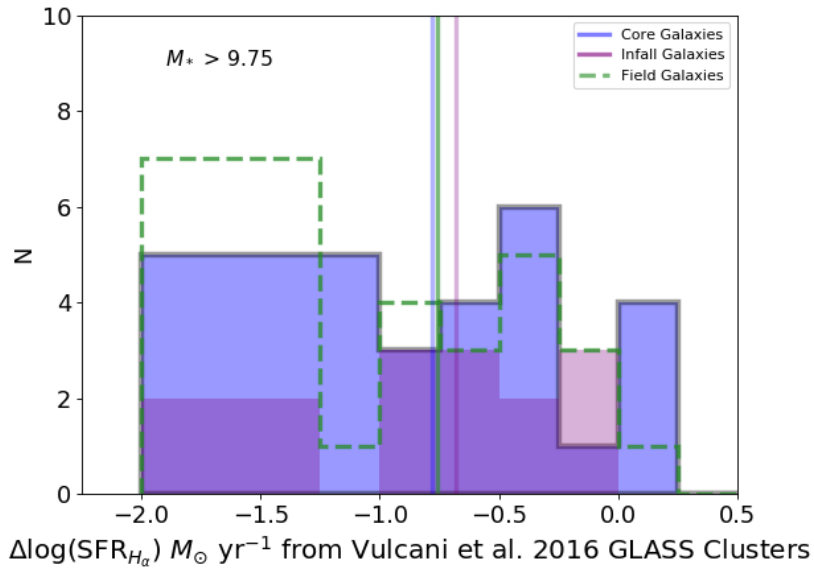


Figure 4.11: The difference in SFR for each of the three environments (blue=core, purple=infall, field=green) from the Vulciani et al. (2016) GLASS clusters  $H\alpha$  main sequence. The median values for each environment are signified by the corresponding vertical line, which are  $\sim 0.7$  dex below the GLASS relation.

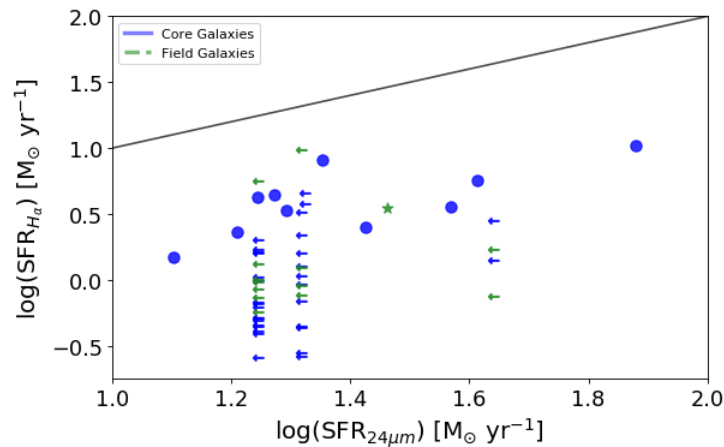


Figure 4.12: The MIPS  $24\mu\text{m}$  SFRs derived from the EDisCS core pointings of this sample from Finn et al. (2010) compared to the  $H\alpha$  SFRs in this study. There are only matches between the core (blue circle) and field (green triangle) because these *Spitzer* pointings did not extend to the infall region. Left arrows are non-detections in  $24\mu\text{m}$  at the 80% completeness limit. The  $\sim 0.7$  dex offset from the  $24\mu$  SFRs is similar to the one seen with GLASS.

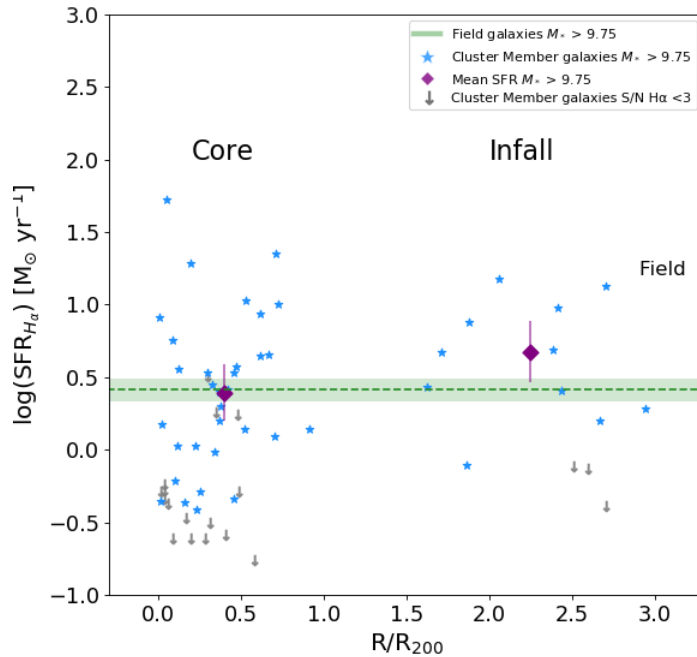


Figure 4.13: The distance from the center of the cluster (defined as the BCG in White et al. (2005)) is computed for each core and infall galaxy and compared to the SFR. The mass-complete sample is shown as blue stars for cluster members and the average for the field is the dashed green line, where error bars on the median are the  $1\sigma$  confidence level from a bootstrap resampling. Galaxies with  $S/N$  in  $H\alpha < 3$  are the grey arrows and are not accounted for in the median values. All but three of these upper limits are for *UVJ* quiescent galaxies and so the apparent radial dependence in the fraction of galaxies with upper limits just reflects the well-known radial dependence in the quiescent fraction in clusters. For the robust  $H\alpha$  detections, no significant radial trend exists for the mass-complete sample.

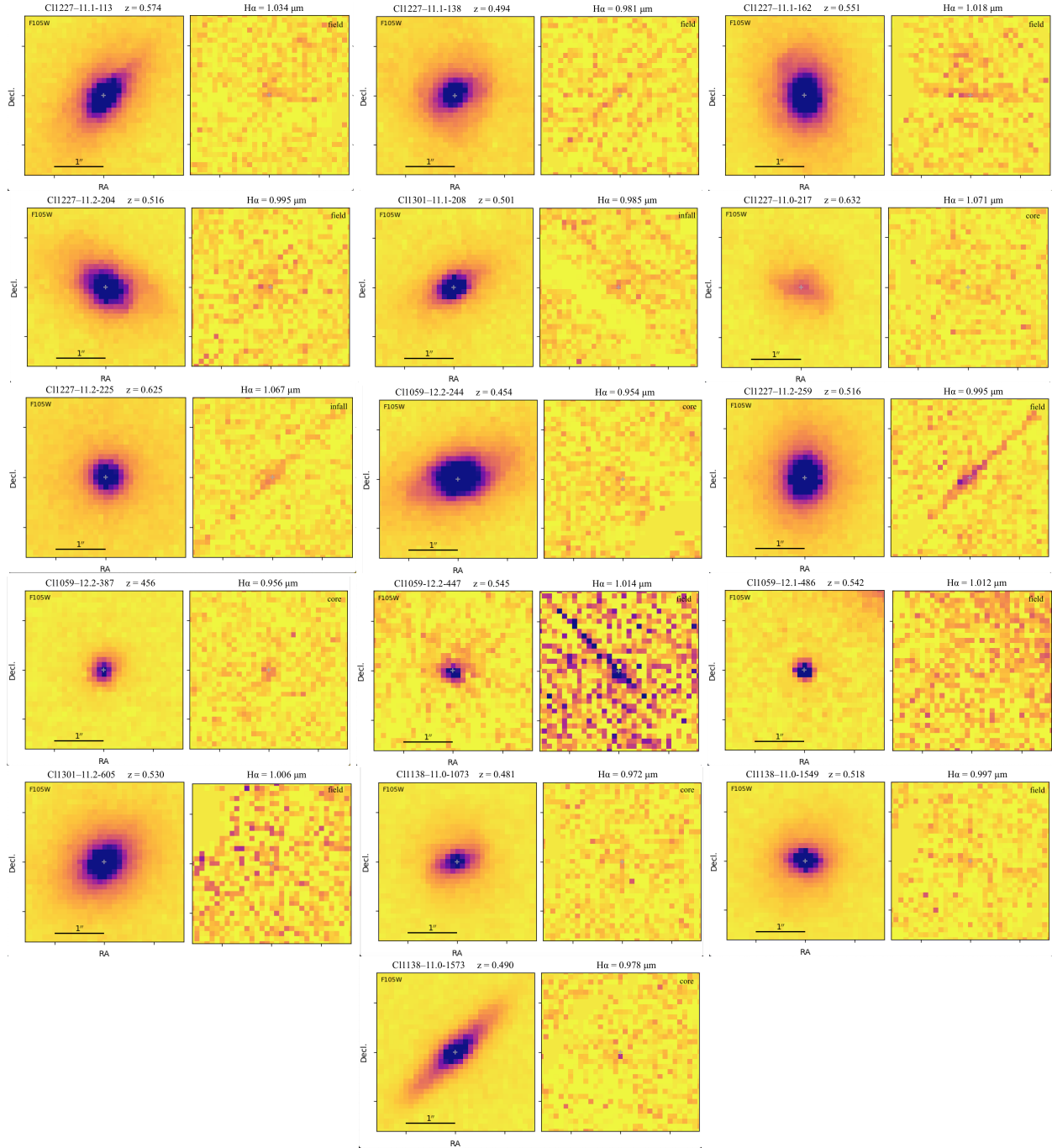


Figure 4.14: The stellar continuum (left) and  $H\alpha$  line emission map (right) for each UVJ quiescent galaxy shown as a pair of images. The direct F105W images for each galaxy show signatures of early-type galaxies with a lack of spiral arms or clumpy morphology. The  $H\alpha$  emission maps are typically low intensity or diffuse distributions, which makes inferences about the gas morphology difficult.

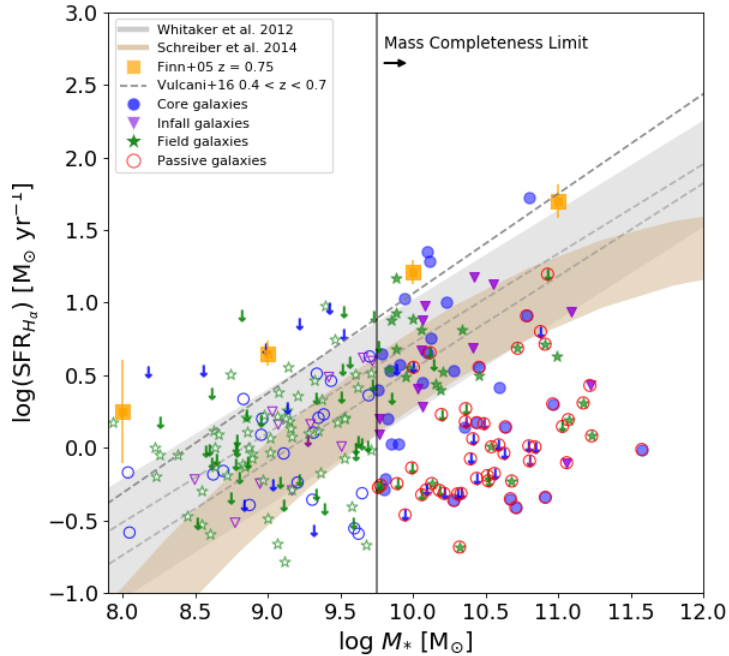


Figure 4.15: The main sequence for the galaxies with  $S/N > 3$  in the core (blue circle), infall (purple triangle) and field (green stars) regions, where  $UVJ$  quiescent galaxies are circled in red and galaxies with less than  $S/N < 3$  are shown as the down arrows. Comparison lines to field main sequence derivations are shown in grey (Whitaker et al., 2012) and brown (Schreiber et al., 2015), which are at least 0.5 dex below the  $H\alpha$  relations.

studies, the papers inspected the main sequence as a function of mass and redshift, which resulted in a easily determined relation for given epoch.

## 4.5 Discussion

In this study, there is no significant difference in the distribution of SFRs between environments. The EDisCS cluster galaxies are roughly aligned with the GLASS clusters  $H\alpha$ -SFRs main sequence relation, which also does not reveal a variation from the field SFRs (Vulcani et al., 2016). Koyama et al. (2013) finds a similar result with  $H\alpha$  observations of clusters, but the SFR limits are not deep enough to detect significantly suppressed galaxies. However, the lack of an environmental dependence on the SFR that is normally seen across all masses contradicts the notion that

dense environments are contributing or directly responsible for gas quenching as evidenced by the buildup of quiescent galaxies (Patel et al., 2009a; Vulcani et al., 2010; Paccagnella et al., 2016). This result can potentially be explained in the following ways. First, our sensitivity limits are not low enough to detect galaxies with significantly suppressed SFRs. This is evident in Figure 4.9 in that the majority of the  $<3$  S/N galaxies appear to populate the bottom of the main sequence. Thus, there may be a tail of galaxies to lower SFRs, but we would be unable to detect this population with our data. The importance of highly sensitive SFR limits to interpret the distribution of SFRs in dense environments is illustrated in Vulcani et al. (2010), in which they do find an excess of galaxies in EDisCS clusters with low SFRs compared to those in the field, but only because they probe well below the main sequence.

It is also possible that the galaxies within our sample have not experienced significant quenching and the reasons for this vary by environment. Within the core, galaxies may have been recently accreted and are still within the "delay" period of the quenching process. In the infall region, the local density is lower than that of the core and may not create conditions capable of quenching.

Secondly, the lack of a difference in field vs. cluster SFRs is that the timescale for the truncation of SF is rapid. In this case, galaxies that are undergoing external quenching will fall below our detection limits before we can observe them in their reduced SFR state. Such a rapid decline in SFRs caused by dense environments is consistent with the excess of post-starburst galaxies in dense environments as seen by Poggianti et al. (2008), Muzzin et al. (2012) and Wild et al. (2016). It is not immediately clear why there is a diversity in the distribution of SFRs in different environments among different published works. It may be that much of the "action" is in the tails of the distribution, which requires not only deep observations, but also large sample sizes to characterize the distribution shapes well away from the median. Observations with the *James Webb Space Telescope* or deep UV+IR observations with WISE in the local universe may satisfy this criteria.

We should also consider that our cluster core and infall samples could likely contain interlopers, which has been estimated to be 15% or more for clusters with historical datasets (Duarte &

Mamon, 2015; Wojtak et al., 2018). These galaxies may appear to be spectroscopic members by superposition or our redshift determination is incorrect.

#### 4.5.1 *UVJ*-quiescent galaxies with $H\alpha$ emission

There are 16 galaxies in the *UVJ* quiescent region that have  $H\alpha$  emission that is detected with  $S/N > 3$  (Figure 4.7). These galaxies lie systematically closer to the dividing line between quiescent and star-forming galaxies than the rest of *UVJ* quiescent galaxies, however they still exist at red colors consistent with the larger passive population. As can be seen in Figure 4.9 these *UVJ*-quiescent  $H\alpha$  emitters also have systematically lower SFRs than *UVJ*-SF galaxies of the same stellar mass, though again a few of them have  $H\alpha$  fluxes that would imply a SFR up to  $10 M_{\odot} \text{ yr}^{-1}$ . Most *UVJ*-quiescent galaxies have SFR around  $1 M_{\odot} \text{ yr}^{-1}$ . Continuum and emission-line postage stamps for all these galaxies are shown in Figure 4.14. The emission is faint but visible in all 2D stamps and in the 1D spectrum and the spectra are free of artifacts. We entertain four possibilities to explain these sources.

First, we must explore the possibility that our rest-frame colors are uncertain and that these nominally *UVJ*-quiescent galaxies with  $H\alpha$  emission actually lie in the SF region but were moved into the quiescent *UVJ* region by random and systematic rest-frame color errors. This is a potential concern especially given the calibration challenges that we experienced with the wide-field data and the additional rest-frame color corrections described in Appendix 2.3.1. We test for this possibility by comparing the *UVJ* colors as derived from the photometry in this paper with the *UVJ* colors derived from the original EDisCS photometry in the cluster cores. The original EDisCS photometry is well calibrated and results in a very well defined passive clump at the correct color location. We verified that the *UVJ* colors derived from the wide-field data are slightly different from the EDisCS *UVJ* colors on a galaxy-by-galaxy basis, but that the differences are not significant enough to move galaxies in and out of the passive region. Therefore, we conclude that these galaxies are indeed in the *UVJ*-quiescent region and that we should discuss the implication of them having significant amounts of  $H\alpha$  emission.

Second, it is possible that weak AGN may be contributing to some of the emission. With our data we cannot explicitly rule out the role of an AGN. Martini et al. (2009) found only two X-ray AGN in 17 clusters at  $z < 0.4$ . There are some objects that have spatially compact and linearly extended residuals in the emission line maps in Figure 4.14, e.g. C11059-12.2-447, C11227-11.2-259. This could be an indicator of the presence of AGN emission, though the emission lines do not look broad in the 1D spectra. We examine the position in the SFR –  $M_*$  plane of the 11 objects with such linear residuals and find that they do not occupy any favored place in either stellar mass or SFR, being sparsely spread in both quantities and not preferentially biasing the main sequence in any parameter. We therefore consider contamination by AGN to be a minor contributor to the  $H\alpha$  flux in this population.

Third, it is possible that the  $H\alpha$  emission comes from a ‘LIER’-like phenomena (Sarzi et al., 2006; Singh et al., 2013; Belfiore et al., 2016; Rudnick et al., 2017) in which gas from mass loss and accretion in quiescent galaxies is being heated by preexisting stellar populations, mostly post-AGB stars. ‘LIER’ stands for "low-ionization emission-line region", which occurs in passive galaxies that have an emission line, much like the subset of  $UVJ$ -passive galaxies with  $H\alpha$  emission. In a similar emission line study, Rudnick et al. (2017) showed that [OII] emission in EDisCS quiescent galaxies was less common in galaxies in the EDisCS clusters and groups than in the field, where quiescent [OII] emitters comprised  $\sim 5\%$  of the quiescent population with  $M_* > 10.4$  in clusters and groups, and 30% in the field. Those authors attributed this suppression of [OII] in clusters to a combination of hydrodynamic stripping and a cutoff of gas accretion in dense environments. We do not have enough galaxies in this EDisCS subsample to make the same comparison but this could be a similar population of red emission line galaxies.

The fourth possibility is that we are catching galaxies as they are in the process of quenching their star formation and moving from the star-forming to quiescent region. In this case the low SFRs and position closer to the boundary of the  $UVJ$ -quiescent region could indicate that these galaxies are leaving the main sequence and joining the population with much lower SFRs (Cantale et al., 2016b; Foltz et al., 2018; Belli et al., 2019; Carnall et al., 2020). These results imply that

caution must be taken in interpreting the true quiescent nature of galaxies classified by *UVJ* techniques as quiescent. To assess if these *UVJ*-quiescent  $H\alpha$  emitters are truly quenching, it would be beneficial to obtain high signal-to-noise spectra at medium resolution to model the spectra and search for evidence of young stellar populations (Webb et al., 2020). We could also obtain deep molecular gas observations to probe the cold gas reservoirs that would be needed to power the observed star formation.

## 4.6 Conclusions & Future Work

In this chapter, we explore the environmental dependence of spectroscopically-derived  $H\alpha$  star-formation in three distinct regimes in the vicinity of four galaxy clusters at  $0.4 < z < 0.7$ : cluster cores, infall regions, and the field. We combine *HST*/WFC3 G102 grism observations at  $1\mu\text{m}$  with photometric and spectroscopic redshift priors to obtain a sample of 67 galaxies with secure redshifts,  $S/N$  in  $H\alpha > 3$  and which are above our mass completeness limit for star-forming galaxies of  $M_* > 10^{9.75}$ .

Our main findings are summarized as the following points:

1. With the combination of grism and redshift priors, we can obtain precise and accurate redshifts for galaxies with a range of stellar masses and intracluster locations.
2. We find no difference in the distribution of SFRs for galaxies in the three environments or as a function of radius from the cluster out to  $3R_{200}$ .
3. We find 16 galaxies that are identified as *UVJ*-quiescent galaxies, but which have significant amounts of  $H\alpha$  emission. We explore possible explanations for this emission that include star formation in quenching galaxies, AGN, and excitation of the gas by post-AGB stars. We conclude that there may be contributions from all of these scenarios.
4. The similarity of the SFR distributions for our core, infall, and field samples may be attributed to the delayed-then-rapid quenching scenario, where galaxies are unaffected for the first two –

four Gyr that they reside in the cluster environment, followed by a rapid quenching event that leaves the distribution of SFRs for star forming galaxies unaffected. We cannot conclusively test this scenario without significantly more galaxies measured to lower SFR sensitivity limits. However, it is possible that our galaxies have not experienced significant quenching processes. For the infall galaxies, this can be because of the relatively low densities that they inhabit while for the core galaxies it may be that they have recently been accreted by the cluster and are still in the “delay” phase of their eventual quenching. Whatever processes do affect star formation in the infall regions and cores of our clusters must do so in a way that preserve the indistinguishable distributions.

One possibility for using this dataset to explore the effect of environment on the star formation properties of galaxies would be to analyze the relative size of the stellar (traced by F105W) and  $H\alpha$  disks. As different processes may result in a different ratio of these sizes, this may provide a new constraint on the quenching process. We will explore this in a future work.

## Chapter 5

### Machine Learning with *HST* grism data

#### Abstract

In this Chapter, we present the machine learning methodology used to classify *HST* grism extractions. In Section 5.1, we present an overview of machine learning and how it can be applied to grism observations. Next, we introduce the convolution neural network in Section 5.1.1. We further discuss the architecture, training data, and defined classes in Sections 5.2 and 5.3. Finally, in Section 5.4 we present the accuracy of the classifier based on numerous groupings of classes and orbit depth. The developed model is then tested on the data from Chapter 4 to compare image screening times for both a human and computer.

#### 5.1 Applications of Machine Learning to *HST* Grism Extractions

In Matharu et al. (2019), the authors noted that approximately 1/3 of the *HST* grism data of [OII] emission in galaxies had to be removed from the final analysis due to poor data quality, which can arise from a number of issues including inaccurate contamination modeling, artifact presence, and edge of chip cutoffs. Similar to the study in Chapter 4, there were only a couple hundred galaxies of interest, it still required a significant amount of time to visually inspect each grism extraction by hand and classify it accordingly. Extrapolating this problem to larger scale surveys with hundreds of thousands of galaxies, such as 3DHST (Momcheva et al., 2016), would take an incredible amount of time. This also has the potential to affect results. Values such as measured fluxes and subsequently derived SFRs can still be completed and appear reasonable, even with unusable data. Thus, in order to present confident results based on imagery, all images need to be

inspected for various problems and misleading contamination. This problem formed the inspiration for this study to develop a neural network capable of analyzing *HST* grism data for data quality and morphology at intermediate redshifts.

### **5.1.1 The Convolutional Neural Network**

The development of artificial neural networks is based upon the biological neural networks found in brains, where a collection of nodes (neurons) transmit signals between each other, just like a synapses. Neural networks are trained on preclassified datasets which have both an "input" and "output" designation that help the computer learn and develop a probability-weighted model. A 1968 paper identified two types of visual cortices that are responsible for recognition tasks (Hubel & Wiesel, 1968), which led to the development of the first neorecognition or convolutional neural network (CNN) by Fukushima (1980).

With image classification by a CNN, the computer is trained to estimate and distinguish between ‘classes’ or the main object of the image. In astronomy, this would be like differentiating between a galaxy and a star. For this purpose, the image should have a main feature that is common among all images in a class and nothing else. Cropping the image to include only one object per frame is necessary to create robust models. The study in this chapter aims only to train the CNN with a single object per image and thus, image classification is a suitable solution.

How the computer learns to classify the inputs is also dependent upon the architecture, which is the organization and cycle of the layers. The chosen architecture will be discussed more in Section 5.2.3. In this study, portable network graphics (PNG) files are used, so the neural network sees a tensor that is a 4-D array, including 1) the number of images per input batch, 2) image height, 3) image width, and 4) number of channels, the latter of which is three for RGB. For ease of processing and training, images are cropped to the same size of  $224 \times 224$  pixels. A visualization of this 3-D RGB channel tensor is shown in Figure 5.1. Several steps need to be taken to help the computer learn and improve the model for the CNN through a set of three layers.

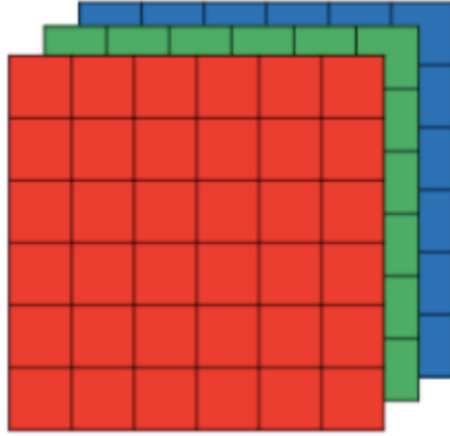


Figure 5.1: The tensor given to the CNN is a 4-D array, where the image height and width are six pixels and the number of channels is 3, one for each of red, green and blue (RGB). The pixel values of each channel are in a matrix of the image dimensions that will be used to create a filter. Each image has these properties and the total number of images analyzed by the CNN at a time is the batch size.

#### 5.1.1.1 Training

First, images are separated into their respective defined classes as required by supervised learning. This is referred to as ‘truthing’ the data, where both the human and computer know which class the image belongs to. The image should only contain the relevant class, otherwise, the computer may not accurately learn. A file structure will consist of sets of each images from each class into train, validate, and test directories, with a suggested 10:1:1 distribution of items among each (Russell & Norvig, 2009). The computer then finds and extracts features from the training set as a matrix of pixel intensities to create a filter, as shown in Figure 5.2. In this example, purple pixels correlate to a higher flux value from an emission line and are the basis of identified features for the new CNN models. Filters are created from randomized orientation, mirroring, and scaling of training images to encompass all possible encounters with a class. Filters are also referred to as the neuron or kernel, which are in the first layer of the CNN.

Memory and computation requirements are minimized with pooling. This means that the matrix of values is reduced to a smaller and more efficient size, which also helps mitigate overfitting. For example, an  $8 \times 8$  matrix can be pooled into a  $4 \times 4$  matrix by saving the largest value within

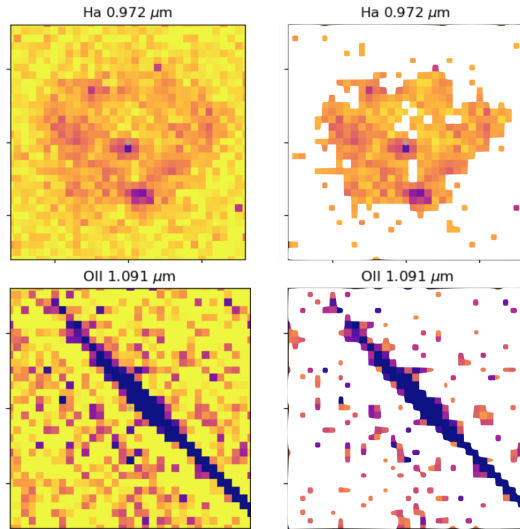


Figure 5.2: Two pairs of grism images show how a filter is created for a galaxy detection in  $H\alpha$  (top) and artifact (bottom). Darker purple indicates a higher flux detection within a given emission line, while yellow is equivalent to no detection. The yellow pixels then are masked out in both images to leave the main feature with purple pixel values of the image that is common among the class.

in each quadrant, as shown in Figure 5.3. This step is completed within the second pooling layer of the CNN.

The locations of image features (filters) with respect to one another create the final output weight that is the CNN model, which is completed in the 3rd fully connected layer. The class is determined through a probability calculation from the weight model produced in the final layer. If the resulting dot product value stored in the weight map is not 0, there is a probability  $> 0$  assigned to the potential class of the receptive field; higher dot product results lead to a higher probability. The probabilities are stored in a vector of length equal to the number of classes, where the sum of values is equal to 1. An example of a grism artifact with probabilities distributed among four classes is shown in Figure 5.4.

The past decade has seen a rapid advancement of technology to allow for quick processing and training of CNNs, which has led to sponsored challenges for the most accurate recognition rate. The best performing groups have achieved an error rate low of 0.23% in 2012 with MNIST, a handwritten database (Cireřan et al., 2012), and 6.6% with GoogLeNet for image recognition with

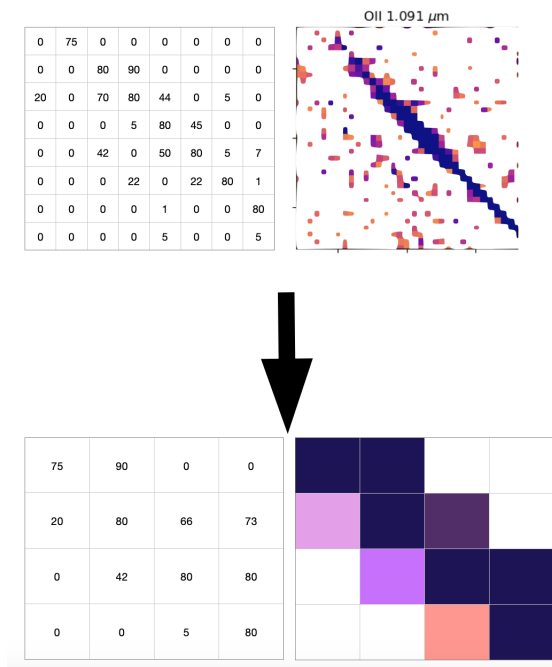


Figure 5.3: The top left matrix, which is an  $8 \times 8$  minimized representation of the artifact filter, can be pooled into a smaller  $4 \times 4$  matrix by keeping the largest value within each set of four cells. The activation map on the bottom row retains the main feature of the artifact filter by reducing the clumps of standalone pixels derived from noise.

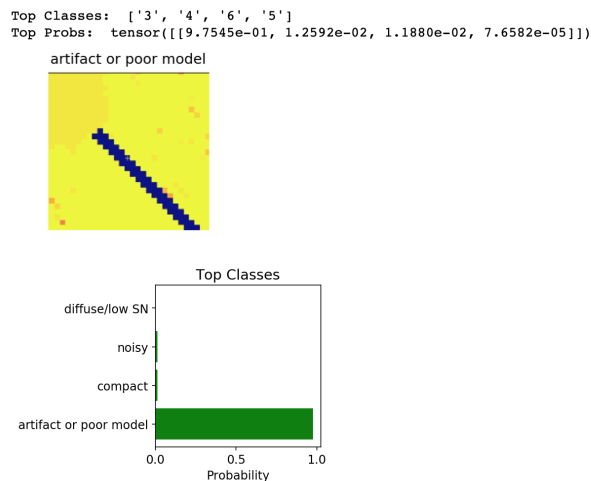


Figure 5.4: (Top) The input image that the CNN is being asked to classify. The computer has already been trained on four classes, which are listed in the bottom panel on the vertical axis. The assigned probability on a scale from zero to one is on the horizontal axis. The CNN determines that this image is more than  $>98\%$  probable to be an artifact, with  $<1\%$  for either a noisy or compact galaxy.

hundreds of classes (Szegedy et al., 2014) in 2014, which is very close to human accuracy.

The final step is classify images with created filters in the model. The filter can be compared to another image to determine the appropriate class. The dot product of the matrix values of the filter and the receptive field are calculated, where masked values of the filter are a 0. The filter then iterates around an image pixel-by-pixel to search for the filter in the new image in various locations and orientations. Results of the dot product are stored in a matrix called an activation map, which completes the convolutional layer.

## **5.2 System Specifics**

This chapter makes use of Python programming and a predefined CNN architecture to create a new model for grism extractions. The specifics of each are discussed in the following Sections.

### **5.2.1 PyTorch: Python's Machine Learning Toolkit**

PyTorch, which is the combination of Python and the Torch library, is a free, open source machine learning library that was developed by Facebook's AI Lab (Paszke et al., 2019) and has a wide versatility in computer vision topics and is even used for self-driving capabilities in Tesla vehicles. Within PyTorch, Python stores and completes tensor computations from each of the layers in fashion similar to NumPy arrays that allows for indexing, slicing, transposing and type-casting. An alternate software solution is Keras, which also uses Python and is even used at CERN.

### **5.2.2 Computer Hardware**

Tensor computations can be accelerated with the use of Graphics Processing Units (GPUs), but this work only utilizes Central Processing Units (CPUs). Hardware in this study includes a standard 2.6 GHz Intel Core i5 CPU in a 2014 MacBook Pro and an Intel(R) Xeon(R) CPU E5-2637 v4 3.5 GHz 8-core (16 CPU equivalent) Linux box. Example code structure of a PyTorch CNN used in

this work is provided in Appendix A and the code repository is available on GitHub <sup>1</sup>. Computation time comparisons between the hardware will be discussed in Section 5.5.

### 5.2.3 vgg16 Architecture

The architecture of a neural network describes the individual processes and steps required to train a model. This study will use vgg16 architecture. vgg16, which is the product of the Large Scale Visual Recognition Challenge 2014 (Simonyan & Zisserman, 2014), is one of the premier CNN architectures and achieves a 92.7% accuracy on the standard dataset ImageNet, which has 14 million images in 1000 classes. This architecture requires a standard input RGB PNG image with a size of  $224 \times 224$  pixels. While most of astronomical data are in Flexible Image Transport System (FITS) formats, the output of GRIZLI for grism is a PNG of the original FITS file. There are five sets of the convolution and pooling layers in the training before moving on to the fully connected layer to produce the weight map. The filters created in the convolutional layers create an activation map based upon a  $3 \times 3$  pixel search area, which was an improvement over the  $7 \times 7$  kernel used before vgg16 was developed. However, there are several drawbacks to vgg16 architecture. The small kernel size and numerous convolution and pooling increases the computation time, meaning that creating a new model is a lengthy process. Additionally, this creates a very large weight map with all of the filter information that can be on the order of hundreds of megabytes. Despite this, it is still a very powerful architecture that is capable of completing training of thousands of images on a modern laptop.

## 5.3 Training Data & Class Definitions

CNNs ‘learn’ to classify data that is initially characterized by hand. The preclassified data is referred to as the training set and is the data that the model is built upon. Here, training sets are *HST* grism datasets from the Cycle 20 EDisCS observations at 2 orbit-depth with G102 and the

---

<sup>1</sup>[github.com/jrcooper91/PyTorchProjects](https://github.com/jrcooper91/PyTorchProjects)

Cycle 21 GLASS observations data at 10-orbit depth with G102, with both imaging galaxies at intermediate to high redshifts. Within each training set, images are separated based upon the main feature, or class of the image. The following six images in Figure 5.5 represent the six classes that are used in this study. The images are run through a Python cropping program to separate out each gas extraction into a  $224 \times 224$  PNG file that is easily read into PyTorch. The F105W images are not used in this study since traditional images from WFC3 have been successfully utilized in other machine learning programs.

Only results of CNN models with four or fewer classes are presented and discussed here due to low accuracy rates with more numerous classes. A CNN with four classes includes edge of chip, contaminated (artifact and poor model), noisy, and detection (diffuse and compact). A reduction to three classes combines noisy and detection to uncontaminated, while edge of chip and contaminated remain. Finally, two classes distributes edge of chip into contaminated or uncontaminated. The training data is fully cycled through the architecture for 20 epochs (or revolutions) in order to train on different patterns that may arise from randomization within the data.

## 5.4 Results

Initially, classification was ambitious with six classes, but results quickly made it apparent that a more constrained set would produce a higher accuracy. The quality and resolution of grism gas extractions at higher redshifts is not refined enough to detect jellyfish, symmetrical, or other complex morphologies, which will be discussed further in Section 5.5. CNN models are developed for two, three, and four classes for both the EDisCS and GLASS datasets, which were trained on 1265 and 1754 images, respectively. The test set is composed of different images that are not in the training set and total  $\sim 10\%$  of the number in the training set. Additionally, the models are tested on the Chapter 4 data, which includes 374  $H\alpha$  extractions comprised of 85% noisy/detection, 13% artifact/poor model, and 2% edge of chip.

The results from these variations of classes (defined in Section 5.3) are shown in Table 5.1. On a MacBook Pro, one epoch takes  $\sim 15 - 20$  minutes, while only taking  $\sim$  two – three minutes on

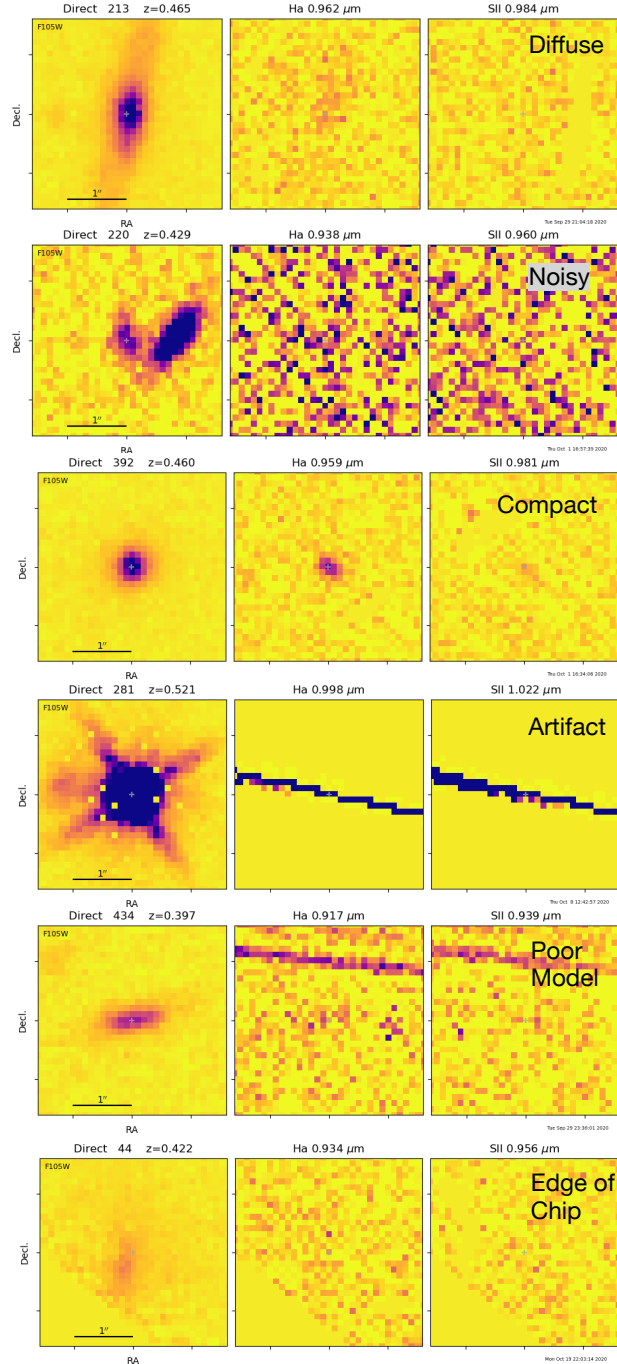


Figure 5.5: Each of the six GRIZLI image sequences shows the F105W stellar component on the left, followed by the H $\alpha$  and [SII] emission line maps within the same FOV for the same source. The defined class is based upon any of the emission maps produced by GRIZLI and is labeled in the upper right corner. These classes are not based solely on scientific classification, but with more emphasis on a visual interpretation to demonstrate the abilities of a CNN. Several classes are combined in the results as follows. The artifact and poor model classes are merged into a single class since the main feature is nearly identical between the two types. Additionally, diffuse and compact are merged as a detection class. The four main classes, starting from the top are detection, noisy, artifact/poor model, and edge of chip.

the 8-core Linux box. Classifying a single emission map with the developed model takes  $\sim 2$ -3 seconds, which would take  $\sim 15$  minutes for the entire Chapter 4  $H\alpha$  dataset on the MacBook or only a few minutes on the Linux box when utilizing every core.

The top performing model is the GLASS 2-class CNN which has an accuracy of 86% on the test set and 80% on the  $H\alpha$  EDisCS data from Chapter 4. Adding an additional class reduces the accuracy on both the EDisCS and GLASS datasets, which suggests that the grism quality is not high enough to create unique enough filters between each of the classes. While all of the listed accuracies are greater than chance, results  $> 90\%$  are desirable for practical and widespread usage.

Comparing the 2 and 10-orbit G102 data only reveals minor differences in the resulting accuracies, indicating that orbit depth is not a major factor in model success. Regardless, the GLASS models consistently perform better on the test set and data from Chapter 4 than the EDisCS data. Additionally,  $\sim 30\%$  more images were used in the training of the GLASS models than in the EDisCS ones. While the number of images from both datasets are the same order of magnitude, larger training sets could potentially increase accuracy. The analysis of the Chapter 4 classifications among the six different CNN models is discussed in detail in Section 5.5.

Differences between the accuracies presented in the test set and Chapter 4 are likely due to the aforementioned composition of the Chapter 4 data. The test set is designed to equally split the number of images in each class while Chapter 4 is mostly noisy or a detection, which is discussed in more depth in Section 5.5.

## 5.5 Discussion

In this study, six convolution neural networks are made based on 10-orbit depth GLASS and 2-orbit depth EDisCS G102 grism data, both of which targeted galaxies in the range  $0.4 < z < 0.8$ . Three CNNs for each dataset were based upon four, three, or two image classes, where the latter aimed to solely distinguish between contaminated and uncontaminated data. The 2-class models are the top performers with accuracies  $> 77\%$  on the test set and  $H\alpha$  extractions from Chapter 4.

One area of misinterpretation involves galaxies with extended gas disks, particularly if they

Dataset	Orbit Depth	Grism	Classes	$N_{images}$	Accuracy % on Test Set	Accuracy % on Ch 4
(1)	(2)	(3)	(4)	(5)	(6)	(7)
EDisCS Cycle 20	2	G102	4	1265	69	52
EDisCS Cycle 20	2	G102	3	1265	75	64
EDisCS Cycle 20	2	G102	2	1265	82	77
GLASS Cycle 21	10	G102	4	1754	77	54
GLASS Cycle 21	10	G102	3	1754	78	62
GLASS Cycle 21	10	G102	2	1754	86	80

Table 5.1: Results for the CNN on the EDisCS Cycle 20 and GLASS Cycle 21 observations. 1. Dataset used in the training, where EDisCS is data from any of the 14 pointings listed in Chapter 4. 2. Orbit depth of the observation. 3. Grism used, where G102 spans the wavelength range from  $0.7 - 1.1\mu\text{m}$ . 4. Number of images used in the training set, where  $\sim \frac{1}{10}$  of this number is available in the test and validation sets. 5. Accuracy on the test set. 6. Accuracy on the 374 H $\alpha$  extractions from Chapter 4. The accuracy increases with a reduction in classes, ultimately leaving the best classifier as the one distinguishing between contaminated and uncontaminated data.

are highly inclined to appear linear. An example of an elongated emission is in Figure 5.6; this appears similar to a contaminated image with an artifact and the resulting probabilities are [0.5914, 0.4068] which corresponds to [contaminated, uncontaminated] in the 2-class model. Interestingly, this same extraction is also identified as contaminated data in the GLASS and EDisCS 3 and 4-class models, with  $\sim 50\%$  probability of contamination and  $\sim 40\%$  detection. In the 2-class model, very low S/N galaxies oftentimes had random noise detected as contamination (Figure 5.7). However, the probability outcome [0.5087, 0.4897] [contaminated, uncontaminated] shows that it is nearly a 50-50 chance of being in either class. In the 2-class model, 20% of the Chapter 4 extractions are misidentified. 60% of these misidentifications have a 2-D tensor probability array [a,b] where a and b are within 0.1. (i.e. [0.45,0.55] where the model is finding a significant probability for either class 1 or 2). In the correctly identified 80% of Chapter 4, 18% have an a and b within 0.1 of each other. The similarity of tensor values indicates that a significant portion of the model doesn't have a clear filter match for a subset of images.

Another common source of misinterpretation are galaxies with large and resolved gas disks, such as in Figure 5.8. At the redshift range of the EDisCS and GLASS observations, these massive

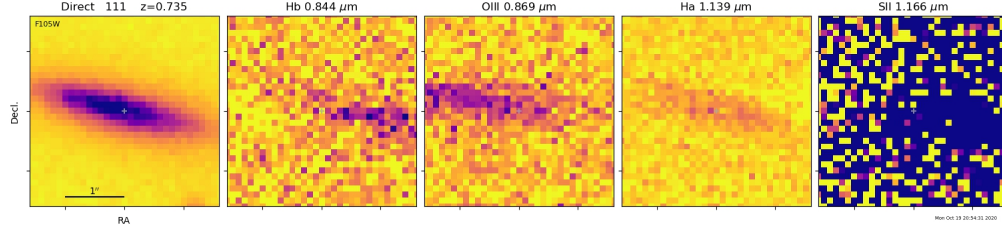


Figure 5.6: In this grism extraction, the  $H\alpha$  disk in the 4th panel is linearly extended, which would easily fit the artifact/poor model filter. The resulting probabilities only result in  $\sim 60\%$  chance that this is contaminated, with a 40% chance of usable data.

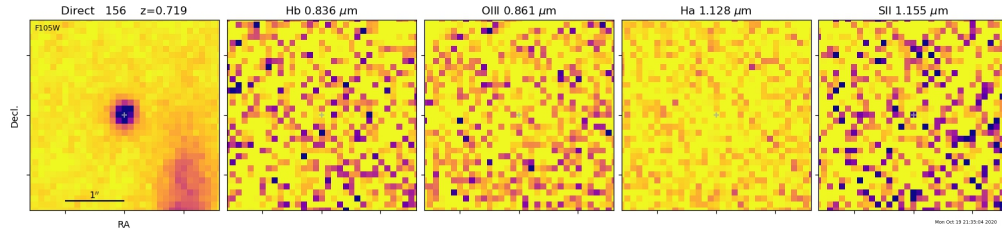


Figure 5.7: In this grism extraction, the  $H\alpha$  disk in the 4th panel is not apparent, but the artifact in the noise on the right hand side likely fits the contamination filter since it is a faint linear line. The resulting probabilities only result in  $\sim 50\%$  chance that this is contaminated or not, indicating that the model did not have a good fit to this image.

galaxies are less common than smaller, compact sources, representing 3% of the total  $H\alpha$  sample. While the  $H\alpha$  emission map in Figure 5.8 is correctly identified as a detection in the 4 and 3-class models, the 2-class CNN identified it as contamination. This is possibly due to the higher proportion of bright (purple) pixels in the image that correlate higher with the contamination filter. Additionally, the probability outputs from all classes are within 10% of the next highest class, which again identifies that the model is not trained well on this type of image.

In the 4-class models for both EDisCS and GLASS, only  $\sim 5\%$  of the Chapter 4  $H\alpha$  had a probability  $> 70\%$  in one class. 100% of these cases are identified as ‘noisy’, and 85% are actually correct. This indicates that the training set and Chapter 4 sets have consistent noise features that are extremely similar between the observation cycles. However, this also suggests that the model is fitting multiple filters to the image and one is not a clearly defined match over the others. This can be attributed to the wide range of gas disk morphologies and low resolution data.

While not very common, images can also contain more than one class. For example, Figure 5.9 contains a detection and an artifact. Additionally, edge of chip images will also likely contain

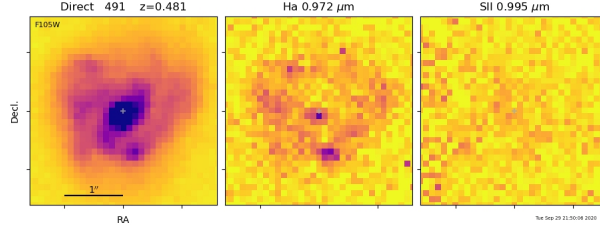


Figure 5.8: In this grism extraction, the  $H\alpha$  disk is resolved and clumpy.

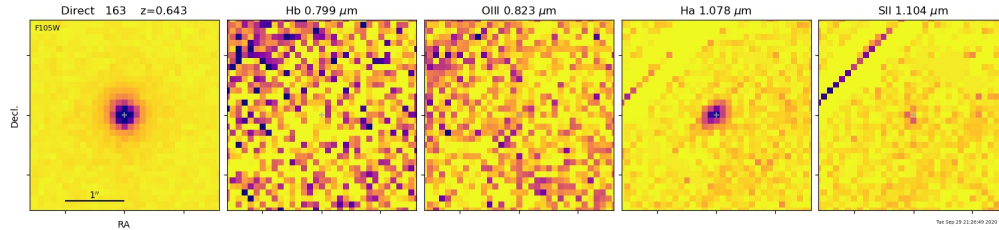


Figure 5.9: In this grism extraction, the  $H\alpha$  disk in the 4th panel is compact and  $\sim 20$  pixels in area. However, there is also an artifact in the top left.

another class unless  $> 50$  of the image is off of the chip. In cases with multiple classes, the model will see matches with multiple filters. For the  $H\alpha$  emission map in Figure 5.9, the 2-class models identify this as an artifact with a 50 – 58% probability. In the 3 and 4-class models, this image is nearly equally classified across all of the defined classes. The yellow pixels around the artifact are similar enough to what the edge of a chip looks like with no pixel values, hence the confusion with this class.

Finally, data quality is certainly a contributing factor to these results. Even though the CNN architecture takes images that are  $224 \times 224$  pixels, the actual grism emission maps themselves are only  $31 \times 31$  pixels. Thus, the model is making low-resolution filters on objects that are only a few pixels wide. A majority of the  $H\alpha$  emission maps span  $< 50$  pixels and not necessarily the same size or shape, which makes the model difficult to constrain during training and even more difficult to classify separately. The  $3 \times 3$  pixel search kernel may be too refined for this dataset and a larger kernel would also reduce the total model computation time.

A major aspect of this study aims to reduce manual labor and time spent classifying images. As previously stated, it takes  $\sim 15$  minutes with a CNN model to classify 374 extractions. Completing this task by hand takes anywhere from 5 – 10 seconds per image totaling an hour or more

accounting for revisits, error, and breaks. This time can also vary depending upon the complexity of the image and experience of the observer. Therefore, it likely takes double or quadruple the amount of time to classify these same images by eye. This gain can be expanded with the use of multi-core machines or computer clusters.

## 5.6 Conclusions & Future Work

A CNN model has been successfully developed on 2 and 10-orbit G102 grism data to distinguish between two, three, and four image classes. These models can be used on other grism data to classify images in less than half the time it would take a human to complete the same task. The top performing model is the 2-class one which distinguishes between contaminated and uncontaminated data. Despite all models having accuracies exceeding random choice, a higher accuracy is desired. Sources of error here are derived mainly from low resolution emission maps, abnormal gas disk morphology, and images with multiple classes. However, this study still proves that a CNN model can be developed on *HST* grism emission maps; this chapter serves predominantly as a proof of concept and small-scale study.

With this in mind, this CNN model is best served as an indicator of data quality, where it is capable of distinguishing between a contamination and usable data. Without visually inspecting the data, false signals can easily present as realistic  $H\alpha$  or other emission line fluxes and using this neural network can easily and quickly flag data that should be omitted from the final sample. Particularly in cases of Large Programs with dozens of orbits, this removes days or even weeks of manual labor to inspect individual extractions and is crucial towards drawing robust conclusions from the data.

There are several avenues in which to expand this study. This work only included grism G102 data, however, G141 which spans higher  $\lambda$  are also available. The soon-to-launch *James Webb Space Telescope* will also have its own grism to produce emission line maps. An interesting study would include testing G102 data on a G141 model and visa versa. The resolution for both grisms are very similar, so similar problems would likely persist in a comparative study.

Additionally, the top CNNs today are trained on millions of images with hundreds of classes. The training sample size here is quite small and could easily be expanded to 100,000+ with the use of datasets from 3DHST. This could aid in refining class definitions, which would ultimately improve the accuracy.

Finally, integration of a CNN model into current astronomical processing steps is pertinent towards this becoming adopted within the community. It would be most helpful to modify the code to output the probabilities into a usable format such as a table. Ideally, this study could be integrated with the current GRIZLI code in the final extraction steps. Once the emission maps are produced, they could be classified with a CNN model and identify any problematic data with a flag or other indicator. Additionally, astronomical datasets produce FITS files, so altering the CNN architecture to read a non-RGB channel tensor is critical towards efficient and rapid processing.

# Chapter 6

## Conclusions

We have investigated the role of environment on galaxy evolution at  $0.4 < z < 0.8$  through two methods with the EDisCS cluster sample. First, we presented the passive fraction,  $f_{passive}$ , as a function of redshift, stellar mass, and cluster-centric radius for 16 EDisCS clusters. This data included deep core data as well as a wide field imaging survey to fully encompass the infall region. The  $f_{passive}$  is determined through a color-color definition in rest-frame  $UVJ$ -space, with a correction for interlopers in the photometric core data.

We show that the buildup of quiescent galaxies in clusters and the field is evident over several billion years through the increasing  $f_{passive}$  with a decrease in look back time (Figures 3.2 and 3.3). The buildup of passive galaxies is apparent in both EDisCS surveys (Figures 3.4 and 3.5). When the cluster  $f_{passive}$  is compared to the field, we see a differentiation from the field at low redshifts as evidence of environmental quenching (Figure 3.5), which is not evident at high- $z$ . This dependence on redshift is less evident in the core than in the infall region.

We then derived the  $f_{passive}$  in relation to stellar mass, which reveals that the most massive galaxies are passive through mass quenching. For the EDisCS core sample, the cluster sample  $f_{passive}$  is mostly indistinguishable from the field at all masses in both redshift regimes (Figure 3.4). However, when using the LDP sample in two intracluster environments, the result varies greatly (Figure 3.6). The  $f_{passive}$  in the core is well above the field relation and in agreement with results from other cluster surveys at similar redshifts, indicating that galaxies may have experienced environmental quenching. The flat relation suggests environmental quenching is also contributing towards SFR suppression and is efficient. The infall relation for the low- $z$  galaxies is similar to the core, where a majority of the galaxies are quiescent; however, the high- $z$  bin has a steep relation

between stellar mass and  $f_{passive}$ , where galaxies with  $\text{Log}M_* < 10.8$  are mostly star-forming to suggest that environmental quenching isn't efficient. The high- $z$  infall is indistinguishable from the field  $f_{passive}$ , suggesting a lack of environmental quenching processes. This dramatic shift for the relation between redshift regimes is interpreted as possible environmental quenching within the cluster. The most massive cluster galaxies are already quenched regardless of location and redshift, but the transition from high to low redshift epochs could contain a period of transformation, but our low sample sizes both in terms of clusters and individual galaxies are not large enough to confirm this.

Finally, we inspect the  $f_{passive}$  as a function of cluster-centric distance, which reveals a similar finding for observed differences in redshift (Figures 3.8 and 3.9). At lower redshifts, there is little dependence on radial distance and stellar mass with the passive fraction, indicating quenching in some combination of extrinsic and intrinsic quenching processes. At higher redshifts, the  $f_{passive}$  decreases outward from the core, which is also seen at  $10^{10.6} < M_* < 10^{11.0}$ . Interestingly, the outskirts of the core at  $4.5R_{200}$  are composed of  $>80\%$  quiescent galaxies at all redshifts.

Following this analysis, *Hubble Space Telescope* observations from select  $z \sim 0.5$  clusters targeting  $H\alpha$  emitters cover both galaxies in the core and infall region. These  $H\alpha$  fluxes are converted to star-formation rates, with corrections accounting for the [NII] doublet blending, post-AGB stellar contributions, and internal extinction. We explore the environmental dependence of spectroscopically-derived  $H\alpha$  star-formation in three distinct regimes in the vicinity of four galaxy clusters at  $0.4 < z < 0.7$ : cluster cores, infall regions, and the field. We combine *HST*/WFC3 G102 grism observations at 1 with photometric and spectroscopic redshift priors to obtain a sample of 67 galaxies with secure redshifts,  $S/N$  in  $H\alpha > 3$  and which are above our mass completeness limit for star-forming galaxies of  $M_* > 10^{9.75}$ . We see no differentiation in the main sequence relations between the three environments (Figure 4.9) on a cluster-by-cluster basis (Figure 4.10).

Finally, a convolutional neural network was trained on more than 1,000 emission line extractions from the *HST* observations on EDisCS and GLASS clusters to classify two, three, or four classes of images (Figure 5.5). A top accuracy of 86% is achieved with the GLASS Cycle 21 data

with two classes defining either contaminated or uncontaminated images (Table 5.1). Accuracy decreases with an increase in the number of classes, which is likely due to low resolution extractions and unique emission maps. While accuracy rates  $>90\%$  are desirable, this neural network proves that grism data can be trained and automatically classified at a rate that takes less than half of the time it would for a human to complete the same task.

Our conclusions are as follows:

1. The passive fraction decreases with increasing redshift, which supports the buildup of red galaxies as the Universe ages. This is seen in both the field and dense environments for all EDisCS clusters. The highest redshift clusters at  $z = 0.8$  have a  $f_{passive} \sim 0.6$ , which gradually increases to  $\sim 1.0$  for the lower redshift sample at 0.45.

2. EDisCS galaxy cluster core and infall regions have a higher passive fraction than in the field from at low- $z$  ( $0.4 < z < 0.6$ ). At high- $z$  ( $0.6 < z < 0.8$ ), this separation is more indistinguishable.

3. The passive fraction increases with stellar mass regardless of environment, which supports the finding that the most massive galaxies are ‘red dead’ from intrinsic mass quenching. While the EDisCS core VLT observations show no indication of environmental quenching, the LDP core and infall samples at low- $z$  show moderate evidence. At redshifts greater than 0.6, the distinction between cluster and field  $f_{passive}$  is less clear in both the core and infall region, which is also seen in conclusion two above. This trend is observed in both the core and infall regions.

4. There is a dependence of  $f_{passive}$  on radial distance at some stellar masses and redshifts. At  $\text{Log}_{10}(M_*/M_\odot) > 11.0$ , mass quenching is in effect and a large majority of galaxies are quiescent at all redshifts. However, at  $\text{Log}_{10}(M_*/M_\odot) > 10.6$  and  $< 11.0$ , only the low- $z$  sample is quenched. The high- $z$  sample displays a sharp decline in  $f_{passive}$  outside of the virial radius. This indicates a possible environmental quenching between the two epochs.

5. With the combination of grism and redshift priors, we can obtain precise and accurate redshifts for galaxies with a range of star-formation histories. Usage of priors with GRIZLI has been uncommon in the past and this demonstrated that it is feasible and important towards  $H\alpha$  line identification. The implementation of this feature improves the capabilities of the software and

allows for more robust extractions from grism observations.

6. We find no difference in the distribution of SFRs for galaxies in the three environments or as a function of radius from the cluster out to  $3R_{200}$ .

7. We find 16 galaxies in the mass-complete sample ( $\sim 24\%$ ) that are identified as *UVJ*-passive galaxies, but which have significant amounts of  $H\alpha$  emission. In the first portion of this study concerning  $f_{passive}$ , these galaxies would be classified as quiescent, but the  $H\alpha$  observations tell another story, much like low-ionization emission line region (LIER) galaxies. These galaxies appear to be falling off of the main sequence and we may be observing them as they are being quenched.

8. The similarity of the infall and field samples may be attributed to the delayed-then-rapid quenching scenario, where galaxies are unaffected for the first two - four Gyr that they reside in the cluster environment. This indicates that these galaxies have recently been accreted by the cluster and have not yet undergone any gas quenching processes and present similar SFRs. However, this does not explain the similarity between the field and core samples.

9. A neural network can be effectively trained to be at least 86% accurate on *HST* grism data to distinguish between a decent extraction and one that is unusable due to contamination or poor modeling.

10. The CNN model can complete a grism classifying task in half of the time or less than it would normally take a human.

## 6.1 Future Work

This work has largely focused on the bimodal classification and emission line parameters of galaxies in varying cosmic densities to give insight on the role of environment on evolution. Several avenues can be explored to further understand the role of dense environments on galaxy evolution with these datasets.

1. The environmental quenching efficiency, or the fraction of galaxies that would have been star-forming in the field that are now passive in clusters, can be determined for the LDP sample.

Within a given mass bin, the fraction of quiescent galaxies in the field are subtracted from the cluster and this number is divided by the star forming fraction in the field at the same mass bin. Similar to the passive fraction study, this can be done at high and low- $z$ . Additionally, the passive fraction can be compared to the halo masses from the parent clusters to search for an environmental effect related to this parameter. As mid-mass clusters, EDisCS clusters are progenitors to local structures and are less massive than many of the cluster surveys in the literature.

2. Modeling is an important step towards defining a quenching timescale within a given environment. The surface density of galaxies across a cluster environment allows for interpretation on star formation within intracluster distances to approximate a more rapid or slow decay as individual galaxies are accreted.

3. Each galaxy from Chapter 4 has an F105W and  $H\alpha$  image counterpart where each disk can be measured (e.g. Sérsic Index) to compare growth between environments and the stellar vs.  $H\alpha$  sizes. External quenching mechanisms such as ram pressure stripping will present as an asymmetric gas disk while internal strangulation can change the relative sizes between the two components. Identification of the quenching process affecting each galaxy will further constrain the mechanisms at play in galaxy evolution. Along with a visual classification of morphology, these findings in conjunction with the SFRs presented here will give a well-rounded insight to these  $z \sim 0.5$  clusters and the processes responsible for varying SFRs. Additionally, a larger sample set of galaxies with SFRs to compare to the *UVJ* classification can help identify galaxies masquerading as quiescent that actually have ongoing star-formation.

## Appendix A

### *HST* Catalogs & Data Products

In Tables A.1, A.2 and A.3, we present the information for *HST*-observed galaxies checked for quality and with  $H\alpha$  detections above our threshold limit of 3 in the core, infall and field environments, respectively. In Table A.4, we present the galaxies with  $S/N$  in  $H\alpha < 3$  that have passed quality checks.

Object ID	R.A.	Dec	z	Distance	Stellar Mass	flux $H\alpha$	SFR $H\alpha$	U-V	V-J	UVJ
(1)	Deg. (2)	Deg. (3)	(4)	Mpc (5)	Log $_{10}(M_*/M_{\odot})$ (6)	$10^{-16}\text{erg s}^{-1}\text{cm}^{-2}$ (7)	$M_{\odot}\text{yr}^{-1}$ (8)	AB (9)	AB (10)	Classification (11)
CI1059-12.1-382	164.7492	-12.8713	0.4555	0.366	8.04	1.11 ±0.12	1.41 ±0.15	0.73	0.73	sf
CI1059-12.1-165	164.7544	-12.8858	0.4617	0.051	10.8	43.5 ±0.4	107.95 ±1.09	0.99	0.92	sf
CI1059-12.1-392	164.7546	-12.8709	0.4602	0.368	9.83	3.33 ±0.16	4.34 ±0.21	1.14	0.75	sf
CI1059-12.1-087	164.7554	-12.8909	0.4583	0.085	10.12	8.54 ±0.26	14.42 ±0.43	1.20	0.93	sf
CI1059-12.1-334	164.7563	-12.8743	0.4596	0.294	10.28	5.02 ±0.32	8.53 ±0.54	1.25	0.97	sf
CI1059-12.1-217	164.7583	-12.8821	0.4565	0.124	10.46	5.48 ±0.34	18.05 ±1.11	1.63	1.20	q
CI1059-12.1-431	164.7654	-12.8686	0.4601	0.407	9.65	1.02 ±0.14	1.33 ±0.18	1.22	0.74	sf
CI1059-12.1-461	164.7692	-12.8664	0.4595	0.453	10.91	1.13 ±0.33	4.24 ±1.25	1.95	1.23	q
CI1059-12.2-320	164.7787	-12.8982	0.4615	0.227	10.71	1.03 ±0.227	3.49 ±0.92	1.88	1.09	q
CI1059-12.2-244	164.7819	-12.9035	0.4538	0.342	11.58	1.73 ±0.49	21.37 ±6.08	2.18	1.41	q
CI1059-12.2-231	164.7829	-12.9050	0.4554	0.374	10.96	3.72 ±0.24	46.23 ±2.94	1.97	1.38	q
CI1059-12.2-261	164.7852	-12.9025	0.4733	0.32	9.63	0.54 ±0.17	0.75 ±0.24	1.06	0.69	sf
CI1059-12.2-192	164.7861	-12.9070	0.4609	0.416	10.6	4.79 ±0.226	11.85 ±0.63	1.43	1.07	sf
CI1059-12.2-325	164.7884	-12.8979	0.4528	0.224	9.85	2.93 ±0.36	3.67 ±0.46	1.09	0.76	sf
CI1059-12.2-434	164.7897	-12.8874	0.4598	0.005	10.78	5.67 ±0.39	21.39 ±1.48	1.81	1.30	q
CI1059-12.2-311	164.7908	-12.8992	0.4587	0.253	9.8	0.95 ±0.16	2.33 ±0.4	1.42	1.09	sf
CI1059-12.2-452	164.7911	-12.8849	0.4577	0.059	5.77	0.99 ±0.14	1.02 ±0.14	0.86	0.51	sf
CI1059-12.2-350	164.7912	-12.8954	0.4573	0.172	8.88	0.79 ±0.17	1.25 ±0.27	0.80	-0.46	sf
CI1059-12.2-441	164.7940	-12.8867	0.4505	0.021	10.44	2.35 ±0.33	7.15 ±1.01	1.62	1.19	sf
CI1059-12.2-466	164.7959	-12.8802	0.4613	0.161	9.31	0.78 ±0.23	1.34 ±0.39	1.00	0.80	sf
CI1059-12.2-449	164.7962	-12.8853	0.4524	0.053	8.62	1.31 ±0.19	2.03 ±0.3	0.58	0.19	sf
CI1059-12.2-463	164.7962	-12.8828	0.4564	0.106	9.39	3.32 ±0.16	4.24 ±0.2	0.85	0.68	sf
CI1059-12.2-387	164.8008	-12.8917	0.4561	0.099	9.81	1.17 ±0.16	1.95 ±0.27	1.37	0.95	sf
CI1059-12.2-395	164.8048	-12.8905	0.455	0.079	9.35	2.96 ±0.13	4.91 ±0.21	0.94	0.83	sf
CI1059-12.2-172	164.8059	-12.9082	0.4613	0.455	9.85	2.84 ±0.18	4.86 ±0.31	1.10	0.96	sf
CI1138-11.0-1772	174.5345	-11.5584	0.4829	0.035	9.32	2.17 ±0.29	2.55 ±0.35	0.87	0.36	sf
CI1138-11.0-1460	174.5358	-11.5635	0.4781	0.047	8.83	3.16 ±0.15	5.90 ±0.27	0.69	0.85	sf
CI1138-11.0-199	174.5399	-11.5897	0.4799	0.452	9.7	3.72 ±0.24	5.36 ±0.34	1.08	0.72	sf
CI1138-11.0-1203	174.5431	-11.5686	0.4785	0.124	9.11	1.6 ±0.29	1.83 ±0.34	0.76	0.34	sf
CI1138-11.0-1073	174.5450	-11.5705	0.481	0.155	10.28	1.04 ±0.3	2.62 ±0.75	1.82	0.92	q
CI1138-11.0-1230	174.5452	-11.5681	0.478	0.117	8.96	2.78 ±0.46	4.91 ±0.81	0.74	0.01	sf
CI1138-11.0-1573	174.5459	-11.5616	0.4902	0.016	10.67	0.88 ±0.26	3.87 ±1.12	2.11	1.22	q
CI1138-11.0-375	174.5464	-11.5843	0.4787	0.368	9.76	4.83 ±0.63	6.92 ±0.9	1.17	0.77	sf
CI1138-11.0-298	174.5464	-11.5867	0.4852	0.406	9.6	0.66 ±0.16	1.68 ±0.4	1.85	0.98	q
CI1138-11.0-1516	174.5496	-11.5626	0.4637	0.032	8.05	0.49 ±0.1	0.81 ±0.17	0.22	-0.12	sf
CI1138-11.0-1409	174.5531	-11.5647	0.4875	0.066	9.7	6.64 ±0.4	9.94 ±0.59	0.95	0.79	sf
CI1138-11.0-1897	174.5574	-11.5566	0.4822	0.064	9.34	5.56 ±0.49	6.44 ±0.56	1.02	0.48	sf
CI1138-11.0-668	174.5624	-11.5779	0.4988	0.275	8.69	1.09 ±0.19	2.14 ±0.37	0.29	-0.38	sf
CI1138-11.0-979	174.5641	-11.5727	0.4851	0.195	10.12	25.1 ±0.78	48.50 ±1.51	1.17	0.99	sf
CI1138-11.0-1265	174.5651	-11.5673	0.4697	0.113	9.9	0.39 ±0.093	5.21 ±1.25	1.93	1.62	sf
CI1227-11.0-126	186.9720	-11.6148	0.6375	0.709	10.1	4.65 ±0.25	130.54 ±6.97	1.37	1.41	sf
CI1227-11.0-332	186.9794	-11.5997	0.626	0.324	10.07	0.76 ±0.23	5.08 ±1.55	1.28	1.22	sf
CI1227-11.0-217	186.9838	-11.6078	0.6321	0.524	10.64	1.44 ±0.23	5.29 ±0.83	1.44	0.57	sf
CI1301-11.0-134	195.3694	-11.6311	0.5003	0.458	9.44	3.78 ±0.54	4.78 ±0.68	0.87	0.48	sf
CI1301-11.0-304	195.3789	-11.6149	0.4681	0.714	9.21	11.6 ±0.52	2.44 ±0.23	0.49	0.29	sf
CI1301-11.0-157	195.3860	-11.6292	0.4871	0.468	9.9	4.86 ±0.48	1.58 ±0.3	1.14	0.79	sf
CI1301-11.0-187	195.3861	-11.6258	0.4823	0.524	9.94	13.9 ±0.44	36.27 ±0.99	1.16	0.86	sf
CI1301-11.1-502	195.3762	-11.6977	0.482	0.715	8.96	2.11 ±0.2	9.49 ±0.94	1.21	0.96	sf
CI1301-11.1-491	195.3847	-11.6989	0.481	0.725	10.23	19.1 ±0.52	38.41 ±1.2	1.16	1.01	sf
CI1301-11.1-525	195.3862	-11.6954	0.4855	0.665	10.1	3.3 ±0.3	9.24 ±0.85	1.08	0.94	sf
CI1301-11.1-560	195.3924	-11.6929	0.4832	0.617	9.78	3.27 ±0.23	9.06 ±0.64	0.93	0.92	sf
CI1301-11.1-324	195.3935	-11.7106	0.4862	0.911	10.35	1.78 ±0.25	5.00 ±0.7	1.28	1.00	sf

Table A.1: Information for core galaxies. 1. Pointing ID - GRIZLI Object ID 2. Right Ascension 3. Declination 4. Redshift 5. Cluster-centric distance in Mpc. 6. Stellar Mass 7.  $H\alpha$  flux in cgs units 8. Star-formation rate. 9.  $U-V$  rest-frame color 10.  $V-J$  rest-frame color 11.  $UVJ$  classification based on Williams et al. (2009) where sf and q represent star-forming and quiescent, respectively.

Object ID	R.A.	Dec	z	Distance	Stellar Mass	flux $H\alpha$	SFR $H\alpha$	$U-V$	$V-J$	$UVJ$
(1)	Deg.	Deg.	(4)	Mpc	$\text{Log}_{10}(M_*/M_{\odot})$	$10^{-16}\text{erg s}^{-1}\text{cm}^{-2}$	$M_{\odot}\text{yr}^{-1}$	AB	AB	Classification
	(2)	(3)		(5)	(6)	(7)	(8)	(9)	(10)	(11)
CI1138-11.2-166	174.3821	-11.4293	0.4812	2.44	10.03	1.04 ± 0.166	2.62 ± 0.42	1.40	1.94	sf
CI1138-11.2-222	174.3956	-11.4266	0.4818	2.41	10.08	3.9 ± 0.219	5.67 ± 0.32	1.17	1.82	sf
CI1138-11.2-213	174.3994	-11.4272	0.4654	2.39	10.42	3.33 ± 0.314	43.58 ± 4.11	1.70	1.45	sf
CI1138-11.2-490	174.4010	-11.4085	0.4735	2.67	9.77	3.37 ± 0.486	4.69 ± 0.68	1.08	0.67	sf
CI1138-11.1-077	174.6872	-11.5849	0.4869	0.7	9.77	2.26 ± 0.624	3.37 ± 0.93	1.16	0.69	sf
CI1138-11.1-137	174.7016	-11.5811	0.4894	0.71	9.07	2.39 ± 0.589	2.90 ± 0.71	0.66	0.27	sf
CI1138-11.1-388	174.7105	-11.5616	0.4945	0.45	9.72	6.39 ± 0.571	7.85 ± 0.70	0.81	0.50	sf
CI1138-11.1-263	174.7122	-11.5714	0.4903	0.61	11.09	5.51 ± 0.973	81.80 ± 14.43	1.67	2.55	sf
CI1227-11.1-088	186.9564	-11.6694	0.6166	2.1	9.30	1.37 ± 0.172	2.91 ± 0.37	0.76	0.32	sf
CI1227-11.1-226	186.9569	-11.6607	0.6383	1.88	10.07	5.49 ± 0.254	38.71 ± 1.79	0.80	1.06	sf
CI1227-11.1-309	186.9807	-11.6551	0.6358	1.71	10.06	3.87 ± 0.253	20.86 ± 1.36	1.00	0.87	sf
CI1227-11.2-225	187.0602	-11.5263	0.6246	1.62	11.22	2.32 ± 0.385	18.37 ± 3.04	1.98	1.37	q
CI1227-11.2-163	187.0621	-11.5297	0.6428	1.54	9.66	3.55 ± 0.162	10.39 ± 0.47	0.79	0.61	sf
CI1227-11.2-347	187.0682	-11.5193	0.6312	1.82	9.03	1.58 ± 0.159	3.56 ± 0.36	0.50	0.37	sf
CI1301-11.3-220	195.2301	-11.5203	0.4683	2.84	8.50	1.11 ± 0.247	1.51 ± 0.34	0.13	0.61	sf
CI1301-11.3-337	195.2334	-11.5130	0.4941	2.95	10.07	3.64 ± 0.244	5.62 ± 0.38	1.01	0.57	sf
CI1301-11.3-144	195.2358	-11.5266	0.4926	2.71	10.55	4.38 ± 0.403	65.68 ± 6.05	1.91	1.78	sf
CI1301-11.3-223	195.2426	-11.5201	0.4947	2.77	8.78	0.49 ± 0.151	0.94 ± 0.29	0.17	-0.11	sf
CI1301-11.1-300	195.3445	-11.5418	0.4974	1.99	9.51	1.35 ± 0.214	20.73 ± 3.28	0.88	1.25	sf
CI1301-11.1-421	195.3487	-11.5294	0.4976	2.19	9.17	0.95 ± 0.249	1.85 ± 0.48	0.94	0.13	sf
CI1301-11.1-061	195.3502	-11.5586	0.4672	1.7	9.42	5.68 ± 0.35	6.09 ± 0.38	0.73	0.53	sf
CI1301-11.1-354	195.3503	-11.5372	0.4944	2.06	10.42	18.8 ± 0.828	38.16 ± 1.68	1.13	0.91	sf
CI1301-11.1-361	195.3542	-11.5363	0.4933	2.06	8.95	0.77 ± 0.22	11.53 ± 3.30	0.42	1.35	sf
CI1301-11.1-208	195.3585	-11.5476	0.501	1.87	11.06	1.48 ± 0.229	6.84 ± 1.06	2.11	1.28	q

Table A.2: Information for infall galaxies. 1. Pointing ID - GRIZLI Object ID 2. Right Ascension 3. Declination 4. Redshift 5. Cluster-centric distance in Mpc. 6. Stellar Mass 7.  $H\alpha$  flux in cgs units 8. Star-formation rate. 9.  $U-V$  rest-frame color 10.  $V-J$  rest-frame color 11.  $UVJ$  classification based on Williams et al. (2009) where sf and q represent star-forming and quiescent, respectively.

Object ID	R.A.	Dec	z	Stellar Mass	flux $H\alpha$	SFR $H\alpha$	$U-V$	$V-J$	$UVJ$
(1)	Deg. (2)	Deg. (3)	(4)	$\text{Log}_{10}(M_{\star}/M_{\odot})$ (5)	$10^{-16}\text{erg s}^{-1}\text{cm}^{-2}$ (6)	$M_{\odot}\text{yr}^{-1}$ (7)	AB (8)	AB (9)	Classification (10)
C11059-12.1-326	164.7441	-12.8751	0.6477	10.19	1.32 ± 0.21	26.93 ± 6.24	1.04	1.99	sf
C11059-12.1-413	164.7442	-12.8697	0.6660	10.46	1.39 ± 0.30	29.61 ± 9.39	1.57	2.09	sf
C11059-12.1-505	164.7475	-12.8625	0.6323	9.15	0.85 ± 0.14	16.19 ± 3.88	1.13	1.97	sf
C11059-12.1-408	164.7506	-12.8697	0.6582	8.54	0.65 ± 0.12	1.56 ± 0.46	0.41	0.19	sf
C11059-12.1-192	164.7514	-12.8837	0.6705	9.12	0.85 ± 0.10	16.89 ± 3.04	0.88	1.70	sf
C11059-12.1-162	164.7514	-12.8859	0.6716	8.54	0.37 ± 0.12	0.97 ± 0.49	0.55	0.86	sf
C11059-12.1-517	164.7520	-12.8617	0.4064	10.05	4.08 ± 0.32	11.74 ± 0.75	1.19	1.35	sf
C11059-12.1-496	164.7523	-12.8632	0.6979	10.99	0.90 ± 0.24	20.82 ± 8.23	1.98	2.24	sf
C11059-12.1-486	164.7528	-12.8638	0.6544	10.32	0.22 ± 0.06	4.55 ± 1.94	2.22	1.58	sf
C11059-12.1-086	164.7536	-12.8908	0.6076	8.45	0.47 ± 0.11	0.85 ± 0.28	0.23	0.74	sf
C11059-12.1-183	164.7580	-12.8842	0.6428	9.16	0.41 ± 0.11	7.87 ± 3.12	1.19	1.64	sf
C11059-12.1-101	164.7626	-12.8893	0.6107	8.22	1.14 ± 0.35	3.92 ± 1.68	0.23	1.01	sf
C11059-12.1-333	164.7639	-12.8740	0.5182	8.60	0.40 ± 0.09	0.51 ± 0.12	0.50	0.46	sf
C11059-12.1-241	164.7699	-12.8805	0.4865	9.85	3.02 ± 0.17	44.02 ± 2.45	1.37	2.06	sf
C11059-12.2-285	164.7730	-12.8781	0.5736	8.63	1.86 ± 0.09	3.26 ± 0.21	0.44	0.70	sf
C11059-12.2-220	164.7780	-12.9053	0.4291	9.71	0.45 ± 0.14	5.61 ± 1.47	1.43	1.75	q
C11059-12.2-405	164.7856	-12.8899	0.5032	8.72	0.87 ± 0.13	1.75 ± 0.27	0.62	0.90	sf
C11059-12.2-289	164.7867	-12.8999	0.4245	9.53	0.66 ± 0.19	8.06 ± 1.97	1.58	1.45	sf
C11059-12.2-310	164.7926	-12.8992	0.4127	9.83	0.84 ± 0.25	9.84 ± 2.49	1.56	1.78	sf
C11059-12.2-447	164.7978	-12.8854	0.5450	10.13	0.99 ± 0.12	4.36 ± 0.60	2.37	1.15	sf
C11059-12.2-396	164.7999	-12.8906	0.5936	9.46	3.29 ± 0.17	59.62 ± 4.10	0.88	1.92	sf
C11059-12.2-399	164.8028	-12.8902	0.4168	8.64	0.64 ± 0.13	1.05 ± 0.17	1.00	0.92	sf
C11059-12.2-390	164.8050	-12.8911	0.4245	9.53	0.76 ± 0.22	9.37 ± 2.28	1.33	1.80	sf
C11138-11.2-158	174.3800	-11.4304	0.4139	9.21	1.36 ± 0.42	1.34 ± 0.34	1.16	1.44	sf
C11138-11.2-090	174.3832	-11.4337	0.4552	9.32	4.38 ± 0.45	6.03 ± 0.57	0.52	1.78	sf
C11138-11.2-060	174.3834	-11.4351	0.6938	9.89	2.82 ± 0.22	15.19 ± 1.91	1.22	1.19	sf
C11138-11.2-504	174.3887	-11.4074	0.6761	9.98	1.85 ± 0.22	9.78 ± 1.80	1.32	1.20	sf
C11138-11.2-376	174.3972	-11.4166	0.6875	9.28	1.26 ± 0.19	2.10 ± 0.51	0.72	1.50	q
C11138-11.2-246	174.3987	-11.4245	0.5759	9.02	1.10 ± 0.24	1.95 ± 0.53	0.80	0.76	sf
C11138-11.2-079	174.4013	-11.4342	0.5195	10.34	2.40 ± 0.46	5.09 ± 1.05	1.31	2.03	sf
C11138-11.0-1481	174.5333	-11.5634	0.6410	8.82	0.99 ± 0.19	2.36 ± 0.67	0.63	-0.27	sf
C11138-11.0-789	174.5375	-11.5756	0.5063	9.58	0.73 ± 0.11	0.91 ± 0.14	1.51	0.59	sf
C11138-11.0-1549	174.5401	-11.5620	0.5182	10.68	1.20 ± 0.24	3.37 ± 0.71	1.98	1.00	sf
C11138-11.0-1403	174.5429	-11.5647	0.5186	8.23	1.01 ± 0.10	1.28 ± 0.14	0.68	0.26	sf
C11138-11.0-180	174.5470	-11.5900	0.6205	8.86	1.70 ± 0.11	2.58 ± 0.24	0.91	0.30	q
C11138-11.0-1973	174.5490	-11.5557	0.6994	8.38	1.12 ± 0.23	1.79 ± 0.66	0.21	0.59	sf
C11138-11.0-2141	174.5566	-11.5758	0.4094	8.26	0.78 ± 0.23	9.47 ± 2.26	1.02	1.98	sf
C11138-11.0-778	174.5613	-11.5758	0.6987	8.66	1.51 ± 0.44	2.48 ± 1.26	0.48	0.24	sf
C11138-11.0-673	174.5676	-11.5779	0.6286	9.40	3.60 ± 0.19	13.29 ± 0.97	1.17	1.20	q
C11138-11.1-1047	174.6884	-11.5869	0.5494	9.89	5.12 ± 0.29	86.30 ± 5.68	1.32	2.73	q
C11138-11.1-364	174.6985	-11.5631	0.4051	8.75	2.88 ± 0.71	8.52 ± 1.68	0.64	2.30	sf
C11138-11.1-411	174.7007	-11.5600	0.4531	9.00	0.60 ± 0.17	1.02 ± 0.26	0.80	0.98	sf
C11138-11.1-193	174.7030	-11.5770	0.6282	10.00	2.80 ± 0.54	10.60 ± 2.81	1.23	1.13	sf
C11138-11.1-273	174.7040	-11.5697	0.6198	9.89	1.45 ± 0.24	3.73 ± 0.84	1.42	1.91	sf
C11227-11.0-382	186.9590	-11.6475	0.5286	9.14	2.80 ± 0.26	5.66 ± 0.59	0.72	-0.22	q
C11227-11.0-402	186.9637	-11.6452	0.5272	8.97	2.59 ± 0.13	3.34 ± 0.18	0.69	0.56	sf
C11227-11.0-413	186.9706	-11.6444	0.4342	9.48	0.68 ± 0.21	8.67 ± 2.37	1.36	1.38	q
C11227-11.0-196	186.9710	-11.6092	0.5473	9.17	1.76 ± 0.24	2.39 ± 0.38	0.82	0.24	q
C11227-11.0-166	186.9742	-11.6632	0.5755	10.20	1.76 ± 0.18	31.52 ± 3.96	1.51	1.62	sf
C11227-11.1-138	186.9822	-11.6656	0.4939	10.54	2.00 ± 0.45	7.83 ± 1.79	1.71	1.18	sf
C11227-11.1-162	186.9869	-11.6119	0.5512	10.91	2.67 ± 0.32	13.67 ± 1.89	1.79	1.32	sf
C11227-11.1-322	186.9890	-11.6003	0.4108	8.85	1.51 ± 0.37	2.42 ± 0.48	0.73	0.84	sf
C11227-11.1-113	186.9907	-11.6159	0.5745	11.07	1.97 ± 0.59	36.02 ± 12.86	2.04	1.46	q
C11227-11.2-136	187.0564	-11.5315	0.5183	9.37	1.24 ± 0.25	1.58 ± 0.34	1.13	0.57	sf
C11227-11.2-362	187.0578	-11.5183	0.4995	9.12	0.27 ± 0.09	0.51 ± 0.17	0.89	-0.19	sf
C11227-11.2-035	187.0636	-11.5409	0.5963	9.62	3.47 ± 0.49	8.49 ± 1.56	0.89	0.81	sf
C11227-11.2-247	187.0677	-11.5249	0.5311	9.02	1.77 ± 0.19	2.30 ± 0.27	0.69	0.29	sf
C11227-11.2-152	187.0722	-11.5304	0.4723	8.63	1.73 ± 0.28	2.00 ± 0.31	0.62	0.32	sf
C11227-11.2-208	187.0804	-11.5276	0.5349	9.37	3.25 ± 0.52	4.28 ± 0.78	0.84	0.41	sf
C11227-11.2-259	187.0843	-11.5248	0.5124	11.17	4.07 ± 0.57	18.94 ± 2.79	2.05	1.23	sf
C11227-11.2-146	187.0855	-11.5309	0.4908	9.34	2.56 ± 0.54	3.09 ± 0.66	0.96	0.53	sf
C11227-11.2-204	187.0903	-11.5276	0.5165	10.72	2.73 ± 0.30	12.79 ± 1.50	1.81	1.31	sf
C11301-11.3-410	195.2339	-11.5075	0.5476	9.16	0.76 ± 0.16	1.29 ± 0.31	0.77	0.45	sf
C11301-11.3-311	195.2408	-11.5145	0.6833	9.07	2.95 ± 0.23	7.97 ± 1.03	0.25	0.70	sf
C11301-11.3-176	195.2446	-11.5234	0.5353	8.85	2.46 ± 0.20	0.63 ± 0.14	0.97	-0.31	sf
C11301-11.3-095	195.2452	-11.5302	0.4281	8.89	1.78 ± 0.39	1.82 ± 0.34	0.83	0.40	sf
C11301-11.3-091	195.2487	-11.5304	0.5213	8.89	1.33 ± 0.15	2.79 ± 0.35	0.53	0.80	sf
C11301-11.3-123	195.2489	-11.5279	0.5358	9.53	2.37 ± 0.42	5.16 ± 1.03	0.75	0.66	sf
C11301-11.3-470	195.2491	-11.5031	0.5178	10.15	4.30 ± 0.54	5.51 ± 0.74	0.89	0.41	sf
C11301-11.3-344	195.2549	-11.5127	0.5986	9.71	4.32 ± 0.35	10.65 ± 1.14	0.73	0.84	sf
C11301-11.1-176	195.3304	-11.5490	0.4339	9.06	0.39 ± 0.10	5.02 ± 0.47	0.29	-0.15	sf
C11301-11.1-242	195.3365	-11.5452	0.5238	9.07	2.54 ± 0.18	4.10 ± 0.32	0.50	0.63	sf
C11301-11.1-441	195.3429	-11.5251	0.5795	9.60	4.43 ± 0.13	10.52 ± 0.37	0.88	0.74	sf
C11301-11.0-044	195.3510	-11.5609	0.4224	8.87	1.98 ± 0.52	2.01 ± 0.44	0.69	0.28	sf
C11301-11.1-262	195.3524	-11.5436	0.5149	8.97	0.95 ± 0.09	1.19 ± 0.12	0.80	0.50	sf
C11301-11.1-356	195.3558	-11.5368	0.4510	7.94	2.26 ± 0.30	5.90 ± 0.71	-0.11	0.91	sf
C11301-11.2-605	195.3697	-11.6895	0.5304	11.23	2.14 ± 0.61	9.28 ± 2.87	2.13	1.23	q
C11301-11.2-641	195.3771	-11.6856	0.5177	9.95	3.77 ± 0.33	14.88 ± 1.40	1.48	1.35	sf
C11301-11.2-685	195.3878	-11.6797	0.4230	9.68	0.50 ± 0.16	0.77 ± 0.20	1.57	-0.39	sf
C11301-11.2-262	195.3880	-11.6186	0.5329	9.14	5.42 ± 0.22	11.05 ± 0.50	0.54	0.02	sf

Table A.3: Information for field galaxies. 1. Pointing ID - GRIZLI Object ID 2. Right Ascension 3. Declination 4. Redshift 5. Stellar Mass 6.  $H\alpha$  flux in cgs units 7. Star-formation rate. 8.  $U-V$  rest-frame color 9.  $V-J$  rest-frame color 10.  $UVJ$  classification based on Williams et al. (2009) where sf and q represent star-forming and quiescent, respectively.

Table A.4:  $S/N_{H\alpha} < 3$  Galaxies

ID	RA Deg.	Dec Deg.	$S/N_{H\alpha}$	Stellar Mass $\log_{10}(M_*/M_{\odot})$	$\log_{10}(\text{SFR}_{H\alpha})$ $M_{\odot}\text{yr}^{-1}$	Loc
1	2	3	4	5	6	7
23	195.38	-11.64	0.68	10.87	1.43	c
59	195.38	-11.64	1.32	9.99	1.01	c
60	195.39	-11.64	-1.29	9.41	0.81	c
67	195.37	-11.64	-1.18	8.84	0.22	f
85	195.26	-11.53	2.81	8.77	0.10	f
92	195.37	-11.63	-2.4	10.08	0.17	c
96	195.39	-11.63	2.63	9.75	0.86	f
99	195.39	-11.63	1.84	9.55	0.66	f
106	195.26	-11.53	-2.6	10.35	1.25	i
109	164.81	-12.91	2.83	9.94	0.19	c
120	174.68	-11.58	-0.6	9.49	0.43	f
143	195.38	-11.63	0.89	8.16	0.63	c
151	195.37	-11.63	1.09	8.81	1.32	f
157	174.69	-11.58	1.23	8.60	0.47	f
157	164.81	-12.91	1.56	10.83	0.68	c
159	195.37	-11.63	-0.47	9.21	0.86	c
162	174.72	-11.58	2.61	9.72	1.01	f
177	187.05	-11.53	2.87	8.94	0.38	f
193	195.37	-11.63	-0.2	8.55	0.73	c
197	195.23	-11.52	1.71	9.59	0.37	f
226	195.26	-11.52	0.82	10.79	0.54	i
231	195.38	-11.62	1.21	10.11	1.04	f
244	186.98	-11.61	-1.57	9.88	1.01	c
264	174.55	-11.59	2.21	9.98	0.45	f
265	195.38	-11.62	0.47	9.51	0.94	f
268	195.23	-11.52	2.65	9.27	0.25	i
272	164.78	-12.90	-2.26	10.43	0.46	c
278	195.23	-11.52	1.3	9.63	0.19	f
279	187.06	-11.52	-0.71	10.13	1.25	f
297	174.55	-11.59	2.33	9.21	-0.04	f
298	195.38	-11.62	1.45	8.97	0.68	c
305	186.98	-11.60	2.49	9.77	0.38	f
319	195.38	-11.71	-0.72	10.35	0.89	f
330	186.95	-11.65	2.68	8.78	0.17	f
348	174.57	-11.58	2.5	9.02	-0.09	c
364	164.79	-12.89	0.03	10.55	0.44	c
368	186.99	-11.60	2.46	10.20	-0.21	c
384	195.37	-11.61	0.94	9.12	0.53	c
396	186.98	-11.65	2.45	11.02	0.82	f
408	195.38	-11.61	-1.16	9.51	1.10	c
409	174.68	-11.56	2.05	9.32	0.61	f
411	174.56	-11.58	1.39	9.10	-0.32	f
411	187.06	-11.51	2.24	8.79	-0.01	f
418	195.22	-11.51	-1.94	10.19	0.31	f
419	186.97	-11.64	2.85	8.50	-0.52	f
429	174.55	-11.58	0.06	8.78	0.25	f
430	174.57	-11.58	-1.12	8.59	0.20	f
434	174.40	-11.41	1.51	10.48	0.82	i
435	164.77	-12.87	-1.56	9.31	0.09	c
446	195.25	-11.51	-0.83	9.57	-0.37	f
446	195.34	-11.52	1.1	9.07	-0.05	f
460	164.79	-12.88	0.683	10.32	0.32	c
482	186.99	-11.59	-0.08	10.39	0.56	c
486	195.37	-11.70	2.11	9.68	0.69	f
514	195.38	-11.70	-0.71	9.38	-0.22	f
519	186.97	-11.59	2.56	8.77	0.20	f
527	186.99	-11.59	-0.36	10.58	0.56	c
558	174.54	-11.58	2.86	8.56	0.17	f
587	195.37	-11.69	2.97	9.84	0.42	f
590	174.55	-11.58	1.93	10.51	0.41	f
603	195.38	-11.69	0.72	10.50	0.44	f
824	174.55	-11.57	1.92	8.24	0.31	f
851	174.57	-11.57	1.93	9.88	0.21	f
955	174.55	-11.57	2.83	10.30	0.30	c
990	174.55	-11.57	2.69	8.82	-0.18	c
1000	174.54	-11.57	2.83	8.85	0.09	f
1136	174.54	-11.57	1.18	9.33	0.14	f
1138	174.54	-11.57	-0.94	9.50	0.84	f
1231	174.54	-11.57	1.9	9.61	0.05	f
1291	174.55	-11.57	0.33	9.75	-0.27	f
1299	174.54	-11.57	-0.08	8.60	0.09	f
1308	174.55	-11.57	-0.16	8.74	-0.34	f
1404	174.54	-11.56	-0.43	10.17	0.17	f
1420	174.55	-11.56	1.9	9.60	0.36	f
1545	174.54	-11.56	1.92	10.62	0.48	c
1623	174.53	-11.56	2.06	10.79	0.63	c
1645	174.54	-11.56	-0.29	10.92	1.60	f
1650	174.54	-11.56	0.44	10.05	0.14	f
1754	174.54	-11.56	2.69	10.40	0.73	c
1779	174.54	-11.56	-1.12	9.71	0.46	f
1791	174.55	-11.56	2.32	7.66	-0.03	f
2084	174.56	-11.55	2.42	8.64	-0.06	f

Information for low S/N galaxies: 1. GRIZLI Object ID 2. Right Ascension in hours 3. Declination in hours 4. Signal-to-noise in  $H\alpha$  5. Stellar Mass 6.  $H\alpha$  star-formation rate 7. Location where c = core, i = infall, f = field

## Appendix B

### GRIZLI Prior Code

The following code can be used after GRIZLI has been completely run through with extractions. A file with the GRIZLI ID, redshift prior and any errors are required.

For use with an LDP redshift:

```
from grizli import multifit , utils , fitting
import numpy as np

f = open('filename.txt', 'r')
lines = f.readlines()[1:]
f.close()

id = []
z_i = []
for line in lines:
    a = line.split()
    id.append(int(a[0]))
    z_i.append(float(a[3]))

id = np.array(id)
z_i = np.array(z_i)
# With prior
```

```

z = np.arange(0,2,.001)
for id_i, z_ii in zip(id, z_i):
    sig = 0.007*(1+z_ii) # times (1+z)
    p_z = np.exp(-(z -
        z_ii)**2/(2*sig**2))/((2*np.pi)**0.5*sig)
    p_z /= np.trapz(p_z, z)
    p_z = np.maximum(p_z, 1.e-10)
    _res = fitting.run_all_parallel(id_i, prior=(z, p_z),
        zr=[0.05, 2], args_file='fit_args.npy', verbose=True,
        group_name=str(id_i) + 'LDP-', fitter=['nnls',
        'bounded'], get_output_data=True)

```

For use with asymmetric photometric redshift:

```

from grizli import multifit, utils, fitting
import numpy as np

f = open('filename.txt', 'r')
lines = f.readlines()[1:]
f.close()

id = []
z_i = []
z_u = []
z_d = []

for line in lines:
    a = line.split()
    id.append(int(a[0]))
    z_i.append(float(a[3]))
    z_u.append(float(a[4]))

```

```

z_d.append(float(a[5]))

id = np.array(id)
z_i = np.array(z_i)
z_u = np.array(z_u)
z_d = np.array(z_d)
# With prior
z = np.arange(0,2,.001)
for id_i, z_ii, z_ui, z_di in zip(id, z_i, z_u, z_d):
    sig = 0.5*(z_ui+z_di)*(1+z_ii) # times (1+z)
    p_z = np.exp(-(z -
        z_ii)**2/(2*sig**2))/((2*np.pi)**0.5*sig)
    p_z /= np.trapz(p_z, z)
    p_z = np.maximum(p_z, 1.e-10)
    _res = fitting.run_all_parallel(id_i, prior=(z,p_z),
        zr=[0.05,2], args_file='fit_args.npy', verbose=True,
        fitter=['nnls', 'bounded'], group_name=str(id_i)
        +'WFI-', get_output_data=True) #negative flux allowance

```

## Appendix C

### PyTorch CNN Code

```
\%matplotlib inline
\%config InlineBackend.figure_format = 'retina'

import os
import matplotlib.pyplot as plt

import torch
import numpy as np
from torch import nn
from torch import optim
import torch.nn.functional as F
from torchvision import datasets, transforms, models
from PIL import Image
from collections import OrderedDict
import json

os.getcwd()
!pwd
#list your directories and to each dataset
```

```

data_dir =
    '/Users/jennifercooper/Projects/thesis/23.3_mag/all/Extractions/
images/PyTorch_Morphology'
train_dir = data_dir + '/train'
valid_dir = data_dir + '/validate'
test_dir = data_dir + '/test'
#if running on gpu, uncomment. Otherwise, this will be run on
    cpu.
#using_gpu = torch.cuda.is_available()

#Define your transforms for the training, validation, and
    testing sets
#rotations, crop to specified length of side of square
train_transforms =
    transforms.Compose([transforms.RandomRotation(30),
                        transforms.RandomResizedCrop(224),
                        transforms.RandomHorizontalFlip(),
                        transforms.ToTensor(),
                        transforms.Normalize([0.485, 0.456, 0.406],
                                             [0.229, 0.224, 0.225])])
testval_transforms = transforms.Compose([transforms.Resize(256),
                                         transforms.CenterCrop(224),
                                         transforms.ToTensor(),
                                         transforms.Normalize([0.485, 0.456, 0.406],
                                                                [0.229, 0.224,
                                                                0.225])])

```

```

# Load the datasets with ImageFolder
image_trainset = datasets.ImageFolder(train_dir ,
    transform=train_transforms)
image_testset = datasets.ImageFolder(test_dir ,
    transform=testval_transforms)
image_valset = datasets.ImageFolder(valid_dir ,
    transform=testval_transforms)

#Using the image datasets and the trainforms , define the
    dataloaders.a higher
#           batch size processes faster but requires more memory.
    With 8GB, 16 would be
#           more manageable so that the computer can still be
    used while it's training
image_trainloader = torch.utils.data.DataLoader(image_trainset ,
    batch_size=16, shuffle=True)
image_testloader = torch.utils.data.DataLoader(image_testset ,
    batch_size=16, shuffle=True)
image_valloader = torch.utils.data.DataLoader(image_valset ,
    batch_size=16, shuffle=True)

#this file lists the classes and their folder location
with open('/Users/jennifercooper/Projects/thesis/23.3_mag/
    _____all/Extractions/images
/PyTorch_Morphology/grism_classifier.json', 'r') as f:
    cat_to_name = json.load(f)

```

```

#Build and train your network
epochs = 20 #how many cycles to train on
lr = 0.001 #learning rate, this is the default value in a class
print_every = 10

# Freeze parameters so we don't backprop through them
hidden_layers = [10, 10] #private to the NN; higher numbers can
    solve more complex problems but require more time to produce
    the output, doesn't have to be this high
def make_model(structure , hidden_layers , lr):
    if structure=="densenet161": #this is for another model
        model = models.densenet161(pretrained=True)
        input_size = 2208
    else:
        model = models.vgg16(pretrained=True) #current model
        input_size = 25088
    output_size = 4 #number of classes
    for param in model.parameters():
        param.requires_grad = False

    classifier = nn.Sequential(OrderedDict([
        ('dropout', nn.Dropout(0.5)),
        ('fc1', nn.Linear(input_size ,
            hidden_layers[0])),
        ('relu1', nn.ReLU()),
        ('fc2',
            nn.Linear(hidden_layers[0],

```

```

        hidden_layers[1])),
    ('relu2', nn.ReLU()),
    ('fc3',
     nn.Linear(hidden_layers[1],
                output_size)),
    ('output', nn.LogSoftmax(dim=1))
]))

```

```

model.classifier = classifier
return model

```

```

model = make_model('vgg16', hidden_layers, lr)
criterion = nn.NLLLoss()
optimizer = optim.Adam(model.classifier.parameters(), lr=lr)

```

```

def cal_accuracy(model, dataloader):
    validation_loss = 0
    accuracy = 0
    for i, (inputs, labels) in enumerate(dataloader):
        optimizer.zero_grad()
        inputs, labels = inputs.to('cpu'),
            labels.to('cpu')
        model.to('cpu')
        with torch.no_grad():
            outputs = model.forward(inputs)
            validation_loss = criterion(outputs, labels)
            ps = torch.exp(outputs).data

```

```

        equality = (labels.data == ps.max(1)[1])
        accuracy +=
            equality.type_as(torch.FloatTensor()).mean()

validation_loss = validation_loss / len(dataloader)
accuracy = accuracy / len(dataloader)

return validation_loss, accuracy

#this will start training the network; grism classifier took
approximately 2 hours to run this cell
def my_DLM(model, image_trainloader, image_valloader, epochs,
print_every, criterion, optimizer, device='cpu'):
    epochs = epochs
    print_every = print_every
    steps = 0
    model.to('cpu')

    for e in range(epochs):
        running_loss = 0
        for ii, (inputs, labels) in enumerate(image_trainloader):
            steps += 1

            inputs, labels = inputs.to('cpu'), labels.to('cpu')

            optimizer.zero_grad()

```

```

# Forward and backward passes
outputs = model.forward(inputs)
loss = criterion(outputs, labels)
loss.backward()
optimizer.step()

running_loss += loss.item()

if steps % print_every == 0:
    model.eval()
    val_loss, train_ac = cal_accuracy(model,
                                     image_valloader)
    print("Epoch: {} / {} ...".format(e+1, epochs),
          "Loss: {:.4f}".format(running_loss / print_every),
          "Validation Loss: {:.4f}".format(val_loss),
          "Accuracy: {:.4f}".format(train_ac))

    running_loss = 0
my_DLM(model, image_trainloader, image_valloader, epochs,
        print_every, criterion, optimizer, 'cpu')

```

## References

- Abadi, M. G., Moore, B., & Bower, R. G. (1999). Ram pressure stripping of spiral galaxies in clusters. , 308(4), 947–954.
- Abolfathi, B., Aguado, D. S., Aguilar, G., Allende Prieto, C., Almeida, A., Ananna, T. T., Anders, F., Anderson, S. F., Andrews, B. H., Anguiano, B., Aragón-Salamanca, A., Argudo-Fernández, M., Armengaud, E., Ata, M., Aubourg, E., Avila-Reese, V., Badenes, C., Bailey, S., Balland, C., Barger, K. A., Barrera-Ballesteros, J., Bartosz, C., Bastien, F., Bates, D., Baumgarten, F., Bautista, J., Beaton, R., Beers, T. C., Belfiore, F., Bender, C. F., Bernardi, M., Bershad, M. A., Beutler, F., Bird, J. C., Bizyaev, D., Blanc, G. A., Blanton, M. R., Blomqvist, M., Bolton, A. S., Boquien, M., Borissova, J., Bovy, J., Bradna Diaz, C. A., Brandt, W. N., Brinkmann, J., Brownstein, J. R., Bundy, K., Burgasser, A. J., Burtin, E., Busca, N. G., Cañas, C. I., Cano-Díaz, M., Cappellari, M., Carrera, R., Casey, A. R., Cervantes Sodi, B., Chen, Y., Cherinka, B., Chiappini, C., Choi, P. D., Chojnowski, D., Chuang, C.-H., Chung, H., Clerc, N., Cohen, R. E., Comerford, J. M., Comparat, J., Correa do Nascimento, J., da Costa, L., Cousinou, M.-C., Covey, K., Crane, J. D., Cruz-Gonzalez, I., Cunha, K., da Silva Ilha, G., Damke, G. J., Darling, J., Davidson, James W., J., Dawson, K., de Icaza Lizaola, M. A. C., de la Macorra, A., de la Torre, S., De Lee, N., de Sainte Agathe, V., Deconto Machado, A., Dell’Agli, F., Delubac, T., Diamond-Stanic, A. M., Donor, J., Downes, J. J., Drory, N., du Mas des Bourboux, H., Duckworth, C. J., Dwelly, T., Dyer, J., Ebelke, G., Davis Eigenbrot, A., Eisenstein, D. J., Elsworth, Y. P., Emsellem, E., Eracleous, M., Erfanianfar, G., Escoffier, S., Fan, X., Fernández Alvar, E., Fernandez-Trincado, J. G., Fernando Cirolini, R., Feuillet, D., Finoguenov, A., Fleming, S. W., Font-Ribera, A., Freischlad, G., Frinchaboy, P., Fu, H., Gómez Maqueo Chew, Y., Galbany, L., García Pérez, A. E., Garcia-Dias, R., García-Hernández, D. A., Garma Oehmichen, L. A., Gaulme, P., Gelfand, J., Gil-Marín, H., Gillespie, B. A., Goddard, D., González Hernández, J. I.,

Gonzalez-Perez, V., Grabowski, K., Green, P. J., Grier, C. J., Gueguen, A., Guo, H., Guy, J., Hagen, A., Hall, P., Harding, P., Hasselquist, S., Hawley, S., Hayes, C. R., Hearty, F., Hekker, S., Hernandez, J., Hernandez Toledo, H., Hogg, D. W., Holley-Bockelmann, K., Holtzman, J. A., Hou, J., Hsieh, B.-C., Hunt, J. A. S., Hutchinson, T. A., Hwang, H. S., Jimenez Angel, C. E., Johnson, J. A., Jones, A., Jönsson, H., Jullo, E., Khan, F. S., Kinemuchi, K., Kirkby, D., Kirkpatrick, Charles C., I., Kitaura, F.-S., Knapp, G. R., Kneib, J.-P., Kollmeier, J. A., Lacerna, I., Lane, R. R., Lang, D., Law, D. R., Le Goff, J.-M., Lee, Y.-B., Li, H., Li, C., Lian, J., Liang, Y., Lima, M., Lin, L., Long, D., Lucatello, S., Lundgren, B., Mackereth, J. T., MacLeod, C. L., Mahadevan, S., Maia, M. A. G., Majewski, S., Manchado, A., Maraston, C., Mariappan, V., Marques-Chaves, R., Masseron, T., Masters, K. L., McDermid, R. M., McGreer, I. D., Melen-  
dez, M., Meneses-Goytia, S., Merloni, A., Merrifield, M. R., Meszaros, S., Meza, A., Minchev, I., Minniti, D., Mueller, E.-M., Muller-Sanchez, F., Muna, D., Muñoz, R. R., Myers, A. D., Nair, P., Nandra, K., Ness, M., Newman, J. A., Nichol, R. C., Nidever, D. L., Nitschelm, C., Noterdaeme, P., O'Connell, J., Oelkers, R. J., Oravetz, A., Oravetz, D., Ortíz, E. A., Osorio, Y., Pace, Z., Padilla, N., Palanque-Delabrouille, N., Palicio, P. A., Pan, H.-A., Pan, K., Parikh, T., Pâris, I., Park, C., Peirani, S., Pellejero-Ibanez, M., Penny, S., Percival, W. J., Perez-Fournon, I., Petitjean, P., Pieri, M. M., Pinsonneault, M., Pisani, A., Prada, F., Prakash, A., Queiroz, A. B. d. A., Raddick, M. J., Raichoor, A., Barboza Rembold, S., Richstein, H., Riffel, R. A., Riffel, R., Rix, H.-W., Robin, A. C., Rodríguez Torres, S., Román-Zúñiga, C., Ross, A. J., Rossi, G., Ruan, J., Ruggeri, R., Ruiz, J., Salvato, M., Sánchez, A. G., Sánchez, S. F., Sanchez Almeida, J., Sánchez-Gallego, J. R., Santana Rojas, F. A., Santiago, B. X., Schiavon, R. P., Schimoia, J. S., Schlafly, E., Schlegel, D., Schneider, D. P., Schuster, W. J., Schwobe, A., Seo, H.-J., Serenelli, A., Shen, S., Shen, Y., Shetrone, M., Shull, M., Silva Aguirre, V., Simon, J. D., Skrutskie, M., Slosar, A., Smethurst, R., Smith, V., Sobek, J., Somers, G., Souter, B. J., Souto, D., Spindler, A., Stark, D. V., Stassun, K., Steinmetz, M., Stello, D., Storchi-Bergmann, T., Streblyanska, A., Stringfellow, G. S., Suárez, G., Sun, J., Szigeti, L., Taghizadeh-Popp, M., Talbot, M. S., Tang, B., Tao, C., Tayar, J., Tembe, M., Teske, J., Thakar, A. R., Thomas, D., Tissera, P., Tojeiro,

- R., Tremonti, C., Troup, N. W., Urry, M., Valenzuela, O., van den Bosch, R., Vargas-González, J., Vargas-Magaña, M., Vazquez, J. A., Villanova, S., Vogt, N., Wake, D., Wang, Y., Weaver, B. A., Weijmans, A.-M., Weinberg, D. H., Westfall, K. B., Whelan, D. G., Wilcots, E., Wild, V., Williams, R. A., Wilson, J., Wood-Vasey, W. M., Wylezalek, D., Xiao, T., Yan, R., Yang, M., Ybarra, J. E., Yèche, C., Zakamska, N., Zamora, O., Zarrouk, P., Zasowski, G., Zhang, K., Zhao, C., Zhao, G.-B., Zheng, Z., Zheng, Z., Zhou, Z.-M., Zhu, G., Zinn, J. C., & Zou, H. (2018). The Fourteenth Data Release of the Sloan Digital Sky Survey: First Spectroscopic Data from the Extended Baryon Oscillation Spectroscopic Survey and from the Second Phase of the Apache Point Observatory Galactic Evolution Experiment. , 235(2), 42.
- Abraham, R. G., Valdes, F., Yee, H. K. C., & van den Bergh, S. (1994). The Morphologies of Distant Galaxies. I. an Automated Classification System. , 432, 75.
- Abramson, L. E., Newman, A. B., Treu, T., Huang, K. H., Morishita, T., Wang, X., Hoag, A., Schmidt, K. B., Mason, C. A., Bradač, M., Brammer, G. B., Dressler, A., Poggianti, B. M., Trenti, M., & Vulcani, B. (2018). The Grism Lens-amplified Survey from Space (GLASS). XII. Spatially Resolved Galaxy Star Formation Histories and True Evolutionary Paths at  $z > 1$ . , 156(1), 29.
- Alpaslan, M., Driver, S., Robotham, A. S. G., Obreschkow, D., Andrae, E., Cluver, M., Kelvin, L. S., Lange, R., Owers, M., Taylor, E. N., Andrews, S. K., Bamford, S., Bland-Hawthorn, J., Brough, S., Brown, M. J. I., Colless, M., Davies, L. J. M., Eardley, E., Grootes, M. W., Hopkins, A. M., Kennedy, R., Liske, J., Lara-López, M. A., López-Sánchez, Á. R., Loveday, J., Madore, B. F., Mahajan, S., Meyer, M., Moffett, A., Norberg, P., Penny, S., Pimbblet, K. A., Popescu, C. C., Seibert, M., & Tuffs, R. (2015). Galaxy And Mass Assembly (GAMA): trends in galaxy colours, morphology, and stellar populations with large-scale structure, group, and pair environments. , 451(3), 3249–3268.
- Atek, H., Malkan, M., McCarthy, P., Teplitz, H. I., Scarlata, C., Siana, B., Henry, A., Colbert, J. W., Ross, N. R., Bridge, C., Bunker, A. J., Dressler, A., Fosbury, R. A. E., Martin, C., & Shim, H.

- (2010). The WFC3 Infrared Spectroscopic Parallel (WISP) Survey. , 723(1), 104–115.
- Baade, D., Meisenheimer, K., Iwert, O., Alonso, J., Augusteijn, T., Beletic, J., Bellemann, H., Benesch, W., Böhm, A., Böhnhardt, H., Brewer, J., Deiries, S., Delabre, B., Donaldson, R., Dupuy, C., Franke, P., Gerdes, R., Gilliotte, A., Grimm, B., Haddad, N., Hess, G., Ihle, G., Klein, R., Lenzen, R., Lizon, J. L., Mancini, D., Münch, N., Pizarro, A., Prado, P., Rahmer, G., Reyes, J., Richardson, F., Robledo, E., Sanchez, F., Silber, A., Sinclaire, P., Wackermann, R., & Zaggia, S. (1999). The Wide Field Imager at the 2.2-m MPG/ESO telescope: first views with a 67-million-facette eye. *The Messenger*, 95, 15–16.
- Baldry, I. K., Glazebrook, K., Brinkmann, J., Ivezić, , Lupton, R. H., Nichol, R. C., & Szalay, A. S. (2004). Quantifying the bimodal color-magnitude distribution of galaxies. *The Astrophysical Journal*, 600(2), 681–694.
- Ball, N. M., Loveday, J., Fukugita, M., Nakamura, O., Okamura, S., Brinkmann, J., & Brunner, R. J. (2004). Galaxy types in the Sloan Digital Sky Survey using supervised artificial neural networks. , 348(3), 1038–1046.
- Balogh, M. L., McGee, S. L., Mok, A., Muzzin, A., van der Burg, R. F. J., Bower, R. G., Finoguenov, A., Hoekstra, H., Lidman, C., Mulchaey, J. S., Noble, A., Parker, L. C., Tanaka, M., Wilman, D. J., Webb, T., Wilson, G., & Yee, H. K. C. (2016). Evidence for a change in the dominant satellite galaxy quenching mechanism at  $z = 1$ . , 456(4), 4364–4376.
- Balogh, M. L., Morris, S. L., Yee, H. K. C., Carlberg, R. G., & Ellingson, E. (1997). Star Formation in Cluster Galaxies at  $0.2 < Z < 0.55$ . , 488(2), L75–L78.
- Balogh, M. L., Morris, S. L., Yee, H. K. C., Carlberg, R. G., & Ellingson, E. (1999). Differential Galaxy Evolution in Cluster and Field Galaxies at  $z \sim 0.3$ . , 527(1), 54–79.
- Barchi, P. H., de Carvalho, R. R., Rosa, R. R., Sautter, R. A., Soares-Santos, M., Marques, B. A. D., Clua, E., Gonçalves, T. S., de Sá-Freitas, C., & Moura, T. C. (2020). Machine and Deep Learning applied to galaxy morphology - A comparative study. *Astronomy and Computing*, 30, 100334.

- Barsanti, S., Owers, M. S., Brough, S., Davies, L. J. M., Driver, S. P., Gunawardhana, M. L. P., Holwerda, B. W., Liske, J., Loveday, J., Pimbblet, K. A., Robotham, A. S. G., & Taylor, E. N. (2018). Galaxy and Mass Assembly (GAMA): Impact of the Group Environment on Galaxy Star Formation. , 857(1), 71.
- Bauer, A. E., Grützbauch, R., Jørgensen, I., Varela, J., & Bergmann, M. (2011). Star formation in the XMMU J2235.3-2557 galaxy cluster at  $z= 1.39$ . , 411(3), 2009–2018.
- Bayliss, M. B., Ashby, M. L. N., Ruel, J., Brodwin, M., Aird, K. A., Bautz, M. W., Benson, B. A., Bleem, L. E., Bocquet, S., Carlstrom, J. E., Chang, C. L., Cho, H. M., Clocchiatti, A., Crawford, T. M., Crites, A. T., Desai, S., Dobbs, M. A., Dudley, J. P., Foley, R. J., Forman, W. R., George, E. M., Gettings, D., Gladders, M. D., Gonzalez, A. H., de Haan, T., Halverson, N. W., High, F. W., Holder, G. P., Holzappel, W. L., Hoover, S., Hrubes, J. D., Jones, C., Joy, M., Keisler, R., Knox, L., Lee, A. T., Leitch, E. M., Liu, J., Lueker, M., Luong-Van, D., Mantz, A., Marrone, D. P., Mawatari, K., McDonald, M., McMahon, J. J., Mehl, J., Meyer, S. S., Miller, E. D., Mocanu, L., Mohr, J. J., Montroy, T. E., Murray, S. S., Padin, S., Plagge, T., Pryke, C., Reichardt, C. L., Rest, A., Ruhl, J. E., Saliwanchik, B. R., Saro, A., Sayre, J. T., Schaffer, K. K., Shirokoff, E., Song, J., Stalder, B., Šuhada, R., Spieler, H. G., Stanford, S. A., Staniszewski, Z., Stark, A. A., Story, K., Stubbs, C. W., van Engelen, A., Vanderlinde, K., Vieira, J. D., Vikhlinin, A., Williamson, R., Zahn, O., & Zenteno, A. (2014). SPT-CL J2040-4451: An SZ-selected Galaxy Cluster at  $z = 1.478$  with Significant Ongoing Star Formation. , 794(1), 12.
- Bekki, K. (2009). Ram-pressure stripping of halo gas in disc galaxies: implications for galactic star formation in different environments. , 399(4), 2221–2230.
- Bekki, K., Couch, W. J., & Shioya, Y. (2002). Passive Spiral Formation from Halo Gas Starvation: Gradual Transformation into S0s. , 577(2), 651–657.
- Belfiore, F., Maiolino, R., Maraston, C., Emsellem, E., Bershady, M. A., Masters, K. L., Yan, R., Bizyaev, D., Boquien, M., Brownstein, J. R., Bundy, K., Drory, N., Heckman, T. M., Law,

- D. R., Roman-Lopes, A., Pan, K., Stanghellini, L., Thomas, D., Weijmans, A.-M., & Westfall, K. B. (2016). SDSS IV MaNGA - spatially resolved diagnostic diagrams: a proof that many galaxies are LIERs. , 461(3), 3111–3134.
- Bell, E. F., McIntosh, D. H., Katz, N., & Weinberg, M. D. (2003). The Optical and Near-Infrared Properties of Galaxies. I. Luminosity and Stellar Mass Functions. , 149(2), 289–312.
- Bell, E. F., Wolf, C., Meisenheimer, K., Rix, H.-W., Borch, A., Dye, S., Kleinheinrich, M., Wisotzki, L., & McIntosh, D. H. (2004). Nearly 5000 Distant Early-Type Galaxies in COMBO-17: A Red Sequence and Its Evolution since  $z \sim 1$ . , 608(2), 752–767.
- Belli, S., Newman, A. B., & Ellis, R. S. (2019). MOSFIRE Spectroscopy of Quiescent Galaxies at  $1.5 < z < 2.5$ . II. Star Formation Histories and Galaxy Quenching. , 874(1), 17.
- Bertin, E. & Arnouts, S. (1996). SExtractor: Software for source extraction. , 117, 393–404.
- Bigelow, B. C., Dressler, A. M., Shectman, S. A., & Epps, H. W. (1998). IMACS: the multiobject spectrograph and imager for the Magellan I telescope. In S. D’Odorico (Ed.), *Optical Astronomical Instrumentation*, volume 3355 of *Society of Photo-Optical Instrumentation Engineers (SPIE) Conference Series* (pp. 225–231).
- Biswas, R., Blackburn, L., Cao, J., Essick, R., Hodge, K. A., Katsavounidis, E., Kim, K., Kim, Y.-M., Le Bigot, E.-O., Lee, C.-H., Oh, J. J., Oh, S. H., Son, E. J., Tao, Y., Vaulin, R., & Wang, X. (2013). Application of machine learning algorithms to the study of noise artifacts in gravitational-wave data. , 88(6), 062003.
- Blanton, M. R., Hogg, D. W., Bahcall, N. A., Baldry, I. K., Brinkmann, J., Csabai, I., Eisenstein, D., Fukugita, M., Gunn, J. E., Ivezić, Ž., Lamb, D. Q., Lupton, R. H., Loveday, J., Munn, J. A., Nichol, R. C., Okamura, S., Schlegel, D. J., Shimasaku, K., Strauss, M. A., Vogeley, M. S., & Weinberg, D. H. (2003). The Broadband Optical Properties of Galaxies with Redshifts  $0.02 < z < 0.22$ . , 594(1), 186–207.

- Boselli, A., Cortese, L., Boquien, M., Boissier, S., Catinella, B., Gavazzi, G., Lagos, C., & Sain-  
tonge, A. (2014). Cold gas properties of the Herschel Reference Survey. III. Molecular gas  
stripping in cluster galaxies. , 564, A67.
- Boselli, A., Cuillandre, J. C., Fossati, M., Boissier, S., Bomans, D., Consolandi, G., Anselmi, G.,  
Cortese, L., Côté, P., Durrell, P., Ferrarese, L., Fumagalli, M., Gavazzi, G., Gwyn, S., Hensler,  
G., Sun, M., & Toloba, E. (2016). Spectacular tails of ionized gas in the Virgo cluster galaxy  
NGC 4569. , 587, A68.
- Boselli, A. & Gavazzi, G. (2006). Environmental Effects on Late-Type Galaxies in Nearby Clus-  
ters. , 118(842), 517–559.
- Bouché, N., Dekel, A., Genzel, R., Genel, S., Cresci, G., Förster Schreiber, N. M., Shapiro, K. L.,  
Davies, R. I., & Tacconi, L. (2010). The Impact of Cold Gas Accretion Above a Mass Floor on  
Galaxy Scaling Relations. , 718(2), 1001–1018.
- Brammer, G., Lundgren, B. F., Marchesini, D., Momcheva, I. G., Pirzkal, N., Ryan, R. E., Vang,  
A., & Wake, D. A. (2016). Grizli: The Grism redshift & Line Database for HST WFC3/IR  
Spectroscopy. HST Proposal.
- Brammer, G. B., van Dokkum, P. G., & Coppi, P. (2008). EAZY: A Fast, Public Photometric  
Redshift Code. , 686(2), 1503–1513.
- Brinchmann, J., Charlot, S., White, S. D. M., Tremonti, C., Kauffmann, G., Heckman, T., &  
Brinkmann, J. (2004a). The physical properties of star-forming galaxies in the low-redshift  
Universe. , 351(4), 1151–1179.
- Brinchmann, J., Charlot, S., White, S. D. M., Tremonti, C., Kauffmann, G., Heckman, T., &  
Brinkmann, J. (2004b). The physical properties of star-forming galaxies in the low-redshift  
Universe. , 351(4), 1151–1179.

- Brodwin, M., Stanford, S. A., Gonzalez, A. H., Zeimann, G. R., Snyder, G. F., Mancone, C. L., Pope, A., Eisenhardt, P. R., Stern, D., Alberts, S., Ashby, M. L. N., Brown, M. J. I., Chary, R. R., Dey, A., Galametz, A., Gettings, D. P., Jannuzi, B. T., Miller, E. D., Moustakas, J., & Moustakas, L. A. (2013). The Era of Star Formation in Galaxy Clusters. , 779(2), 138.
- Bundy, K., Scarlata, C., Carollo, C. M., Ellis, R. S., Drory, N., Hopkins, P., Salvato, M., Leauthaud, A., Koekemoer, A. M., Murray, N., Ilbert, O., Oesch, P., Ma, C.-P., Capak, P., Pozzetti, L., & Scoville, N. (2010). The Rise and Fall of Passive Disk Galaxies: Morphological Evolution Along the Red Sequence Revealed by COSMOS. , 719(2), 1969–1983.
- Butcher, H. & Oemler, A., J. (1978). The evolution of galaxies in clusters. I. ISIT photometry of Cl 0024+1654 and 3C 295. , 219, 18–30.
- Byrd, G. & Valtonen, M. (1990). Tidal Generation of Active Spirals and S0 Galaxies by Rich Clusters. , 350, 89.
- Calzetti, D., Armus, L., Bohlin, R. C., Kinney, A. L., Koornneef, J., & Storchi-Bergmann, T. (2000). The Dust Content and Opacity of Actively Star-forming Galaxies. , 533(2), 682–695.
- Cantale, N., Jablonka, P., Courbin, F., Rudnick, G., Zaritsky, D., Meylan, G., Desai, V., De Lucia, G., Aragón-Salamanca, A., Poggianti, B. M., Finn, R., & Simard, L. (2016a). Disc colours in field and cluster spiral galaxies at  $0.5 < z < 0.8$ . , 589, A82.
- Cantale, N., Jablonka, P., Courbin, F., Rudnick, G., Zaritsky, D., Meylan, G., Desai, V., De Lucia, G., Aragón-Salamanca, A., Poggianti, B. M., Finn, R., & Simard, L. (2016b). Disc colours in field and cluster spiral galaxies at  $0.5 < z < 0.8$ . , 589, A82.
- Carleton, T., Guo, Y., Nayyeri, H., Cooper, M., Rudnick, G., & Whitaker, K. (2020). Evidence for non-smooth quenching in massive galaxies at  $z \sim 1$ . , 491(2), 2822–2833.
- Carnall, A. C., Walker, S., McLure, R. J., Dunlop, J. S., McLeod, D. J., Cullen, F., Wild, V., Amorin, R., Bolzonella, M., Castellano, M., Cimatti, A., Cucciati, O., Fontana, A., Gargiulo,

- A., Garilli, B., Jarvis, M. J., Pentericci, L., Pozzetti, L., Zamorani, G., Calabro, A., Hathi, N. P., & Koekemoer, A. M. (2020). Timing the earliest quenching events with a robust sample of massive quiescent galaxies at  $2 < z < 5$ . , 496(1), 695–707.
- Cassata, P., Guzzo, L., Franceschini, A., Scoville, N., Capak, P., Ellis, R. S., Koekemoer, A., McCracken, H. J., Mobasher, B., Renzini, A., Ricciardelli, E., Scodreggio, M., Taniguchi, Y., & Thompson, D. (2007). The Cosmic Evolution Survey (COSMOS): The Morphological Content and Environmental Dependence of the Galaxy Color-Magnitude Relation at  $z \sim 0.7$ . , 172(1), 270–283.
- Cayatte, V., van Gorkom, J. H., Balkowski, C., & Kotanyi, C. (1990). VLA Observations of Neutral Hydrogen in Virgo Cluster Galaxies. I. The Atlas. , 100, 604.
- Chabrier, G. (2003). Galactic Stellar and Substellar Initial Mass Function. , 115(809), 763–795.
- Cireşan, D., Meier, U., & Schmidhuber, J. (2012). Multi-column Deep Neural Networks for Image Classification. *arXiv e-prints*, (pp. arXiv:1202.2745).
- Clarke, A. O., Scaife, A. M. M., Greenhalgh, R., & Griguta, V. (2020). Identifying galaxies, quasars, and stars with machine learning: A new catalogue of classifications for 111 million SDSS sources without spectra. , 639, A84.
- Clowe, D., Schneider, P., Aragón-Salamanca, A., Bremer, M., De Lucia, G., Halliday, C., Jablonka, P., Milvang-Jensen, B., Pelló, R., Poggianti, B., Rudnick, G., Saglia, R., Simard, L., White, S., & Zaritsky, D. (2006). Weak lensing mass reconstructions of the ESO Distant Cluster Survey. , 451(2), 395–408.
- Conselice, C. J. (2003). The Relationship between Stellar Light Distributions of Galaxies and Their Formation Histories. , 147(1), 1–28.
- Conselice, C. J. (2014). The Evolution of Galaxy Structure Over Cosmic Time. , 52, 291–337.

- Couch, W. J., Ellis, R. S., Godwin, J., & Carter, D. (1983). Spectral energy distributions for galaxies in high redshift clusters. I. Methods and application to three clusters with  $0.22 \leq z \leq 0.31$ . , 205, 1287–1312.
- Couch, W. J. & Sharples, R. M. (1987). A spectroscopic study of three rich galaxy clusters at  $z=0.31$ . , 229, 423–456.
- Cousins, A. W. J. (1976). VRI standards in the E regions. , 81, 25.
- Cox, T. J., Dutta, S. N., Hopkins, P. F., & Hernquist, L. (2008). Galaxy Mergers: Driving Galaxy Formation. In T. Kodama, T. Yamada, & K. Aoki (Eds.), *Panoramic Views of Galaxy Formation and Evolution*, volume 399 of *Astronomical Society of the Pacific Conference Series* (pp. 284).
- Crowl, H. H. & Kenney, J. D. P. (2008). The Stellar Populations of Stripped Spiral Galaxies in the Virgo Cluster. , 136(4), 1623–1644.
- da Cunha, E., Charlot, S., & Elbaz, D. (2008). A simple model to interpret the ultraviolet, optical and infrared emission from galaxies. , 388(4), 1595–1617.
- Daddi, E., Dickinson, M., Morrison, G., Chary, R., Cimatti, A., Elbaz, D., Frayer, D., Renzini, A., Pope, A., Alexander, D. M., Bauer, F. E., Giavalisco, M., Huynh, M., Kurk, J., & Mignoli, M. (2007). Multiwavelength Study of Massive Galaxies at  $z \sim 2$ . I. Star Formation and Galaxy Growth. , 670(1), 156–172.
- Davies, L. J. M., Robotham, A. S. G., Lagos, C. d. P., Driver, S. P., Stevens, A. R. H., Bahé, Y. M., Alpaslan, M., Bremer, M. N., Brown, M. J. I., Brough, S., Bland-Hawthorn, J., Cortese, L., Elahi, P., Grootes, M. W., Holwerda, B. W., Ludlow, A. D., McGee, S., Owers, M., & Phillipps, S. (2019). Galaxy and Mass Assembly (GAMA): environmental quenching of centrals and satellites in groups. , 483(4), 5444–5458.
- de Diego, José A., Nadolny, Jakub, Bongiovanni, Ángel, Cepa, Jordi, Pović, Mirjana, Pérez García, Ana María, Padilla Torres, Carmen P., Lara-López, Maritza A., Cerviño, Miguel, Martínez,

- Ricardo Pérez, Alfaro, Emilio J., Castañeda, Héctor O., Fernández-Lorenzo, Miriam, Gallego, Jesús, González, J. Jesús, González-Serrano, J. Ignacio, Pintos-Castro, Irene, Sánchez-Portal, Miguel, Cedrés, Bernabé, González-Otero, Mauro, Heath Jones, D., & Bland-Hawthorn, Joss (2020). Galaxy classification: deep learning on the otelo and cosmos databases. *A&A*, 638, A134.
- De Lucia, G., Poggianti, B. M., Aragón-Salamanca, A., Clowe, D., Halliday, C., Jablonka, P., Milvang-Jensen, B., Pelló, R., Poirier, S., Rudnick, G., Saglia, R., Simard, L., & White, S. D. M. (2004). The Buildup of the Red Sequence in Galaxy Clusters since  $z \sim 0.8$ . , 610(2), L77–L80.
- De Lucia, G., Weinmann, S., Poggianti, B. M., Aragón-Salamanca, A., & Zaritsky, D. (2012). The environmental history of group and cluster galaxies in a  $\Lambda$  cold dark matter universe. , 423(2), 1277–1292.
- Dekel, A. & Silk, J. (1986). The Origin of Dwarf Galaxies, Cold Dark Matter, and Biased Galaxy Formation. , 303, 39.
- Desai, V., Dalcanton, J. J., Aragón-Salamanca, A., Jablonka, P., Poggianti, B., Gogarten, S. M., Simard, L., Milvang-Jensen, B., Rudnick, G., Zaritsky, D., Clowe, D., Halliday, C., Pelló, R., Saglia, R., & White, S. (2007). The Morphological Content of 10 EDisCS Clusters at  $0.5 < z < 0.8$ . , 660(2), 1151–1164.
- Diaz, J. D., Bekki, K., Forbes, D. A., Couch, W. J., Drinkwater, M. J., & Deeley, S. (2019). Classifying the formation processes of S0 galaxies using Convolutional Neural Networks. , 486(4), 4845–4862.
- Dickey, C. M., van Dokkum, P. G., Oesch, P. A., Whitaker, K. E., Momcheva, I. G., Nelson, E. J., Leja, J., Brammer, G. B., Franx, M., & Skelton, R. E. (2016). The Relation between  $[\text{O III}]/\text{H}\beta$  and Specific Star Formation Rate in Galaxies at  $z \sim 2$ . , 828(1), L11.
- Dieleman, S., Willett, K. W., & Dambre, J. (2015). Rotation-invariant convolutional neural networks for galaxy morphology prediction. , 450(2), 1441–1459.

- Domínguez Sánchez, H., Bongiovanni, A., Lara-López, M. A., Oteo, I., Cepa, J., Pérez García, A. M., Sánchez-Portal, M., Ederoclite, A., Lutz, D., Cresci, G., Delvecchio, I., Berta, S., Mag-nelli, B., Popesso, P., Pozzi, F., & Riguccini, L. (2014). Herschel far-IR counterparts of SDSS galaxies: analysis of commonly used star formation rate estimates. , 441(1), 2–23.
- Dressler, A. (1980). Galaxy morphology in rich clusters: implications for the formation and evo-lution of galaxies. , 236, 351–365.
- Dressler, A. & Gunn, J. E. (1983). Spectroscopy of galaxies in distant clusters. II. The population of the 3C 295 cluster. , 270, 7–19.
- Dressler, A., Hare, T., Bigelow, B. C., & Osip, D. J. (2006). IMACS: the wide-field imaging spectrograph on Magellan-Baade. In I. S. McLean & M. Iye (Eds.), *Society of Photo-Optical Instrumentation Engineers (SPIE) Conference Series*, volume 6269 of *Society of Photo-Optical Instrumentation Engineers (SPIE) Conference Series* (pp. 62690F).
- Dressler, A., Oemler, Augustus, J., Poggianti, B. M., Gladders, M. D., Abramson, L., & Vulcani, B. (2013). The IMACS Cluster Building Survey. II. Spectral Evolution of Galaxies in the Epoch of Cluster Assembly. , 770(1), 62.
- Duarte, M. & Mamon, G. A. (2015). MAGGIE: Models and Algorithms for Galaxy Groups, Interlopers and Environment. , 453(4), 3848–3874.
- Dutton, A. A., Conroy, C., van den Bosch, F. C., Prada, F., & More, S. (2010). The kinematic connection between galaxies and dark matter haloes. , 407(1), 2–16.
- Elbaz, D., Daddi, E., Le Borgne, D., Dickinson, M., Alexander, D. M., Chary, R. R., Starck, J. L., Brand t, W. N., Kitzbichler, M., MacDonald, E., Nonino, M., Popesso, P., Stern, D., & Vanzella, E. (2007). The reversal of the star formation-density relation in the distant universe. , 468(1), 33–48.

- Erfanianfar, G., Popesso, P., Finoguenov, A., Wilman, D., Wuyts, S., Biviano, A., Salvato, M., Mirkazemi, M., Morselli, L., Ziparo, F., Nandra, K., Lutz, D., Elbaz, D., Dickinson, M., Tanaka, M., Altieri, M. B., Aussel, H., Bauer, F., Berta, S., Bielby, R. M., Brandt, N., Cappelluti, N., Cimatti, A., Cooper, M. C., Fadda, D., Ilbert, O., Le Floch, E., Magnelli, B., Mulchaey, J. S., Nordon, R., Newman, J. A., Poglitsch, A., & Pozzi, F. (2016). Non-linearity and environmental dependence of the star-forming galaxies main sequence. , 455(3), 2839–2851.
- Fabian, A. C. (2012). Observational Evidence of Active Galactic Nuclei Feedback. , 50, 455–489.
- Fang, J. J., Faber, S. M., Koo, D. C., Rodríguez-Puebla, A., Guo, Y., Barro, G., Behroozi, P., Brammer, G., Chen, Z., Dekel, A., Ferguson, H. C., Gawiser, E., Giavalisco, M., Kartaltepe, J., Kocevski, D. D., Koekemoer, A. M., McGrath, E. J., McIntosh, D., Newman, J. A., Pacifici, C., Pandya, V., Pérez-González, P. G., Primack, J. R., Salmon, B., Trump, J. R., Weiner, B., Willner, S. P., Acquaviva, V., Dahlen, T., Finkelstein, S. L., Finlator, K., Fontana, A., Galametz, A., Grogin, N. A., Gruetzbauch, R., Johnson, S., Mobasher, B., Papovich, C. J., Pforr, J., Salvato, M., Santini, P., van der Wel, A., Wiklind, T., & Wuyts, S. (2018). Demographics of Star-forming Galaxies since  $z \sim 2.5$ . I. The UVJ Diagram in CANDELS. , 858(2), 100.
- Ferrari, F., de Carvalho, R. R., & Trevisan, M. (2015). Morfometryka—A New Way of Establishing Morphological Classification of Galaxies. , 814(1), 55.
- Ferreira, L., Conselice, C. J., Duncan, K., Cheng, T.-Y., Griffiths, A., & Whitney, A. (2020). Galaxy Merger Rates up to  $z \sim 3$  Using a Bayesian Deep Learning Model: A Major-merger Classifier Using IllustrisTNG Simulation Data. , 895(2), 115.
- Finn, R. A., Desai, V., Rudnick, G., Poggianti, B., Bell, E. F., Hinz, J., Jablonka, P., Milvang-Jensen, B., Moustakas, J., Rines, K., & Zaritsky, D. (2010). Dust-obscured Star Formation in Intermediate Redshift Galaxy Clusters. , 720(1), 87–98.
- Finn, R. A., Zaritsky, D., McCarthy, Donald W., J., Poggianti, B., Rudnick, G., Halliday, C.,

- Milvang-Jensen, B., Pelló, R., & Simard, L. (2005).  $H\alpha$ -derived Star Formation Rates for Three  $z \sim 0.75$  EDisCS Galaxy Clusters. , 630(1), 206–227.
- Foltz, R., Rettura, A., Wilson, G., van der Burg, R. F. J., Muzzin, A., Lidman, C., Demarco, R., Nantais, J., DeGroot, A., & Yee, H. (2015). Evidence for the Universality of Properties of Red-sequence Galaxies in X-Ray- and Red-Sequence-Selected Clusters at  $z \sim 1$ . , 812(2), 138.
- Foltz, R., Wilson, G., Muzzin, A., Cooper, M. C., Nantais, J., van der Burg, R. F. J., Cerulo, P., Chan, J., Fillingham, S. P., Surace, J., Webb, T., Noble, A., Lacy, M., McDonald, M., Rudnick, G., Lidman, C., Demarco, R., Hlavacek-Larrondo, J., Yee, H. K. C., Perlmutter, S., & Hayden, B. (2018). The Evolution of Environmental Quenching Timescales to  $z \sim 1.6$ : Evidence for Dynamically Driven Quenching of the Cluster Galaxy Population. , 866(2), 136.
- Fossati, M., Wilman, D. J., Mendel, J. T., Saglia, R. P., Galametz, A., Beifiori, A., Bender, R., Chan, J. C. C., Fabricius, M., Bandara, K., Brammer, G. B., Davies, R., Förster Schreiber, N. M., Genzel, R., Hartley, W., Kulkarni, S. K., Lang, P., Momcheva, I. G., Nelson, E. J., Skelton, R., Tacconi, L. J., Tadaki, K., Übler, H., van Dokkum, P. G., Wisnioski, E., Whitaker, K. E., Wuyts, E., & Wuyts, S. (2017). Galaxy Environment in the 3D-HST Fields: Witnessing the Onset of Satellite Quenching at  $z \sim 1-2$ . , 835(2), 153.
- Fukushima, K. (1980). Neocognitron: A Self-organizing Neural Network Model for a Mechanism of Pattern Recognition Unaffected by Shift in Position. *Biological Cybernetics*, 36, 193–202.
- Fumagalli, M., Labbé, I., Patel, S. G., Franx, M., van Dokkum, P., Brammer, G., da Cunha, E., Förster Schreiber, N. M., Kriek, M., Quadri, R., Rix, H.-W., Wake, D., Whitaker, K. E., Lundgren, B., Marchesini, D., Maseda, M., Momcheva, I., Nelson, E., Pacifici, C., & Skelton, R. E. (2014). How Dead are Dead Galaxies? Mid-infrared Fluxes of Quiescent Galaxies at Redshift  $0.3 < z < 2.5$ : Implications for Star Formation Rates and Dust Heating. , 796(1), 35.
- Galametz, A., Vernet, J., De Breuck, C., Hatch, N. A., Miley, G. K., Kodama, T., Kurk, J., Overzier,

- R. A., Rettura, A., Röttgering, H. J. A., Seymour, N., Venemans, B. P., & Zirm, A. W. (2010). Galaxy protocluster candidates at  $1.6 < z < 2$ . , 522, A58.
- Gavazzi, G., Bonfanti, C., Sanvito, G., Boselli, A., & Scodeggio, M. (2002). Spectrophotometry of Galaxies in the Virgo Cluster. I. The Star Formation History. , 576(1), 135–151.
- Gavazzi, G., Consolandi, G., Gutierrez, M. L., Boselli, A., & Yoshida, M. (2018). Ubiquitous ram pressure stripping in the Coma cluster of galaxies. , 618, A130.
- Geach, J. E., Smail, I., Ellis, R. S., Moran, S. M., Smith, G. P., Treu, T., Kneib, J. P., Edge, A. C., & Kodama, T. (2006). A Panoramic Mid-Infrared Survey of Two Distant Clusters. , 649(2), 661–672.
- George, D. & Huerta, E. A. (2018a). Deep Learning for real-time gravitational wave detection and parameter estimation: Results with Advanced LIGO data. *Physics Letters B*, 778, 64–70.
- George, D. & Huerta, E. A. (2018b). Deep neural networks to enable real-time multimessenger astrophysics. , 97(4), 044039.
- Gómez, P. L., Nichol, R. C., Miller, C. J., Balogh, M. L., Goto, T., Zabludoff, A. I., Romer, A. K., Bernardi, M., Sheth, R., Hopkins, A. M., Castander, F. J., Connolly, A. J., Schneider, D. P., Brinkmann, J., Lamb, D. Q., SubbaRao, M., & York, D. G. (2003). Galaxy Star Formation as a Function of Environment in the Early Data Release of the Sloan Digital Sky Survey. , 584(1), 210–227.
- Gonzalez, A. H., Zaritsky, D., Dalcanton, J. J., & Nelson, A. (2001). The Las Campanas Distant Cluster Survey: The Catalog. , 137(1), 117–138.
- Grogin, N. A., Kocevski, D. D., Faber, S. M., Ferguson, H. C., Koekemoer, A. M., Riess, A. G., Acquaviva, V., Alexander, D. M., Almaini, O., Ashby, M. L. N., Barden, M., Bell, E. F., Bournaud, F., Brown, T. M., Caputi, K. I., Casertano, S., Cassata, P., Castellano, M., Challis, P., Chary, R.-R., Cheung, E., Cirasuolo, M., Conselice, C. J., Roshan Cooray, A., Croton, D. J.,

- Daddi, E., Dahlen, T., Davé, R., de Mello, D. F., Dekel, A., Dickinson, M., Dolch, T., Donley, J. L., Dunlop, J. S., Dutton, A. A., Elbaz, D., Fazio, G. G., Filippenko, A. V., Finkelstein, S. L., Fontana, A., Gardner, J. P., Garnavich, P. M., Gawiser, E., Giavalisco, M., Grazian, A., Guo, Y., Hathi, N. P., Häussler, B., Hopkins, P. F., Huang, J.-S., Huang, K.-H., Jha, S. W., Kartaltepe, J. S., Kirshner, R. P., Koo, D. C., Lai, K., Lee, K.-S., Li, W., Lotz, J. M., Lucas, R. A., Madau, P., McCarthy, P. J., McGrath, E. J., McIntosh, D. H., McLure, R. J., Mobasher, B., Moustakas, L. A., Mozena, M., Nandra, K., Newman, J. A., Niemi, S.-M., Noeske, K. G., Papovich, C. J., Pentericci, L., Pope, A., Primack, J. R., Rajan, A., Ravindranath, S., Reddy, N. A., Renzini, A., Rix, H.-W., Robaina, A. R., Rodney, S. A., Rosario, D. J., Rosati, P., Salimbeni, S., Scarlata, C., Siana, B., Simard, L., Smidt, J., Somerville, R. S., Spinrad, H., Straughn, A. N., Strolger, L.-G., Telford, O., Teplitz, H. I., Trump, J. R., van der Wel, A., Villforth, C., Wechsler, R. H., Weiner, B. J., Wiklind, T., Wild, V., Wilson, G., Wuyts, S., Yan, H.-J., & Yun, M. S. (2011). CANDELS: The Cosmic Assembly Near-infrared Deep Extragalactic Legacy Survey. , 197(2), 35.
- Gullieuszik, M., Poggianti, B. M., Moretti, A., Fritz, J., Jaffé, Y. L., Hau, G., Bischko, J. C., Bellhouse, C., Bettoni, D., Fasano, G., Vulcani, B., D'Onofrio, M., & Biviano, A. (2017). GASP. IV. A Muse View of Extreme Ram-pressure-stripping in the Plane of the Sky: The Case of Jellyfish Galaxy JO204. , 846(1), 27.
- Gunn, J. E. & Gott, J. Richard, I. (1972). On the Infall of Matter Into Clusters of Galaxies and Some Effects on Their Evolution. , 176, 1.
- Haines, C. P., Pereira, M. J., Smith, G. P., Egami, E., Babul, A., Finoguenov, A., Ziparo, F., McGee, S. L., Rawle, T. D., Okabe, N., & Moran, S. M. (2015). LoCuSS: The Slow Quenching of Star Formation in Cluster Galaxies and the Need for Pre-processing. , 806(1), 101.
- Halliday, C., Milvang-Jensen, B., Poirier, S., Poggianti, B. M., Jablonka, P., Aragón-Salamanca, A., Saglia, R. P., De Lucia, G., Pelló, R., Simard, L., Clowe, D. I., Rudnick, G., Dalcanton, J. J., White, S. D. M., & Zaritsky, D. (2004). Spectroscopy of clusters in the ESO Distant

- Cluster Survey (EDisCS). Redshifts, velocity dispersions and substructure for 5 clusters. , 427, 397–413.
- Hatch, N. A., Kurk, J. D., Pentericci, L., Venemans, B. P., Kuiper, E., Miley, G. K., & Röttgering, H. J. A. (2011). H $\alpha$  emitters in  $z \sim 2$  protoclusters: evidence for faster evolution in dense environments. , 415(4), 2993–3005.
- Haynes, M. P., Giovanelli, R., & Chincarini, G. L. (1984). The Influence of Environment on the H I Content of Galaxies. , 22, 445–470.
- Henrion, M., Mortlock, D. J., Hand, D. J., & Gandhi, A. (2011). A Bayesian approach to star-galaxy classification. , 412(4), 2286–2302.
- Hess, K. M. & Wilcots, E. M. (2013). Evolution in the H I Gas Content of Galaxy Groups: Pre-processing and Mass Assembly in the Current Epoch. , 146(5), 124.
- Hopkins, P. F., Hernquist, L., Cox, T. J., Di Matteo, T., Robertson, B., & Springel, V. (2006). A Unified, Merger-driven Model of the Origin of Starbursts, Quasars, the Cosmic X-Ray Background, Supermassive Black Holes, and Galaxy Spheroids. , 163(1), 1–49.
- Hopkins, P. F., Kereš, D., Oñorbe, J., Faucher-Giguère, C.-A., Quataert, E., Murray, N., & Bullock, J. S. (2014). Galaxies on FIRE (Feedback In Realistic Environments): stellar feedback explains cosmologically inefficient star formation. , 445(1), 581–603.
- Hoyle, B. (2016). Measuring photometric redshifts using galaxy images and Deep Neural Networks. *Astronomy and Computing*, 16, 34–40.
- Hubble, E. P. (1926). Extragalactic nebulae. , 64, 321–369.
- Hubel, D. H. & Wiesel, T. N. (1968). Receptive fields and functional architecture of monkey striate cortex. *The Journal of Physiology*, 195, 215–243.
- Jaffé, Y. L., Poggianti, B. M., Moretti, A., Gullieuszik, M., Smith, R., Vulcani, B., Fasano, G., Fritz, J., Tonnesen, S., Bettoni, D., Hau, G., Biviano, A., Bellhouse, C., & McGee, S. (2018).

- GASP. IX. Jellyfish galaxies in phase-space: an orbital study of intense ram-pressure stripping in clusters. , 476(4), 4753–4764.
- Jaffé, Y. L., Smith, R., Candlish, G. N., Poggianti, B. M., Sheen, Y.-K., & Verheijen, M. A. W. (2015). BUDHIES II: a phase-space view of H I gas stripping and star formation quenching in cluster galaxies. , 448(2), 1715–1728.
- Jaffé, Y. L., Verheijen, M. A. W., Haines, C. P., Yoon, H., Cybulski, R., Montero-Castaño, M., Smith, R., Chung, A., Deshev, B. Z., Fernández, X., van Gorkom, J., Poggianti, B. M., Yun, M. S., Finoguenov, A., Smith, G. P., & Okabe, N. (2016). BUDHIES - III: the fate of H I and the quenching of galaxies in evolving environments. , 461(2), 1202–1221.
- James, P. A., Shane, N. S., Beckman, J. E., Cardwell, A., Collins, C. A., Etherton, J., de Jong, R. S., Fathi, K., Knapen, J. H., Peletier, R. F., Percival, S. M., Pollacco, D. L., Seigar, M. S., Stedman, S., & Steele, I. A. (2004). The H $\alpha$  galaxy survey. I. The galaxy sample, H $\alpha$  narrow-band observations and star formation parameters for 334 galaxies. , 414, 23–43.
- Jarrett, T. H., Chester, T., Cutri, R., Schneider, S., Skrutskie, M., & Huchra, J. P. (2000). 2MASS Extended Source Catalog: Overview and Algorithms. , 119(5), 2498–2531.
- Jian, H.-Y., Lin, L., Oguri, M., Nishizawa, A. J., Takada, M., More, S., Koyama, Y., Tanaka, M., & Komiyama, Y. (2018). First results on the cluster galaxy population from the Subaru Hyper Suprime-Cam survey. I. The role of group or cluster environment in star formation quenching from  $z = 0.2$  to  $1.1$ . , 70, S23.
- Johnson, H. L. & Morgan, W. W. (1953). Fundamental stellar photometry for standards of spectral type on the Revised System of the Yerkes Spectral Atlas. , 117, 313.
- Just, D. W., Kirby, M., Zaritsky, D., Rudnick, G., Desjardins, T., Cool, R., Moustakas, J., Clowe, D., Lucia, G. D., Aragón-Salamanca, A., & et al. (2019). Preprocessing among the infalling galaxy population of ediscs clusters. *The Astrophysical Journal*, 885(1), 6.

- Kapferer, W., Sluka, C., Schindler, S., Ferrari, C., & Ziegler, B. (2009). The effect of ram pressure on the star formation, mass distribution and morphology of galaxies. , 499(1), 87–102.
- Karim, A., Schinnerer, E., Martínez-Sansigre, A., Sargent, M. T., van der Wel, A., Rix, H. W., Ilbert, O., Smolčić, V., Carilli, C., Pannella, M., Koekemoer, A. M., Bell, E. F., & Salvato, M. (2011). The Star Formation History of Mass-selected Galaxies in the COSMOS Field. , 730(2), 61.
- Karl, S. J., Naab, T., Johansson, P. H., Kotarba, H., Boily, C. M., Renaud, F., & Theis, C. (2010). One Moment in Time—Modeling Star Formation in the Antennae. , 715(2), L88–L93.
- Kauffmann, G., Heckman, T. M., White, S. D. M., Charlot, S., Tremonti, C., Brinchmann, J., Bruzual, G., Peng, E. W., Seibert, M., Bernardi, M., Blanton, M., Brinkmann, J., Castander, F., Csábai, I., Fukugita, M., Ivezić, Z., Munn, J. A., Nichol, R. C., Padmanabhan, N., Thakar, A. R., Weinberg, D. H., & York, D. (2003). Stellar masses and star formation histories for  $10^5$  galaxies from the Sloan Digital Sky Survey. , 341(1), 33–53.
- Kauffmann, G., White, S. D. M., Heckman, T. M., Ménard, B., Brinchmann, J., Charlot, S., Tremonti, C., & Brinkmann, J. (2004). The environmental dependence of the relations between stellar mass, structure, star formation and nuclear activity in galaxies. , 353(3), 713–731.
- Kawata, D. & Mulchaey, J. S. (2008). Strangulation in Galaxy Groups. , 672(2), L103.
- Kenney, J. (2004). Ram Pressure Stripping of the Virgo Spiral NGC 4569 (M90). Chandra Proposal.
- Kenney, J. D. P. & Young, J. S. (1989). The Effects of Environment on the Molecular and Atomic Gas Properties of Large Virgo Cluster Spirals. , 344, 171.
- Kennicutt, Robert C., J. (1998). The Global Schmidt Law in Star-forming Galaxies. , 498(2), 541–552.

- Kennicutt, R. C. & Evans, N. J. (2012). Star Formation in the Milky Way and Nearby Galaxies. , 50, 531–608.
- Kewley, L. J. & Ellison, S. L. (2008). Metallicity Calibrations and the Mass-Metallicity Relation for Star-forming Galaxies. , 681(2), 1183–1204.
- Kodama, T., Tanaka, I., Kajisawa, M., Kurk, J., Venemans, B., De Breuck, C., Vernet, J., & Lidman, C. (2007). The first appearance of the red sequence of galaxies in proto-clusters at  $2 < z < 3$ . , 377(4), 1717–1725.
- Koyama, Y., Smail, I., Kurk, J., Geach, J. E., Sobral, D., Kodama, T., Nakata, F., Swinbank, A. M., Best, P. N., Hayashi, M., & Tadaki, K.-i. (2013). On the evolution and environmental dependence of the star formation rate versus stellar mass relation since  $z \sim 2$ . , 434(1), 423–436.
- Kroupa, P. (2001). On the variation of the initial mass function. , 322(2), 231–246.
- Lanusse, F., Ma, Q., Li, N., Collett, T. E., Li, C.-L., Ravanbakhsh, S., Mandelbaum, R., & Póczos, B. (2018). CMU DeepLens: deep learning for automatic image-based galaxy-galaxy strong lens finding. , 473(3), 3895–3906.
- Larson, R. B., Tinsley, B. M., & Caldwell, C. N. (1980). The evolution of disk galaxies and the origin of S0 galaxies. , 237, 692–707.
- Lee, J. C., Ly, C., Spitler, L., Labbé, I., Salim, S., Persson, S. E., Ouchi, M., Dale, D. A., Monson, A., & Murphy, D. (2012). A dual-narrowband survey for h emitters at redshift of 2.2: Demonstration of the technique and constraints on the h luminosity function1. *Publications of the Astronomical Society of the Pacific*, 124(917), 782–797.
- Lee-Brown, D. B., Rudnick, G. H., Momcheva, I. G., Papovich, C., Lotz, J. M., Tran, K.-V. H., Henke, B., Willmer, C. N. A., Brammer, G. B., Brodwin, M., Dunlop, J., & Farrah, D. (2017). The Ages of Passive Galaxies in a  $z = 1.62$  Protocluster. , 844(1), 43.

- Lewis, I., Balogh, M., De Propriis, R., Couch, W., Bower, R., Offer, A., Bland-Hawthorn, J., Baldry, I. K., Baugh, C., Bridges, T., Cannon, R., Cole, S., Colless, M., Collins, C., Cross, N., Dalton, G., Driver, S. P., Efstathiou, G., Ellis, R. S., Frenk, C. S., Glazebrook, K., Hawkins, E., Jackson, C., Lahav, O., Lumsden, S., Maddox, S., Madgwick, D., Norberg, P., Peacock, J. A., Percival, W., Peterson, B. A., Sutherland, W., & Taylor, K. (2002). The 2dF Galaxy Redshift Survey: the environmental dependence of galaxy star formation rates near clusters. , 334(3), 673–683.
- Madgwick, D. S. (2003). Correlating galaxy morphologies and spectra in the 2dF Galaxy Redshift Survey. *Monthly Notices of the Royal Astronomical Society*, 338(1), 197–207.
- Margoniner, V. E., de Carvalho, R. R., Gal, R. R., & Djorgovski, S. G. (2001). The Butcher-Oemler Effect in 295 Clusters: Strong Redshift Evolution and Cluster Richness Dependence. , 548(2), L143–L146.
- Martig, M., Bournaud, F., Teyssier, R., & Dekel, A. (2009). Morphological Quenching of Star Formation: Making Early-Type Galaxies Red. , 707(1), 250–267.
- Martin, D. C., Wyder, T. K., Schiminovich, D., Barlow, T. A., Forster, K., Friedman, P. G., Morrissey, P., Neff, S. G., Seibert, M., Small, T., Welsh, B. Y., Bianchi, L., Donas, J., Heckman, T. M., Lee, Y.-W., Madore, B. F., Milliard, B., Rich, R. M., Szalay, A. S., & Yi, S. K. (2007). The UV-Optical Galaxy Color-Magnitude Diagram. III. Constraints on Evolution from the Blue to the Red Sequence. , 173(2), 342–356.
- Martini, P., Sivakoff, G. R., & Mulchaey, J. S. (2009). The Evolution of Active Galactic Nuclei in Clusters of Galaxies to Redshift 1.3. , 701(1), 66–85.
- Matharu, J., Muzzin, A., Brammer, G. B., van der Burg, R. F. J., Auger, M. W., Hewett, P. C., van der Wel, A., van Dokkum, P., Balogh, M., Chan, J. C. C., Demarco, R., Marchesini, D., Nelson, E. J., Noble, A., Wilson, G., & Yee, H. K. C. (2019). HST/WFC3 grism observations

of  $z \sim 1$  clusters: the cluster versus field stellar mass-size relation and evidence for size growth of quiescent galaxies from minor mergers. , 484(1), 595–617.

McGee, S. L., Balogh, M. L., Wilman, D. J., Bower, R. G., Mulchaey, J. S., Parker, L. C., & Oemler, A. (2011). The Dawn of the Red: star formation histories of group galaxies over the past 5 billion years. , 413(2), 996–1012.

Milvang-Jensen, B., Noll, S., Halliday, C., Poggianti, B. M., Jablonka, P., Aragón-Salamanca, A., Saglia, R. P., Nowak, N., von der Linden, A., De Lucia, G., Pelló, R., Moustakas, J., Poirier, S., Bamford, S. P., Clowe, D. I., Dalcanton, J. J., Rudnick, G. H., Simard, L., White, S. D. M., & Zaritsky, D. (2008). Spectroscopy of clusters in the ESO distant cluster survey (EDisCS). II. Redshifts, velocity dispersions, and substructure for clusters in the last 15 fields. , 482(2), 419–449.

Momcheva, I. G., Brammer, G. B., van Dokkum, P. G., Skelton, R. E., Whitaker, K. E., Nelson, E. J., Fumagalli, M., Maseda, M. V., Leja, J., Franx, M., Rix, H.-W., Bezanson, R., Da Cunha, E., Dickey, C., Förster Schreiber, N. M., Illingworth, G., Kriek, M., Labbé, I., Ulf Lange, J., Lundgren, B. F., Magee, D., Marchesini, D., Oesch, P., Pacifici, C., Patel, S. G., Price, S., Tal, T., Wake, D. A., van der Wel, A., & Wuyts, S. (2016). The 3D-HST Survey: Hubble Space Telescope WFC3/G141 Grism Spectra, Redshifts, and Emission Line Measurements for  $\sim 100,000$  Galaxies. , 225(2), 27.

Moore, B., Lake, G., Quinn, T., & Stadel, J. (1999). On the survival and destruction of spiral galaxies in clusters. , 304(3), 465–474.

Moran, S. M., Ellis, R. S., Treu, T., Smith, G. P., Rich, R. M., & Smail, I. (2007). A Wide-Field Survey of Two  $z \sim 0.5$  Galaxy Clusters: Identifying the Physical Processes Responsible for the Observed Transformation of Spirals into S0s. , 671(2), 1503–1522.

Morishita, T., Abramson, L. E., Treu, T., Vulcani, B., Schmidt, K. B., Dressler, A., Poggianti, B. M., Malkan, M. A., Wang, X., Huang, K.-H., Trenti, M., Bradač, M., & Hoag, A. (2017).

- The Grism Lens-amplified Survey from Space (Glass). IX. The Dual Origin of Low-mass Cluster Galaxies as Revealed by New Structural Analyses. , 835(2), 254.
- Muldrew, S. I., Hatch, N. A., & Cooke, E. A. (2015). What are protoclusters? - Defining high-redshift galaxy clusters and protoclusters. , 452(3), 2528–2539.
- Muzzin, A., Marchesini, D., Stefanon, M., Franx, M., Milvang-Jensen, B., Dunlop, J. S., Fynbo, J. P. U., Brammer, G., Labbé, I., & van Dokkum, P. (2013). A Public  $K_s$ -selected Catalog in the COSMOS/ULTRAVISTA Field: Photometry, Photometric Redshifts, and Stellar Population Parameters. , 206(1), 8.
- Muzzin, A., van der Burg, R. F. J., McGee, S. L., Balogh, M., Franx, M., Hoekstra, H., Hudson, M. J., Noble, A., Taranu, D. S., Webb, T., Wilson, G., & Yee, H. K. C. (2014). The Phase Space and Stellar Populations of Cluster Galaxies at  $z \sim 1$ : Simultaneous Constraints on the Location and Timescale of Satellite Quenching. , 796(1), 65.
- Muzzin, A., Wilson, G., Yee, H. K. C., Gilbank, D., Hoekstra, H., Demarco, R., Balogh, M., van Dokkum, P., Franx, M., Ellingson, E., Hicks, A., Nantais, J., Noble, A., Lacy, M., Lidman, C., Rettura, A., Surace, J., & Webb, T. (2012). The Gemini Cluster Astrophysics Spectroscopic Survey (GCLASS): The Role of Environment and Self-regulation in Galaxy Evolution at  $z \sim 1$ . , 746(2), 188.
- Naim, A., Lahav, O., Sodre, L., J., & Storrie-Lombardi, M. C. (1995). Automated morphological classification of APM galaxies by supervised artificial neural networks. , 275(3), 567–590.
- Nelson, E. J., van Dokkum, P. G., Brammer, G., Förster Schreiber, N., Franx, M., Fumagalli, M., Patel, S., Rix, H.-W., Skelton, R. E., Bezanson, R., Da Cunha, E., Kriek, M., Labbe, I., Lundgren, B., Quadri, R., & Schmidt, K. B. (2012). Spatially Resolved  $H\alpha$  Maps and Sizes of 57 Strongly Star-forming Galaxies at  $z \sim 1$  from 3D-HST: Evidence for Rapid Inside-out Assembly of Disk Galaxies. , 747(2), L28.

- Nelson, E. J., van Dokkum, P. G., Förster Schreiber, N. M., Franx, M., Brammer, G. B., Momcheva, I. G., Wuyts, S., Whitaker, K. E., Skelton, R. E., Fumagalli, M., Hayward, C. C., Kriek, M., Labbé, I., Leja, J., Rix, H.-W., Tacconi, L. J., van der Wel, A., van den Bosch, F. C., Oesch, P. A., Dickey, C., & Ulf Lange, J. (2016). Where Stars Form: Inside-out Growth and Coherent Star Formation from HST H $\alpha$  Maps of 3200 Galaxies across the Main Sequence at  $0.7 < z < 1.5$ . , 828(1), 27.
- Nelson, E. J., van Dokkum, P. G., Momcheva, I., Brammer, G., Lundgren, B., Skelton, R. E., Whitaker, K. E., Da Cunha, E., Förster Schreiber, N., Franx, M., Fumagalli, M., Kriek, M., Labbe, I., Leja, J., Patel, S., Rix, H.-W., Schmidt, K. B., van der Wel, A., & Wuyts, S. (2013). The Radial Distribution of Star Formation in Galaxies at  $z \sim 1$  from the 3D-HST Survey. , 763(1), L16.
- Newman, A. B., Treu, T., Ellis, R. S., Sand, D. J., Nipoti, C., Richard, J., & Jullo, E. (2013). The density profiles of massive, relaxed galaxy clusters. i. the total density over three decades in radius. *The Astrophysical Journal*, 765(1), 24.
- Noeske, K. G., Weiner, B. J., Faber, S. M., Papovich, C., Koo, D. C., Somerville, R. S., Bundy, K., Conselice, C. J., Newman, J. A., Schiminovich, D., Le Floc'h, E., Coil, A. L., Rieke, G. H., Lotz, J. M., Primack, J. R., Barmby, P., Cooper, M. C., Davis, M., Ellis, R. S., Fazio, G. G., Guhathakurta, P., Huang, J., Kassin, S. A., Martin, D. C., Phillips, A. C., Rich, R. M., Small, T. A., Willmer, C. N. A., & Wilson, G. (2007). Star Formation in AEGIS Field Galaxies since  $z=1.1$ : The Dominance of Gradually Declining Star Formation, and the Main Sequence of Star-forming Galaxies. , 660(1), L43–L46.
- Oemler, Augustus, J., Dressler, A., Gladders, M. G., Fritz, J., Poggianti, B. M., Vulcani, B., & Abramson, L. (2013). The IMACS Cluster Building Survey. III. The Star Formation Histories of Field Galaxies. , 770(1), 63.
- Old, P., Hautala, S. L., & Thompson, L. (2019). Differences in Eastern North Pacific Stratification

and Their Potential Impact on the Depth of Winter Mixing in CMIP5 Models. , 46(21), 12,136–12,145.

Overzier, R. A., Bouwens, R. J., Cross, N. J. G., Venemans, B. P., Miley, G. K., Zirm, A. W., Benítez, N., Blakeslee, J. P., Coe, D., Demarco, R., Ford, H. C., Homeier, N. L., Illingworth, G. D., Kurk, J. D., Martel, A. R., Mei, S., Oliveira, I., Röttgering, H. J. A., Tsvetanov, Z. I., & Zheng, W. (2008). Lyman Break Galaxies, Ly $\alpha$  Emitters, and a Radio Galaxy in a Protocluster at  $z = 4.1$ . , 673(1), 143–162.

Paccagnella, A., Vulcani, B., Poggianti, B. M., Moretti, A., Fritz, J., Gullieuszik, M., Couch, W., Bettoni, D., Cava, A., D’Onofrio, M., & Fasano, G. (2016). Slow Quenching of Star Formation in OMEGAWINGS Clusters: Galaxies in Transition in the Local Universe. , 816(2), L25.

Pannella, M., Carilli, C. L., Daddi, E., McCracken, H. J., Owen, F. N., Renzini, A., Strazzullo, V., Civano, F., Koekemoer, A. M., Schinnerer, E., Scoville, N., Smolčić, V., Taniguchi, Y., Aussel, H., Kneib, J. P., Ilbert, O., Mellier, Y., Salvato, M., Thompson, D., & Willott, C. J. (2009). Star Formation and Dust Obscuration at  $z \approx 2$ : Galaxies at the Dawn of Downsizing. , 698(2), L116–L120.

Paszke, A., Gross, S., Massa, F., Lerer, A., Bradbury, J., Chanan, G., Killeen, T., Lin, Z., Gimelshein, N., Antiga, L., Desmaison, A., Kopf, A., Yang, E., DeVito, Z., Raison, M., Tejani, A., Chilamkurthy, S., Steiner, B., Fang, L., Bai, J., & Chintala, S. (2019). Pytorch: An imperative style, high-performance deep learning library. In H. Wallach, H. Larochelle, A. Beygelzimer, F. d’Alché-Buc, E. Fox, & R. Garnett (Eds.), *Advances in Neural Information Processing Systems 32* (pp. 8024–8035). Curran Associates, Inc.

Patel, S. G., Holden, B. P., Kelson, D. D., Illingworth, G. D., & Franx, M. (2009a). The Dependence of Star Formation Rates on Stellar Mass and Environment at  $z \sim 0.8$ . , 705(1), L67–L70.

Patel, S. G., Kelson, D. D., Holden, B. P., Franx, M., & Illingworth, G. D. (2011). The Star-

- formation-rate-Density Relation at  $0.6 < z < 0.9$  and the Role of Star-forming Galaxies. , 735(1), 53.
- Patel, S. G., Kelson, D. D., Holden, B. P., Illingworth, G. D., Franx, M., van der Wel, A., & Ford, H. (2009b). A Wide-Field Study of the  $z \sim 0.8$  Cluster RX J0152.7-1357: The Role of Environment in the Formation of the Red Sequence. , 694(2), 1349–1363.
- Peebles, P. J. E. (1982). Large-scale background temperature and mass fluctuations due to scale-invariant primeval perturbations. , 263, L1–L5.
- Pelló, R., Rudnick, G., De Lucia, G., Simard, L., Clowe, D. I., Jablonka, P., Milvang-Jensen, B., Saglia, R. P., White, S. D. M., Aragón-Salamanca, A., Halliday, C., Poggianti, B., Best, P., Dalcanton, J., Dantel-Fort, M., Fort, B., von der Linden, A., Mellier, Y., Rottgering, H., & Zaritsky, D. (2009). Photometric redshifts and cluster tomography in the ESO Distant Cluster Survey. , 508(3), 1173–1191.
- Peng, Y.-j., Lilly, S. J., Kovač, K., Bolzonella, M., Pozzetti, L., Renzini, A., Zamorani, G., Ilbert, O., Knobel, C., Iovino, A., Maier, C., Cucciati, O., Tasca, L., Carollo, C. M., Silverman, J., Kampczyk, P., de Ravel, L., Sanders, D., Scoville, N., Contini, T., Mainieri, V., Scodeggio, M., Kneib, J.-P., Le Fèvre, O., Bardelli, S., Bongiorno, A., Caputi, K., Coppa, G., de la Torre, S., Franzetti, P., Garilli, B., Lamareille, F., Le Borgne, J.-F., Le Brun, V., Mignoli, M., Perez Montero, E., Pello, R., Ricciardelli, E., Tanaka, M., Tresse, L., Vergani, D., Welikala, N., Zucca, E., Oesch, P., Abbas, U., Barnes, L., Bordoloi, R., Bottini, D., Cappi, A., Cassata, P., Cimatti, A., Fumana, M., Hasinger, G., Koekemoer, A., Leauthaud, A., Maccagni, D., Marinoni, C., McCracken, H., Memeo, P., Meneux, B., Nair, P., Porciani, C., Presotto, V., & Scaramella, R. (2010). Mass and Environment as Drivers of Galaxy Evolution in SDSS and zCOSMOS and the Origin of the Schechter Function. , 721(1), 193–221.
- Pinkowski, J. (2010). How to Classify a Million Galaxies in Three Weeks. *Time Magazine*.

Pintos-Castro, I., Yee, H. K. C., Muzzin, A., Old, L., & Wilson, G. (2019). The Evolution of the Quenching of Star Formation in Cluster Galaxies since  $z \sim 1$ . , 876(1), 40.

Planck Collaboration, Ade, P. A. R., Aghanim, N., Arnaud, M., Ashdown, M., Aumont, J., Bacigalupi, C., Banday, A. J., Barreiro, R. B., Bartlett, J. G., Bartolo, N., Battaner, E., Battye, R., Benabed, K., Benoît, A., Benoit-Lévy, A., Bernard, J. P., Bersanelli, M., Bielewicz, P., Bock, J. J., Bonaldi, A., Bonavera, L., Bond, J. R., Borrill, J., Bouchet, F. R., Boulanger, F., Bucher, M., Burigana, C., Butler, R. C., Calabrese, E., Cardoso, J. F., Catalano, A., Challinor, A., Chamballu, A., Chary, R. R., Chiang, H. C., Chluba, J., Christensen, P. R., Church, S., Clements, D. L., Colombi, S., Colombo, L. P. L., Combet, C., Coulais, A., Crill, B. P., Curto, A., Cuttaia, F., Danese, L., Davies, R. D., Davis, R. J., de Bernardis, P., de Rosa, A., de Zotti, G., Delabrouille, J., Désert, F. X., Di Valentino, E., Dickinson, C., Diego, J. M., Dolag, K., Dole, H., Donzelli, S., Doré, O., Douspis, M., Ducout, A., Dunkley, J., Dupac, X., Efstathiou, G., Elsner, F., Enßlin, T. A., Eriksen, H. K., Farhang, M., Fergusson, J., Finelli, F., Forni, O., Frailis, M., Fraisse, A. A., Franceschi, E., Frejsel, A., Galeotta, S., Galli, S., Ganga, K., Gauthier, C., Gerbino, M., Ghosh, T., Giard, M., Giraud-Héraud, Y., Giusarma, E., Gjerløw, E., González-Nuevo, J., Górski, K. M., Gratton, S., Gregorio, A., Gruppuso, A., Gudmundsson, J. E., Hamann, J., Hansen, F. K., Hanson, D., Harrison, D. L., Helou, G., Henrot-Versillé, S., Hernández-Monteagudo, C., Herranz, D., Hildebrandt, S. R., Hivon, E., Hobson, M., Holmes, W. A., Hornstrup, A., Hovest, W., Huang, Z., Huffenberger, K. M., Hurier, G., Jaffe, A. H., Jaffe, T. R., Jones, W. C., Juvela, M., Keihänen, E., Keskitalo, R., Kisner, T. S., Kneissl, R., Knoche, J., Knox, L., Kunz, M., Kurki-Suonio, H., Lagache, G., Lähteenmäki, A., Lamarre, J. M., Lasenby, A., Lattanzi, M., Lawrence, C. R., Leahy, J. P., Leonardi, R., Lesgourgues, J., Levrier, F., Lewis, A., Liguori, M., Lilje, P. B., Linden-Vørnle, M., López-Caniego, M., Lubin, P. M., Macías-Pérez, J. F., Maggio, G., Maino, D., Mandolesi, N., Mangilli, A., Marchini, A., Maris, M., Martin, P. G., Martinelli, M., Martínez-González, E., Masi, S., Matarrese, S., McGeehee, P., Meinhold, P. R., Melchiorri, A., Melin, J. B., Mendes, L., Mennella, A., Migliaccio, M., Millea, M., Mitra, S., Miville-Deschênes, M. A., Moneti, A., Montier, L., Morgante, G.,

Mortlock, D., Moss, A., Munshi, D., Murphy, J. A., Naselsky, P., Nati, F., Natoli, P., Netterfield, C. B., Nørgaard-Nielsen, H. U., Noviello, F., Novikov, D., Novikov, I., Oxborrow, C. A., Paci, F., Pagano, L., Pajot, F., Paladini, R., Paoletti, D., Partridge, B., Pasian, F., Patanchon, G., Pearson, T. J., Perdereau, O., Perotto, L., Perrotta, F., Pettorino, V., Piacentini, F., Piat, M., Pierpaoli, E., Pietrobon, D., Plaszczynski, S., Pointecouteau, E., Polenta, G., Popa, L., Pratt, G. W., Prézeau, G., Prunet, S., Puget, J. L., Rachen, J. P., Reach, W. T., Rebolo, R., Reinecke, M., Remazeilles, M., Renault, C., Renzi, A., Ristorcelli, I., Rocha, G., Rosset, C., Rossetti, M., Roudier, G., Rouillé d'Orfeuil, B., Rowan-Robinson, M., Rubiño-Martín, J. A., Rusholme, B., Said, N., Salvatelli, V., Salvati, L., Sandri, M., Santos, D., Savelainen, M., Savini, G., Scott, D., Seiffert, M. D., Serra, P., Shellard, E. P. S., Spencer, L. D., Spinelli, M., Stolyarov, V., Stompor, R., Sudiwala, R., Sunyaev, R., Sutton, D., Suur-Uski, A. S., Sygnet, J. F., Tauber, J. A., Terenzi, L., Toffolatti, L., Tomasi, M., Tristram, M., Trombetti, T., Tucci, M., Tuovinen, J., Türler, M., Umata, G., Valenziano, L., Valiviita, J., Van Tent, F., Vielva, P., Villa, F., Wade, L. A., Wandelt, B. D., Wehus, I. K., White, M., White, S. D. M., Wilkinson, A., Yvon, D., Zacchei, A., & Zonca, A. (2016). Planck 2015 results. XIII. Cosmological parameters. , 594, A13.

Poggianti, B. M., Aragón-Salamanca, A., Zaritsky, D., De Lucia, G., Milvang-Jensen, B., Desai, V., Jablonka, P., Halliday, C., Rudnick, G., Varela, J., Bamford, S., Best, P., Clowe, D., Noll, S., Saglia, R., Pelló, R., Simard, L., von der Linden, A., & White, S. (2009). The Environments of Starburst and Post-Starburst Galaxies at  $z = 0.4-0.8$ . , 693(1), 112–131.

Poggianti, B. M., Desai, V., Finn, R., Bamford, S., De Lucia, G., Varela, J., Aragón-Salamanca, A., Halliday, C., Noll, S., Saglia, R., Zaritsky, D., Best, P., Clowe, D., Milvang-Jensen, B., Jablonka, P., Pelló, R., Rudnick, G., Simard, L., von der Linden, A., & White, S. (2008). The Relation between Star Formation, Morphology, and Local Density in High-Redshift Clusters and Groups. , 684(2), 888–904.

Poggianti, B. M., Fasano, G., Omizzolo, A., Gullieuszik, M., Bettoni, D., Moretti, A., Paccagnella,

- A., Jaffé, Y. L., Vulcani, B., Fritz, J., Couch, W., & D’Onofrio, M. (2016). Jellyfish Galaxy Candidates at Low Redshift. , 151(3), 78.
- Poggianti, B. M., Jaffé, Y. L., Moretti, A., Gullieuszik, M., Radovich, M., Tonnesen, S., Fritz, J., Bettoni, D., Vulcani, B., Fasano, G., Bellhouse, C., Hau, G., & Omizzolo, A. (2017). Ram-pressure feeding of supermassive black holes. , 548(7667), 304–309.
- Poggianti, B. M., Smail, I., Dressler, A., Couch, W. J., Barger, A. J., Butcher, H., Ellis, R. S., & Oemler, Augustus, J. (1999). The Star Formation Histories of Galaxies in Distant Clusters. , 518(2), 576–593.
- Poggianti, B. M., von der Linden, A., De Lucia, G., Desai, V., Simard, L., Halliday, C., Aragón-Salamanca, A., Bower, R., Varela, J., Best, P., Clowe, D. I., Dalcanton, J., Jablonka, P., Milvang-Jensen, B., Pello, R., Rudnick, G., Saglia, R., White, S. D. M., & Zaritsky, D. (2006). The Evolution of the Star Formation Activity in Galaxies and Its Dependence on Environment. , 642(1), 188–215.
- Postman, M., Franx, M., Cross, N. J. G., Holden, B., Ford, H. C., Illingworth, G. D., Goto, T., Demarco, R., Rosati, P., Blakeslee, J. P., Tran, K. V., Benítez, N., Clampin, M., Hartig, G. F., Homeier, N., Ardila, D. R., Bartko, F., Bouwens, R. J., Bradley, L. D., Broadhurst, T. J., Brown, R. A., Burrows, C. J., Cheng, E. S., Feldman, P. D., Golimowski, D. A., Gronwall, C., Infante, L., Kimble, R. A., Krist, J. E., Lesser, M. P., Martel, A. R., Mei, S., Menanteau, F., Meurer, G. R., Miley, G. K., Motta, V., Sirianni, M., Sparks, W. B., Tran, H. D., Tsvetanov, Z. I., White, R. L., & Zheng, W. (2005). The Morphology-Density Relation in  $z \sim 1$  Clusters. , 623(2), 721–741.
- Pović, M., Sánchez-Portal, M., Pérez García, A. M., Bongiovanni, A., Cepa, J., Alfaro, E., Castañeda, H., Fernández Lorenzo, M., Gallego, J., González-Serrano, J. I., González, J. J., & Lara-López, M. A. (2009). OTELO Survey: Deep BVRI Broadband Photometry of the Groth Strip. II. Optical Properties of X-Ray Emitters. , 706(1), 810–823.

- Quadri, R. F., Williams, R. J., Franx, M., & Hildebrandt, H. (2012). Tracing the Star-formation-Density Relation to  $z \sim 2$ . , 744(2), 88.
- Quilis, V., Moore, B., & Bower, R. (2000). Gone with the Wind: The Origin of S0 Galaxies in Clusters. *Science*, 288(5471), 1617–1620.
- Quiroza, C., Rocha-Pinto, H. J., & Maciel, W. J. (2007). Bayesian posterior classification of planetary nebulae according to the Peimbert types. , 475(1), 217–231.
- Rakos, K. D. & Schombert, J. M. (1995). Color Evolution from  $Z = 0$  to  $Z = 1$ . , 439, 47.
- Rasmussen, J., Ponman, T. J., & Mulchaey, J. S. (2006). Gas stripping in galaxy groups - the case of the starburst spiral NGC 2276. , 370(1), 453–467.
- Rasmussen, J., Ponman, T. J., Verdes-Montenegro, L., Yun, M. S., & Borthakur, S. (2008). Galaxy evolution in Hickson compact groups: the role of ram-pressure stripping and strangulation. , 388(3), 1245–1264.
- Richards, J. W., Starr, D. L., Butler, N. R., Bloom, J. S., Brewer, J. M., Crellin-Quick, A., Higgins, J., Kennedy, R., & Rischard, M. (2011). On Machine-learned Classification of Variable Stars with Sparse and Noisy Time-series Data. , 733(1), 10.
- Roberts, M. S. (1963). The Content of Galaxies: Stars and Gas. , 1, 149.
- Roberts, M. S. & Haynes, M. P. (1994). Physical Parameters along the Hubble Sequence. , 32, 115–152.
- Rodighiero, G., Daddi, E., Baronchelli, I., Cimatti, A., Renzini, A., Aussel, H., Popesso, P., Lutz, D., Andreani, P., Berta, S., Cava, A., Elbaz, D., Feltre, A., Fontana, A., Förster Schreiber, N. M., Franceschini, A., Genzel, R., Grazian, A., Gruppioni, C., Ilbert, O., Le Floch, E., Magdis, G., Magliocchetti, M., Magnelli, B., Maiolino, R., McCracken, H., Nordon, R., Poglitsch, A., Santini, P., Pozzi, F., Riguccini, L., Tacconi, L. J., Wuyts, S., & Zamorani, G. (2011). The Lesser Role of Starbursts in Star Formation at  $z = 2$ . , 739(2), L40.

- Roediger, E. & Brüggen, M. (2007). Ram pressure stripping of disc galaxies orbiting in clusters - I. Mass and radius of the remaining gas disc. , 380(4), 1399–1408.
- Roediger, E. & Hensler, G. (2005). Ram pressure stripping of disk galaxies. From high to low density environments. , 433(3), 875–895.
- Romeo, A. B. & Fathi, K. (2016). What powers the starburst activity of NGC 1068? Star-driven gravitational instabilities caught in the act. , 460(3), 2360–2367.
- Rudnick, G., Jablonka, P., Moustakas, J., Aragón-Salamanca, A., Zaritsky, D., Jaffé, Y. L., De Lucia, G., Desai, V., Halliday, C., Just, D., Milvang-Jensen, B., & Poggianti, B. (2017). Determining the Halo Mass Scale Where Galaxies Lose Their Gas. , 850(2), 181.
- Rudnick, G., von der Linden, A., Pelló, R., Aragón-Salamanca, A., Marchesini, D., Clowe, D., De Lucia, G., Halliday, C., Jablonka, P., Milvang-Jensen, B., Poggianti, B., Saglia, R., Simard, L., White, S., & Zaritsky, D. (2009). The Rest-frame Optical Luminosity Function of Cluster Galaxies at  $z < 0.8$  and the Assembly of the Cluster Red Sequence. , 700(2), 1559–1588.
- Russell, S. & Norvig, P. (2009). *Artificial Intelligence: A Modern Approach*. USA: Prentice Hall Press, 3rd edition.
- Saglia, R. P., Sánchez-Blázquez, P., Bender, R., Simard, L., Desai, V., Aragón-Salamanca, A., Milvang-Jensen, B., Halliday, C., Jablonka, P., Noll, S., Poggianti, B., Clowe, D. I., De Lucia, G., Pelló, R., Rudnick, G., Valentiniuzzi, T., White, S. D. M., & Zaritsky, D. (2010). The fundamental plane of EDisCS galaxies. The effect of size evolution. , 524, A6.
- Sandage, A. (2005). The Classification of Galaxies: Early History and Ongoing Developments. , 43(1), 581–624.
- Sarzi, M., Falcón-Barroso, J., Davies, R. L., Bacon, R., Bureau, M., Cappellari, M., de Zeeuw, P. T., Emsellem, E., Fathi, K., Krajnović, D., Kuntschner, H., McDermid, R. M., & Peletier,

- R. F. (2006). The SAURON project - V. Integral-field emission-line kinematics of 48 elliptical and lenticular galaxies. , 366(4), 1151–1200.
- Schmidt, M. (1959). The Rate of Star Formation. , 129, 243.
- Schreiber, C., Pannella, M., Elbaz, D., Béthermin, M., Inami, H., Dickinson, M., Magnelli, B., Wang, T., Aussel, H., Daddi, E., Juneau, S., Shu, X., Sargent, M. T., Buat, V., Faber, S. M., Ferguson, H. C., Giavalisco, M., Koekemoer, A. M., Magdis, G., Morrison, G. E., Papovich, C., Santini, P., & Scott, D. (2015). The Herschel view of the dominant mode of galaxy growth from  $z = 4$  to the present day. , 575, A74.
- Shallue, C. J. & Vanderburg, A. (2018). Identifying Exoplanets with Deep Learning: A Five-planet Resonant Chain around Kepler-80 and an Eighth Planet around Kepler-90. , 155(2), 94.
- Shimakawa, R., Kodama, T., Tadaki, K. I., Tanaka, I., Hayashi, M., & Koyama, Y. (2014). Identification of the progenitors of rich clusters and member galaxies in rapid formation at  $z > 2$ . , 441, L1–L5.
- Simard, L., Clowe, D., Desai, V., Dalcanton, J. J., von der Linden, A., Poggianti, B. M., White, S. D. M., Aragón-Salamanca, A., De Lucia, G., Halliday, C., Jablonka, P., Milvang-Jensen, B., Saglia, R. P., Pelló, R., Rudnick, G. H., & Zaritsky, D. (2009). Evolution of the early-type galaxy fraction in clusters since  $z = 0.8$ . , 508(3), 1141–1159.
- Simonyan, K. & Zisserman, A. (2014). Very Deep Convolutional Networks for Large-Scale Image Recognition. *arXiv e-prints*, (pp. arXiv:1409.1556).
- Singh, R., van de Ven, G., Jahnke, K., Lyubenova, M., Falcón-Barroso, J., Alves, J., Cid Fernandes, R., Galbany, L., García-Benito, R., Husemann, B., Kennicutt, R. C., Marino, R. A., Márquez, I., Masegosa, J., Mast, D., Pasquali, A., Sánchez, S. F., Walcher, J., Wild, V., Wisotzki, L., & Ziegler, B. (2013). The nature of LINER galaxies: Ubiquitous hot old stars and rare accreting black holes. , 558, A43.

- Smith, R. J., Lucey, J. R., Hammer, D., Hornschemeier, A. E., Carter, D., Hudson, M. J., Marzke, R. O., Mouhcine, M., Eftekhazadeh, S., James, P., Khosroshahi, H., Kourkchi, E., & Karick, A. (2010). Ultraviolet tails and trails in cluster galaxies: a sample of candidate gaseous stripping events in Coma. , 408(3), 1417–1432.
- Speagle, J. S., Steinhardt, C. L., Capak, P. L., & Silverman, J. D. (2014). A Highly Consistent Framework for the Evolution of the Star-Forming “Main Sequence” from  $z \sim 0-6$ . , 214(2), 15.
- Spérone-Longin, D., Jablonka, P., Combes, F., Castignani, G., Krips, M., Rudnick, G., Zaritsky, D., Finn, R. A., De Lucia, G., & Desai, V. (2020). SEEDisCS I. Molecular gas in galaxy clusters and their large scale structure: the case of CL1411.1–1148 at  $z \sim 0.5$ . *arXiv e-prints*, (pp. arXiv:2012.09592).
- Strom, A. L., Steidel, C. C., Rudie, G. C., Trainor, R. F., Pettini, M., & Reddy, N. A. (2017). Nebular Emission Line Ratios in  $z \sim 2-3$  Star-forming Galaxies with KBSS-MOSFIRE: Exploring the Impact of Ionization, Excitation, and Nitrogen-to-Oxygen Ratio. , 836(2), 164.
- Suchkov, A. A., Hanisch, R. J., & Margon, B. (2005). A Census of Object Types and Redshift Estimates in the SDSS Photometric Catalog from a Trained Decision Tree Classifier. , 130(6), 2439–2452.
- Szegedy, C., Liu, W., Jia, Y., Sermanet, P., Reed, S., Anguelov, D., Erhan, D., Vanhoucke, V., & Rabinovich, A. (2014). Going Deeper with Convolutions. *arXiv e-prints*, (pp. arXiv:1409.4842).
- Tacchella, S., Dekel, A., Carollo, C. M., Ceverino, D., DeGraf, C., Lapiner, S., Mandelker, N., & Primack, J. R. (2016). The confinement of star-forming galaxies into a main sequence through episodes of gas compaction, depletion and replenishment. , 457(3), 2790–2813.
- Taranu, D. S., Hudson, M. J., Balogh, M. L., Smith, R. J., Power, C., Oman, K. A., & Krane, B. (2014). Quenching star formation in cluster galaxies. , 440(3), 1934–1949.

- Taylor, E. N., Hopkins, A. M., Baldry, I. K., Brown, M. J. I., Driver, S. P., Kelvin, L. S., Hill, D. T., Robotham, A. S. G., Bland -Hawthorn, J., Jones, D. H., Sharp, R. G., Thomas, D., Liske, J., Loveday, J., Norberg, P., Peacock, J. A., Bamford, S. P., Brough, S., Colless, M., Cameron, E., Conselice, C. J., Croom, S. M., Frenk, C. S., Gunawardhana, M., Kuijken, K., Nichol, R. C., Parkinson, H. R., Phillipps, S., Pimbblet, K. A., Popescu, C. C., Prescott, M., Sutherland, W. J., Tuffs, R. J., van Kampen, E., & Wijesinghe, D. (2011). Galaxy And Mass Assembly (GAMA): stellar mass estimates. , 418(3), 1587–1620.
- Tempel, E., Saar, E., Liivamägi, L. J., Tamm, A., Einasto, J., Einasto, M., & Müller, V. (2011). Galaxy morphology, luminosity, and environment in the SDSS DR7. , 529, A53.
- Tiley, A. L., Vaughan, S. P., Stott, J. P., Davies, R. L., Prichard, L. J., Bunker, A., Bureau, M., Cappellari, M., Jarvis, M., Robotham, A., Cortese, L., Bellstedt, S., & Ansarinejad, B. (2020). K-CLASH: spatially resolving star-forming galaxies in field and cluster environments at  $z \approx 0.2$ . , 496(1), 649–675.
- Tonnesen, S. (2019). The Journey Counts: The Importance of Including Orbits when Simulating Ram Pressure Stripping. , 874(2), 161.
- Toomre, A. & Toomre, J. (1972). Galactic Bridges and Tails. , 178, 623–666.
- Treu, T., Ellis, R. S., Kneib, J.-P., Dressler, A., Smail, I., Czoske, O., Oemler, A., & Natarajan, P. (2003). A Wide-Field Hubble Space Telescope Study of the Cluster Cl 0024+16 at  $z = 0.4$ . I. Morphological Distributions to 5 Mpc Radius. , 591(1), 53–78.
- Treu, T., Schmidt, K. B., Brammer, G. B., Vulcani, B., Wang, X., Bradač, M., Dijkstra, M., Dressler, A., Fontana, A., Gavazzi, R., Henry, A. L., Hoag, A., Huang, K. H., Jones, T. A., Kelly, P. L., Malkan, M. A., Mason, C., Pentericci, L., Poggianti, B., Stiavelli, M., Trenti, M., & von der Linden, A. (2015). The Grism Lens-Amplified Survey from Space (GLASS). I. Survey Overview and First Data Release. , 812(2), 114.

- Urquhart, S. A., Willis, J. P., Hoekstra, H., & Pierre, M. (2010). An environmental Butcher-Oemler effect in intermediate-redshift X-ray clusters. , 406(1), 368–381.
- van der Burg, R. F. J., McGee, S., Aussel, H., Dahle, H., Arnaud, M., Pratt, G. W., & Muzzin, A. (2018). The stellar mass function of galaxies in Planck-selected clusters at  $0.5 < z < 0.7$ : new constraints on the timescale and location of satellite quenching. , 618, A140.
- Voigt, L. M. & Bridle, S. L. (2010). Limitations of model-fitting methods for lensing shear estimation. , 404(1), 458–467.
- Vollmer, B. (2013). *The Influence of Environment on Galaxy Evolution*, volume 6, (pp. 207).
- Vollmer, B., Balkowski, C., Cayatte, V., van Driel, W., & Huchtmeier, W. (2004). NGC 4569: Recent evidence for a past ram pressure stripping event. , 419, 35–46.
- Vollmer, B., Cayatte, V., Balkowski, C., & Duschl, W. J. (2001). Ram Pressure Stripping and Galaxy Orbits: The Case of the Virgo Cluster. , 561(2), 708–726.
- Vulcani, B., Aragón-Salamanca, A., Poggianti, B. M., Milvang-Jensen, B., von der Linden, A., Fritz, J., Jablonka, P., Johnson, O., & Zaritsky, D. (2012). Cl 1103.7-1245 at  $z = 0.96$ : the highest redshift galaxy cluster in the EDisCS survey. , 544, A104.
- Vulcani, B., Poggianti, B. M., Aragón-Salamanca, A., Fasano, G., Rudnick, G., Valentinuzzi, T., Dressler, A., Bettoni, D., Cava, A., D’Onofrio, M., Fritz, J., Moretti, A., Omizzolo, A., & Varela, J. (2011a). Galaxy stellar mass functions of different morphological types in clusters, and their evolution between  $z = 0.8$  and 0. , 412(1), 246–268.
- Vulcani, B., Poggianti, B. M., Dressler, A., Fasano, G., Valentinuzzi, T., Couch, W., Moretti, A., Simard, L., Desai, V., Bettoni, D., D’Onofrio, M., Cava, A., & Varela, J. (2011b). The evolution of early-type galaxies in clusters from  $z \sim 0.8$  to  $z \sim 0$ : the ellipticity distribution and the morphological mix. , 413(2), 921–941.

- Vulcani, B., Poggianti, B. M., Finn, R. A., Rudnick, G., Desai, V., & Bamford, S. (2010). Comparing the Relation Between Star Formation and Galaxy Mass in Different Environments. , 710(1), L1–L6.
- Vulcani, B., Poggianti, B. M., Gullieuszik, M., Moretti, A., Tonnesen, S., Jaffé, Y. L., Fritz, J., Fasano, G., & Bettoni, D. (2018). Enhanced Star Formation in Both Disks and Ram-pressure-stripped Tails of GASP Jellyfish Galaxies. , 866(2), L25.
- Vulcani, B., Poggianti, B. M., Oemler, A., Dressler, A., Aragón-Salamanca, A., De Lucia, G., Moretti, A., Gladders, M., Abramson, L., & Halliday, C. (2013). The galaxy stellar mass function and its evolution with time show no dependence on global environment. , 550, A58.
- Vulcani, B., Treu, T., Schmidt, K. B., Morishita, T., Dressler, A., Poggianti, B. M., Abramson, L., Bradač, M., Brammer, G. B., Hoag, A., Malkan, M., Pentericci, L., & Trenti, M. (2016). The Grism Lens-Amplified Survey from Space (GLASS). VII. The Diversity of the Distribution of Star Formation in Cluster and Field Galaxies at  $0.3 < z \leq 0.7$ . , 833(2), 178.
- Vulcani, B., Treu, T., Schmidt, K. B., Poggianti, B. M., Dressler, A., Fontana, A., Bradač, M., Brammer, G. B., Hoag, A., Huang, K.-H., Malkan, M., Pentericci, L., Trenti, M., von der Linden, A., Abramson, L., He, J., & Morris, G. (2015). The Grism Lens-Amplified Survey from Space (GLASS). V. Extent and Spatial Distribution of Star Formation in  $z \sim 0.5$  Cluster Galaxies. , 814(2), 161.
- Wagner, C. R., Courteau, S., Brodwin, M., Stanford, S. A., Snyder, G. F., & Stern, D. (2017). The Evolution of Star formation Activity in Cluster Galaxies over  $0.15 < z < 1.5$ . , 834(1), 53.
- Webb, K., Balogh, M. L., Leja, J., van der Burg, R. F. J., Rudnick, G., Muzzin, A., Boak, K., Cerulo, P., Gilbank, D., Lidman, C., Old, L. J., Pintos-Castro, I., McGee, S., Shipley, H., Biviano, A., Chan, J. C. C., Cooper, M., De Lucia, G., Demarco, R., Forrest, B., Jablonka, P., Kukstas, E., McCarthy, I. G., McNab, K., Nantais, J., Noble, A., Poggianti, B., Reeves, A.

- M. M., Vulcani, B., Wilson, G., Yee, H. K. C., & Zaritsky, D. (2020). The GOGREEN survey: post-infall environmental quenching fails to predict the observed age difference between quiescent field and cluster galaxies at  $z > 1$ . , 498(4), 5317–5342.
- Webb, T., Noble, A., DeGroot, A., Wilson, G., Muzzin, A., Bonaventura, N., Cooper, M., Delahaye, A., Foltz, R., Lidman, C., Surace, J., Yee, H. K. C., Chapman, S., Dunne, L., Geach, J., Hayden, B., Hildebrandt, H., Huang, J., Pope, A., Smith, M. W. L., Perlmutter, S., & Tudorica, A. (2015a). An Extreme Starburst in the Core of a Rich Galaxy Cluster at  $z = 1.7$ . , 809(2), 173.
- Webb, T. M. A., Muzzin, A., Noble, A., Bonaventura, N., Geach, J., Hezaveh, Y., Lidman, C., Wilson, G., Yee, H. K. C., Surace, J., & Shupe, D. (2015b). The Star Formation History of BCGs to  $z = 1.8$  from the SpARCS/SWIRE Survey: Evidence for Significant In Situ Star Formation at High Redshift. , 814(2), 96.
- Wetzel, A. R., Tinker, J. L., & Conroy, C. (2012). Galaxy evolution in groups and clusters: star formation rates, red sequence fractions and the persistent bimodality. , 424(1), 232–243.
- Wetzel, A. R., Tinker, J. L., Conroy, C., & van den Bosch, F. C. (2013). Galaxy evolution in groups and clusters: satellite star formation histories and quenching time-scales in a hierarchical Universe. , 432(1), 336–358.
- Whiley, I. M., Aragón-Salamanca, A., De Lucia, G., von der Linden, A., Bamford, S. P., Best, P., Bremer, M. N., Jablonka, P., Johnson, O., Milvang-Jensen, B., Noll, S., Poggianti, B. M., Rudnick, G., Saglia, R., White, S., & Zaritsky, D. (2008). The evolution of the brightest cluster galaxies since  $z \sim 1$  from the ESO Distant Cluster Survey (EDisCS). , 387(3), 1253–1263.
- Whitaker, K. E., Bezanson, R., van Dokkum, P. G., Franx, M., van der Wel, A., Brammer, G., Förster-Schreiber, N. M., Giavalisco, M., Labbé, I., Momcheva, I. G., Nelson, E. J., & Skelton, R. (2017). Predicting Quiescence: The Dependence of Specific Star Formation Rate on Galaxy Size and Central Density at  $0.5 < z < 2.5$ . , 838(1), 19.

- Whitaker, K. E., Franx, M., Leja, J., van Dokkum, P. G., Henry, A., Skelton, R. E., Fumagalli, M., Momcheva, I. G., Brammer, G. B., Labbé, I., Nelson, E. J., & Rigby, J. R. (2014). Constraining the Low-mass Slope of the Star Formation Sequence at  $0.5 < z < 2.5$ . , 795(2), 104.
- Whitaker, K. E., van Dokkum, P. G., Brammer, G., & Franx, M. (2012). The Star Formation Mass Sequence Out to  $z = 2.5$ . , 754(2), L29.
- White, S. D. M., Clowe, D. I., Simard, L., Rudnick, G., De Lucia, G., Aragón-Salamanca, A., Bender, R., Best, P., Bremer, M., Charlot, S., Dalcanton, J., Dantel, M., Desai, V., Fort, B., Halliday, C., Jablonka, P., Kauffmann, G., Mellier, Y., Milvang-Jensen, B., Pelló, R., Poggianti, B., Poirier, S., Rottgering, H., Saglia, R., Schneider, P., & Zaritsky, D. (2005). EDisCS - the ESO distant cluster survey: Sample definition and optical photometry. *A&A*, 444(2), 365–379.
- White, S. D. M. & Zaritsky, D. (1992). Models for Galaxy Halos in an Open Universe. , 394, 1.
- Wild, V., Almaini, O., Dunlop, J., Simpson, C., Rowlands, K., Bowler, R., Maltby, D., & McLure, R. (2016). The evolution of post-starburst galaxies from  $z=2$  to 0.5. , 463(1), 832–844.
- Williams, R. J., Quadri, R. F., Franx, M., van Dokkum, P., & Labbé, I. (2009). Detection of Quiescent Galaxies in a Bicolor Sequence from  $Z = 0-2$ . , 691(2), 1879–1895.
- Wojtak, R., Old, L., Mamon, G. A., Pearce, F. R., de Carvalho, R., Sifón, C., Gray, M. E., Skibba, R. A., Croton, D., Bamford, S., Gifford, D., von der Linden, A., Muñoz-Cuartas, J. C., Müller, V., Pearson, R. J., Rozo, E., Rykoff, E., Saro, A., Sepp, T., & Tempel, E. (2018). Galaxy Cluster Mass Reconstruction Project - IV. Understanding the effects of imperfect membership on cluster mass estimation. , 481(1), 324–340.
- Wuyts, S., Förster Schreiber, N. M., Lutz, D., Nordon, R., Berta, S., Altieri, B., Andreani, P., Aussel, H., Bongiovanni, A., Cepa, J., Cimatti, A., Daddi, E., Elbaz, D., Genzel, R., Koekemoer, A. M., Magnelli, B., Maiolino, R., McGrath, E. J., Pérez García, A., Poglitsch, A., Popesso, P., Pozzi, F., Sanchez-Portal, M., Sturm, E., Tacconi, L., & Valtchanov, I. (2011). On Star Formation Rates and Star Formation Histories of Galaxies Out to  $z \sim 3$ . , 738(1), 106.

- Wuyts, S., Förster Schreiber, N. M., Nelson, E. J., van Dokkum, P. G., Brammer, G., Chang, Y.-Y., Faber, S. M., Ferguson, H. C., Franx, M., Fumagalli, M., Genzel, R., Grogin, N. A., Kocevski, D. D., Koekemoer, A. M., Lundgren, B., Lutz, D., McGrath, E. J., Momcheva, I., Rosario, D., Skelton, R. E., Tacconi, L. J., van der Wel, A., & Whitaker, K. E. (2013). A CANDELS-3D-HST synergy: Resolved Star Formation Patterns at  $0.7 < z < 1.5$ . , 779(2), 135.
- Yagi, M., Yoshida, M., Komiyama, Y., Kashikawa, N., Furusawa, H., Okamura, S., Graham, A. W., Miller, N. A., Carter, D., Mobasher, B., & Jogee, S. (2010). A Dozen New Galaxies Caught in the Act: Gas Stripping and Extended Emission Line Regions in the Coma Cluster. , 140(6), 1814–1829.
- Yoshida, M., Yagi, M., Komiyama, Y., Furusawa, H., Kashikawa, N., Hattori, T., & Okamura, S. (2012). Kinematics and Excitation of the Ram Pressure Stripped Ionized Gas Filaments in the Coma Cluster of Galaxies. , 749(1), 43.
- Zahid, H. J., Dima, G. I., Kudritzki, R.-P., Kewley, L. J., Geller, M. J., Hwang, H. S., Silverman, J. D., & Kashino, D. (2014). The Universal Relation of Galactic Chemical Evolution: The Origin of the Mass-Metallicity Relation. , 791(2), 130.